THE EFFECT OF METAL OXIDE ADDITIVES ON THE HYDROGEN SORPTION BEHAVIOUR OF MAGNESIUM HYDRIDE

Deborah Louise Croston

Thesis submitted to the University of Nottingham for the degree of Doctor of Philosophy

March 2007

Abstract

MgH_2 is considered to be one of the most promising options for a solid state hydrogen storage material. For practical use it is still imperative to find a convenient means of overcoming its slow kinetics and high stability. In this investigation, a range of binary and ternary metal oxides of aluminium, silicon, titanium, and zirconium, as well as Pd-modified TiO_2 samples, were prepared and characterised. The prepared oxides were ball milled with MgH_2, and the hydrogen sorption behaviour of the ball milled mixtures was investigated using DSC-TGA-MS, Sieverts and IGA. Thermodynamic parameters including enthalpies and entropies of hydrogen desorption were determined from experimental data, and activation energy calculations along with modelling of the kinetics were used to understand the mechanism and rate-limiting step of dehydrogenation.

Oxide components, calcination temperature, and surface area were found to have a significant impact on the hydrogen sorption behaviour of MgH_2 in the ball milled mixtures. Of the prepared binary and ternary oxides, TiO_2 and mixed oxides with a TiO_2 component were found to lower the dehydrogenation onset temperature by as much as 100°C, while additions of Pd - modified TiO_2 resulted in the lowest dehydrogenation onset temperature of 205°C, compared to 360°C for ball milled MgH_2. In addition, rates of hydrogen desorption and absorption were significantly increased as a result of the TiO_2 and

TiO_2 - Pd additives. Dehydrogenation of 90 % of the full H_2 capacity took 6 min at 300°C, compared to 230 min for milled MgH_2 at 350°C.

It was found that a reduction of the TiO_2 oxide resulted in the active species responsible for the enhanced dehydrogenation behaviour. Through analysis of the reaction kinetics, the mechanism of dehydrogenation was found to change from a surface controlled, contracting volume model for ball milled MgH_2 to one of a Johnson - Mehl - Avrami model of two - dimensional nucleation and growth upon addition of TiO_2 and TiO_2 - Pd.

Acknowledgements

Firstly, I would like to thank my supervisors, Gavin Walker and David Grant, for providing me with the opportunity to carry out this research, and for the invaluable guidance and support they have given me throughout the project.

I would also like to thank the research and technical staff in the School of Mechanical, Materials and Manufacturing Engineering for their assistance. In particular, I would like to thank Emily Smith and Hannah Edwards for their expertise in collecting XPS and TEM data, respectively.

To all the Wolfson postgrads, many thanks for making my time at Nottingham an enjoyable and memorable experience. Special thanks go to Hannah, Simon, and Dan, who have shared the PhD experience with me from start to finish.

I would like to thank my parents for their support, and also for the much needed chance to escape to the Scottish seaside occasionally, and climb Clachnaben (again!). I would also like to thank my sister, Judith, for listening whenever I needed a chat, and for all her advice and encouragement.

Finally, I would like to thank Neil for his patience, support and understanding, without which this would not have been possible.

The work carried out for this thesis was funded by the EPSRC as part of the UK - Sustainable Hydrogen Energy Consortium (SHEC) under the SUPERGEN initiative.

List of Abbreviations

ABO	Aluminium tri sec butoxide
AFC	Alkaline fuel cell
BET	Brunauer-Emmett-Teller
CHP	Combined heat and power
CV	Contracting volume
DMFC	Direct methanol fuel cell
DOE	Department of Energy
DRIFTS	Diffuse reflectance infrared Fourier transform spectroscopy
DSC	Differential scanning calorimetry
DTI	Department for Trade and Industry
EDX	Energy dispersive analysis of X-rays
FT-IR	Fourier transform infrared spectroscopy
ICE	Internal combustion engine
IGA	Intelligent gravimetric analyser
IPA	Isopropyl alcohol
JMA	Johnson-Mehl-Avrami
MCFC	Molten carbonate fuel cell
MS	Mass spectrometry
MWNT	Multi-walled nanotube
PAFC	Phosphoric acid fuel cell
PCI	Pressure composition isotherm
PEMFC	Proton exchange membrane fuel cell
PPM	Parts per million

PTFE	Polytetraflouroethylene
RMA	Reactive mechanical alloying
RPM	Revolutions per minute
SEM	Scanning electron microscopy
SOFC	Solid oxide fuel cell
TDW	Triply de-ionised water
TEM	Transmission electron microscopy
TEOS	Tetraethoxysilane
TGA	Thermogravimetric analysis
TIP	Titanium iso-propoxide
TPRS	Temperature programmed reaction spectrometry
XPS	X-ray photoelectron spectroscopy
XRD	X-ray diffraction
ZIP	Zirconium iso-propoxide

Table of Contents

1. Introduction

1.1. Renewable energy technologies

Evidence of global climate change resulting from CO_2 emissions associated with the burning of oil and gas [1], in addition to concerns over diminishing supplies of these fossil fuels, has provided the incentive for finding secure, non-polluting and renewable means of meeting future energy demands. For example, the current UK government has made a commitment to cut CO_2 emissions by 20 % and to provide 10 % of UK electricity from renewable sources by 2010 [2]. Over 75 % of UK CO_2 emissions are produced by road transport and industry and it is therefore important to implement clean, renewable energy technology in both mobile and stationary applications. Sources of renewable energy include solar, wind, wave, biomass, and geothermal. Renewable energy may be utilised in stationary and mobile applications by hydrogen powered fuel cell technology. It is likely that a combination of these methods will be used to provide energy in the future.

Fuel cells have the potential to provide energy in large and small scale stationary applications such as electricity for businesses and homes, as power supplies in portable devices like laptop computers or mobile phones, and in mobile applications to run cars and larger vehicles. They can also be used to provide a buffer for intermittent energy sources such as wind farms. Table 1.1 shows the major types of fuel cells, their operating conditions and applications where they may be used. The

majority of these fuel cells share the requirement for hydrogen as the energy carrier.

Fuel Cell Type	Operating Temperature / °C	Electrical Power range / kW	Fuel	Applications
Proton Exchange Membrane (PEMFC)	60-110	0.01-250	Hydrogen	Mobile, portable, low power generation.
Alkaline (AFC)	70-130	0.1-50	Hydrogen	Space, military, mobile.
Direct Methanol (DMFC)	60-120	0.001-100	Methanol	Portable, mobile
Phosphoric Acid (PAFC)	175-210	50-1000	Hydrogen	Medium to large scale power and CHP.
Molten Carbonate (MCFC)	550-650	200-100000	Hydrogen	Large scale power.
Solid Oxide (SOFC)	500-1000	0.5-2000	Hydrogen, hydrocarbons	Medium to large scale power and CHP, large scale transport.

Table 1.1: Summary of fuel cell types, adapted from [3].

1.2. Hydrogen as an energy vector

Hydrogen is the most abundant element in the universe, and has a higher energy density per unit weight than any chemical fuel (33.3 kWh kg^{-1}) [4]. Hydrogen could provide a power source for fuel cells for applications including motor vehicles, electricity supply to homes and businesses, and small portable devices. A crucial factor in the application of hydrogen to energy production is the need to develop safe and compact methods of storage.

Hydrogen in the environment is found in combination with other elements in compounds such as water and hydrocarbons, but can be released by processes including electrolysis [5], methane reforming [6], or photoconversion of water [7]. Under standard conditions (room temperature and atmospheric pressure), hydrogen is a gas (H_2) with a density of 0.08988 kg m^{-3}. This means that for compact storage as a gas, compression into large and heavy containers is required. A typical steel storage container for hydrogen operates at a pressure of 200 bar, and weighs 30 times more than the equivalent amount of gasoline [4], although pressurised tanks up to 700 bar are now also becoming available. To store hydrogen as a liquid, extremely low temperatures are necessary (< -253°C) and safety is a serious concern, as open systems are required to prevent excessive pressures (> 100 bar) building up due to high volatility [8]. The safest compact way of storing hydrogen is therefore in a solid form.

1.3. Solid-state hydrogen storage

Solid hydrogen storage is an important and very active area of research and development for achieving a practical means of providing hydrogen for the various applications discussed in Section 1.1. For the different applications and fuel cell types, the key requirements for an ideal hydrogen storage material include a high volumetric/gravimetric capacity, fast absorption and desorption of hydrogen at practical temperatures and pressures, and a high tolerance to cycling. For vehicular applications specifically, a guideline 2010 target of 5-6 wt. %

desorbed at 100°C and 0.1 MPa has been set by the US Department of Energy (DOE), while Japan and the International Energy Agency have similar targets of 5.0 wt. % and 5.5 wt. % released at 80°C and 150°C respectively [9]. For hydrogen storage materials to be used for on-board vehicular or off-board hydrogen storage, desirable properties include low cost, abundance, and safe handling, to allow them to be readily brought into widespread use safely and at the lowest possible cost. Hydrogen can be stored in solid form as part of a chemical compound such as a metal hydride or a complex hydride, or adsorbed onto the surface or in the pores of a material such as a zeolite or an activated carbon. Examples of the different categories of hydrogen storage materials, along with their capacities and operating temperatures, are listed in Table 1.2.

Storage Material Type	Examples	Capacity and typical operating conditions
High surface area and porous structures	Activated carbon Zeolites Metal organic frameworks Carbon nanostructures	Storage based on physisorption at -193°C. Capacity generally between 1 and 6 wt. % H_2. Can chemisorb 5 -15 wt. % H_2, requiring temperatures > 400°C to desorb.
Binary light metal hydrides	Magnesium hydride (MgH_2)	Capacity of 7.6 wt. % H_2. Temperature of >300°C to desorb hydrogen at 1 atm.
Interstitial and alloy metal hydrides	Lanthanum pentanickel hydride ($LaNi_5H_7$) Iron titanium hydride ($FeTiH_{1.95}$)	1-2 wt. % H_2 capacity, at an operating temperature of ~100°C.
Complex light metal hydrides	Sodium alanate ($NaAlH_4$) Lithium borohydride ($LiBH_4$)	7.5 wt. % H_2 desorbed at 100°C 18.5 wt. % H_2 desorbed at 300°C

Table 1.2: Examples of hydrogen storage materials.

1.4. Magnesium hydride

Magnesium hydride (MgH_2) is a light, inexpensive and readily available metal hydride with a hydrogen capacity of 7.6 wt. %. Its use is unfortunately hampered by its high thermodynamic stability, requiring an unfavourable combination of elevated temperatures (> 300°C) and long times (> 15 h) for sorption of hydrogen [10].

Recent studies have shown that the sorption kinetics can be improved through milling [11], mechanical alloying [12,13], and addition of various additives ranging from single metals [14,15], metal alloys and metal oxides [16,17], to graphite and other carbon structures [18-21]. These studies have shown that it is possible to bring modified MgH_2 closer to

meeting targets such as those set by the DOE. There is still great potential to improve further on its basic properties with research into as yet unexplored additives and activation methods.

1.5. Aims and scope of the research

This thesis covers research into a range of oxide-based additives aimed at improving the hydrogen sorption properties of MgH_2 to produce materials with decreased onset temperatures of hydrogen desorption, faster rates of hydrogen desorption and absorption, and consistent behaviour under cycling. The beneficial effects of oxide additives for MgH_2 have been reported in the past, but mixed oxides have not previously been investigated, nor have the effects of preparation and heat treatment of the oxides been studied in the context of their effect on the hydrogenation and dehydrogenation properties of MgH_2. In this investigation, sol-gel prepared oxides based on Al_2O_3, SiO_2, TiO_2 and ZrO_2, and combinations of these oxides have been ball milled with MgH_2 to produce novel materials.

In addition, Pd is known to be an effective catalyst for desorption of hydrogen from MgH_2, but it is possible that by dispersing the Pd onto a support such as TiO_2, an improvement in properties coupled with a reduction in the amount of costly Pd required could be achieved. An investigation of the possible synergistic effects of combining Pd with oxides for addition to MgH_2 has therefore also been carried out.

The materials have been thoroughly characterised using a number of techniques including powder X-ray diffraction (XRD), scanning electron microscopy (SEM), transmission electron microscopy (TEM), X-ray photoelectron spectroscopy (XPS), and diffuse reflectance infrared Fourier transform spectroscopy (DRIFTS), and their hydrogen sorption behaviour has been investigated through volumetric and gravimetric methods. Kinetics of hydrogen absorption and desorption of the prepared materials have been analysed, and mechanisms have been proposed to explain the kinetic behaviour of the mixtures and how they are affected by the different additives.

1.6. Thesis overview

Chapter 2 provides a critical review of the currently published literature relating to MgH_2 and the tried methods of improving on its thermodynamic and kinetic properties including ball milling, alloying, and the range of additives already studied by other research groups. In Chapter 3, the experimental methods used in preparing the materials studied in this work are described, along with an explanation of the different characterisation techniques used in studying the prepared materials. Chapters 4 and 5 contain the results of the materials characterisation and hydrogen sorption studies. Chapter 4 includes the characterisation of the binary and tertiary metal oxide additives based on Al_2O_3, SiO_2, TiO_2 and ZrO_2, as well as Pd-modified TiO_2 materials. In Chapter 5, results of the investigation of hydrogen desorption behaviour of MgH_2 milled with the additives described in Chapter 4 are presented.

Chapter 5 also includes thermodynamic, kinetic, and cycling results. In Chapter 6, the results from Chapters 4 and 5 are summarised and discussed in the context of the prior literature reviewed in Chapter 2. Conclusions of the work are presented in Chapter 7, and a discussion of future work arising from the research presented in this thesis is the subject of Chapter 8.

2. Literature Review

2.1. Outline

As stated in the introduction to this thesis, the search for renewable low carbon energy technologies has sparked a great deal of recent research into storage materials for hydrogen energy. The following review will include a general synopsis of metal hydrides and the wide range of hydrides that have been studied for their potential use as effective hydrogen storage materials, followed by a detailed review of research relating to magnesium hydride. This review will cover work on understanding the thermodynamics and kinetics of MgH_2 formation and decomposition, and the methods that have been employed to enhance the hydrogen storage properties of the material, including ball milling, and additives including metals, alloys, and oxides. Finally, the summary in Section 2.5 explains the aims of the research undertaken for this thesis in the context of the work that is already reported in the literature.

2.2. Metal hydride properties

In a metal hydride, such as MgH_2, the hydrogen is stored as a chemically bonded component of the compound. The generic equation for hydride formation is as follows:

$$M_{(s)} + x/2\ H_{2(g)} \rightarrow MH_{x(s)}$$

For any given temperature, an equilibrium hydrogen pressure exists above which the hydride will form, and below which the hydride will decompose into the component metal and hydrogen gas. The formation of the metal hydride as H_2 pressure is increased proceeds via the following steps [4]: Firstly, the H_2 molecules adsorb onto the metal surface, and then dissociate into H atoms. These then diffuse into the metal crystal lattice. A critical concentration and pressure are reached at which the metal is saturated with hydrogen, and the metal hydride phase begins to form. Hydrogen uptake continues at this equilibrium or plateau pressure until all of the metal is converted to hydride.

Metal hydrides offer benefits including high volumetric hydrogen densities, as well as a safe and sustainable storage medium from which the hydrogen is released by heating. The heat required to release hydrogen gas is directly proportional to the stability of the hydride, thus a more stable hydride will require a greater amount of heat to produce hydrogen.

The thermodynamic properties of hydrides can be understood through the pressure - composition - isotherm (PCI), which relates the hydrogen capacity and pressure at a given temperature. A typical PCI is shown in Figure 2.1.

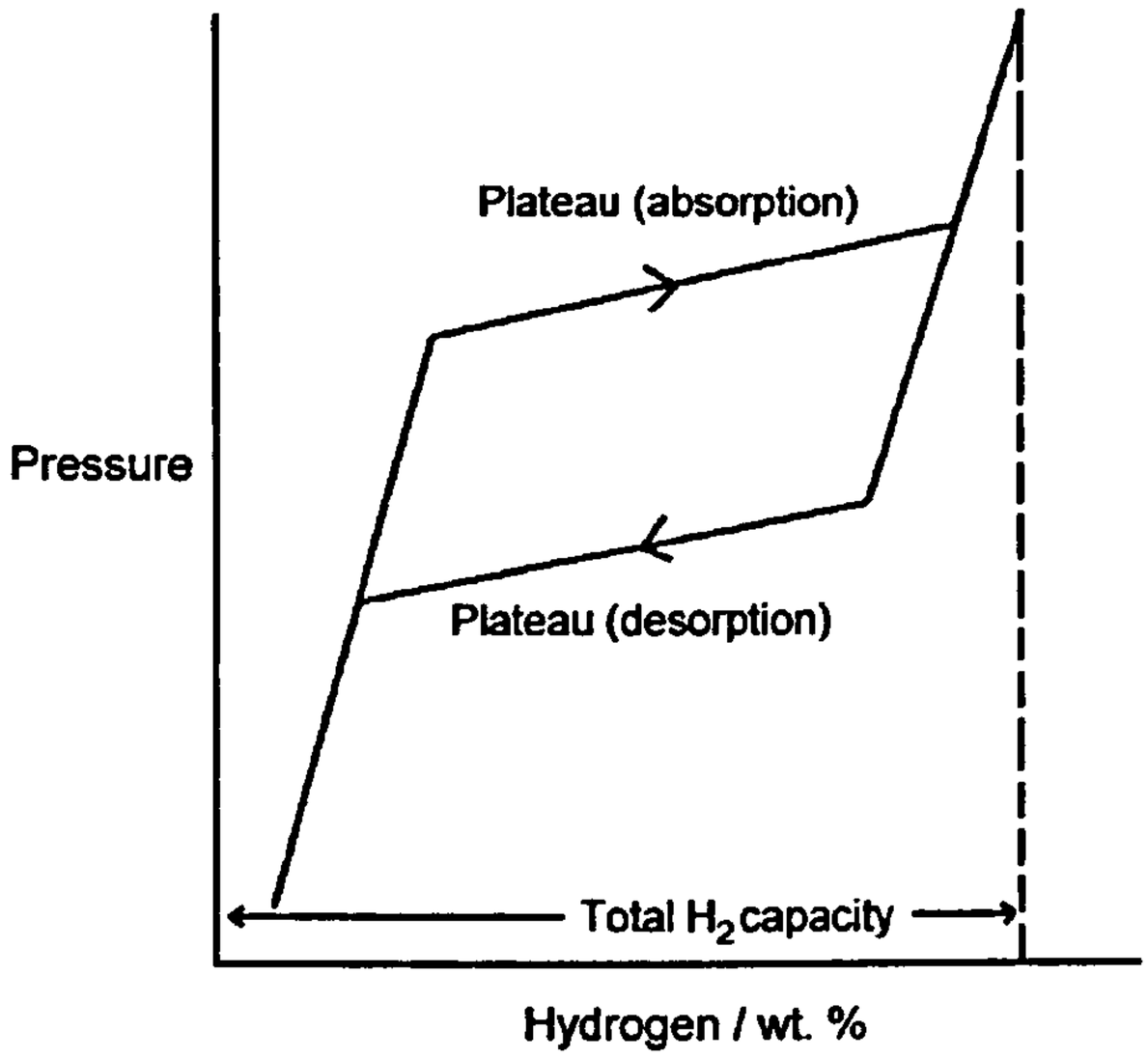

Figure 2.1: Example of PCI

The plateau or equilibrium pressures for hydrogen absorption and desorption shown on the graph correspond to the pressures required for hydrogen absorption and desorption at the given temperature. These values will increase with increasing temperature, and this relationship between plateau pressure and temperature, following the van't Hoff equation (equation 2.1) [22], allows the enthalpy (ΔH) and entropy (ΔS) of the reaction (absorption or desorption) to be determined. Example van't Hoff plots for some binary metal hydrides are shown in Figure 2.2.

$$\ln P = \frac{\Delta H}{RT} - \frac{\Delta S}{R} \qquad \text{equation 2.1}$$

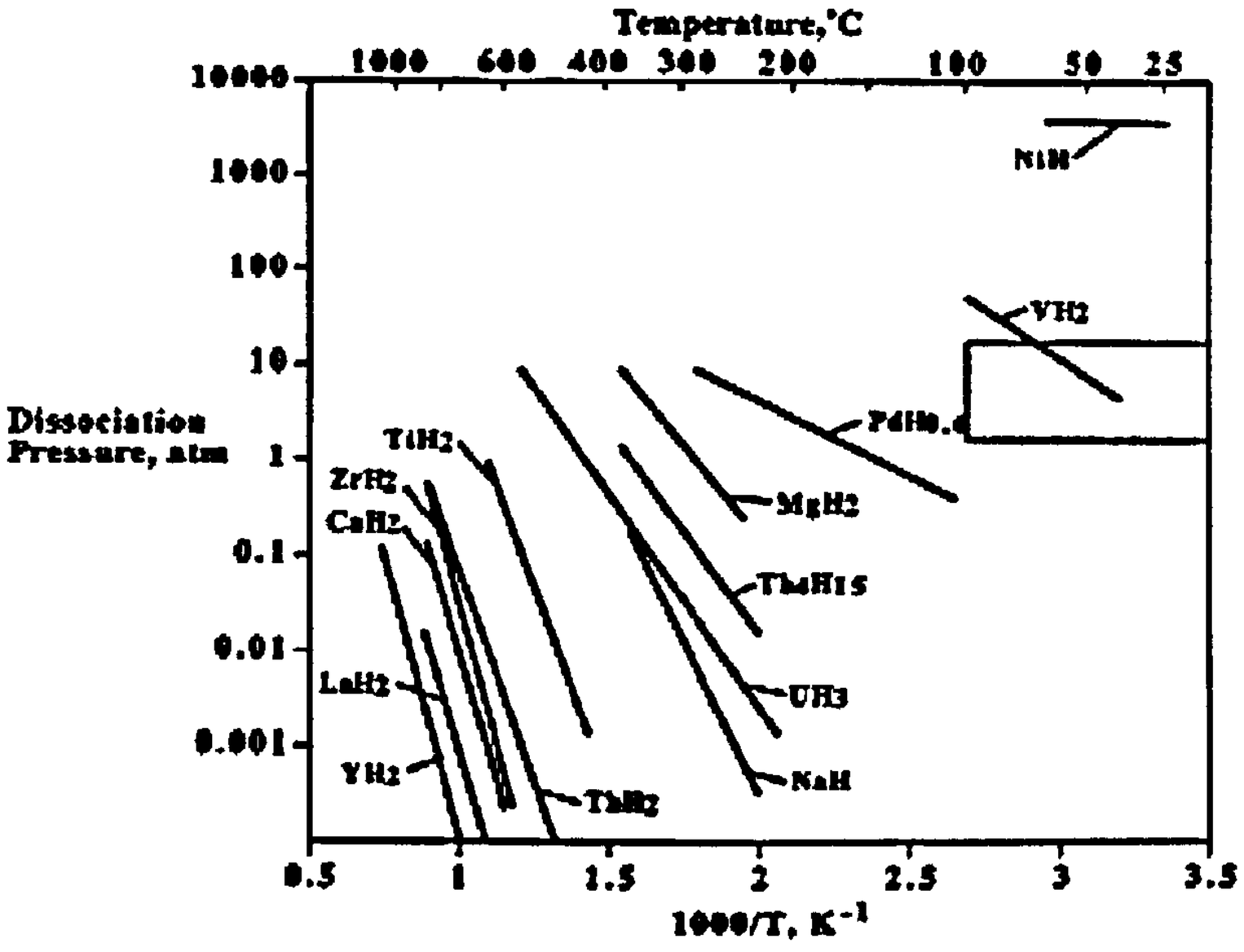

Figure 2.2: van't Hoff plots for some binary metal hydrides [23].

The values of ΔH and ΔS of hydrogen desorption for a given hydride give an indication of its thermal stability, with a higher value indicating a more stable hydride. From the equation relating them to the Gibb's free energy (ΔG) (equation 2.2), an equilibrium temperature (T), can be obtained, where $\Delta G = 0$. This is the temperature above which the desorption of hydrogen from the hydride will occur spontaneously under 1 bar of H_2 pressure.

$$\Delta G = \Delta H - T\Delta S \qquad \text{equation 2.2}$$

It should be noted that these values only provide means of describing and comparing the thermodynamic stability of given hydrides, and do not provide any information on how quickly the absorption or desorption of hydrogen will occur, *i.e.* the reaction kinetics, which are also of great importance. While a low temperature for hydrogen desorption and absorption is a key requirement for the practical application of hydrides for hydrogen storage (particularly in vehicular applications, where an operating temperature of 100°C or less is demanded) there is also a need for fast rates of hydrogen desorption and absorption, to allow for fast discharging and recharging of the hydride. For vehicular application, a refuelling time of 5 min or less is required, according to US DOE targets.

2.3. Candidate hydrides for storage applications

The range of potential hydrides for application in hydrogen storage is extensive, and a comprehensive database of hydride materials that have been studied for hydrogen storage applications has been compiled and is available online (hydpark.ca.sandia.gov).

The hydrides can be divided into three general categories: the intermetallic hydrides, the binary or elemental hydrides, and the complex hydrides. Detailed reviews of these hydride types and their properties are available in the literature [23-25], and a brief summary, with some specific examples, is given in Table 2.1.

Hydride Type	Examples	Capacity / wt. % H_2	Decomposition Temperature / °C	Comments
Intermetallic	AB_5 ($LaNi_5$, $CeCo_5$)	1.4-1.9	ambient	Generally moderate to rapid kinetics - as low as a few seconds for decomposition.
	AB (FeTi, TiAl)	≤1.8		
	AB_2 (ZrV_2, $ZrCr_2$)	1.5-2.0		Low capacities.
	Others ($ErCo_3$, Th_2Fe_7)	≤ 1.6		Cycling stability can degrade after 300-400 cycles.
Binary (elemental)	MgH_2	7.6	330	
	CaH_2	4.8	600	Slow kinetics, with activation and catalysts required.
	NaH	4.2	425	Low cost (Mg, Ca, Na metals) is an advantage.
	LiH	12.6	720	
Complex	$NaAlH_4$	5.5	125	Li compounds irreversible.
	$NaBH_4$	13.0	400	Expensive.
	$LiBH_4$	18.5	380	

Table 2.1: Summary of different metal hydride groups and examples of commonly studied hydrides.

Binary or elemental hydrides can be formed by most of the elements in the periodic table given the right conditions of temperature and pressure, however, most are unsuitable for hydrogen storage due to their low capacities, or the high pressures and temperatures required for hydrogen sorption [23]. To achieve the highest possible gravimetric hydrogen densities, candidate hydrides are effectively limited to those containing the light elements: Li, Be, Na, Mg, and Al [26]. Lithium and sodium hydrides are highly stable requiring temperatures of 720°C and 425°C for decomposition, respectively. Beryllium hydride is extremely hard to make and is therefore costly, and polymeric aluminium trihydride does not form reversibly from the elements. As shown in Table 2.1., MgH_2 offers the best balance between hydrogen capacity and decomposition temperature, as well as low cost. Slow kinetics of hydrogen sorption are a barrier to the use of these materials for hydrogen storage, and a number of approaches to improve storage capacities and kinetics at low temperature have been researched. It is commonly acknowledged that the most effective means of developing a hydrogen storage material of the desired low cost, reversibility, and low temperature hydrogen sorption involves the study of catalysts in combination with ball milling or reactive mechanical grinding [24], as discussed in more detail in Section 2.4.

The intermetallic hydrides were historically developed with the aim of tailoring the thermodynamic properties of the hydrides to achieve reversible hydrogen storage under practical operating conditions. In

general, elements are selected that form hydrides with very different thermodynamic stabilities. These elements are combined to form an intermetallic with intermediate hydride forming properties. The classic example of an intermetallic hydride is $LaNi_5$. The individual components, La and Ni, form hydrides which are relatively stable ($\Delta H_{decomposition}$ LaH = 208 kJ mol^{-1}) and relatively unstable ($\Delta H_{decomposition}$ NiH = 8.8 kJ mol^{-1}), respectively. When alloyed, the resulting intermetallic hydride has an intermediate thermodynamic stability ($\Delta H_{decomposition}$ $LaNi_5H_6$ = 30.9 kJ mol^{-1}). This phenomenon has been widely explored, and a vast range of element combinations have been used to create alloys with tailored hydrogen storage properties [23]. Examples of the elements used and types of intermetallics formed are given in Table 2.1. Although fast kinetics (a few seconds for complete desorption at ambient temperature) can be achieved with these materials, they suffer from low hydrogen capacities (<2.0 wt. %) which limits their use for mobile applications where high gravimetric densities are demanded.

Complex hydrides are ionic compounds formed from the light elements (Li, Be, Na, Ca, Mg, Al, and B). The principal materials studied in this category include the alanates and borates, generally of the form mnH_4, where *m* is either lithium or sodium, and *n* is either aluminium or boron. The resulting hydrides have high hydrogen capacities ranging from 5.5 wt. % for $NaAlH_4$ to 18.5 wt. % for $LiBH_4$. These hydrides are known to release high capacities of hydrogen by hydrolysis, but the reactions are not fully reversible in the gas phase. In addition to their irreversibility,

the higher capacity materials require high temperatures in order to achieve hydrogen release rates that are fast enough for mobile applications. To date, attempts to improve low temperature kinetics and achieve reversibility in complex metal hydrides have primarily been focussed on the addition of titanium and zirconium catalysts added by ball milling with $TiCl_3$, $ZrCl_3$, $Ti(OBu^n)_4$, $Zr(OPr^n)_4$, nanoparticulate Ti and TiN [27-33]. This catalytic effect was first reported by Bogdanovic *et al.* [32], who found that at 160°C, undoped $NaAlH_4$ released hydrogen at a negligible rate, while $NaAlH_4$ with 2 mol. % addition of $Ti(OBu^n)_4$ released close to its full capacity of 4.2 wt. % within 6-8 h. Over the course of 35 cycles, the rate of hydrogenation of the doped sample was found to decrease, resulting in an apparent lowering in the H_2 capacity to 3.1 wt. % reached during the time period of 21 h. More recently, the nanoparticulate nature of the catalysts have been shown to be important in maintaining the cycling stability of the hydride. Additions of 2 mol. % nanoparticulate TiN to $NaAlH_4$ resulted in a storage capacity of 5 wt. % that was maintained over 17 cycles [33]. From XRD studies of $NaAlH_4$ with $TiCl_3$, it has been shown that the additive reacts with the hydride upon milling, resulting in the formation of NaCl [34]. It has been suggested that the resulting Ti^{3+} ions are substituted into the lattice of the hydride, causing a distortion of the lattice [31]. In spite of high levels of recent research activity in this area, the exact nature of the catalysts and how they act in enhancing the dehydriding and rehydriding of complex hydrides is still not well understood [24].

Although the high hydrogen capacities of the complex hydrides make them appear good candidates for hydrogen storage materials, particularly for mobile applications, the cost of these complex materials and the irreversibility of their decomposition are still significant barriers to their use. Further understanding of the mechanisms of the catalytic action of Ti and Zr additives is also still required.

2.4. Magnesium Hydride

Current investigations have not yet resulted in a hydride with properties near to meeting the combined targets such as those set by the US DOE for mobile applications of 6 wt. % H_2 evolved at 100°C and 0.1 MPa. In general terms, the choice of a practical material is limited by a number of criteria. These include ease of formation and decomposition, stability, abundance, cost, tolerance to cycles of charging and discharging, and safety [35]. An ideal material should evolve hydrogen relatively quickly at low temperature.

Of the simple light metal hydrides, excluding the complex alanates and borates, magnesium hydride (MgH_2) offers the best combination of high hydrogen content (7.6 wt. %) and associated energy density (9 MJ kg^{-1}) for reversible hydrogen storage, coupled with the relatively low decomposition temperature of 330°C. The formation of β - phase MgH_2 was first reported in 1912, from the pyrolysis of ethylmagnesium iodide [36]. It was subsequently found to form from the elements Mg and H, in a very slow reaction requiring high temperature and hydrogen pressure

[37-39]. As H is introduced into the hexagonally close packed Mg metal lattice, the H atoms initially occupy tetrahedral interstitial sites, forming the α - phase, a solid solution of H in Mg, for H concentrations up to a maximum of *ca.* 9 at. % near the melting temperature of *ca.* 650°C [40]. Upon further addition of H, the β - MgH_2 phase is formed. β - MgH_2 has a tetragonal crystal structure, of the rutile form, with space group *P42/mnm* and lattice parameters a and b = 0.451 nm and c = 0.302 nm [40]. The Mg atoms are octahedrally coordinated to six H atoms, while the H atoms are coordinated to 3 Mg atoms in planar coordination. The structure and bonding in β - MgH_2 was investigated by Noritake *et al.*, using synchrotron radiation powder data. Their results showed very weak ionic and covalent bonding between the Mg and H within MgH_2 [41]. The structure is represented in the following diagram, Figure 2.3, which shows the location of the Mg and H atoms within the tetragonal unit cell.

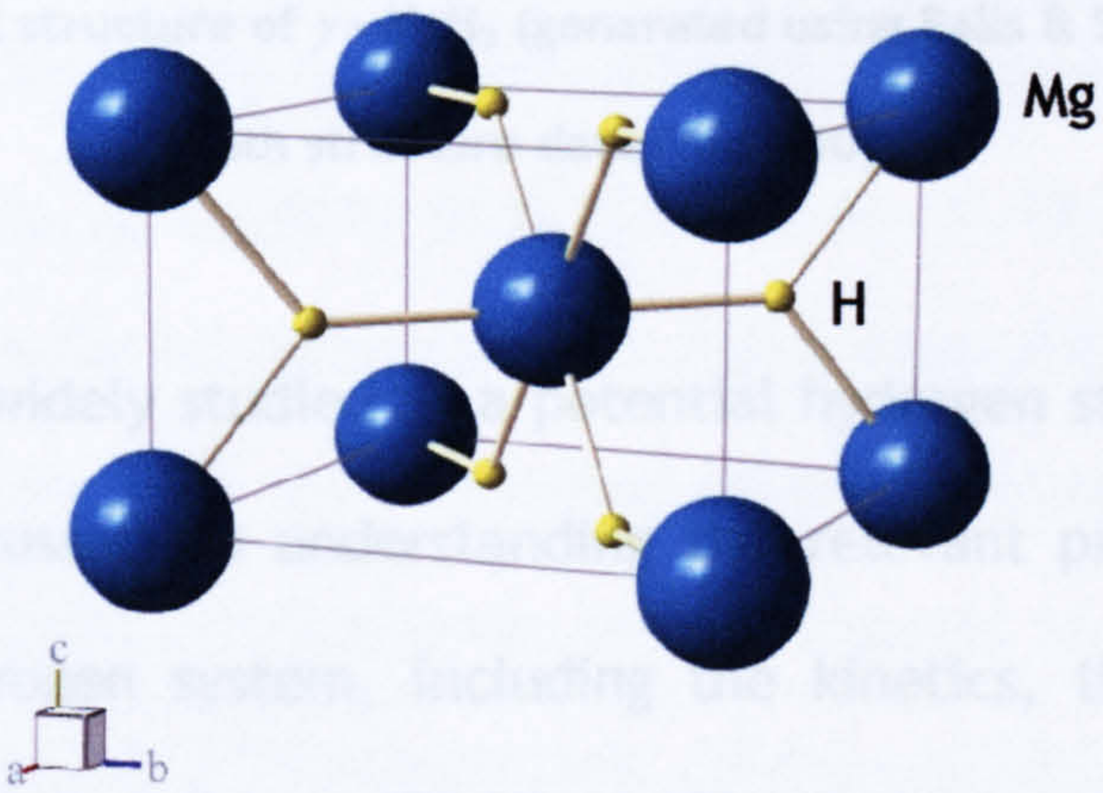

Figure 2.3: Crystal structure of β - MgH_2 (generated using Balls & Sticks version 1.51 with structure data from [40]).

When subjected to high compressive stress (7 - 8 GPa), β - MgH_2 is known to transform into the metastable γ - phase of MgH_2 [42,43]. γ - MgH_2 has an orthorhombic structure analogous to α - PbO_2, with space group *Pbcn* and lattice parameters a = 0.453 nm, b = 0.544 nm, and c = 0.493 nm [43]. The packing and coordination of the Mg and H atoms are not affected by the transformation, but the H octahedra surrounding each Mg atom are deformed, as the straight octahedral chains take on a zig-zag form. The unit cell of γ - MgH_2 and the positions of the Mg and H atoms are shown in Figure 2.4.

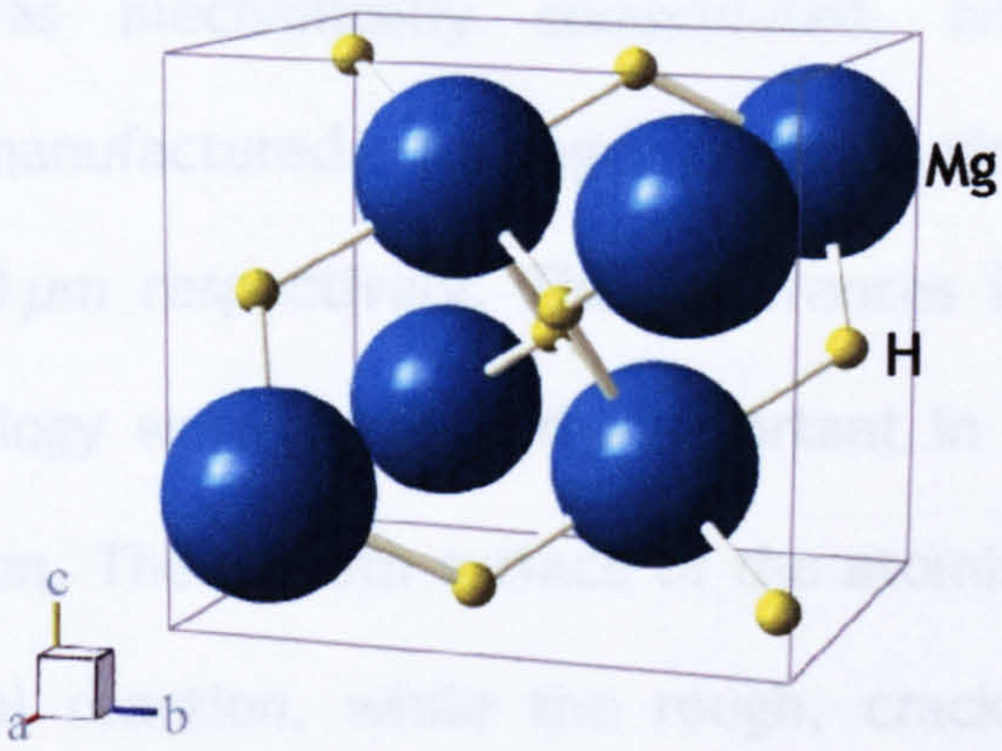

Figure 2.4: Crystal structure of γ - MgH_2 (generated using Balls & Sticks version 1.51 with structure data from [40]).

MgH_2 has been widely studied as a potential hydrogen storage material, with efforts focussed on understanding the relevant properties of the magnesium hydrogen system, including the kinetics, thermodynamics, activation, and reversibility [37,38,44,45]. Methods of improving the hydrogen storage capability have been the subject of investigation by a number of research groups around the world. The key areas of work

include methods of milling and grinding [11-13], doping with additions of transition metals [14,15], carbon materials [18-20] and oxides [16,17].

In the early 1980s, Vigeholm *et al.* published results of thermogravimetric analysis of the absorption and desorption of hydrogen from three different magnesium samples, observing the effects of variation in pressure at constant temperature, variation in temperature at constant pressure, cycling, and particle structure of the starting material [10]. The three different samples, all of approximately 99.9 % purity, varied in terms of preparation method: The first was atomised, the second was mechanically comminuted, and the third was mechanically manufactured. Average particle sizes were 12.5 μm, <50 μm, and 50 μm respectively. The differences in particle size and surface morphology were particularly important in terms of activation for hydrogenation. The smooth surface of the atomised sample resulted in a slow initial reaction, while the rough, cracked surfaces of the mechanically produced samples were more immediately reactive. In cycling experiments using a high pressure microbalance, there were no apparent changes in capacity over the course of 10-30 absorption - desorption cycles for all three samples. Equilibrium enthalpy (ΔH_H) and entropy (ΔS_H) values of the hydriding reaction calculated from the experimental equilibrium isotherms were measured to be -70 kJ mol^{-1} and -126 J K^{-1} mol^{-1} (± 1 %) respectively. These values have since been refined by calorimetric measurements carried out by Bogdanovic *et al.*, who calculated the enthalpy and enthalpy of MgH_2 formation as

-72.9 kJ mol^{-1} and -132.2 J K^{-1} mol^{-1} respectively [45]. A small dependence of these values on Mg particle size was also observed, with a difference of *ca.* 2 kJ mol^{-1} in the enthalpy value for an increase in Mg particle size from 25-40 μm to 70-100 μm.

Belkbir *et al.* investigated the absorption and desorption mechanism of MgH_2 using thermogravimetry and microscopy [46]. It was found that at elevated temperature (327°C), the hydride formed at the grain surface, and its rate of formation was controlled by the density of nucleation sites. The reaction stopped when a hydride layer covered the surface of the magnesium. In decomposition, the magnesium formed as pellets on the grain surface, which then developed into the grains. The original grain size was maintained.

Based on results of differential scanning calorimetry (DSC) experiments, a more detailed 3-stage dehydrogenation process was proposed by Bohmhammel *et al.*, involving the initial formation of α - Mg at the surface of a particle, followed by the formation and growth of Mg - nuclei. Finally, the Mg phase is formed, accompanied by a contraction in particle volume and the formation of cracks aiding diffusion through the particle [44].

Due to its relative abundance, low cost, and high hydrogen capacity, MgH_2 is recognised as one of the most promising hydrides for energy storage. In recent years there has been a resurgence of effort in

developing practical hydrogen storage materials, with a number of groups endeavouring to improve on the low temperature kinetics of the hydride formation/decomposition, as discussed in the following sections on ball milling and additives.

2.4.1. Ball milling of MgH_2

Ball milling has been studied extensively as a method of improving the hydrogen sorption behaviour of a number of hydrogen storage materials including MgH_2. A range of different types of ball mills have been used, with the majority of experiments carried out using either a vibratory or shaker style mill (such as a Spex 8000) or a planetary style mill (*e.g.* a Fritsch P5). Studies of impact energies and temperatures in these mills during milling have shown significant differences between the different types of mills [47,48]. Local ball temperatures have been found to be below 100°C in shaker type ball mills, while temperatures above 200°C have been reported for planetary style mills. Different milling vial and ball materials and sizes, as well as ball to powder weight ratios, all have an effect on the particle size, degree of agglomeration, presence of contaminants, and structure of the resulting powders.

In order to improve on the sorption kinetics of MgH_2, Huot *et al.* studied the effects of high energy ball milling in a shaker style Spex 8000 ball mill with hardened steel vial and balls [11]. Pure magnesium hydride with an average particle size of 20 μm was ball milled for up to 20 h. XRD experiments at various stages of milling revealed a transformation

after only two hours, to a mixed phase sample containing 74 wt. % β - MgH_2, 18 wt. % γ - MgH_2, and 8 wt. % MgO. The specific surface area increased from 1.2 $m^2 g^{-1}$ to 9.9 $m^2 g^{-1}$ over the total 20 h milling time. SEM images revealed a corresponding decrease in particle size, agglomeration, and increase in surface roughness. From pressured DSC experiments under 2 bar of hydrogen with a heating rate of 10°C min^{-1}, ball milling for 20 h was found to reduce the hydrogen desorption temperature by 64°C, from 420°C to 356°C, and to improve the rate of desorption at 350°C by 5 times, from > 3000 s for full desorption from an unmilled sample to 600 s after ball milling. These improvements were explained by the increased surface area and introduction of defects, which increased nucleation sites and reduced the diffusion path length for hydrogen leaving the hydride.

Further studies on the effects of ball milling on the properties of MgH_2 have confirmed the effect of particle size on the desorption of H_2. Varin *et al.* analysed samples of MgH_2 milled for time periods from 0.25 - 100 h in a planetary style mill (Uniball 5) and found that the smallest particles, with a mean size of 400 - 600 nm, had the lowest desorption onset temperature of 340 - 360°C, when measured using DSC [49]. Figure 2.5 shows a graphical representation of Varin *et al.*'s results of the relationship between average MgH_2 particle size measured from SEM, and the onset temperature of H_2 desorption.

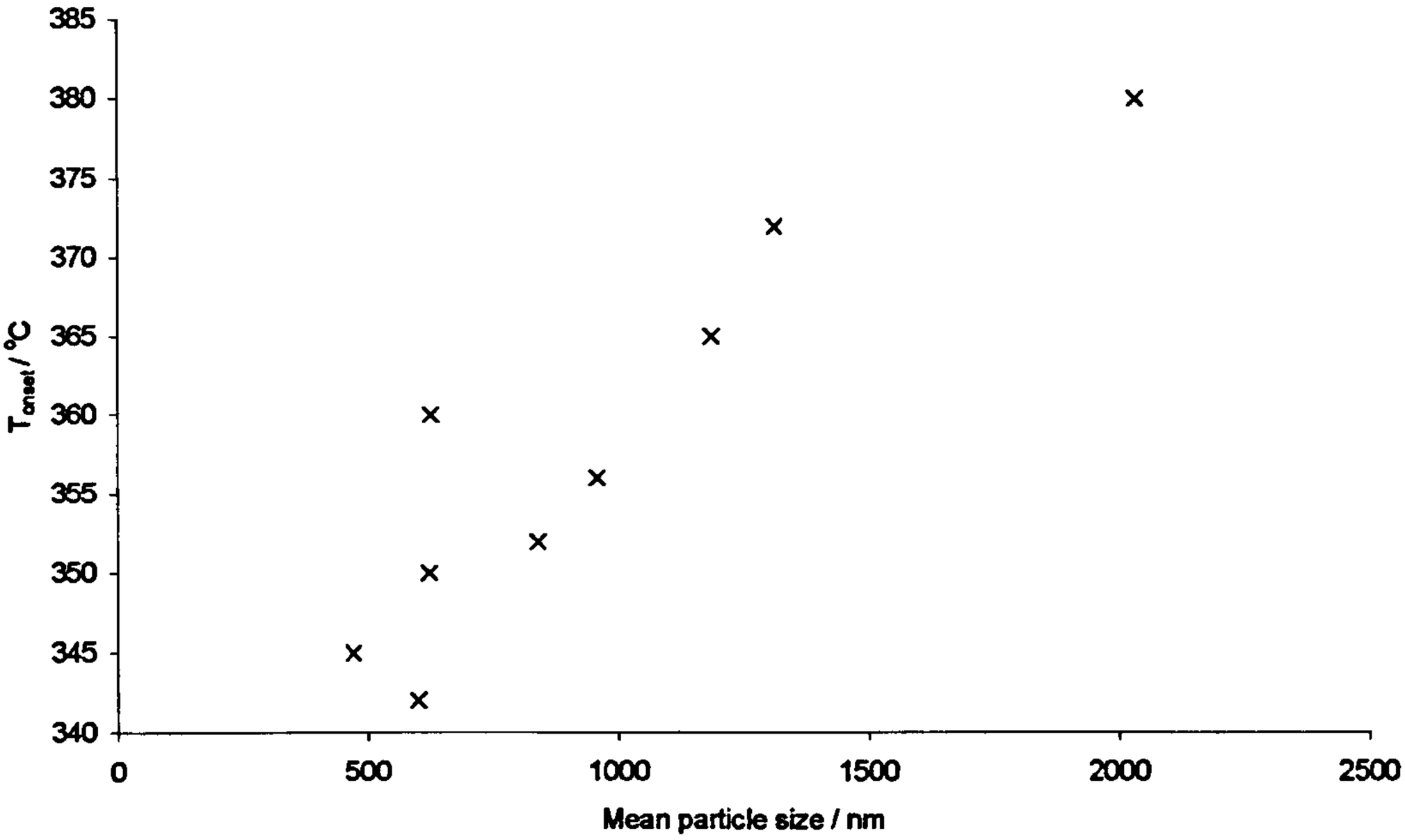

Figure 2.5: Effect of MgH_2 particle size on onset temperature of H_2 desorption (plotted from data in [50]).

In addition to reduced particle size, they also suggest the involvement of the γ-MgH_2 phase in lowering the desorption onset temperature by decomposing at lower temperature, and destabilising the remaining β-MgH_2.

As an alternative to the direct ball milling of MgH_2 in an inert atmosphere, a number of groups have studied the use of reactive mechanical alloying (RMA) in a hydrogen atmosphere [12,51-54]. In RMA, particles of Mg are ball milled in an atmosphere of H_2 gas, resulting in a mixture of γ and β - MgH_2 of small particle size.

Regardless of the method used to prepare milled MgH_2, agreement has not yet been reached on the exact mechanisms of H_2 desorption from

ball milled MgH_2. The rate limiting step in the desorption of hydrogen from MgH_2 has been proposed to be either the diffusion of H_2 through Mg forming at the surface of particles as hydrogen is desorbed [55], or the recombination of H_2 molecules on the particle surface prior to desorption [56]. In both cases, a reduction in particle size resulting from ball milling could be expected to enhance the rate of hydrogen desorption, either by reducing diffusion path lengths for H_2, or by increased surface area available for recombination of H_2 molecules.

2.4.2. Additives to MgH_2

Although linear extrapolation of the data presented in Figure 2.5 suggests a lower limit of desorption temperature for MgH_2 of 335°C, Varin et al. have proposed a critical threshold of particle size below which the desorption onset temperature decreases more rapidly, predicting that reducing MgH_2 particle size to the nanometre scale could achieve hydrogen desorption at temperatures as low as 200°C [49], In addition, modelling using *ab initio* and density functional theory calculations has shown the destabilisation of MgH_2 with decreasing cluster size, and that a crystallite size of 0.9 nm could result in a desorption temperature of 200°C [57]. To date, however, ball milling has only achieved a lowering of the MgH_2 desorption temperature to *ca.* 340°C. In order to further improve the hydrogen sorption properties of MgH_2, a range of additives have been mixed with magnesium hydride in the ball milling process, including metals, alloys, metal oxides, and carbon materials. Metal and alloy additives studied include transition

metals such as Ni [14], Co [14], Ti [58,59], Fe [14], V [58,60,61], Pd [62-67], and Nb [68-70], as well as intermetallics such as $LaNi_5$ and FeTi [71].

The effect of V metal additives on MgH_2 have been presented in a number of reports [58,60,61]. Liang *et al.* formed a nanocomposite of β - MgH_2 + γ - MgH_2 + $VH_{0.81}$ by milling together MgH_2 powder with 5 at. % (*ca.* 9.7 wt. %) vanadium [60]. Sorption kinetics were studied after 20 h of milling, using volumetric measurements from an automated Sieverts apparatus. Key results from their work include the complete desorption of hydrogen occurring after 200 s at 300°C, as opposed to 2000 s for 2 wt. % desorption from pure MgH_2; a reduction in activation energy for the desorption process from 120 kJ mol^{-1} to 64 kJ mol^{-1}; and a re-absorption of 2 wt. % H_2 in 1000 s, at room temperature. Ti metal has been show to behave in a similar way to V, with fast kinetics reported, of 5 min for complete hydrogen desorption from MgH_2 at 300°C for a sample of MgH_2 ball milled with 9 wt. % Ti [59].

Another metal that has been studied as an additive for MgH_2 is Pd [62-67]. Zaluska *et al.* studied the effect of Pd nanoparticles on the absorption and desorption of H_2 from MgH_2 [64]. Additions of up to 1 wt. % Pd were added to the MgH_2 powder during ball milling in a shaker style Spex 8000 ball mill, resulting in dispersed nanoparticles of Pd on the MgH_2 surface. Hydrogen absorption and desorption rates were measured using a volumetric method at temperatures ranging from 230 to 330°C, with an absorption pressure of 10 bar H_2, and a desorption

pressure of 1 bar H_2. Rates were significantly improved by the presence of the Pd, with full absorption of hydrogen (*ca.* 6 wt. %) occurring in less than 40 min, compared to 120 min for ball milled MgH_2 of a similar particle size (30 nm) with no added Pd. The strong dissociative effect of Pd on H_2 at the Mg surface overcame the detrimental effect of surface oxidation, and eliminated the need for an activation process. The expense of Pd was noted by the authors and studies of other metal nanoparticle catalysts found Fe to also be effective in enhancing the kinetics of hydrogen absorption and desorption from MgH_2.

Nanocomposite hydrogen storage materials have also been formed by milling magnesium hydride with intermetallics of Mg_2Ni, FeTi, $LaNi_5$ [71], PdFe [65], or $MmNi_{5-x}$ $(CoAlMn)_x$ [72]. The intermetallic phases, with faster hydriding kinetics, are used to catalyse the hydriding of the magnesium. The fast adsorption of hydrogen at or near the magnesium surface by the intermetallic phase floods the metal with hydrogen atoms, reducing the activation energy by diminishing the effect of the oxide barrier at the metal surface. Liang et al. found that a 50/50 weight ratio mixture of $LaNi_5$ and Mg formed a Mg + LaH_x + Mg_2Ni composite on hydrogen cycling at 300°C. The resulting composite was found to release 2.5 wt. % H_2 in 500s at room temperature and a pressure of 1.5 MPa H_2. Key factors in tailoring the hydrogen sorption properties of these composites include retaining small particle size, optimising the ratio of the components, and selecting an intermetallic with high dissociation efficiency for H_2.

A number of groups have used a different approach to forming mixtures, involving RMA of magnesium with additives. RMA is similar to ball milling, except that it is performed under hydrogen gas, rather than in an inert atmosphere, and the hydride therefore forms *in situ*. Additives including Co[12] [73], V [21], Ge [15], Ni [73,74], Nb [75], and Fe [21,73] have been used to catalyse the formation of magnesium hydride by this method. Huot *et al.* found that a mixture of Mg + 5 at. % V + graphite was hydrided after an hour of milling at 300°C, 4 bar H_2 [21].

The mechanisms at work in RMA are not yet fully understood. Bobet *et al.* studied RMA of magnesium with 10 wt. % Co, Ni, or Fe, in an attempt to identify the effects of RMA on the hydriding properties [73]. They concluded that the embrittlement of the Mg caused by the hydrogen gas during milling aided a reduction in particle size, while the elemental additions increased the amount of MgH_2 formed at room temperature. Co and Fe were found to be particularly effective at catalysing hydride formation, reportedly due to the lower stability of Mg - Co and Mg - Fe phases compared to more stable Mg-Ni compounds. RMA also prevented the formation of a detrimental oxide layer, due to accelerated hydride formation over the surface of the metal.

Carbon materials that have been milled with Mg or MgH_2 have included graphite [18,20,21] and multi-walled carbon nanotubes (MWNT) [19]. The presence of the graphite was thought to enhance H_2 dissociation close to the Mg/MgH_2 surface, and to reduce the detrimental MgO oxide

formation on the surface of Mg particles [18]. In volumetric sorption studies of MgH_2 formed from Mg via RMA with graphite under 4 bar of H_2 at 563 K for 5 h, it was found that the absorption and desorption rates on the first cycle were significantly faster than for a commercial MgH_2 sample. The first desorption of *ca.* 6.5 wt. % occurred in 800 s, compared with >5000 s for the commercial sample. The first absorption was equally fast, however, the effect did not continue for subsequent cycles, suggesting that the graphite acts only to enhance the initial activation of the Mg [21] by preventing the formation of the detrimental oxide layer at the Mg surface.

The following summary table, Table 2.2, compares the different additives that have been discussed in the preceding section, including examples of metal, alloy, and carbon materials.

Additive Type	Examples	Conditions of Milling	Effect of Additive on H_2 Desorption		Reference
			Thermodynamics	Kinetics	
Metal	V (9.7 wt. %)	Ball milled under Ar for up to 20 h.	T_{onset} not reported. ΔH_{des} = 74.4 kJ mol^{-1} ΔS_{des} = 133.5 J mol^{-1} K^{-1}	Complete in 15 min at 250°C in 0.015 MPa H_2. E_a = 62 kJ mol^{-1}.	[60]
	Ti (9 wt. %)	Ball milled under Ar for up to 20 h.	T_{onset} not reported ΔH_{des} = 77 kJ mol^{-1}* ΔS_{des} = 136 J mol^{-1} K^{-1}*	Complete in 4 min at 300°C in 0.015 MPa H_2. E_a = 71.1 kJ mol^{-1}.	[59]
	Pd (1 wt. %)	Ball milled under Ar for up to 20 h.	Not reported.	Complete in 40 min at 330°C (pressure not reported). E_a not reported.	[64]
	Ni (4.5 wt. %)	Ball milled under H_2 for up to 2 h.	T_{onset} = 150°C (heating rate 5°C min^{-1} under flowing H_2). ΔH_{des} and ΔS_{des} not reported.	90 % complete in 100 min at 163°C under flowing He. E_a = 94 kJ mol^{-1}.	[14]
	Nb (18 wt. %)	Ball milled under Ar for up to 20 h.	Not reported.	90 % complete in 13 min at 250°C in 0.015 MPa H_2. E_a = 62 kJ mol^{-1}.	[70]
	Nb (18 wt. %)	RMA of Mg under H_2 for up to 48 h.	T_{onset} = 270°C (heating rate 20°C min^{-1} under flowing Ar). ΔH_{des} and ΔS_{des} not reported.	Not reported.	[75]
Alloy	$LaNi_5$ (50 wt. %)	Ball milled under Ar for 20 h.	Not reported.	Almost complete in 17 min at 275°C in 0.05 MPa H_2. E_a not reported.	[71]
	$PdFe_3$ (82 wt. %)	Ball milled under Ar.	T_{onset} = 127°C ΔH_{des} and ΔS_{des} not reported.	Not reported.	[65]
Carbon	Graphite (4.6 wt. %)	Ball milled under Ar for up to 15 h.	T_{onset} = 400°C ΔH_{des} and ΔS_{des} not reported.	Similar to MgH_2.	[18]
	MWNT (5 wt. %)	RMA of Mg under H_2 for 3 h.	Not reported.	Complete in 30 min at 200°C in vacuum. E_a not reported.	[19]

Table 2.2: Comparison of metal, alloy, and carbon additives to MgH_2.

Reported properties are generally not directly comparable due to differing analysis techniques and conditions, however, it can be noted that low wt. % additions of a wide range of metal additives are effective in lowering desorption onset temperatures and increasing rates of H_2 desorption from MgH_2. In most cases, these effects are kinetic, with the additive resulting in a lower activation energy for H_2 desorption. In the case of Ni, which is known to readily form an alloy with MgH_2, a reduction in the thermodynamic stability of the hydride may result in a lower T_{onset} of H_2 desorption.

The alloy additives are generally added in very high weight percentages of ≥ 50 wt. %, and as such, the reported properties reflect an intermediate system between the dehydrogenation behaviour of the alloy and that of MgH_2. Although the capacities of these mixtures are higher than the alloys on their own, they are still lower than those demanded for most applications, and are therefore not very practical hydrogen storage materials.

Finally, the carbon additives do not appear to greatly affect the hydrogen desorption of MgH_2, particularly after the first cycle. This would suggest that there is little benefit in adding them to MgH_2 for use as a hydrogen storage material where the ability to maintain hydrogen sorption kinetics over repeated cycles of hydrogenation and dehydrogenation is crucial.

2.4.3. Oxide additives

A number of groups have looked at improving the sorption kinetics of MgH_2 by the addition of a variety of metal oxides. To date, this has been focussed on low wt. % additions of primarily commercially available Sc_2O_3 [16], TiO_2 [16,76], V_2O_5 [16], Nb_2O_5 [77-80], Cr_2O_3 [16,81,82], Mn_2O_3 [16], Fe_2O_3 [83], CuO [16], CoO [52], Al_2O_3 [16], and SiO_2 [16], via ball milling or reactive mechanical alloying. Oelerich *et al.* found that additions of only 0.05 wt. % oxide to MgH_2 powder, followed by milling for 120 h resulted in no phase changes, but did notably enhance the adsorption and desorption kinetics at 300°C [16]. The different oxides and their effect on hydrogen sorption could be divided into those that had mixed valency, which enhanced the kinetics, and those that had only a single oxidation state, and had no accelerating effects. This suggests that the mechanism of catalysis may require the presence of variable oxidation states.

For Cr_2O_3, it has been suggested that oxide preparation method, and resulting oxide particle size have a role to play in the effectiveness of the additive. A number of groups have studied the $MgH_2 . Cr_2O_3$ nanocomposite in more detail, and the effect of repeated hydrogenation - dehydrogenation cycles. Bobet *et al.* showed that reactive mechanical grinding of Mg with amorphous Cr_2O_3 obtained from a supercritical fluid method offered improvements in hydrogen absorption measured at 300°C, with desorption of more than 50 % of the hydrogen occurring in 30 min, compared with 45 min for the mixture

with crystalline Cr_2O_3. [81]. In ball milled MgH_2 - 0.2 mol. % Cr_2O_3 after 1000 absorption - desorption cycles at 300°C, Dehouche *et al.* found that good absorption kinetics were maintained, while desorption rates decreased by a factor of four over the course of the cycles. Storage capacity was shown to increase from 5.9 wt. % to 6.4 wt. %. These effects corresponded to a microstructural coarsening of the MgH_2 from 21 nm to 84 nm [82].

Another argument relating to the benefit of oxide additives is that the presence of brittle oxides, when combined with ball milling, simply causes structural refinement to help break down the hydride into smaller particles. Güvendiren *et al.* studied the effects of Al_2O_3 additives on the average particulate size of MgH_2 [84]. After milling MgH_2 with 5 wt. % Al_2O_3 for 3 h under argon, the average crystallite size of the β - MgH_2 phase had decreased from 31.2 nm to 20.4 nm according to XRD peak broadening measurements. Although results of H_2 sorption studies on this particular mixture have not been presented, studies of other additives by the same group led them to conclude that sorption kinetics were not directly dependent on structural size, and chemical properties of the additive also played a role.

Detailed studies of Nb_2O_5 additives by a number of groups [56,77-80] have led to further understanding of the effect of the oxide additive on the H_2 sorption behaviour of MgH_2. Additive loadings ranging from 0.4 wt. % to 17 wt. % Nb_2O_5 have been examined. Barkhordarian *et al.*

found that full desorption from a MgH_2 - 4 wt. % Nb_2O_5 mixture occurred in 90 s at 300°C [56]. This result is attributed to the Nb_2O_5 acting as a catalyst for chemisorption at the sample surface, resulting in a decrease in activation energy for hydrogen desorption from 120 kJ mol^{-1} to 62 kJ mol^{-1}.

Neither Barkhordarian *et al.* nor Fatay *et al.*, in similar studies, found evidence of any structural transformation of the Nb_2O_5 phase, both suggesting that the Nb_2O_5 acts as the catalyst for H_2 desorption. Friedrichs *et al.*, on the other hand, used XPS analysis and showed a reduction in the Nb species present after cycling, and evidence of a $MgNb_2O_{3.67}$ phase in XRD taken after cycling of ball milled MgH_2 - Nb_2O_5. This data suggests that Nb_2O_5 is not the active catalyst in this case, and Friedrichs *et al.* propose a reaction mechanism involving niobium oxide species of lower oxidation state forming a network of 'pathways' for hydrogen diffusion within the MgH_2 phase. Their study supports the theory and earlier observation by Oelerich *et al.*[16] that the variable oxidation state of the oxide is a key factor in the effectiveness of the additive.

A limited number of studies on Mg milled with TiO_2 have also been reported [16,76]. In a study of Mg - 20 wt. % rutile TiO_2 prepared by RMA in a H_2 atmosphere, it was found that complete H_2 desorption occurred in 9 min at 350°C in 0.1 MPa H_2 [76]. In the survey of a range of oxide materials by Oelerich *et al.*, a 0.03 wt. % TiO_2 addition to ball milled

MgH_2 resulted in a material which took only 7 min for complete desorption at 300°C in vacuum [16]. Details of the oxide structure of the starting material are not presented, and there is no thermodynamic data for MgH_2 - TiO_2, nor is the activation energy for H_2 desorption reported.

Table 2.3 is a summary of the oxide additives to Mg and MgH_2 shown in the literature to be effective in improving the desorption of H_2 from MgH_2. The different weight percentages of oxides added, milling and experimental conditions make comparison between the different oxides difficult, although some general conclusions can be drawn. Most reports focus on the kinetic behaviour of the MgH_2 with added oxide, and Nb_2O_5 is shown to be the most effective of the oxides studied at enhancing the H_2 desorption rate from MgH_2. Rutile TiO_2 does not appear to be as effective as Nb_2O_5, with MgH_2 - 20 wt. % TiO_2 taking 9 min for full desorption at 350°C compared to MgH_2 - 5 wt. % Nb_2O_5, which had fully desorbed in a similar time, but at the lower temperature of 250°C. The TiO_2 used by Oelerich *et al.*, on the other hand, appears to cause a faster H_2 desorption rate of 7 min at 300°C in vacuum, although details of the oxide structure and particle size are not presented.

Oxide	Form of oxide	Amount of Oxide added	Initial Oxide particle size	Milling conditions	Average MgH_2 grain size after milling	Effect of Oxide on H_2 Desorption		Reference
						Thermodynamics	Kinetics	
Cr_2O_3	Nanocrystalline	5 wt. %	Not reported.	RMA of Mg under H_2 for up to 5 h.	20 nm	Not reported.	> 50 % complete in 30 min at 300°C in 0.05 MPa H_2.	[81]
	Commercial, crystalline.	1.2 wt. %	Not reported.	Ball milled under Ar for 20 h + 100 h.	21 nm	Not reported.	Complete in 15 min at 300°C in vacuum. (Deteriorates on cycling).	[82]
Nb_2O_5	Commercial, crystalline.	5 wt. %	Not reported.	Ball milled under Ar for 20 h + 100 h.	Not reported.	Not reported.	Complete in 8.5 min at 250°C in vacuum. E_a = 62 kJ mol^{-1}.	[78]
	Nanocrystalline	20 wt. %	Not reported.	Ball milled under H_2 for 120 min + 15 min.	10 nm	T_{onset} = 380°C (heating rate 20°C min^{-1}).	No rate data reported. E_a = 83 kJ mol^{-1}.	[80]
	Commercial, nanocrystalline.	10 wt. %	15 nm	Ball milled under Ar for 20 h + 15 min.	Not reported.	Not reported.	Complete in 8.5 min at 300°C in 0.1 kPa H_2.	[79]
TiO_2	Commercial, Rutile.	20 wt. %	≤ 74 μm	RMA of Mg under H_2 for up to 6 h.	20 nm	Not reported.	Complete in 9 min at 350°C in 0.1 MPa H_2.	[76]
	No details given.	3 wt. %	Not reported.	Ball milled under Ar for 20 h + 100 h.	20 nm	Not reported.	Complete in 8 min at 300°C in vacuum.	[16]
Fe_2O_3	Nanocrystalline	10 wt. %	≤ 5 μm	RMA of Mg under H_2 for 2 h.	Not reported.	Not reported.	1 wt. % H_2 desorbed in 60 min at 320°C in 1 bar H_2.	[83]

Table 2.3: Comparison of oxide additives to MgH_2. For references where varying conditions were reported, best results are summarised here.

2.4.4. Cycling behaviour of MgH_2

In addition to requirements of low decomposition temperature and fast kinetics of hydrogen desorption and absorption, a hydrogen storage material also needs the ability to withstand repeated cycles of hydrogen desorption and absorption without a decrease in H_2 capacity or rate of reaction. A number of cycling experiments on MgH_2 have been reported [85-87], as well as how additives including V [61], and Cr_2O_3 [82] influence MgH_2 cycling behaviour. For polycrystalline MgH_2 it has been shown that both reaction kinetics and H_2 capacity were reduced as a result of prolonged cycling due to a coarsening of the MgH_2 grain size [86,87]. This is in contrast to other hydrogen storage materials, particularly the alloy hydrides such as $LaNi_5$, which have been shown to maintain their behaviour even after 40000 cycles [87]. For both V and Cr_2O_3 additives, improved cycling stability has been reported, with a slight increase in H_2 capacity (*ca.* 0.2 wt. %) observed for a MgH_2 - 5 at. % V mixture after 2000 cycles [61]. While the H_2 absorption rate was unchanged on cycling, for both V and Cr_2O_3 additives, a slightly lowered desorption rate was reported, which was attributed to crystal growth of the MgH_2 phase [82].

2.5. Summary

From this literature review on the subject of MgH_2 as a hydrogen storage material, it can be seen that a wide range of additives, in conjunction with ball milling or reactive mechanical alloying, have been studied to

improve the kinetics of hydrogen absorption and desorption. Due to the wide range of materials preparation techniques used, including ball milling with different types of ball mills, as well as reactive mechanical alloying with a range of milling temperatures and atmospheres, samples prepared from the same starting materials can exhibit significantly different characteristics and hydrogen sorption behaviour. In addition, the wide variety of techniques and operating conditions used to analyse hydrogen absorption and desorption, including gravimetric and volumetric techniques, static and flowing gas systems, temperature ramping and isothermal methods, makes it difficult to directly compare results to determine the most effective additives at lowering temperatures and increasing rates of hydrogen absorption and desorption in MgH_2.

The additives studied to date have not yet resulted in a material of the required combination of sufficient H_2 capacity, fast reaction kinetics, and ability to be cycled, which are demanded for practical applications. In general, transition metal oxides, with the ability to take on different oxidation states, have shown great promise in improving the hydrogen sorption behaviour of MgH_2. Nb_2O_5 has been shown to be highly effective, while TiO_2 has also shown positive results. Reports of the behaviour of metal oxides raise questions on the mechanisms by which these additives influence the behaviour of MgH_2. The reports on the effect of TiO_2 suggest that this may be a highly effective additive; however, effects of TiO_2 crystal structure and particle size have been ignored.

There is therefore scope for further development of novel materials as well as for more research into the reactions of hydrogen absorption and desorption in these materials, in order to obtain a greater understanding of the complex mechanisms involved. The work carried out for this thesis aims to contribute to both these areas of research and development, by studying oxide-based additives that have not previously been milled with MgH_2, as well as characterising these materials with the aim of gaining further insight into the reaction mechanisms at work.

3. Experimental Methods

3.1. Introduction

In this chapter, the experimental methods used to prepare the materials studied are described, and the sample nomenclature used throughout this thesis is explained. The handling of the prepared materials and the techniques used for materials characterisation and hydrogen storage studies are discussed.

3.2. Preparation of single and mixed oxides

Oxides of aluminium, silicon, titanium and zirconium were prepared from the alkoxide precursors (Alfa Aesar) aluminium-tri-sec-butoxide (ABO,$C_{12}H_{27}O_3Al$), tetraethoxysilane (TEOS,$C_8H_{20}O_4Si$), titanium iso-propoxide (TIP,$C_{12}H_{28}O_4Ti$), and zirconium iso-propoxide (ZIP,$C_{12}H_{28}O_4Zr$), respectively. The required quantity of precursor for a 5 g yield of stoichiometric oxide was dissolved in 50 cm^3 IPA (propan-2-ol, Fisher, analytical grade) in a round bottomed flask. The slurry was hydrolysed by the addition of triply de-ionised water (TDW) (100 mol. % excess) while stirring with a mechanical stirrer. After stirring for 2 h, the suspension was transferred to an evaporating dish and dried in air at 70°C for 18 h. A portion of each of the dried powders was subsequently subjected to a further calcination for 2 h at 120°C, 400°C, or 800°C. Table 3.1 contains details of the different oxide samples prepared, and the amounts of reactants used in their preparation.

Sample	Weight of precursor used for 5 g yield of oxide / g			
	ABO	TEOS	TIP	ZIP
Al_2O_3	24.16	0	0	0
SiO_2	0	17.34	0	0
TiO_2	0	0	17.79	0
ZrO_2	0	0	0	13.30
$90Al_2O_3$-$10SiO_2$	21.74	1.73	0	0
$50Al_2O_3$-$50SiO_2$	12.08	8.67	0	0
$10Al_2O_3$-$90SiO_2$	2.42	15.61	0	0
$90TiO_2$-$10Al_2O_3$	2.42	0	16.00	0
$50TiO_2$-$50Al_2O_3$	12.07	0	8.90	0
$10TiO_2$-$90Al_2O_3$	21.74	0	1.78	0
$90TiO_2$-$10SiO_2$	0	1.73	16.01	0
$50TiO_2$-$50SiO_2$	0	8.67	8.90	0
$10TiO_2$-$90SiO_2$	0	15.60	1.78	0

Table 3.1: Summary of oxide samples prepared.

Mixed two-component oxides of alumina-silica, titania-alumina, and titania-silica were also prepared from the same alkoxide precursors, with nominal weight ratios of 90/10, 50/50, and 10/90. To prepare the mixed oxides, the required amounts of the two precursors for a total yield of 5 g were dissolved in IPA (50 cm^3) and then hydrolysed, dried and calcined using the same method as for the single oxide preparation.

Titanium oxide dried at 70°C was used to prepare Pd - modified TiO_2 via wet impregnation using $Pd(NO_3)_2$ (Palladium (II) Nitrate Hydrate, Aldrich) as a Pd precursor. To prepare 1 wt. % and 5 wt. % Pd modified samples, the required amount of $Pd(NO_3)_2$ was dissolved in TDW (200 cm^3) in a round-bottomed flask. TiO_2 powder (1 g) was added to the flask, while mixing with a mechanical stirrer. After 2 h of stirring, the dispersion was transferred to an evaporating dish and dried for 18 h at 70°C. The dried powder was calcined for 4 h at 300°C to decompose the $Pd(NO_3)_2$

particles to PdO, followed by a heat treatment in a flowing H_2 atmosphere (100 ml min^{-1} H_2 / 500 ml min^{-1} Ar) at 500°C for 2 h to reduce the PdO to metallic Pd. The transformations of the Pd species were confirmed using powder XRD.

3.3. Preparation of milled hydride and hydride/oxide mixtures

MgH_2 is sensitive to moisture and oxygen in the atmosphere, and exposure must therefore be avoided to prevent sample degradation. All preparation of samples for ball milling was carried out in an Ar glove box with O_2 and H_2O levels maintained at less than 0.1 ppm. The milling pots were sealed inside the glovebox before transfer to the ball mill, to ensure milling took place in an inert atmosphere. Subsequent storage and handling of prepared materials was all carried out within an Ar glove box. In some cases, for characterisation and hydrogen storage testing, brief exposure of samples to the air was unavoidable. Details of inert sample loading procedures or limited exposure times are explained for the individual techniques in Sections 3.5 and 3.6.

A rotary ball mill (Fritsch P5) was used to mill the MgH_2 (Alfa Aesar) and MgH_2/oxide mixtures. A total of 5 g of powder was added to a stainless steel pot (vol = 80 cm^3) containing 30 stainless balls (Ø = 10 mm), giving a ball to powder weight ratio of 24:1. A PTFE sealing ring and stainless steel lid were placed onto the pot, and the pot was clamped into the mill. The mill was run at a speed of 250 rpm for 1 h, followed by a rest for 30 min. This cycle of milling and resting was repeated to give a total

milling time of 20 h. For milled MgH_2 with oxide addition, 20 wt. % of the desired oxide was mixed into the as received MgH_2 powder using a stainless steel spatula, and the mixed powder was then milled using the conditions described above. After milling, samples were scraped from the milling pots using a stainless steel spatula.

3.4. Sample nomenclature

A consistent sample nomenclature will be used in this and subsequent chapters when referring to the different samples discussed. A summary of the nomenclature for the different types of samples is given in Table 3.2. Single oxide samples will be referred to as *X T*, where *X* is the metal species of the given oxide and *T* is the temperature in °C at which the oxide was heat treated. For example, a single oxide TiO_2 sample, heat treated for 2 h at 400°C, will be referred to as Ti400. For mixed oxides, the sample names will take the form *aX - bY T*, where *a* and *b* are the ratio of the two oxide components *X* and *Y*, and T is the temperature at which the mixed oxide was heat treated. A mixed Al_2O_3 - SiO_2 sample with a 90/10 wt. % ratio of the two components dried at 70°C and subjected to no further heat treatment will thus be referred to as 90Al10Si70. Pd modified TiO_2 samples will be written as TicPd, where *c* is the theoretical wt. % loading of Pd. A loading of 5 wt. % Pd will therefore be referred to as Ti5Pd. Milled MgH_2 and MgH_2/oxide mixtures will take the nomenclature MgH_2 - *D*, where *D* is the oxide named using the nomenclature described above. Unless stated, the wt. % of oxide present is 20 wt. %. When a different wt. % of oxide is present, the wt. %

will be stated in the sample name. For example, a sample of MgH_2 milled with 20 wt. % $50TiO_2$ - $50Al_2O_3$ 120°C will be referred to as MgH_2 - 50Ti50Al120, and a sample of MgH_2 milled with 2 wt. % TiO_2 70°C will be referred to as MgH_2 - 2 wt. % Ti70.

Sample	MgH_2	a	X	b	Y	T	c	Nomenclature
Al_2O_3 70°C SiO_2 120°C TiO_2 400°C ZrO_2 800°C	no	-	Al Si Ti Zr	-	-	70 120 400 800	-	Al70 Si120 Ti400 Zr800
MgH_2 20 wt.% TiO_2 70°C MgH_2 10 wt.% TiO_2 70°C	yes	-	Ti	-	-	70	-	MgH_2 -Ti70 MgH_2 -10wt.% Ti70
$10Al_2O_3$-$90SiO_2$ 120°C $50TiO_2$-$50Al_2O_3$ 400°C $90TiO_2$-$10SiO_2$ 800°C	no	10 50 90	Al Ti Ti	90 50 10	Si Al Si	120 400 800	-	10Al90Si120 50Ti50Al400 90Ti10Si800
MgH_2 20wt.% $50Al_2O_3$-$50SiO_2$ 120°C	yes	50	Al	50	Si	120	-	MgH_2 -50Al50Si120
TiO_2-5 wt.% Pd	no	-	Ti	-	-	-	5	Ti5Pd

Table 3.2: Sample nomenclature.

3.5. Materials characterisation techniques

3.5.1. Powder X-ray diffraction (XRD)

Powder X-ray diffraction patterns for the prepared oxide materials and the MgH_2/oxide mixtures were collected using a Bruker D8 diffractometer with Cu Kα X-ray source operating at 40 kV and 40 mA, and a Sol-X detector. Diffraction patterns were collected over the 2θ range of 20° to 80°, with a step size of 0.02 2θ and a time of 1 s per step. Data was analysed using Bruker's Eva software, and referenced to known compounds using the JCPDS-ICDD Powder Diffraction File.

Oxide and MgH_2 samples were prepared for XRD by first grinding the powder with a mortar and pestle, then mounting the ground powder into a Perspex sample holder. For samples containing MgH_2, this preparation was carried out in an Ar glove box, and an amorphous tape was applied to seal the samples from the atmosphere during the analysis.

Average crystallite sizes and internal strain measurements were calculated from the collected diffraction patterns using the Williamson - Hall method, which accounts for the line broadening in a diffraction pattern caused by small crystallite size and the presence of internal strain. In a crystalline sample, X-ray diffraction results from constructive and destructive interference caused by scattering of X-rays from atoms in a regular array, with diffraction lines appearing at angles that satisfy

Bragg's law (equation 3.1), where *n* is the order of diffraction, λ the X-ray wavelength, *d* the interplanar spacing, and θ the angle of diffraction.

$$n\lambda = 2d\sin\theta \qquad \text{equation 3.1 [88]}$$

When crystallites are small enough that they do not contain enough atomic planes within them to fully cancel out scattering at angles close to a given Bragg angle, line broadening occurs. The Scherrer formula (equation 3.2), relates the line broadening (*b*) to the size of the crystallites (*t*), where b is the total line broadening (full width half maximum, FWHM) with the instrument line broadening β subtracted.

$$t = \frac{0.9\lambda}{b\cos\theta} \qquad \text{equation 3.2 [88]}$$

Line broadening can also result from internal strain within crystallites, which distorts the interplanar spacings, once again resulting in scattering at angles close to the Bragg angle. Differentiating Bragg's law gives the following equation (equation 3.3), which allows the sum of the compressive and tensile microstrain ($\Delta d/d$) to be determined from the measured broadening (*b*).

$$b = -2\frac{\Delta d}{d}\tan\theta \qquad \text{equation 3.3 [88]}$$

Rearranging and combining the equations for line broadening due to crystallite size and internal strain results in the following equation (equation 3.4).

$$b\cos\theta = -2\frac{\Delta d}{d}\sin\theta + \frac{\lambda}{t} \qquad \text{equation 3.4 [88]}$$

Thus a Williamson - Hall plot of $b(\cos\theta)/\lambda$ versus $(\sin\theta)/\lambda$ gives a slope of $-2\Delta d/d$, and a y-intercept of $1/t$, allowing the internal strain and crystallite size to be estimated [88].

In situ XRD was carried out on a Bruker D8 diffractometer using a pressure and temperature stage (MRI-TCP20) with alumina crucible and a Ta Ω- heater. Samples were loaded into the alumina crucible inside the glove box, and were then transferred quickly to the XRD stage which was then immediately evacuated and filled with argon (1 bar). The X-ray source and detector were as described above. The temperature stage was used to heat samples from room temperature to 600°C at a rate of 10°C per minute. Temperature ramping was interrupted every 50°C, for a scan to be carried out. XRD scan settings were as above, except that a narrower 2θ range was used (24-30°) to decrease overall experiment time.

3.5.2. N_2 physisorption

The adsorption and desorption of nitrogen gas (N_2) onto a fixed weight of sample in bulk powder form can be used to estimate the surface area of the specimen using the BET (Brunauer-Emmett-Teller) equation (equation 3.5).

$$\frac{V}{V_{mon}} = \frac{cz}{[1-z][1-(1-c)z]} \qquad \text{equation 3.5}$$

The z term in the BET equation represents pressure, and the c term corresponds to the enthalpies of adsorption and desorption of the N_2 ($\Delta_{des}H$ and $\Delta_{vap}H$), and to the temperature (T), via the following Arrhenius relationship (equation 3.6).

$$c = \exp\left[\frac{\Delta_{des}H^{o} - \Delta_{vap}H^{o}}{RT}\right] \qquad \text{equation 3.6}$$

Determining the volume (V) of gas adsorbed at different pressures allows the monolayer volume (V_{mon}) to be calculated. This can be converted to a number of moles, and subsequently to the surface area of the specimen.

Surface area measurements were collected using a Quantachrome Autosorb-1 Automated Gas Sorption System, and the accompanying software, Autosorb for Windows V1.24. The parameters for the Autosorb set-up are listed in Table 3.1. For air-sensitive samples containing MgH_2, powder was loaded into a glass sample tube inside an Ar glove box, and

the top was sealed with tape, which was removed a few seconds prior to evacuation of the tube for outgassing on the Autosorb instrument.

Parameter	Value
Mass of sample	~0.5 g
Outgas temperature	70 - 300 °C
Outgas time	18 hr
Bath temperature	-195.65°C
Analysis time	~55 minutes
Number of BET points measured	7

Table 3.1: BET set-up parameters.

3.5.3. Scanning electron microscopy (SEM)

A JEOL 6400 scanning electron microscope was used to examine surface topography and morphology of MgH_2. Attached equipment for the energy dispersive analysis of X-rays (EDX) was used for elemental analysis. Samples for SEM were prepared inside an Ar glove box. For observations of powder particle size, shape and agglomeration, powder was lightly sprinkled on a carbon tab. For EDX, where a flat sample surface is required, powder samples were pressed into pellets (Ø = 8 mm) using a hand press prior to attaching to an aluminium sample disc using conductive carbon cement. Both the powder and pellet samples were then removed from the glove box and immediately carbon coated prior to transfer to the microscope.

3.5.4. Transmission electron microscopy (TEM)

TEM analysis of MgH_2/oxide samples was carried out using a JEOL FX III microscope. Samples were prepared inside an Ar glove box, by rubbing a

lacy carbon grid (300 mesh) through a small amount of powder. Samples were then mounted into the TEM transfer rod and sealed within a Perspex cover prior to removal from the glove box. The Perspex cover was removed immediately prior to transfer to the vacuum chamber of the TEM. Micrographs and selected area electron diffraction patterns were collected, and EDX was used for elemental analysis. The selected area diffraction patterns were analysed to extract the lattice spacing, *d*, from the crystalline samples. In the TEM, the electrons are diffracted at very small angles (1-2°), where $\theta \approx \tan\theta$, and the *d* spacings can therefore be calculated from the following re-arrangement of the Bragg equation (equation 3.1) where L is the distance between the camera and the sample, λ is the incident electron wavelength, and *r* is the radius of the diffraction ring.

$$L\lambda = rd \qquad \text{equation 3.7}$$

The *d* spacings can be matched to known lattice spacings to identify the phases present in the diffracting region.

3.5.5. X-ray photoelectron spectroscopy (XPS)

XPS analysis of the MgH_2 and MgH_2/oxide samples was carried out on a Kratos AXIS ULTRA XPS system with monochromated Al Kα X-ray source operated at 10 mA and 15 kV and a hemispherical analyser with eight channeltrons. Samples were prepared inside an Ar glove box, by

mounting powders onto double-sided tape attached to a sample bar. Mounted samples were sealed within an air-tight jar and removed from the glove box. Samples were loaded inertly into the XPS instrument using a N_2 filled glove bag.

In XPS analysis, the surface of a sample is irradiated by a monochromatic beam of X-rays, causing emission of electrons of binding energy (BE) specific to the local environment of the atoms from which they originate. The measured kinetic energy (KE) is directly related to binding energy (BE) by the following relationship (equation 3.8), where $h\nu$ is the energy of a photon and ϕ is the work function, the minimum energy required to move an electron from the highest occupied energy level in the solid to the vacuum level.

$$BE = h\nu - KE - \phi \qquad \text{equation 3.8 [89]}$$

A wide scan was collected for all samples across the kinetic energy range 0 - 1500 eV using a step size of 1 eV and a pass energy of 80 eV. High resolution scans were then run over the desired regions specific to each sample, using a step size of 0.1 eV and a pass energy of 20 eV.

Analysis of the XPS data was carried out using CasaXPS software (version 2.3.10). The C 1s peak at 285 eV was used for charge correction. For peak fitting, the background was corrected using a non-linear Shirley

background type and Gaussian/Lorentzian contributions of 30/70 were used for the fitted components.

3.5.6. Diffuse reflectance infra-red spectroscopy (DRIFTS)

DRIFTS was used to probe the nature of the species at the surface of the oxide samples. The instrument used for this characterisation was a Bruker Optics Ltd Tensor 27 FT-IR unit in diffuse reflectance mode, with the settings as given in Table 3.2. For DRIFTS experiments oxide powders were ground with KBr powder (1/10 volume ratio) for 60 s with a mortar and pestle. Ground KBr was used for the background reference material.

Source	**MIR**
Detector	**LN-MCT Mid**
Aperture	**6 mm**
Velocity	**20 kHz**
Number of Scans	**30**
Resolution	**4**
Apodization	**Blackman-Harris 3 Term**
Acquisition Mode	**Double-Sided, Forward-Backward**

Table 3.2: Set-up parameters for DRIFTS data acquisition.

3.5.7. Differential scanning calorimetry - thermogravimetry - residual gas analysis (DSC-TGA-MS)

A TA Instruments SDT600 DSC-TGA was used to quantify the weight loss and heat flow to and from oxide samples during heating, coupled with a Hiden Analytical HPR-20 mass spectrometer used for evolved gas analysis. Approximately 15 - 30 mg of sample was loaded into an alumina pan, with an empty pan used as a reference. Samples were heated under flowing Ar (100 ml min^{-1}) to 600°C at a rate of 10°C min^{-1}. The mass

spectrometry data was gathered using the HPR-20 residual gas analyser controlled by Hiden's MasSoft software, while the thermogravimetric analysis was controlled and analysed using TA Instruments Universal Analysis software.

While the DSC-TGA directly recorded the sample temperature, the mass spectrometry data was recorded only as a function of time, which had to be converted to temperature for subsequent analysis. An electronic link between the two apparatus was used to start collection of data by the mass spectrometer at a known sample temperature recorded on the DSC-TGA. This starting temperature and the temperature ramp rate of 10°C min^{-1} were then used to convert from time to temperature giving an x - axis of temperature for the plotted mass spectrometry data. For this method, a linear temperature ramp rate was assumed. However, the ramp rate of the DSC-TGA was actually found to deviate from linearity during the endothermic hydrogen desorption reactions. A sample DSC - TGA trace is shown in Figure 3.1, indicating the actual temperature over the course of a dehydrogenation experiment.

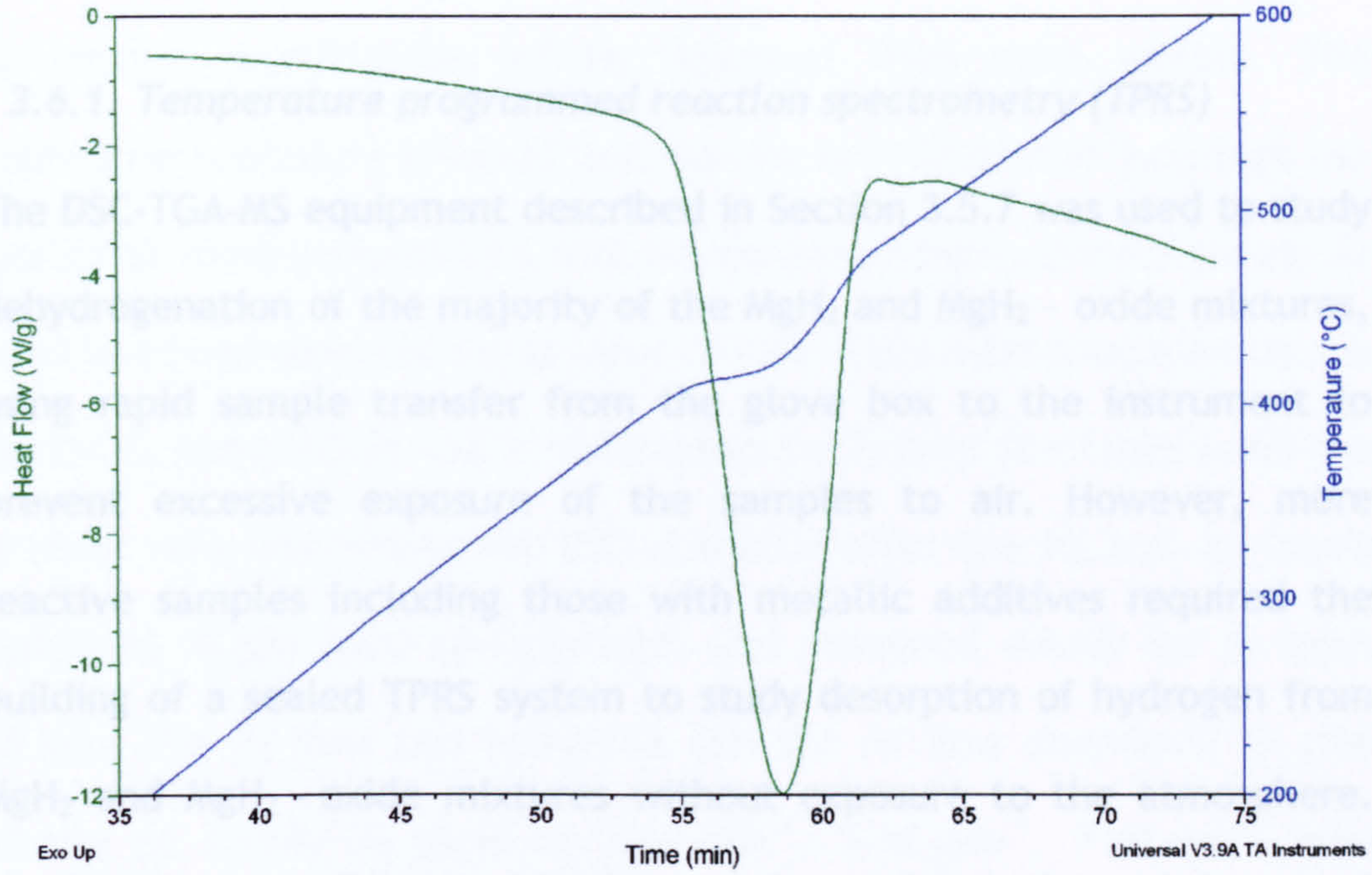

Figure 3.1: Heat flow and sample temperature during heating of milled MgH_2.

This deviation from the linear temperature ramp rate, shown between 55 and 60 min in the example given, resulted in an error in the temperature scale of the mass spectrometry data. As a result of this, it should be noted that on DSC-TGA-MS traces presented in Chapters 4 and 5, the peak positions of the mass spectrometry traces are in general at slightly higher than the true sample temperature. This does not affect any subsequent data analysis, as temperature values were exclusively taken from the more accurate DSC-TGA data.

3.6. Hydrogen storage measurements

3.6.1. Temperature programmed reaction spectrometry (TPRS)

The DSC-TGA-MS equipment described in Section 3.5.7 was used to study dehydrogenation of the majority of the MgH_2 and MgH_2 - oxide mixtures, using rapid sample transfer from the glove box to the instrument to prevent excessive exposure of the samples to air. However, more reactive samples including those with metallic additives required the building of a sealed TPRS system to study desorption of hydrogen from MgH_2 and MgH_2 - oxide mixtures without exposure to the atmosphere. The TPRS set-up, illustrated in Figure 3.2, consisted of a stainless steel reaction vessel which could be loaded and sealed within an Ar glove box. Once sealed and removed from the glovebox, the sample vessel was placed within a ring heater and attached to a flowing gas system and a mass spectrometer (Hiden HPR-20) for exhaust gas analysis via quick release sealing valves (Swagelok). Samples were then heated to 600°C at 10°C min^{-1} under flowing Ar (100 ml min^{-1}).

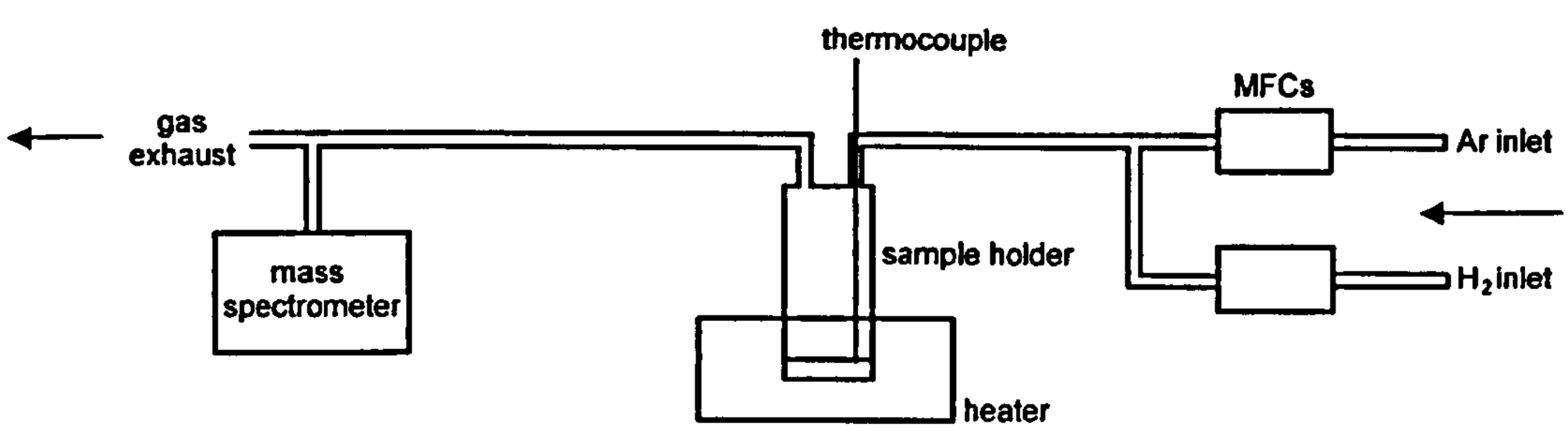

Figure 3.2: Schematic of TPRS set-up.

Regular calibration of the mass spectrometer for H_2 gas was carried out, to enable quantification of H_2 desorbed from each sample. The calibration procedure involved first flowing Ar (100 ml min^{-1}) through the system at room temperature with no sample present. Once a steady Ar level had been observed for at least 10 min in the mass spectrometer, H_2 gas (BOC, purity N5.0) was introduced to the system (1 ml min^{-1}) and the Ar flow rate was decreased (99 ml min^{-1}). After the H_2 and Ar levels stabilised in the mass spectrometer and remained steady for at least 10 min, the H_2 flow was increased and the Ar flow decreased to give 10 min of steady H_2 flow at 3 ml min^{-1}, 5 ml min^{-1}, 7 ml min^{-1}, and 10 ml min^{-1}, maintaining a total flow rate of 100 ml min^{-1} with the Ar balance. The average background and contribution of water (0.7 %) to the m/z = 2 trace were subtracted from the raw data to give a partial pressure for H_2, and the areas under the m/z traces for each of the known amounts of H_2 passed through the system were integrated. A graph of mass of H_2 against integrated area was plotted giving a straight line with a slope corresponding to a calibration factor which could be used in converting the area under the H_2 trace from a given sample into an amount of H_2 desorbed from the sample.

A number of samples were studied in both the DSC-TGA-MS and TPRS equipment, to confirm that the dehydrogenation temperatures, hydrogen profiles and weight losses were the same. A difference in dehydrogenation temperature of ± 5°C was observed, with calculated

weight loss from TPRS within 0.2 wt. % of measured weight loss from DSC-TGA-MS.

Activation energies for the dehydrogenation of each sample were determined by constructing Kissinger plots using different heating rates of 10, 20, 30, and 40 °C min^{-1}. In the Kissinger equation (equation 3.9) β is the heating rate, T_p is the temperature at the desorption maximum, and E_a is the activation energy.

$$E_a\beta / (RT_p^2) = A \exp [-E_a/RT_p] \qquad \text{equation 3.9}$$

By plotting $\ln(\beta/T_p^2)$ against $1/T_p$, the activation energy, E_a, can be calculated from the slope of the straight line obtained.

3.6.2. Volumetric hydrogen sorption

For volumetric hydrogen sorption studies, a Sieverts apparatus was designed and built. The Sieverts apparatus, illustrated in Figure 3.3, consisted of a stainless steel sample cell (A) which could be loaded and sealed inside the Ar glove box, connected to a manifold volume (B) via stainless steel pipework and a ball valve (V1). The sample cell fitted into a ring heater (C) capable of heating the sample to 400°C. A 10 bar absolute pressure transducer (Druck PMP 4010, accuracy 0.04 % FS) (D) was connected to the manifold. The system was also connected to a turbomolecular drag pump (Pfeiffer) (E), and a gas inlet system (F) to

allow He (BOC, purity N5.0) and H_2 (BOC, purity N5.0) to enter the system through a liquid nitrogen moisture trap (G). Stainless steel Swagelok fittings were used for all joints and valves throughout the system. The system was enclosed within a Perspex box (H) fitted with a heater and two fans to maintain a constant temperature. Temperature was monitored throughout each experiment to ensure that no variation occurred. Enclosure temperature was stable to within ± 1°C.

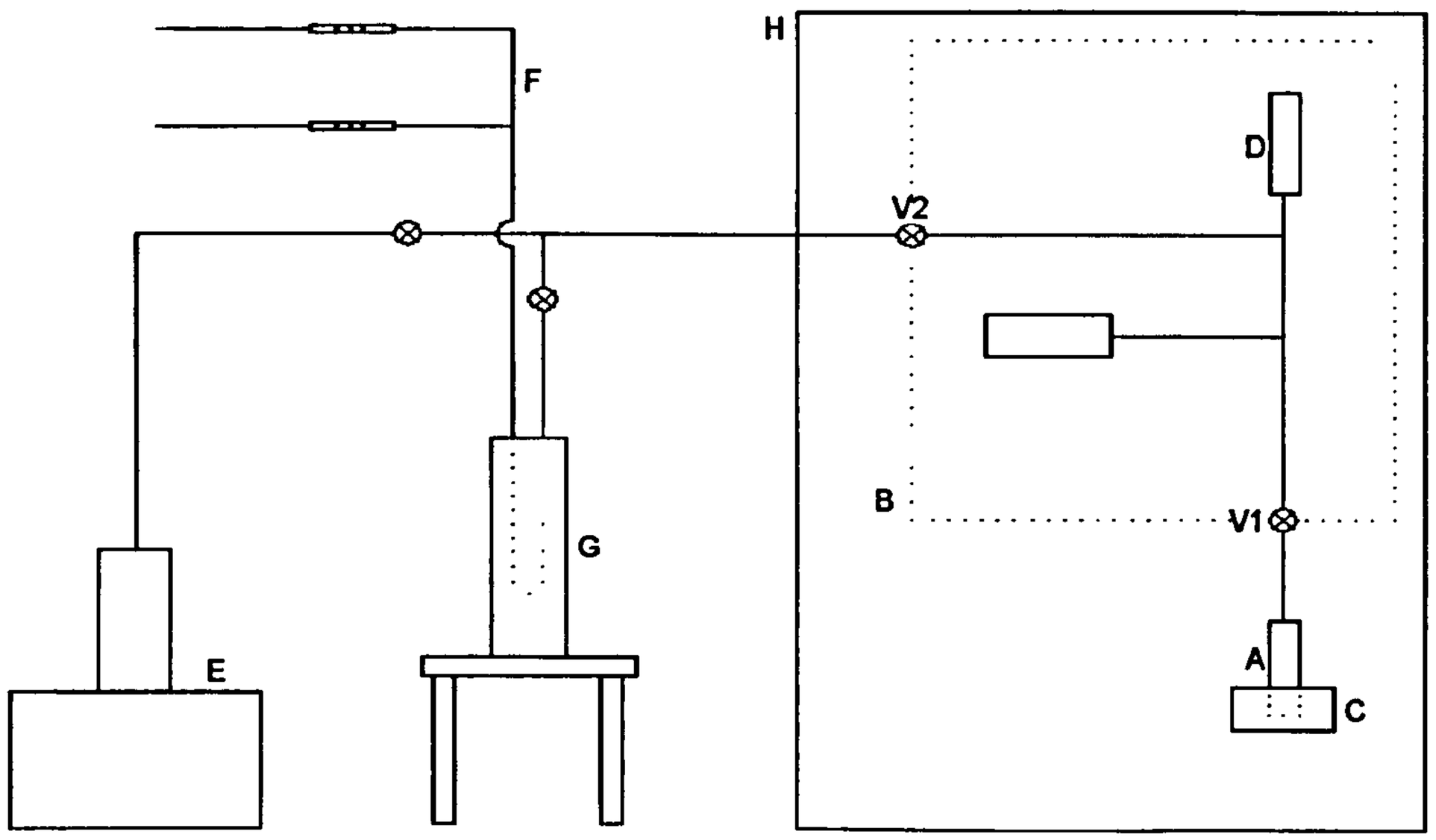

Figure 3.3: Schematic of Sieverts apparatus showing sample cell (A), manifold (B), heating block (C), pressure transducer (D), pumping station (E), gas inlets (F), liquid nitrogen dewar (G), and enclosure (H).

Calibration of the sample and manifold volumes of the equipment was carried out using He gas. Different known volumes of stainless steel ball bearings were added to the sample cell, thus reducing its volume by a known amount, and the pressure changes occurring when a known

pressure of gas was introduced into the sample cell from the manifold were monitored with the pressure transducer. These were converted to densities (ρ) using the Virial equation (equation 3.10), where p is the pressure, R is the gas constant, T is the temperature, and $B(T)$ and $C(T)$ are the second and third virial coefficients for the given gas at temperature T. Virial coefficients for He and H_2 gases at the required temperatures were obtained from NIST Standard Reference Database 134 - Database of the Thermophysical Properties of Gases Used in the Semiconductor Industry (properties.nist.gov/fluidsci/semiprop/).

$$\frac{pV}{nRT} = 1 + B(T)\frac{n}{V} + C(T)\frac{n^2}{V^2} \qquad \text{equation 3.10}$$

Dividing the molar mass of the gas by the molar volume calculated from the Virial equation gave the density of gas in the system. Given that the total mass of gas in the system is constant, the following relationship (equation 3.11) was then used to calibrate the volume of the sample cell:

$$\left[\left(\frac{\rho_1}{\rho_2}\right) - 1\right] V_1 = V_2 - V_3 \qquad \text{equation 3.11}$$

In the equation above, V_1 is the manifold volume, V_2 is the sample cell volume, and V_3 is the added (known) volume of stainless steel. ρ_1 and ρ_2 are the corresponding manifold and total system gas densities. By plotting a graph of $[(\rho_1/\rho_2)-1]$ versus the added volume V_3 for varying V_3,

the manifold and sample cell volumes can be extracted. Figure 3.4 shows calibration plots for the Sieverts apparatus using He gas at different starting pressures. The manifold and sample cell volumes were thus determined to be 35.3 ± 0.2 cm^3 and 14.9 ± 0.1 cm^3 respectively.

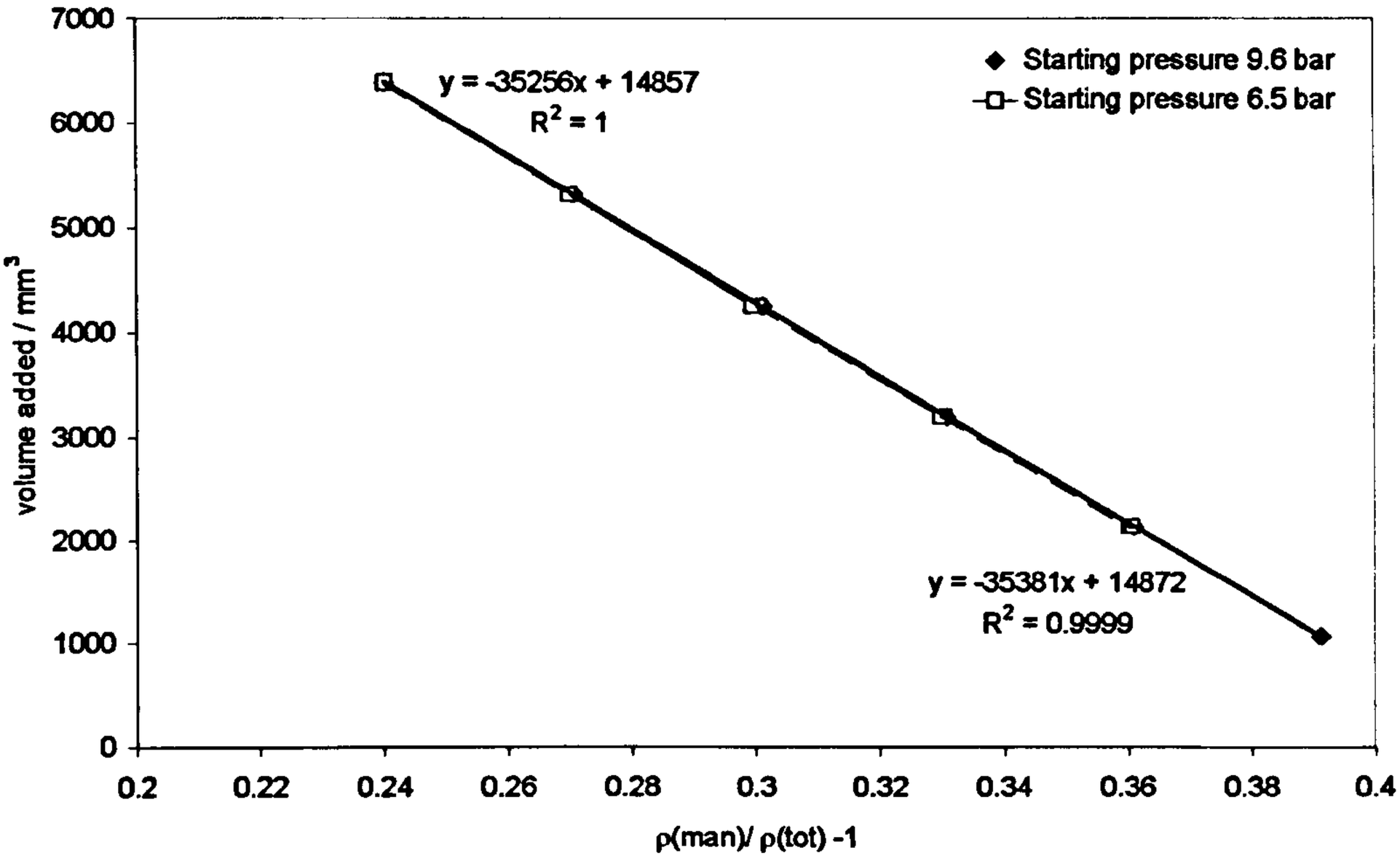

Figure 3.4: Calibration plots at starting pressures of 9.6 bar He and 6.5 bar He showing equations for manifold and sample cell volumes.

The experimental procedure in obtaining pressure composition isotherms (PCIs) for the MgH_2 and MgH_2/oxide samples consisted of loading a known weight of sample (100-200 mg) into the sample container within an Ar glove box, and then mounting the sealed sample container onto the Sieverts apparatus. When the enclosure temperature was stable, an initial leak check of the system with He was carried out by slowly filling the manifold and sample volume with approx. 8 bar of He and monitoring the pressure over the course of 1-2 h. If a drop in pressure was observed,

the joint attaching the sample cell to the manifold was tightened, and the leak check repeated until a stable pressure was maintained. The sample was then dehydrided by heating for 18 h under vacuum (pressure at pump *ca.* 1×10^{-6} mbar) to a temperature above the desorption onset for the given sample. The temperature was then changed to the desired temperature for the pressure composition isotherm. To account for the direct relationship between gas pressure and temperature, He was used to determine the effective volume of the sample cell at the given temperature. A specific amount of gas at the elevated temperature of the sample volume was equivalent to the same amount of gas occupying a smaller volume at the manifold temperature. To calculate this smaller, 'effective volume', an external thermocouple was used to ensure that the temperature of the pipework making up the manifold volume was unaffected by heating of the sample cell. By letting a known amount of gas (ρ_1)into the manifold of known volume (V_1), and then opening this up to the sample cell (ρ_2), the effective sample cell volume (V_2) could be determined using the following relationship (equation 3.12).

$$\rho_1 V_1 = \rho_2 (V_1 + V_2) \qquad \text{equation 3.12}$$

PCIs were determined at three different temperatures for each sample. A pressure increment of 0.5 bar was used, and stable manifold and equilibrium total pressures were recorded. These were then converted into densities using the virial equation (equation 3.10), and then into weights by multiplying the density by the known volume of the system.

In this way the weight absorbed or desorbed per step could be calculated, and an isotherm of equilibrium pressure against wt. % H_2 could be constructed for the given temperature used.

By determining PCIs at three different temperatures for each sample, van't Hoff plots can be constructed to obtain thermodynamic information including ΔH and ΔS of dehydrogenation. The van't Hoff equation (equation 3.13) relates the plateau pressure midpoint, p_{eq}, for a given reaction temperature T, to the enthalpy ΔH and entropy ΔS of the reaction.

$$\ln p_{eq} = -\Delta H/RT + \Delta S/R \qquad \text{equation 3.13}$$

A plot of $\ln p_{eq}$ against 1/T gives a straight line with slope of $-\Delta H/R$, and intercept of $\Delta S/R$.

3.6.3. Gravimetric hydrogen sorption

Gravimetric analysis of the hydrogen sorption of MgH_2 and mixed MgH_2/oxide samples was carried out using a Hiden Isochema Intelligent Gravimetric Analyser (IGA-003). Samples (50-80 mg) were loaded into stainless steel sample buckets inside the Ar glove box, and transferred to the IGA without air exposure using a N_2 purged inert loader (Hiden Isochema). Samples were initially dehydrided by heating for 18 h under vacuum (1×10^{-2} mbar) to a temperature above the desorption onset for

the given sample (300 or 350 °C). Following this initial dehydrogenation, each sample was cycled 10 times between 6 bar and 1 x 10^{-2} bar, at the same constant temperature used for the initial dehydrogenation, to complete 10 H_2 absorption and desorption cycles. Unlike the volumetric method described in the previous Section, which measures hydrogen gain and loss from pressure changes during absorption and desorption, the IGA uses an electronic beam balance that measures force, and gives a reading of the difference in mass between a reference arm and the sample arm. When gas is present in the IGA, buoyancy effects must be taken into account. For one object of mass m and density ρ_m in a gas of density, ρ_g, the buoyancy force, C_b, at a given temperature, is given by the following equation (equation 3.14), where g is the force due to gravity.

$$C_b = mg\,\rho_g/\rho_m \qquad \text{equation 3.14}$$

The correction for buoyancy used by the IGASwin software takes into account the various objects present in the weighing system, including the sample, any reacted gas, the sample container, the counterweight, and the hangdowns attaching the sample and counterweight to the balance arms. The combined correction factor is therefore a sum of the buoyancy force for all objects acting on the sample arm, minus the sum of the buoyancy force for objects acting on the reference arm.

For the isothermal cycling experiments carried out here, the raw data was collected as sample weight (corrected for buoyancy) against time. This was then converted to a weight percent, with initial weight taken as the weight at the starting point of each absorption or desorption step.

4. Results of oxide characterisation

4.1. Introduction

Previous studies reported in the literature indicate that metal oxides can have a beneficial effect on the desorption temperature and kinetics of hydrogen sorption when ball milled with Mg or MgH_2 [16,77,81]. The oxides used in the studies in the literature are generally commercial, crystalline single oxides and, as discussed in the literature review in Chapter 2, the mechanisms by which these oxides affect the desorption and absorption of hydrogen from MgH_2 are not yet fully understood. The work presented in this chapter includes results and discussion of the characterisation of single oxides Al_2O_3, SiO_2, TiO_2, and ZrO_2 formed from alkoxide precursors and heat treated at one of a range of calcination temperatures. The preparation method and heat treatments resulted in a range of oxides with varying bulk and surface structure, and a wide range of crystallinities and surface areas.

Mixed metal oxides have not previously been studied as additives to improve the hydrogen sorption properties of MgH_2, but they are used in a wide range of other applications as catalysts and catalyst support materials [90]. In order to explore the potential of using mixed metal oxides as additives to aid the desorption and absorption of hydrogen in MgH_2, a range of mixed oxides based on Al_2O_3 - SiO_2, TiO_2 - Al_2O_3, and TiO_2 - SiO_2 were prepared and characterised. The mixed oxides were prepared by a similar method to the single oxides, using hydrolysis of

alkoxide precursors. A series of heat treatments at temperatures identical to those used to treat the single oxides resulted in a range of mixed oxides with varying composition, bulk and surface properties.

Methods of dispersing precious metals onto metal oxide materials are widely used to make catalysts for a range of applications [91,92], and the catalytic effect of Pd as a hydrogen dissociation catalyst has been reported in the literature [63], but metals dispersed onto metal oxide materials have not been previously reported as catalysts for the sorption of hydrogen in MgH_2. To determine the effects of a dispersed metal/metal oxide material on the hydrogen sorption of MgH_2, a Pd - modified TiO_2 system was prepared and studied.

In Chapter 5, the effects of the single, Pd - modified, and mixed metal oxides on the hydrogen sorption properties of MgH_2 are discussed. To explain the behaviour of the oxides when ball milled with MgH_2, the prepared oxide materials were first characterised, in order to develop an understanding of the nature of their bulk and surface structure and properties, and the effect that the different oxide components and heat treatments have on these properties. The characterisation of the prepared oxide materials is the focus of this chapter.

Section 4.2 includes the results of characterisation of the prepared single and mixed oxide materials using XRD, N_2 Physisorption, DSC-TGA-MS, and DRIFTS. In Section 4.3, the results from the characterisation of

metal modified TiO_2 samples are presented. These materials were characterised using XRD and XPS.

4.2. Characterisation of single and mixed oxides

4.2.1. XRD

Powder X-ray diffraction was used to study the prepared Al_2O_3, SiO_2, TiO_2, and ZrO_2 samples dried at 70°C and those calcined for 2 h at 120°C, 400°C, or 800°C. Figures 4.1 - 4.4 show the diffraction patterns for the Al_2O_3, SiO_2, TiO_2 and ZrO_2 materials respectively.

The aluminium based samples had a boehmite AlO(OH) structure when dried at 70°C. The broadness of the diffraction lines indicated a nanocrystalline powder, with a crystallite size measured to be 5 nm. After calcination at 120°C, the boehmite structure was maintained, with the crystallite size remaining at 5 nm. A transformation to a γ-alumina structure was observed for the higher calcination temperatures, with the sample heated to 400°C showing broad diffraction lines for both boehmite and γ-alumina, most noticeable by the broad hump appearing at 2θ = 45°. After calcination at 800°C, the diffraction lines present corresponded to a γ-alumina structure, and boehmite was no longer observed to be present in the sample.

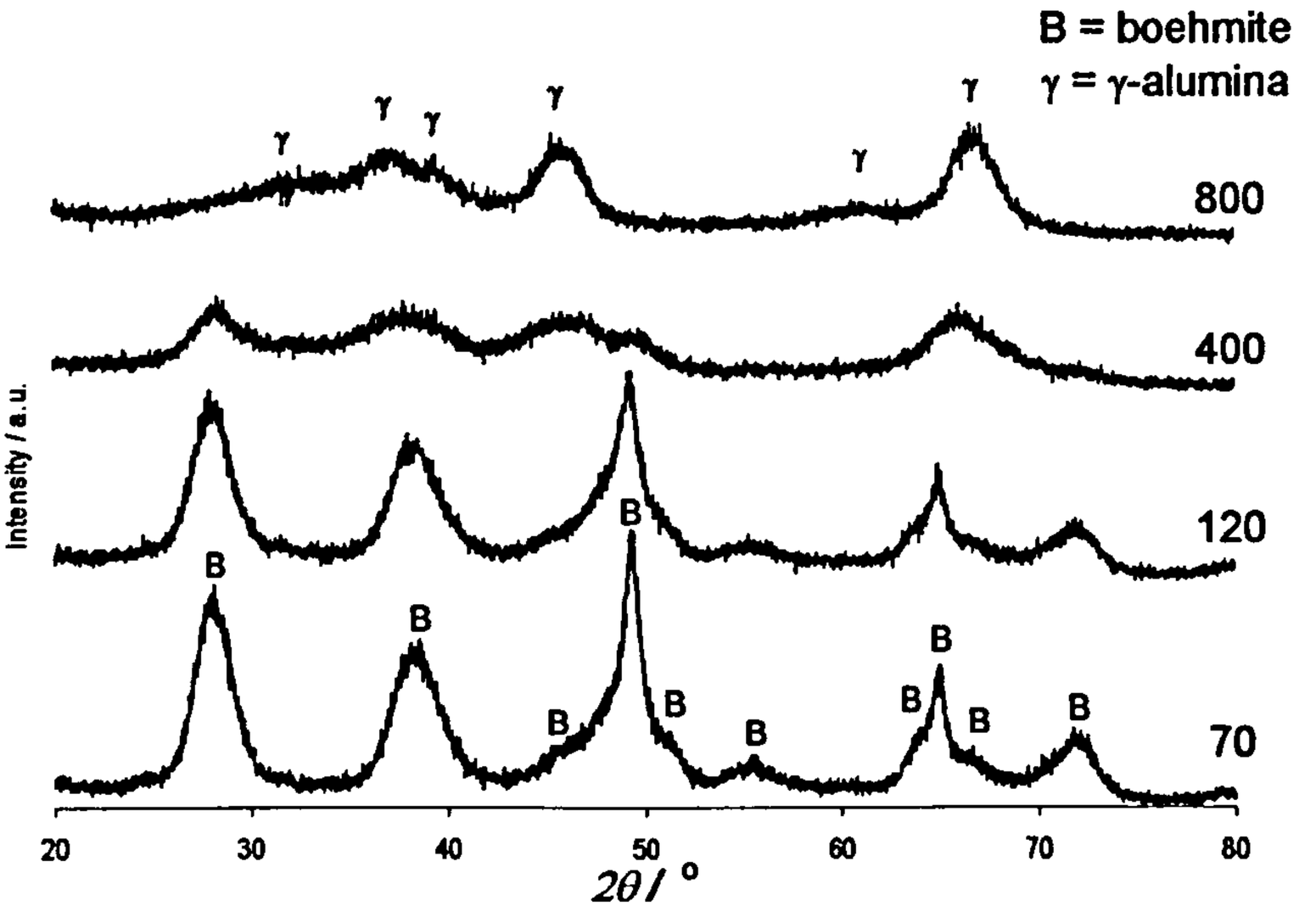

Figure 4.1: XRD patterns of Al70, Al120, Al400, Al800. Calcination temperature (in °C) given against respective plot.

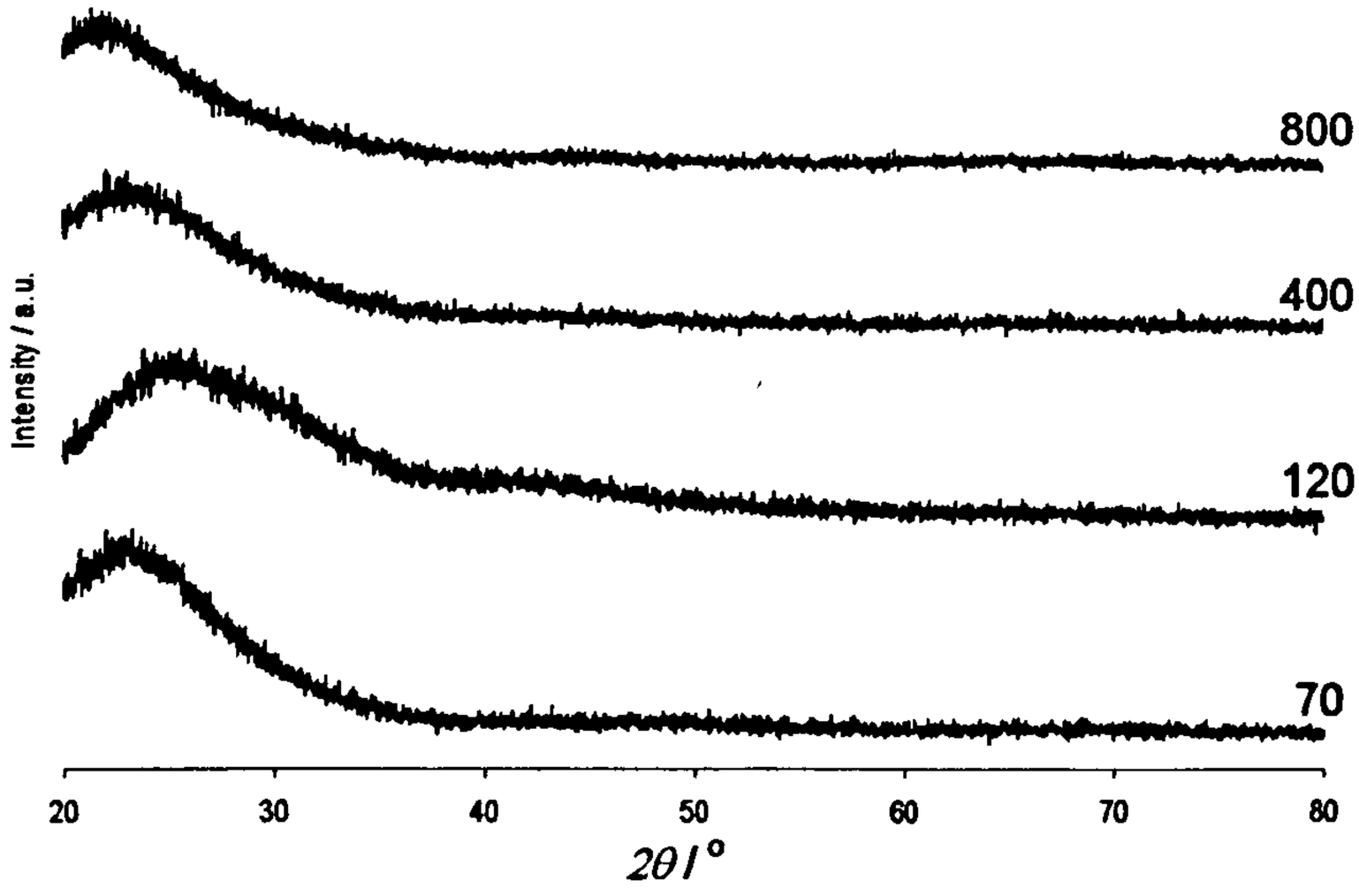

Figure 4.2: XRD patterns of Si70, Si120, Si400, Si800. Calcination temperature (in °C) given against respective plot.

The diffraction patterns for the silicon oxide samples (Figure 4.2) all displayed a broad hump indicative of an amorphous structure even after calcining 800°C, suggesting that the samples remained amorphous.

Figure 4.3 shows the diffraction patterns for the Ti based samples. The samples treated at lower temperatures (70°C and 120°C) were amorphous, displaying no diffraction lines. After calcination at 400°C, an anatase TiO_2 structure was formed. The average crystallite size of this phase was 10 nm. Calcining at 800°C induced the transformation to a rutile TiO_2 structure, with a small amount of anatase still present. The average size of the rutile and anatase crystallites was 250 nm and 220 nm respectively.

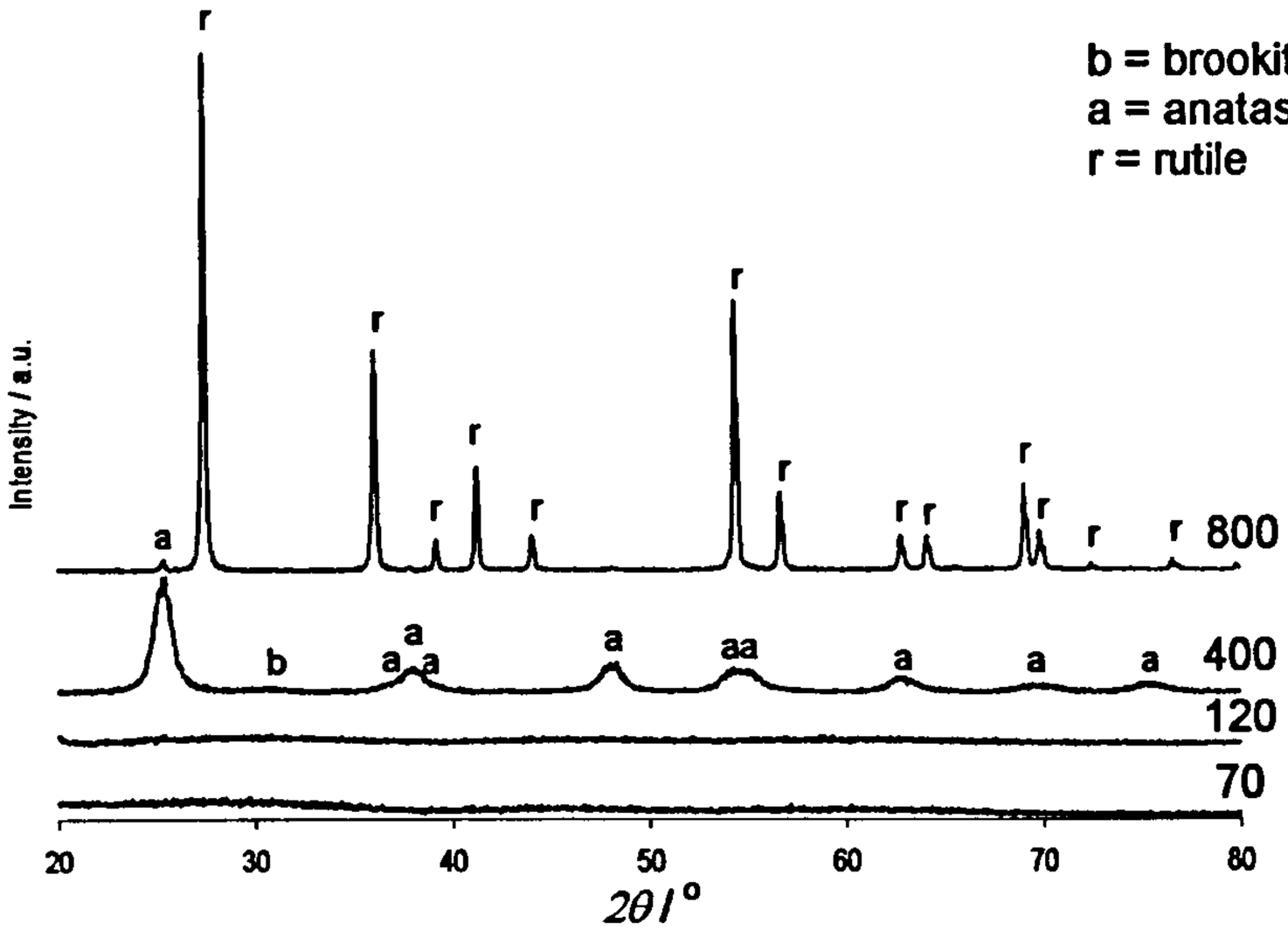

Figure 4.3: XRD patterns of Ti70, Ti120, Ti400, Ti800. Calcination temperature (in °C) given against respective plot.

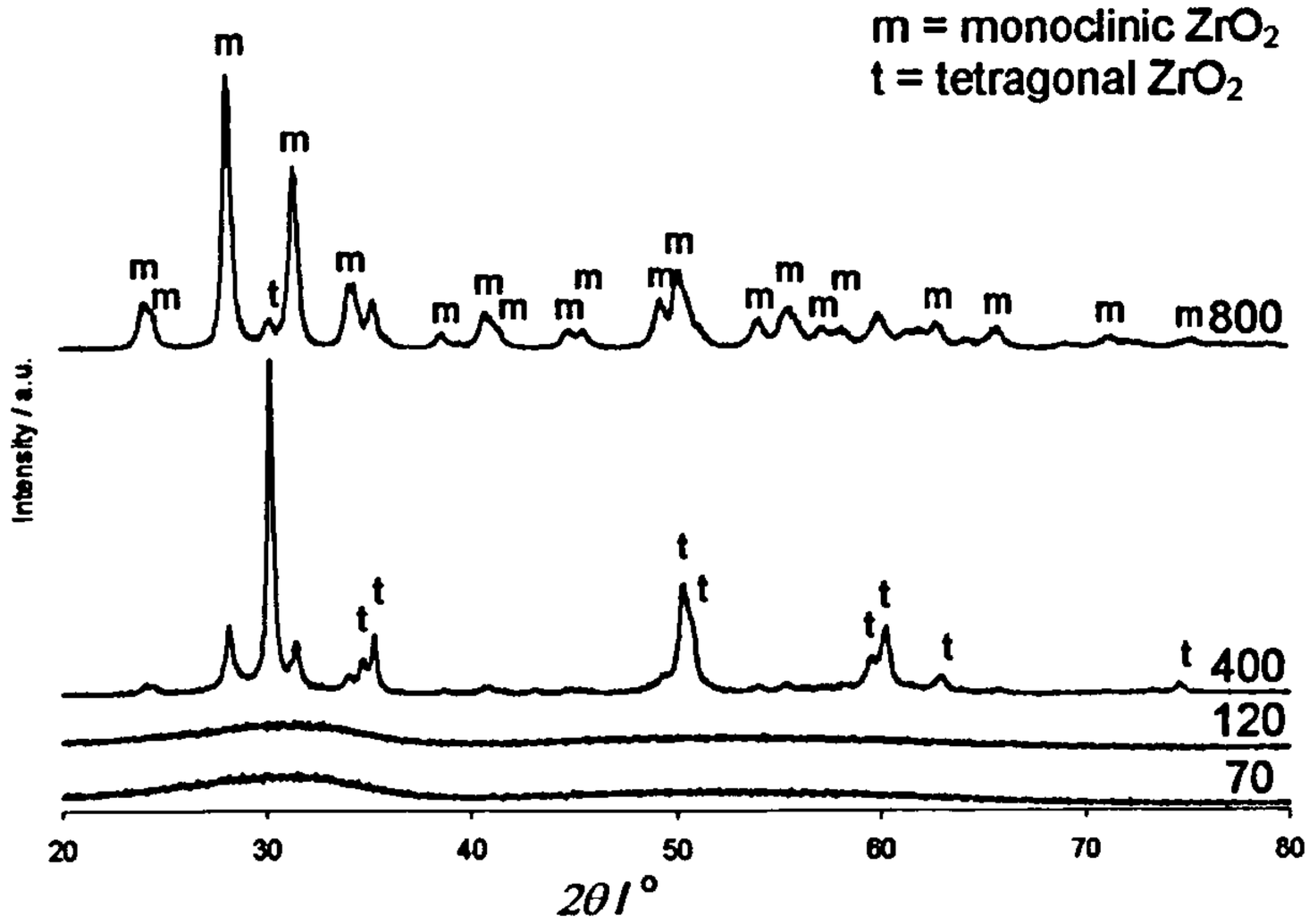

Figure 4.4: XRD patterns of Zr70, Zr120, Zr400, Zr800. Calcination temperature (in °C) given against respective plot.

The XRD patterns for ZrO_2 (Figure 4.4) follow a similar trend to those for TiO_2. The samples after treatment at 70°C and 120°C were amorphous. Two crystalline phases were observed after calcination at 400°C, with the tetragonal ZrO_2 phase, with an average crystallite size of 50 nm, being the most abundant. A small proportion of monoclinic ZrO_2 was also observed, with an average crystallite size of 40 nm. After calcination at 800°C, the ratio of the intensity of the diffraction lines for monoclinic ZrO_2 compared to those for the tetragonal phase had increased, indicating that the majority of the sample had the monoclinic structure. The average crystallite size of the tetragonal and monoclinic phases for the ZrO_2 sample calcined at 800°C was 30 nm and 50 nm respectively.

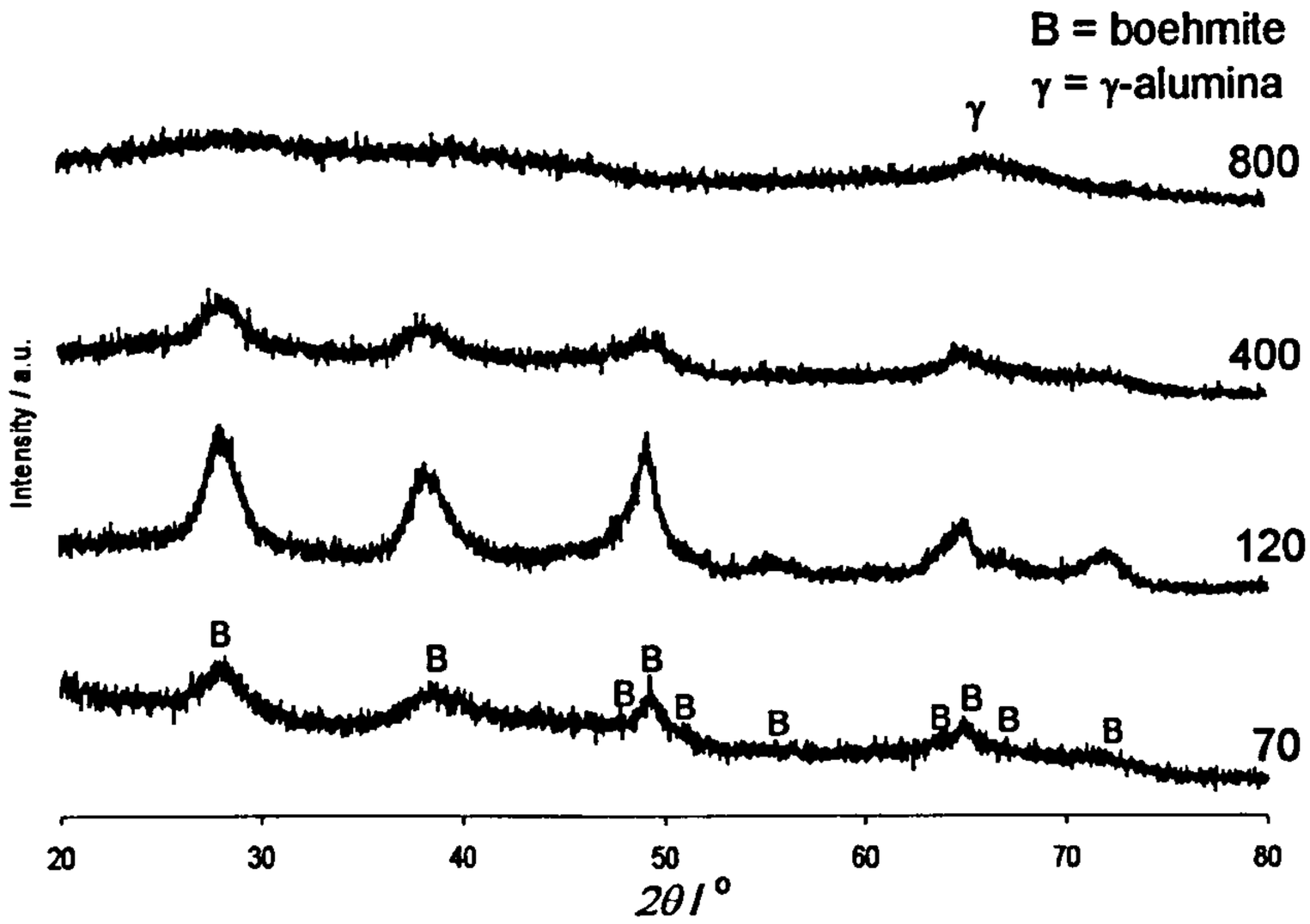

Figure 4.5: XRD patterns of 90Al10Si70, 90Al10Si120, 90Al10Si400, 90Al10Si800.

Calcination temperature (in °C) given against respective plot.

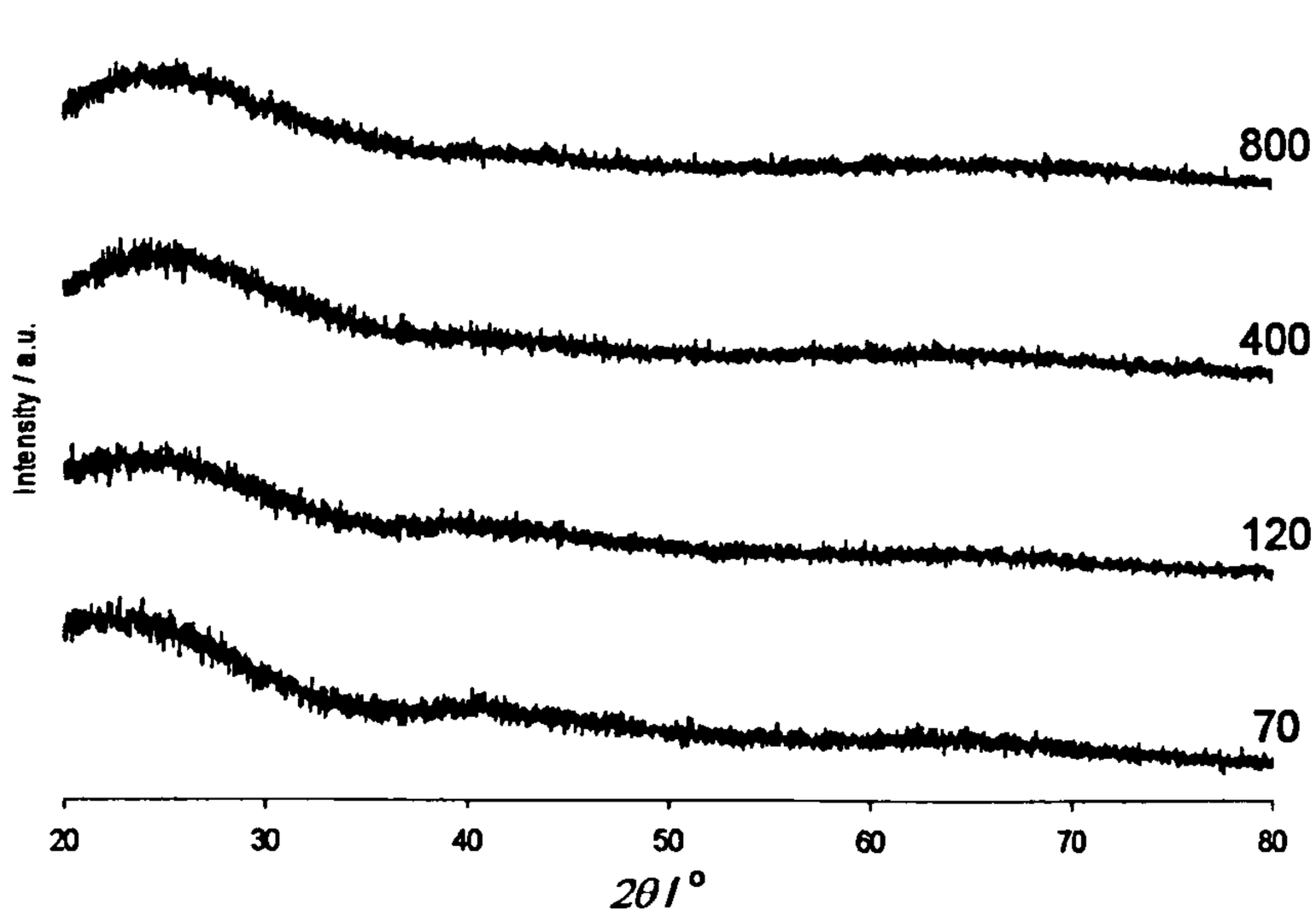

Figure 4.6: XRD patterns of 50Al50Si70, 50Al50Si120, 50Al50Si400, 50Al50Si800.

Calcination temperature (in °C) given against respective plot.

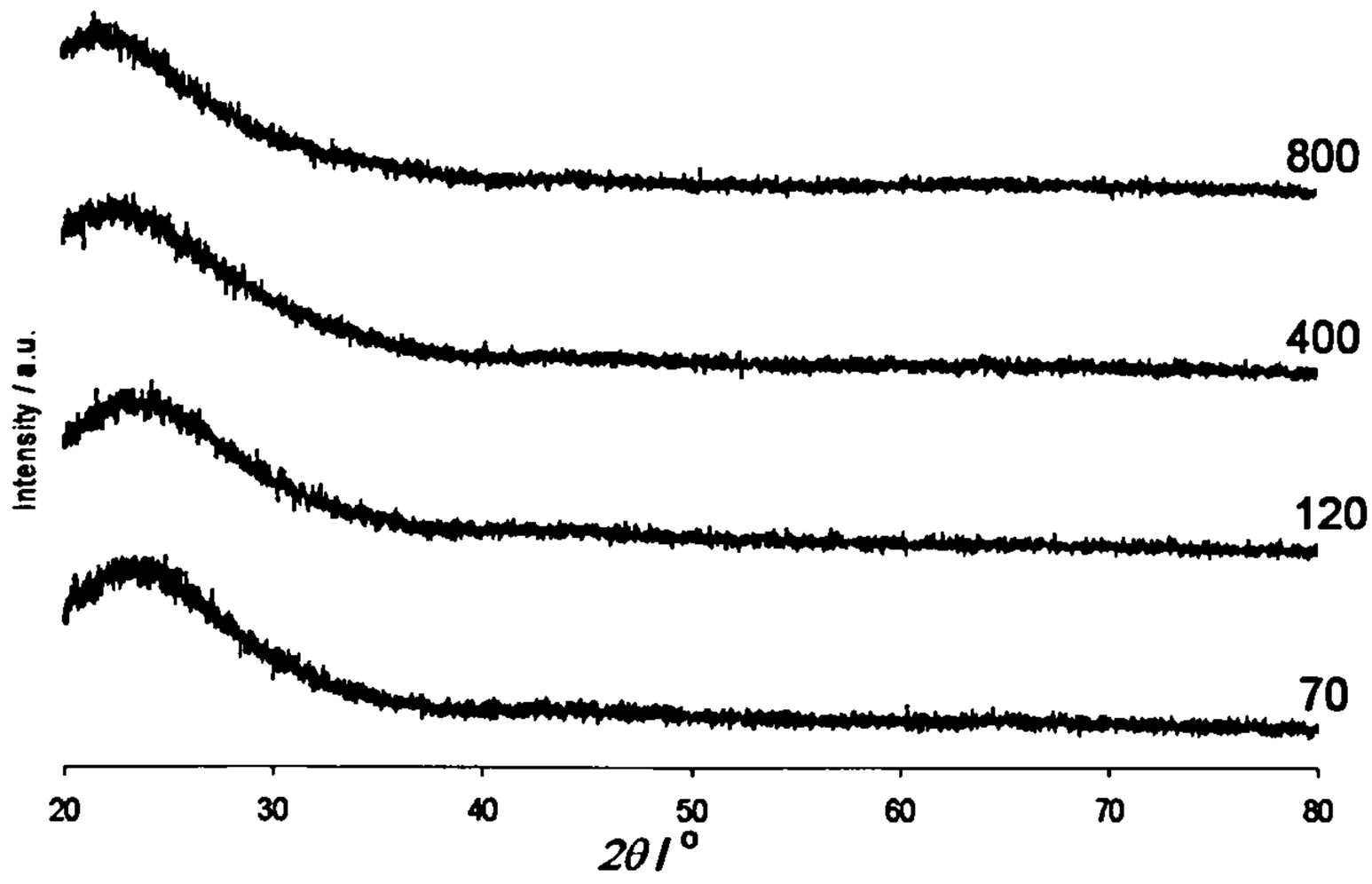

Figure 4.7: XRD patterns of 10Al90Si70, 10Al90Si120, 10Al90Si400, 10Al90Si800. Calcination temperature (in °C) given against respective plot.

XRD patterns for the 90Al10Si, 50Al50Si, and 10Al90Si mixed oxides are shown in Figures 4.5, 4.6, and 4.7, respectively. The XRD patterns of 90Al10Si70 and 90Al10Si120 both show broad diffraction lines corresponding to a nanocrystalline boehmite structure, with average crystallite sizes of 4 nm and 5 nm respectively. After calcination at 400°C, diffraction lines from the boehmite phase were still present, with a lower intensity that those observed for 90Al10Si120. The average crystallite size of the boehmite phase in 90Al10Si400 was 5 nm. The diffraction lines from the boehmite phase were not observed in the XRD pattern of 90Al10Si800, which shows some very broad humps, most noticeably the one with a maximum peaking at 2θ = 66°, which corresponds to the most intense diffraction line of γ-alumina. Both the 50Al50Si and 10Al90Si mixed oxides exhibited diffraction patterns characteristic of amorphous materials, with no distinct diffraction lines

corresponding to crystalline phases observed for any of the samples, regardless of calcination temperature.

Figure 4.8 shows the XRD patterns of the 90Ti10Al mixed oxides. 90Ti10Al70 and 90Ti10Al120 were both amorphous materials, with no diffraction lines appearing in the XRD patterns. After calcination at 400°C, broad peaks corresponding to anatase TiO_2 were present in the diffraction pattern. The average crystallite size of the anatase phase in 90Ti10Al400 was found to be 12 nm. From the diffraction pattern of 90Ti10Al800, both the anatase and rutile phases of TiO_2 were present in this sample, with slightly more anatase than rutile phase. The average crystallite sizes of the two phases were 50 nm and 140 nm for anatase and rutile respectively.

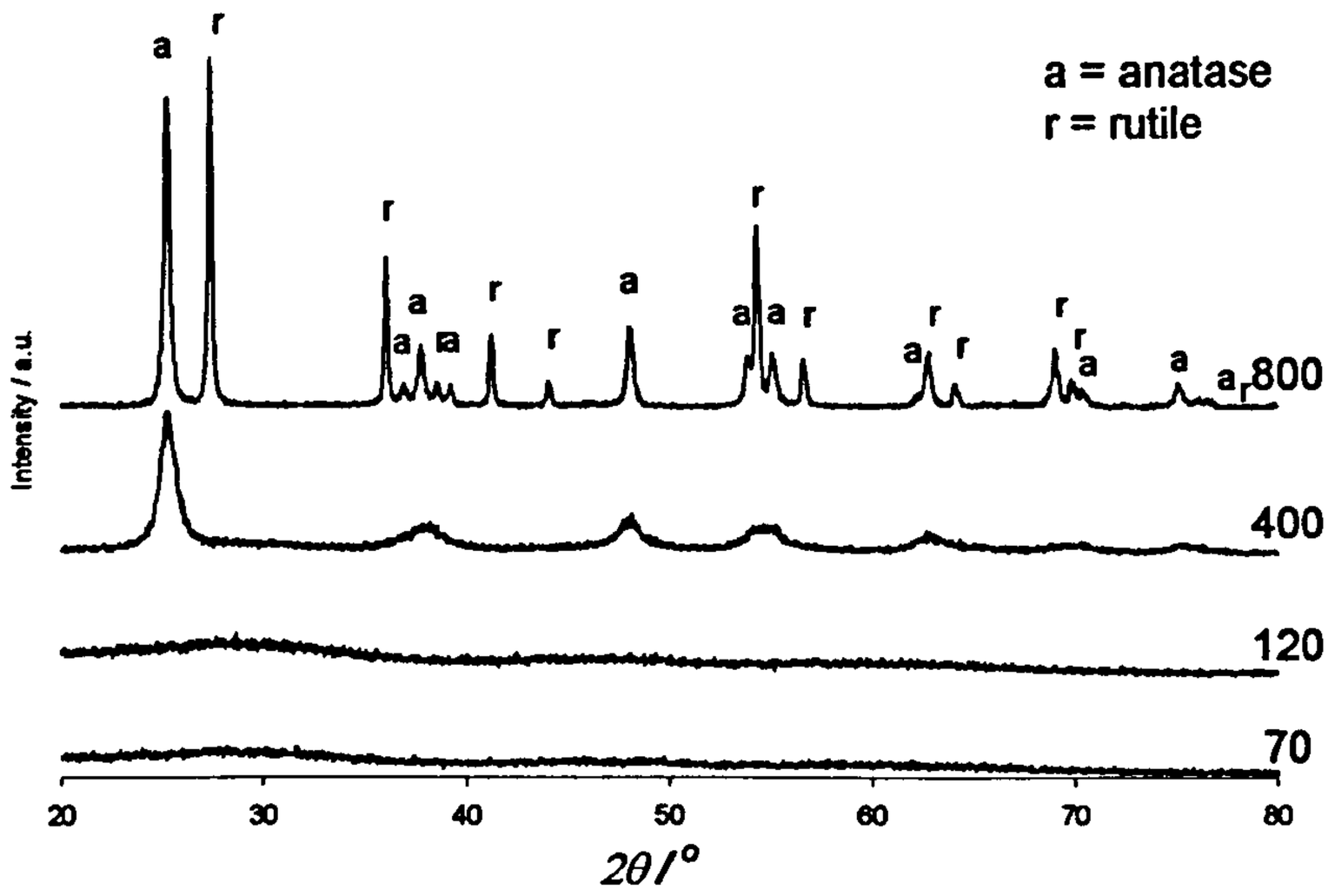

Figure 4.8: XRD patterns of 90Ti10Al70, 90Ti10Al120, 90Ti10Al400, 90Ti10Al800.

Calcination temperature (in °C) given against respective plot.

The 50Ti50Al mixed oxide (Figure 4.9) exhibited diffraction lines corresponding to the boehmite AlO(OH) structure when dried at 70°C, and after calcination at 120°C. The average crystallite size for the boehmite in 50Ti50Al70 and 50Ti50Al120 was 4 nm and 5 nm respectively. Broad diffraction lines corresponding to the anatase TiO_2 phase with an average crystallite size of 12 nm were present in the pattern for 50Ti50Al400. After calcination at 800°C, 50Ti50Al displayed diffraction lines from both anatase and rutile TiO_2, with anatase being the dominant phase present. The average crystallite sizes of the anatase and rutile phases were 40 nm and 130 nm respectively. 50Ti50Al800 also contained some γ-alumina, indicated by the very broad humps appearing at 2θ values of 48° and 68°.

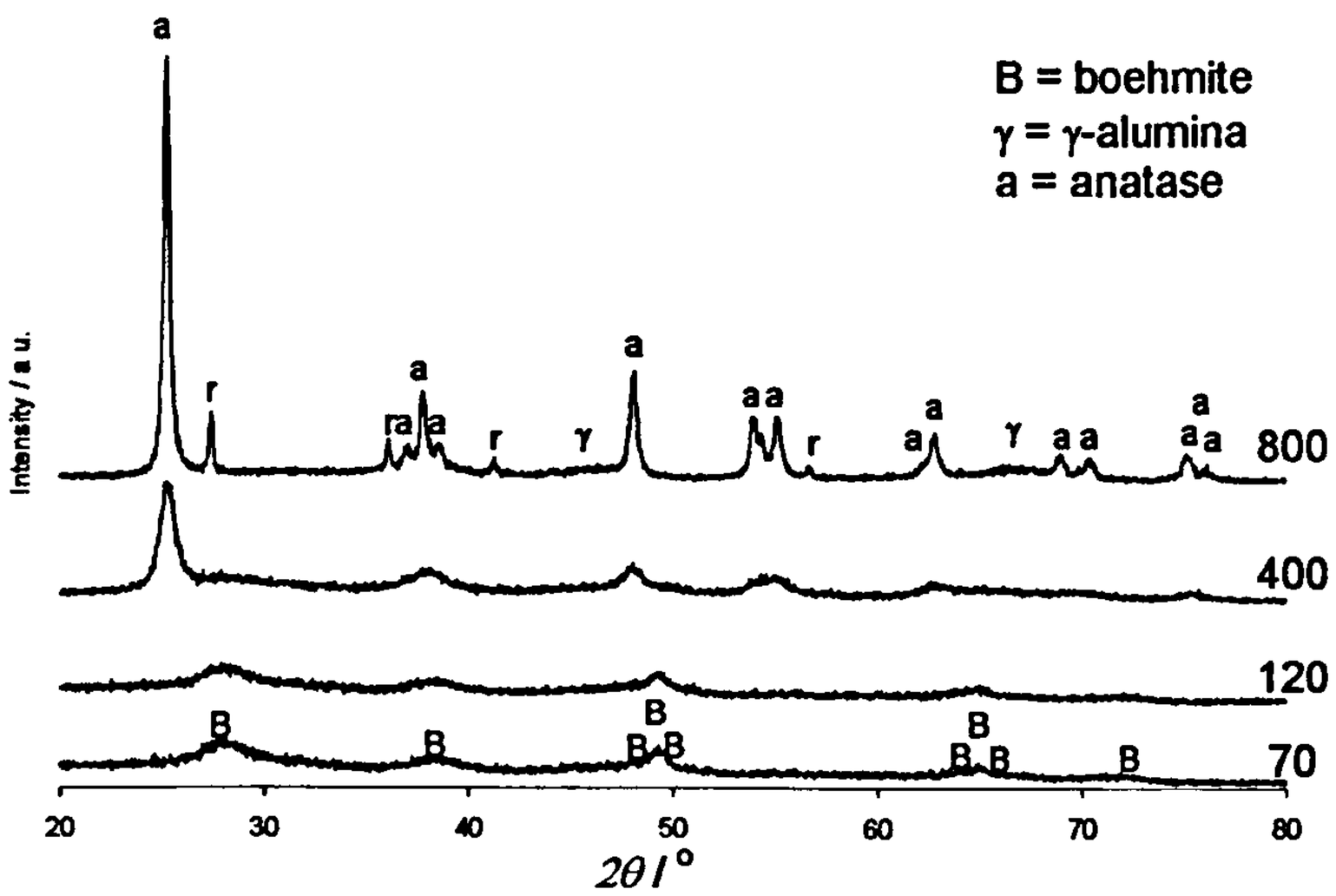

Figure 4.9: XRD patterns of 50Ti50Al70, 50Ti50Al120, 50Ti50Al400, 50Ti50Al800.

Calcination temperature (in °C) given against respective plot.

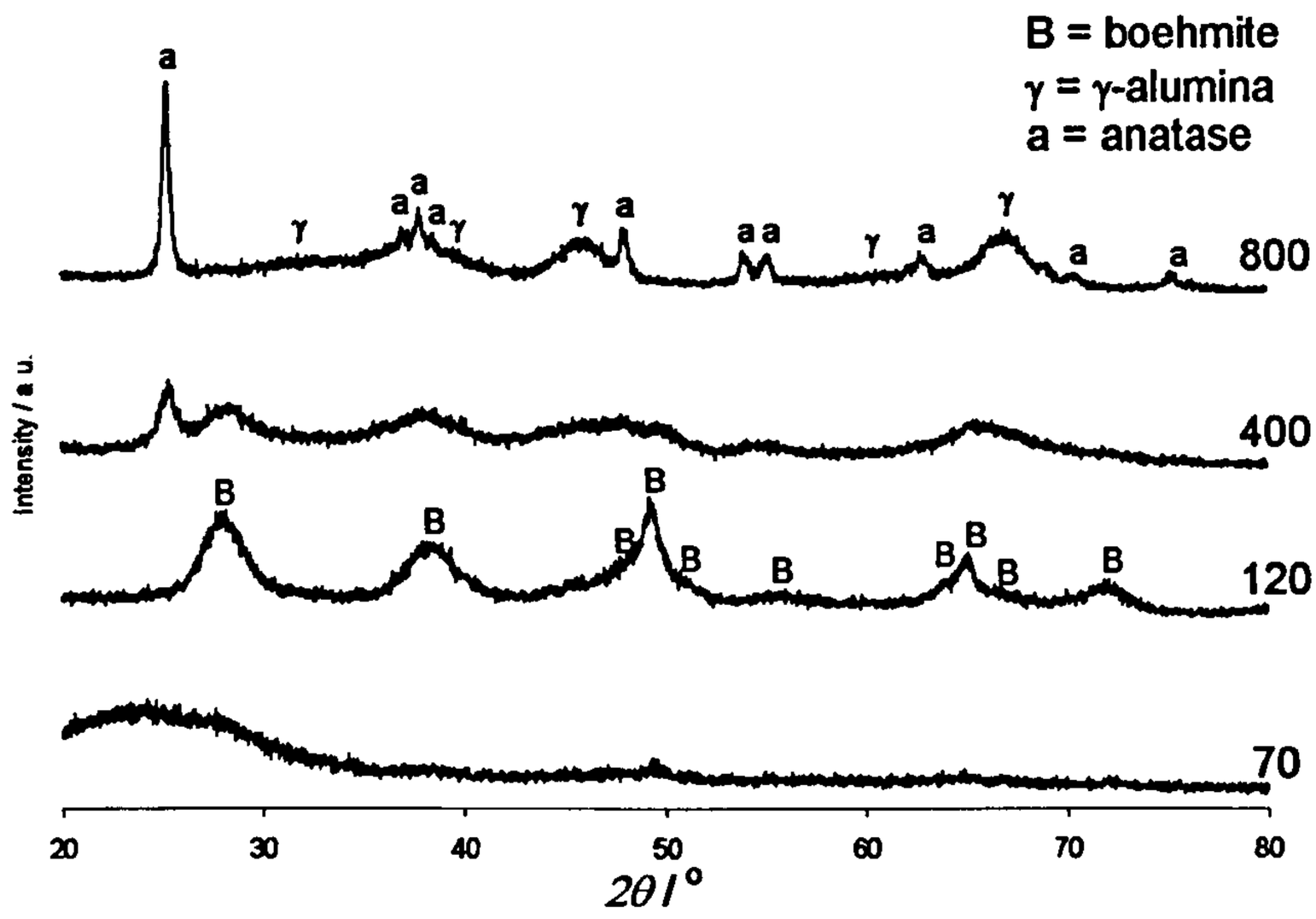

Figure 4.10: XRD patterns of 10Ti90Al70, 10Ti90Al120, 10Ti90Al400, 10Ti90Al800. Calcination temperature (in °C) given against respective plot.

Figure 4.10 shows the XRD patterns for the 10Ti90Al mixed oxides. The 10Ti90Al70 and 10Ti90Al120 samples showed diffraction lines for the boehmite phase, with average crystallite sizes calculated as 4 nm and 5 nm for the 70°C and 120°C samples respectively. 10Ti90Al400 displayed broad diffractions corresponding to the boehmite and γ-alumina phases, as well as anatase TiO_2, which had an average crystallite size of 15 nm. Anatase TiO_2 was the dominant phase present in the 10Ti90Al800 sample, with an average crystallite size of 40 nm. Broad diffraction lines from γ-alumina were also present in the trace for 10Ti90Al800.

Figures 4.11 - 4.13 show the XRD patterns for the 90Ti10Si, 50Ti50Si and 10Ti90Si mixed oxides. For all three oxide ratios, the samples dried at 70°C, and calcined at 120°C or 400°C did not show any diffraction lines, indicating that these samples had amorphous structures. The 90Ti10Si

and 50Ti50Si samples calcined at 800°C showed diffraction lines corresponding to anatase TiO_2. Average crystallite sizes for the anatase phase present in 90Ti10Si800 and 50Ti50Si800 were 10 nm and 4 nm, respectively.

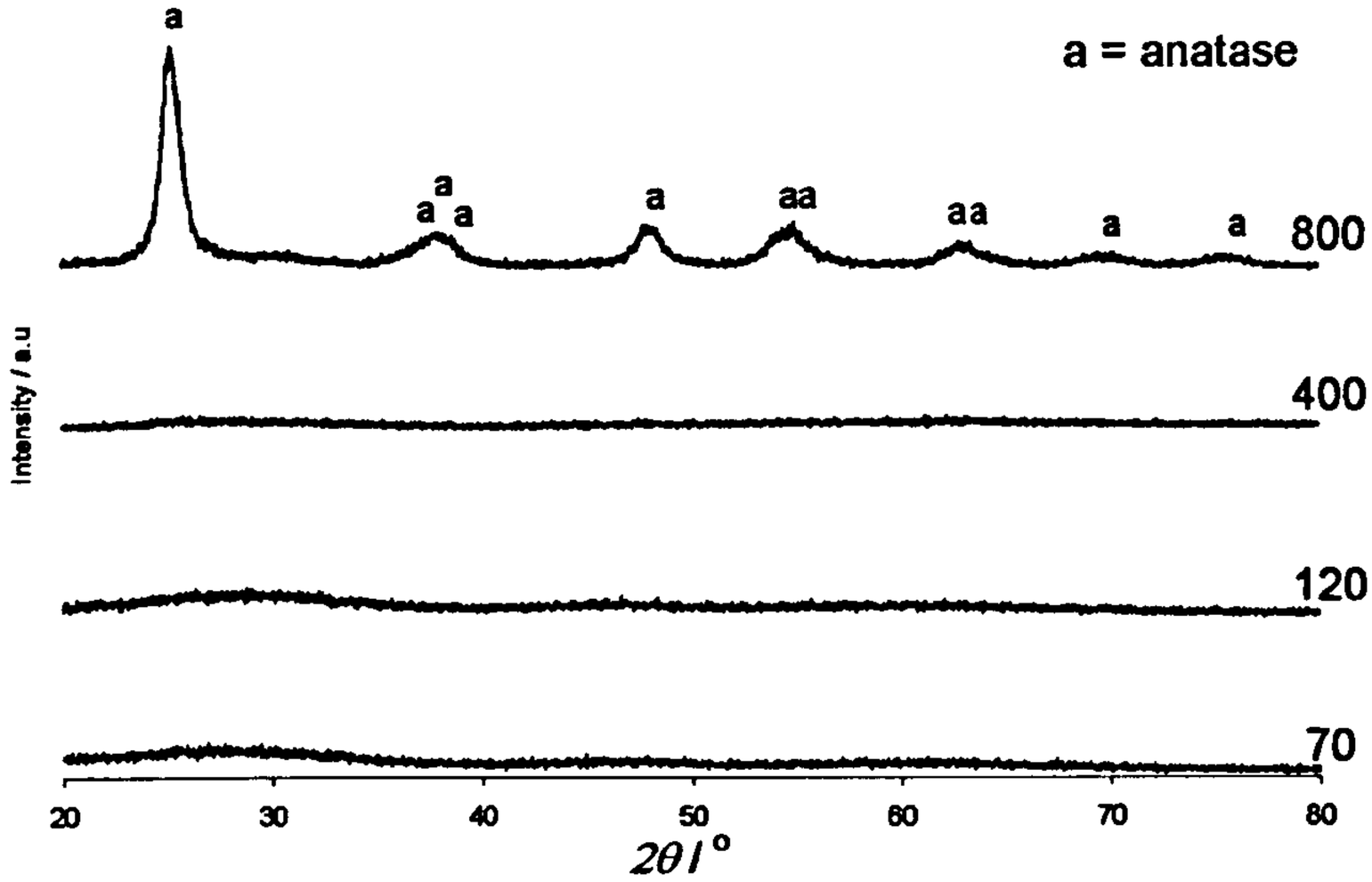

Figure 4.11: XRD patterns of 90Ti10Si70, 90Ti10Si120, 90Ti10Si400, 90Ti10Si800. Calcination temperature (in °C) given against respective plot.

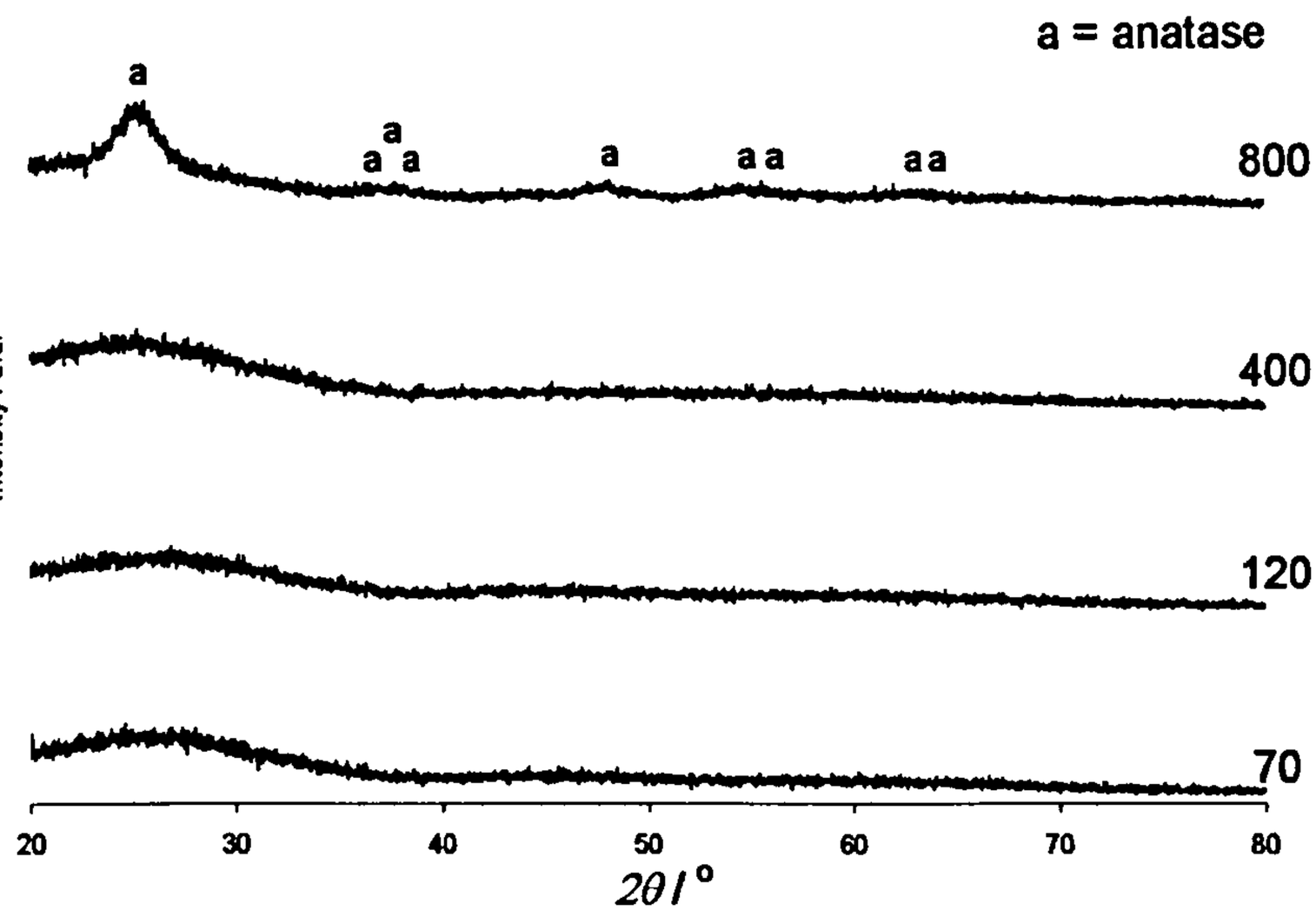

Figure 4.12: XRD patterns of 50Ti50Si70, 50Ti50Si120, 50Ti50Si400, 50Ti50Si800. Calcination temperature (in °C) given against respective plot.

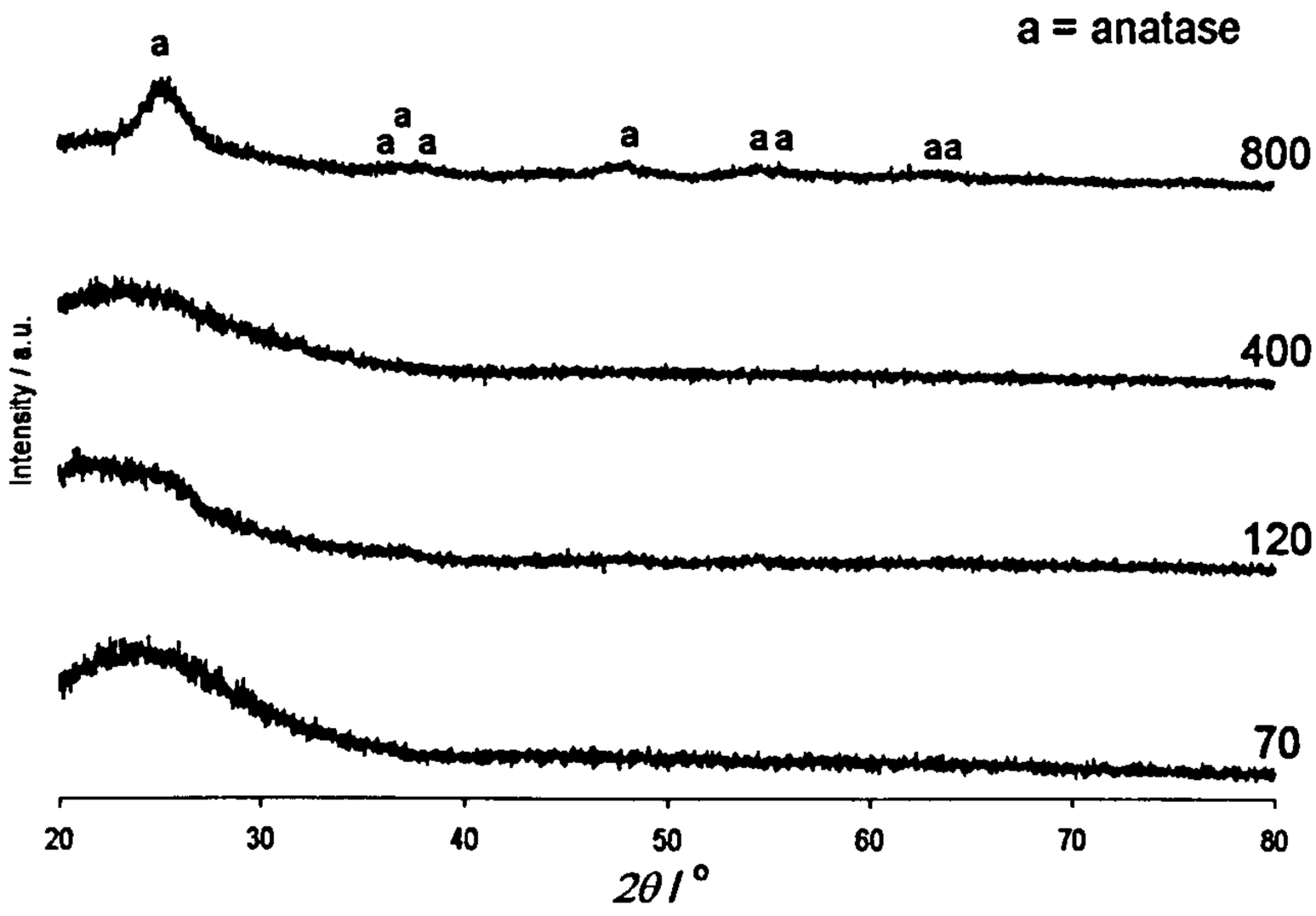

Figure 4.13: XRD patterns of 10Ti90Si70, 10Ti90Si120, 10Ti90Si400, 10Ti90Si800. Calcination temperature (in °C) given against respective plot.

4.2.2. N_2 Physisorption

N_2 physisorption was used to calculate BET surface areas of the single and mixed oxide samples. The results of the surface area measurements are summarised in Table 4.1. For the Al_2O_3 samples, the sample dried at 70°C had the highest surface area of 414 $m^2 g^{-1}$. The surface area was lower (310 $m^2 g^{-1}$) after calcination at 120°C, but then increased to 360 $m^2 g^{-1}$ after calcination at 400°C before dropping again to 250 $m^2 g^{-1}$ after the 800°C heat treatment. For SiO_2, there was an increase in surface area for calcination temperatures up to a maximum of 560 $m^2 g^{-1}$ after the 400°C calcination, followed by a decrease to 305 $m^2 g^{-1}$ after the 800°C heat treatment. The surface areas of the TiO_2 and ZrO_2 single oxide samples both decreased with increasing calcination temperature,

from 455 $m^2 g^{-1}$ for Ti70 to 15 $m^2 g^{-1}$ for Ti800, and from 190 $m^2 g^{-1}$ for Zr70 to 25 $m^2 g^{-1}$ for Zr800.

Oxide	BET surface area / $m^2 g^{-1}$	Oxide	BET surface area / $m^2 g^{-1}$
Al70	415	*10Al90Si400*	90
Al120	310	*10Al90Si800*	60
Al400	360	*90Ti10Al70*	500
Al800	250	*90Ti10Al120*	550
Si70	385	*90Ti10Al400*	385
Si120	450	*90Ti10Al800*	55
Si400	560	*50Ti50Al70*	490
Si800	305	*50Ti50Al120*	430
Ti70	455	*50Ti50Al400*	310
Ti120	390	*50Ti50Al800*	145
Ti400	135	*10Ti90Al70*	400
Ti800	15	*10Ti90Al120*	420
Zr70	190	*10Ti90Al400*	360
Zr120	165	*10Ti90Al800*	265
Zr400	40	*90Ti10Si70*	355
Zr800	25	*90Ti10Si120*	345
90Al10Si70	460	*90Ti10Si400*	160
90Al10Si120	305	*90Ti10Si800*	60
90Al10Si400	360	*50Ti50Si70*	385
90Al10Si800	330	*50Ti50Si120*	365
50Al50Si70	440	*50Ti50Si400*	315
50Al50Si120	520	*50Ti50Si800*	120
50Al50Si400	315	*10Ti90Si70*	450
50Al50Si800	360	*10Ti90Si120*	410
10Al90Si70	270	*10Ti90Si400*	75
10Al90Si120	120	*10Ti90Si800*	15

Table 4.1: BET surface areas of single and mixed oxide samples. For samples of surface area > 200 $m^2 g^{-1}$, average error is 5 %. For samples of surface area < 200 $m^2 g^{-1}$, average error is 10 %. Error calculated from measurements repeated 5 times.

The 90Al10Si mixed oxides followed the same trend in surface area with increasing calcination temperature as the Al single oxides, with the 90Al10Si70 sample having the highest surface area of 460 $m^2 g^{-1}$, followed by a drop to 305 $m^2 g^{-1}$ for 90Al10Si120. The surface area then increased to 360 $m^2 g^{-1}$ for 90Al10Si400, before dropping slightly to 330 $m^2 g^{-1}$ for

90Al10Si800. For the 50Al50Si oxides, the sample calcined at 120°C had the highest surface area of 520 $m^2 g^{-1}$, with the surface area decreasing to 315 $m^2 g^{-1}$ and then increasing again to 360 $m^2 g^{-1}$ for 50Al50Si400 and 50Al50Si800, respectively. A decrease in surface area with increasing calcination temperature was observed for the 10Al90Si samples, from 270 $m^2 g^{-1}$ for 10Al90Si70 to 60 $m^2 g^{-1}$ for 10Al90Si800.

For the 90Ti10Al samples, the surface area initially increased from 500 $m^2 g^{-1}$ for 90Ti10Al70 to 550 $m^2 g^{-1}$ for 90Ti10Al120. The surface area then decreased to 385 $m^2 g^{-1}$ for 90Ti10Al400, and to 55 $m^2 g^{-1}$ for 90Ti10Al800. The surfaces areas of the 50Ti50Al mixed oxides decreased with increasing calcination temperature, from a maximum of 490 $m^2 g^{-1}$ for 50Ti50Al70 to a minimum of 145 $m^2 g^{-1}$ for 50Ti50Al800. For the 10Ti90Al samples, the trend in surface area was similar to that found for the 90Ti10Al samples, with an initial surface area of 400 $m^2 g^{-1}$ for the 10Ti90Al70 oxide, which increased slightly to 420 $m^2 g^{-1}$ for 10Ti90Al120, and then decreased to 360 $m^2 g^{-1}$ and 265 $m^2 g^{-1}$ for 10Ti90Al400 and 10Ti90Al800, respectively.

All of the Ti-Si based mixed oxide systems followed a trend of decreasing surface area with increasing heat treatment temperature. The 90Ti10Si samples had a maximum surface area of 355 $m^2 g^{-1}$ for the sample dried at 70°C, which decreased to 60 $m^2 g^{-1}$ for the sample calcined at 800°C. For the 50Ti50Si oxides, the 50Ti50Si70 sample had the highest surface area, of 385 $m^2 g^{-1}$. After calcination at 800°C, the surface area of

50Ti50Si had decreased to 120 $m^2 g^{-1}$. Finally, the surface area of the 10Ti90Si samples decreased from 450 $m^2 g^{-1}$ for 10Ti90Si70, to 15 $m^2 g^{-1}$ for 10Ti90Si800.

4.2.3. DSC-TGA-MS

The water desorbed from the single and mixed oxide samples dried at 70°C, during heating to 500°C at a rate of 10°C min^{-1}, was measured using DSC-TGA coupled to a mass spectrometer. Figures 4.14 to 4.17 show the MS water traces (m/z 18) and TGA weight loss traces for the single oxides, Al - Si mixed oxides, Ti - Al mixed oxides and Ti - Si mixed oxides, respectively. The DSC data showed endothermic reactions occurred as water was desorbed from each sample, and the TGA data quantifies the amount of water that evolved from each oxide during heating.

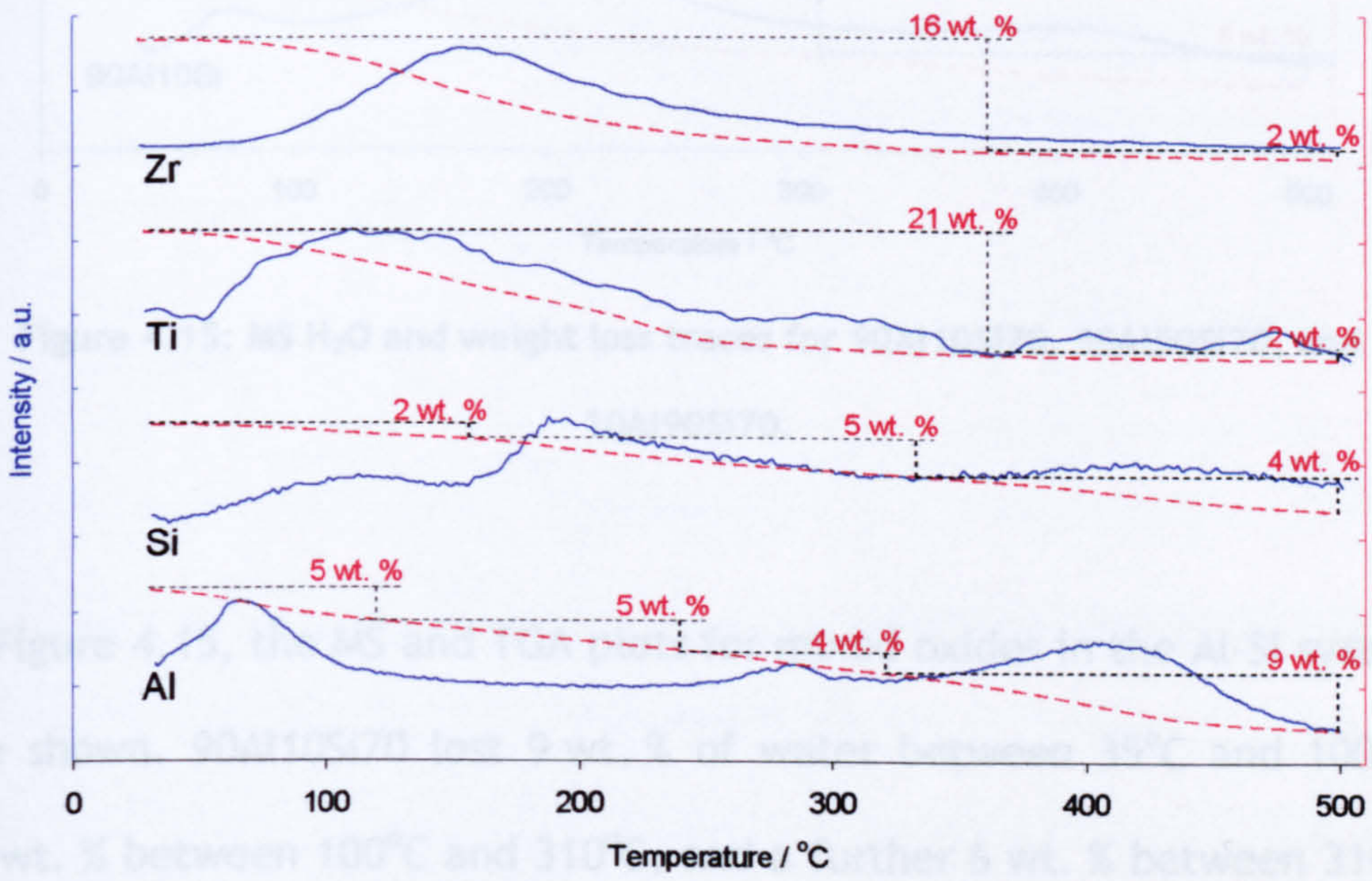

Figure 4.14: MS H_2O and weight loss traces for Al70, Si70, Ti70, and Zr70.

The Al70 boehmite sample lost a total of 23 wt. % during heating, which can be attributed to three main water loss peaks, occurring at 35 - 120°C, 250 - 320°C, and 320 - 500°C. Si70 also had three water loss peaks, between 35 - 150°C, 150 - 330°C, and 330 - 500°C, with a total water loss amounting to 11 wt. %. The other oxide samples, Ti70 and Zr70, both exhibited a single water loss peak between 60°C and 350°C, with a total weight loss for Ti70 of 23 wt. %, and a total weight loss for Zr70 of 18 wt. %.

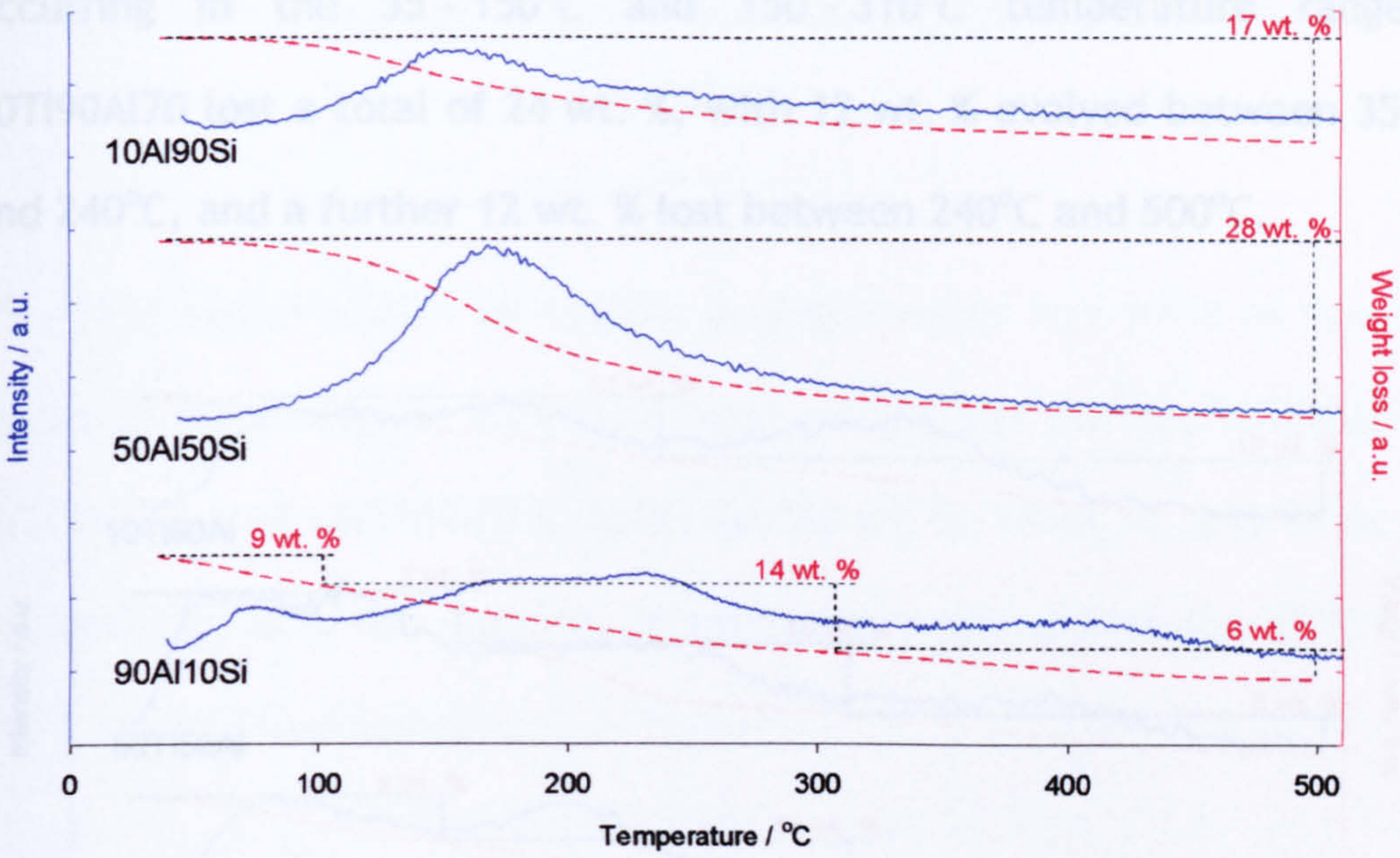

Figure 4.15: MS H_2O and weight loss traces for 90Al10Si70, 50Al50Si70, and 10Al90Si70.

In Figure 4.15, the MS and TGA plots for mixed oxides in the Al-Si system are shown. 90Al10Si70 lost 9 wt. % of water between 35°C and 100°C, 14 wt. % between 100°C and 310°C, and a further 6 wt. % between 310°C and 500°C. The 50Al50Si70 and 10Al90Si70 materials both exhibited a

single water loss peak over the 35 - 500°C heating range. 50Al50Si70 lost a total of 28 wt. %, while 17 wt. % was evolved from 10Al90Si70.

The MS and TGA traces for the Ti-Al based oxides are given in Figure 4.16. The 90Ti10Al70 and 50Ti50Al70 samples displayed similar MS traces for water evolved from the samples. 90Ti10Al70 lost a total of 23 wt. % with the main water loss peaks occurring in the temperature ranges 35 - 150°C and 150 - 310°C. A total of 23 wt. % was also lost from 50Ti50Al70 during heating, with the main weight loss peaks also occurring in the 35 - 150°C and 150 - 310°C temperature ranges. 10Ti90Al70 lost a total of 24 wt. %, with 12 wt. % evolved between 35°C and 240°C, and a further 12 wt. % lost between 240°C and 500°C.

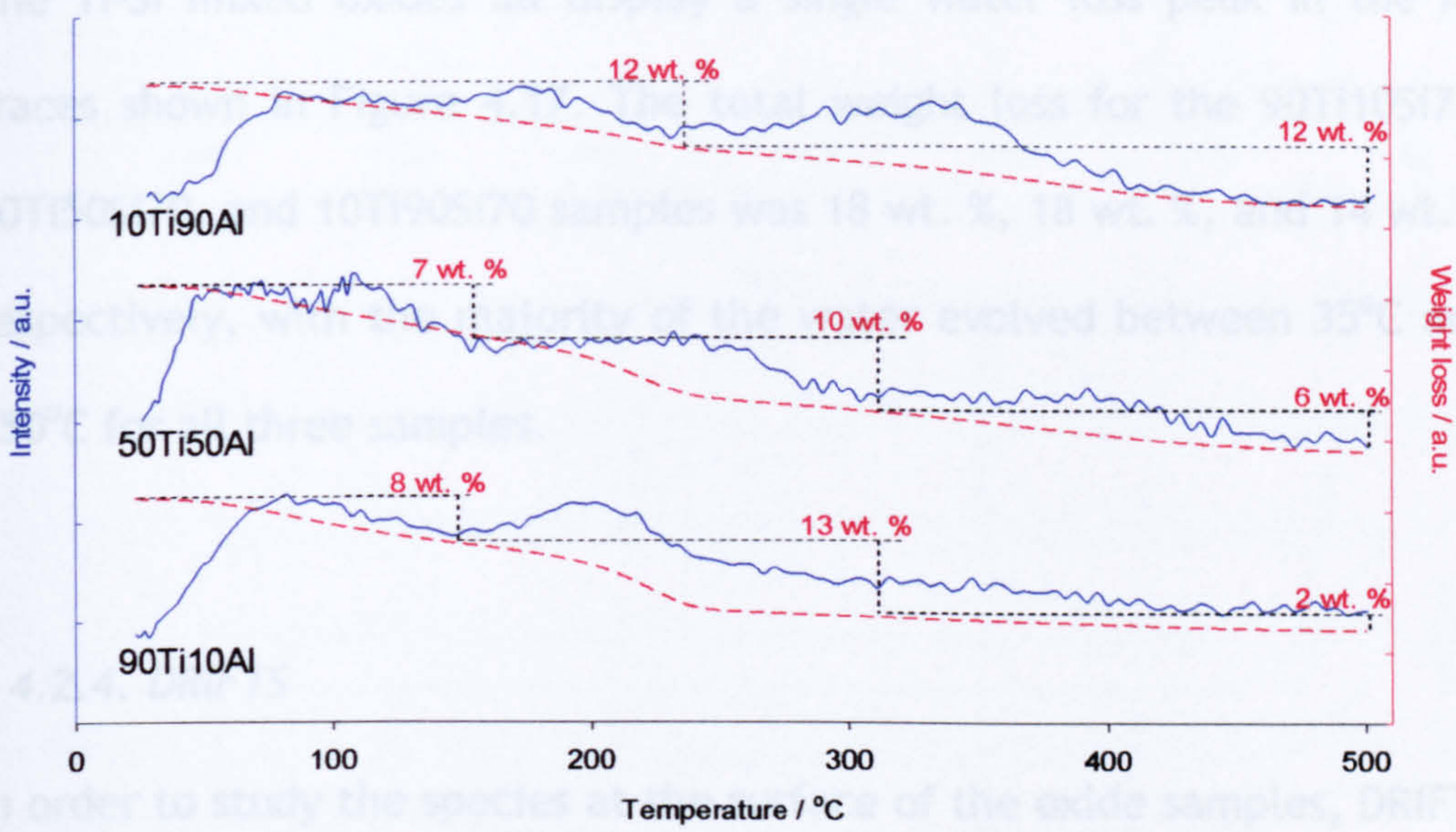

Figure 4.16: MS H_2O and weight loss traces for 90Ti10Al70, 50Ti50Al70, and 10Ti90Al70.

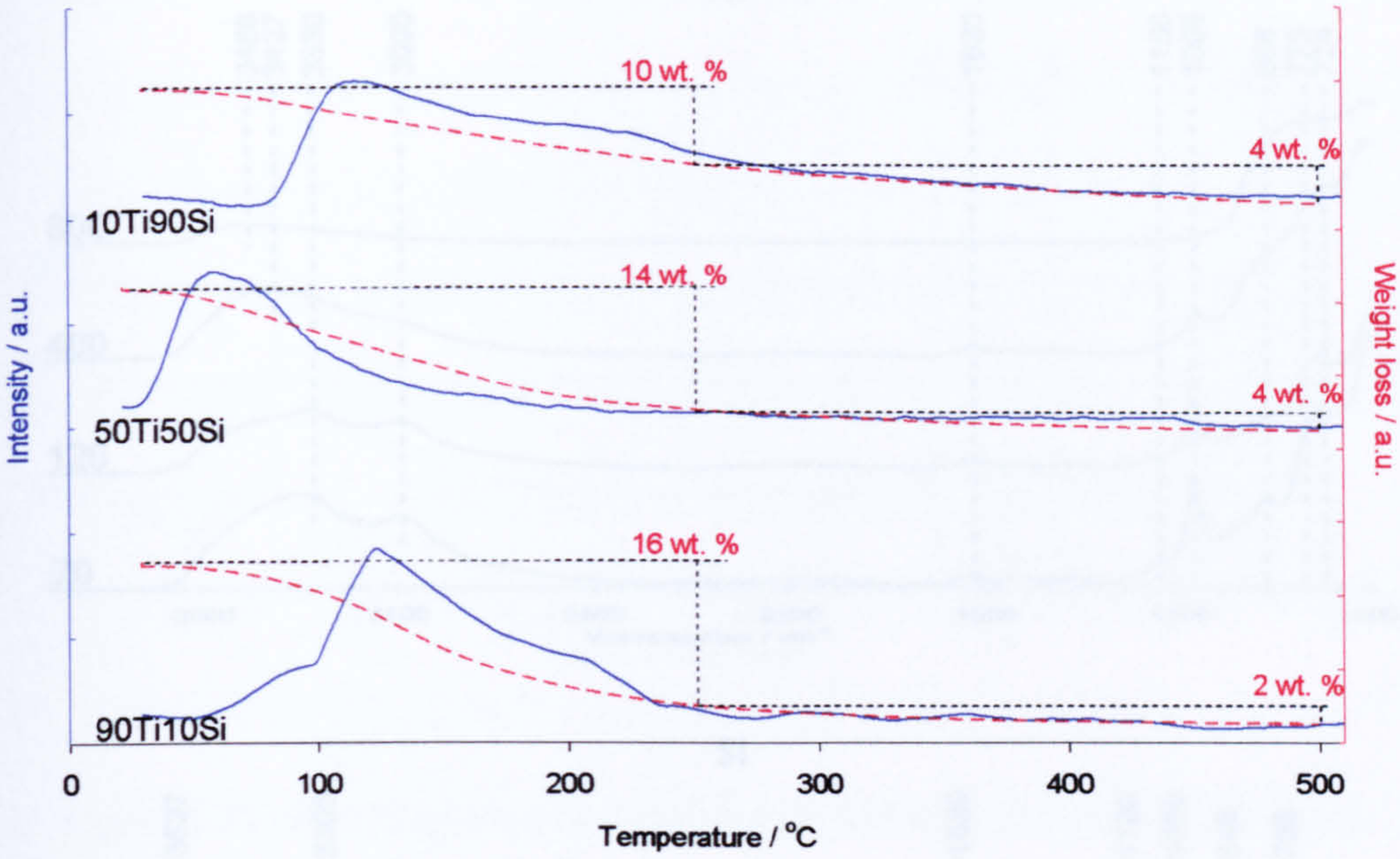

Figure 4.17: MS H_2O and weight loss traces for 90Ti10Si70, 50Ti50Si70, and 10Ti90Si70.

The Ti-Si mixed oxides all display a single water loss peak in the MS traces shown in Figure 4.17. The total weight loss for the 90Ti10Si70, 50Ti50Si70, and 10Ti90Si70 samples was 18 wt. %, 18 wt. %, and 14 wt. % respectively, with the majority of the water evolved between 35°C and 250°C for all three samples.

4.2.4. DRIFTS

In order to study the species at the surface of the oxide samples, DRIFTS data was collected for the Al_2O_3, SiO_2, TiO_2 and ZrO_2 samples and for the Al - Si, Ti - Al, and Ti - Si mixed oxides. Figures 4.18 to 4.30 show the data for each of the oxides, after heat treatments at 70, 120, 400, and 800°C.

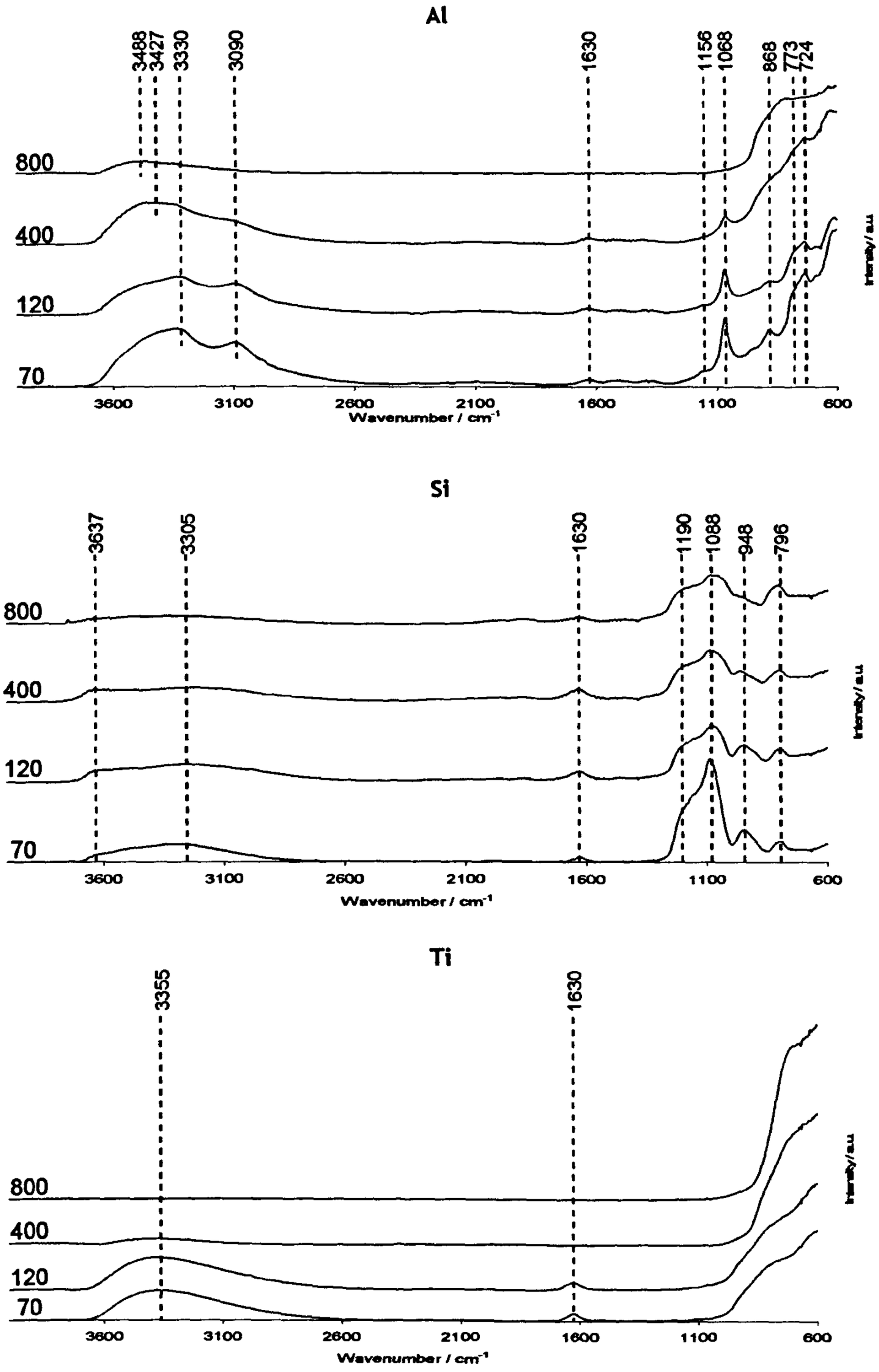

Figure 4.18: DRIFTS spectra of Al, Si, and Ti oxides calcined at 70, 120, 400, and 800°C. Calcination temperature (in °C) given against respective plot.

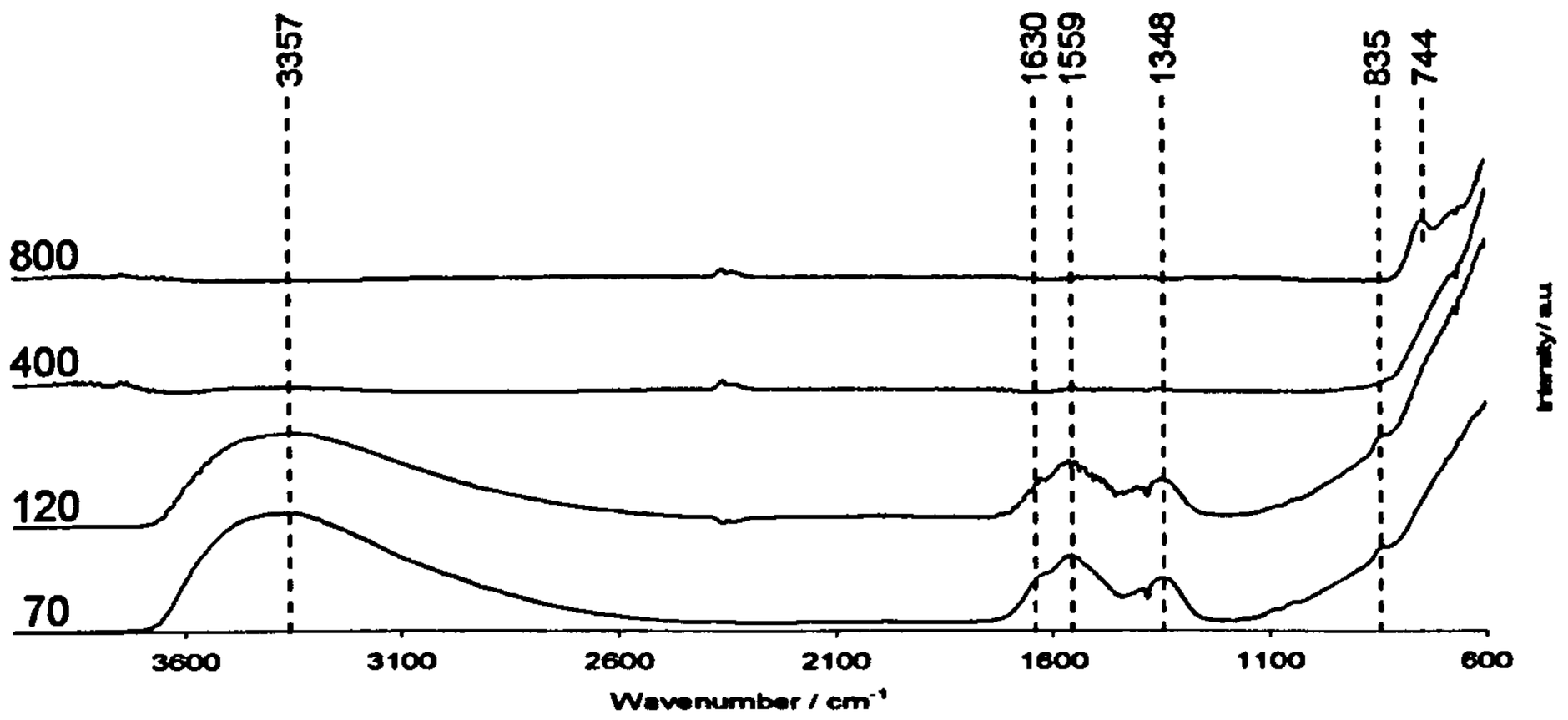

Figure 4.19: DRIFTS spectra of Zr70, Zr120, Zr400, and Zr800. Calcination temperature (in °C) given against respective plot.

The Al70 and Al120 samples (Figure 4.18) gave similar DRIFTS patterns, with distinct peaks at 3330, 3090, 1630 and 1068 cm^{-1} from -OH stretching and bending vibrations [93]. With increased calcination temperature, for Al400, the peak due to -OH bending was diminished, and the -OH stretching peak position shifted to 3427 cm^{-1}. After a higher calcination temperature of 800°C the Al800 sample did not show a peak at 1068 cm^{-1}, and the -OH stretching peak had shifted to 3488 cm^{-1}. In the lower wavenumber region, peaks due to Al-O bonds were present in the DRIFTS traces of all four of the 100Al samples, at *ca.* 620 cm^{-1} and 674 cm^{-1} [94].

The 100Si samples all displayed similar DRIFTS spectra, with peaks in the -OH stretching region at 3300 cm^{-1} for Si70 and Si120, and a shoulder at 3630 cm^{-1} that was most prominent in the DRIFTS pattern of Si400. A

peak at 1630 cm^{-1} due to -OH bending was also observed, present in all four samples with diminishing intensity as calcination temperature was increased. In the 600 to 1200 cm^{-1} region, all four traces showed peaks in the same positions, at 1088, 948 and 796 cm^{-1}, which diminished in intensity with increasing calcination temperature. These peaks correspond to Si-O-, Si-OH, and O-Si-O bonds respectively [94].

The Ti70 and Ti120 samples gave rise to -OH stretching and bending peaks at 3355 and 1630 cm^{-1} respectively. The peak at 3355 cm^{-1} was also present in the DRIFTS pattern for Ti400, but was less intense than in the traces for the samples dried or calcined at lower temperatures. None of the 100Ti single oxides displayed any distinct peaks from bonds with Ti metal species.

With the exception of the Zr800 sample, DRIFTS spectra for the 100Zr samples (Figure 4.19) contained a peak due to -OH stretching at 3357 cm^{-1}. Zr70 and Zr120 also gave rise to peaks at 1559, 1348, and 835 cm^{-1}, with a shoulder at 1630 cm^{-1} due to the bending of -OH bonds. The peaks at 1559 and 835 cm^{-1} are due to Zr-OH and Zr-O bonds. No peaks were evident in the DRIFTS pattern of Zr400. Zr800 displayed a single distinct peak at 744 cm^{-1} due to Zr-O_2-Zr asymmetric stretching [95].

The 90Al10Si, 50Al50Si, and 10Al90Si samples all resulted in similar DRIFTS patterns (Figure 4.20), with peaks arising at 3620, 3300, and

3090 cm^{-1} in the -OH stretching region. These peaks all diminished in intensity as calcination temperature of the sample was increased. A peak at 1620 cm^{-1} due to -OH bending was also present in the traces from the 90Al10Si and 50Al50Si samples, but not in the spectra for the 10Al90Si samples. In the 600 - 1200 cm^{-1} a similar pattern of peaks was observed for all of the samples, however, the positions of the peaks varied with the Al - Si ratio. For the 90Al10Si70 sample, peaks at 1158, 1100, 1052, and 730 cm^{-1} were present, with a small shoulder at 770 cm^{-1}. These peaks were also present for the 90Al10Si120 sample, with the exception of the peak at 1158 cm^{-1}. The DRIFTS spectra from the 90Al10Si400 and 90Al10Si800 samples did not show any distinct peaks in this region. For the 50Al50Si samples, all four of the samples gave rise to peaks at 1130, 988, 851 and 687 cm^{-1}. A small peak at 764 cm^{-1} was also observed in the spectra from 50Al50Si400 and 50Al50Si800.

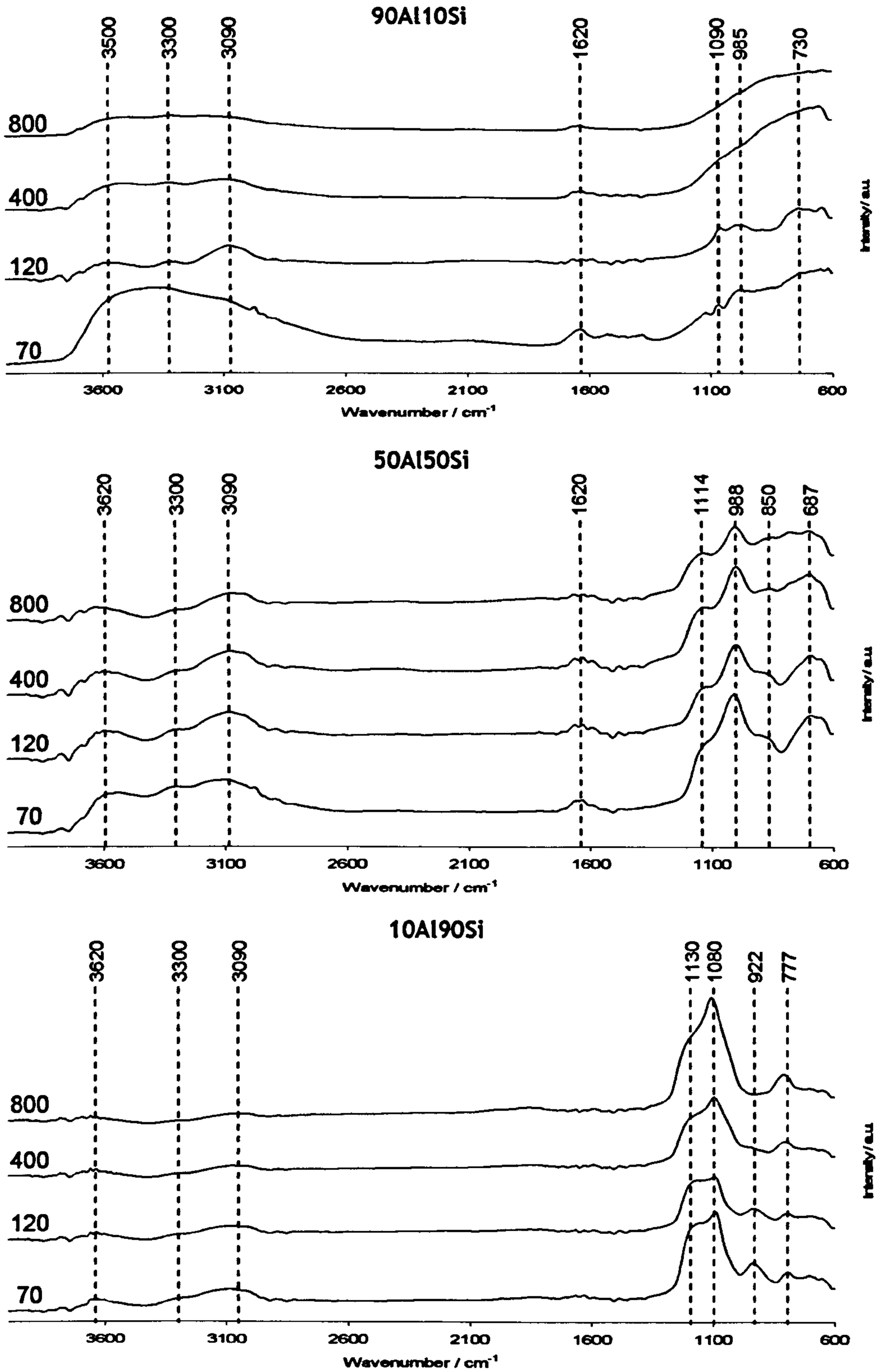

Figure 4.20: DRIFTS spectra of 90Al10Si, 50Al50Si, and 10Al90Si oxides calcined at 70, 120, 400, and 800°C. Calcination temperature (in °C) given by respective plot.

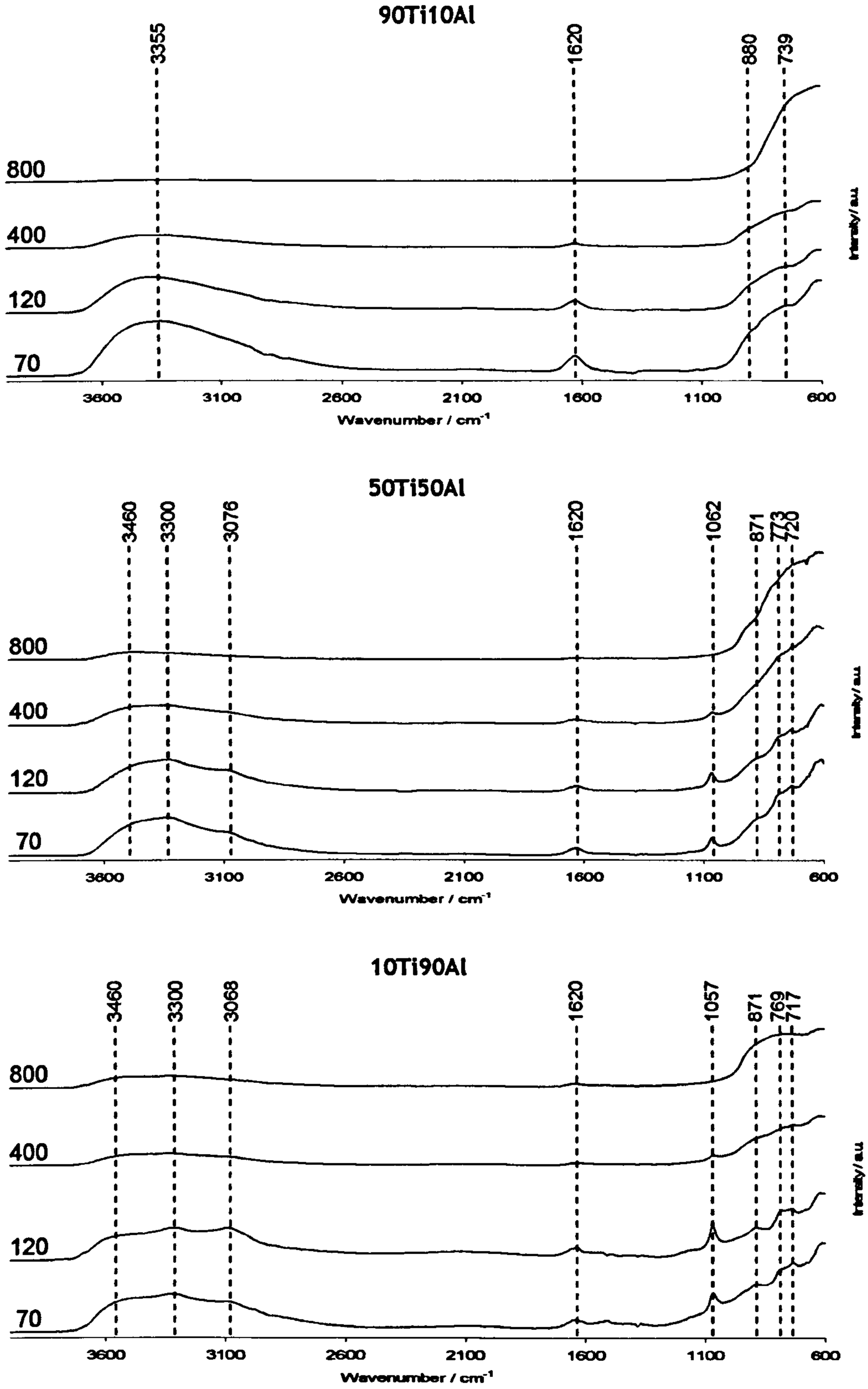

Figure 4.21: DRIFTS spectra of 90Ti10Al, 50Ti50Al, and 10Ti90Al oxides calcined at 70, 120, 400, and 800°C. Calcination temperature (in °C) given by respective plot.

The DRIFTS spectra from the 90Ti10Al, 50Ti50Al, and 10Ti90Al samples are shown in Figure 4.21. The 90Ti10Al samples all displayed one rounded peak with a maximum at 3355 cm^{-1} in the -OH stretching region, and a sharper peak at 1620 cm^{-1}, which both became less intense as calcination temperature of the oxide was increased. For the 90Ti10Al70, 90Ti10Al120, and 90Ti10Al400 samples, shoulders in the patterns at positions of 880 and 739 cm^{-1} were also observed.

The 50Ti50Al and 10Ti90Al samples all displayed very similar DRIFTS spectra. Peaks were present at 3460, 3300, and 3070 cm^{-1} in the -OH stretching region, with decreasing intensity as calcination temperature was increased. A peak at 1620 cm^{-1} due to -OH bending was also observed for all samples, which also decreased in intensity as calcination temperature was increased. Peaks at 1057, 872, 760 and 720 cm^{-1} were also observed for all samples.

Figure 4.22 shows the DRIFTS spectra for the 90Ti10Si, 50Ti50Si, and 10Ti90Si samples. All of these samples had a peak in the -OH stretching region at *ca.* 3330 cm^{-1}. The 90Ti10Al120, 90Ti10Al400, and 90Ti10Al800 samples also all gave rise to peaks at 3060 cm^{-1} and at 3580 cm^{-1}, as did the 10Ti90Si70 and 10Ti90Si120 samples. All of samples also displayed a peak at 1620 cm^{-1}, which became less intense as the calcination temperature increased. In the case of the 10Ti90Si samples, the peak at 1620 cm^{-1} was no longer observed to be present in the 10Ti90Si400 and 10Ti90Si800 samples. In the 600 - 1200 cm^{-1} region, similar patterns were

observed for all of the Ti - Si samples. The most intense peaks were found at 1180 and 1070 cm^{-1}, with less intense peaks at 930 cm^{-1} and 780 cm^{-1}.

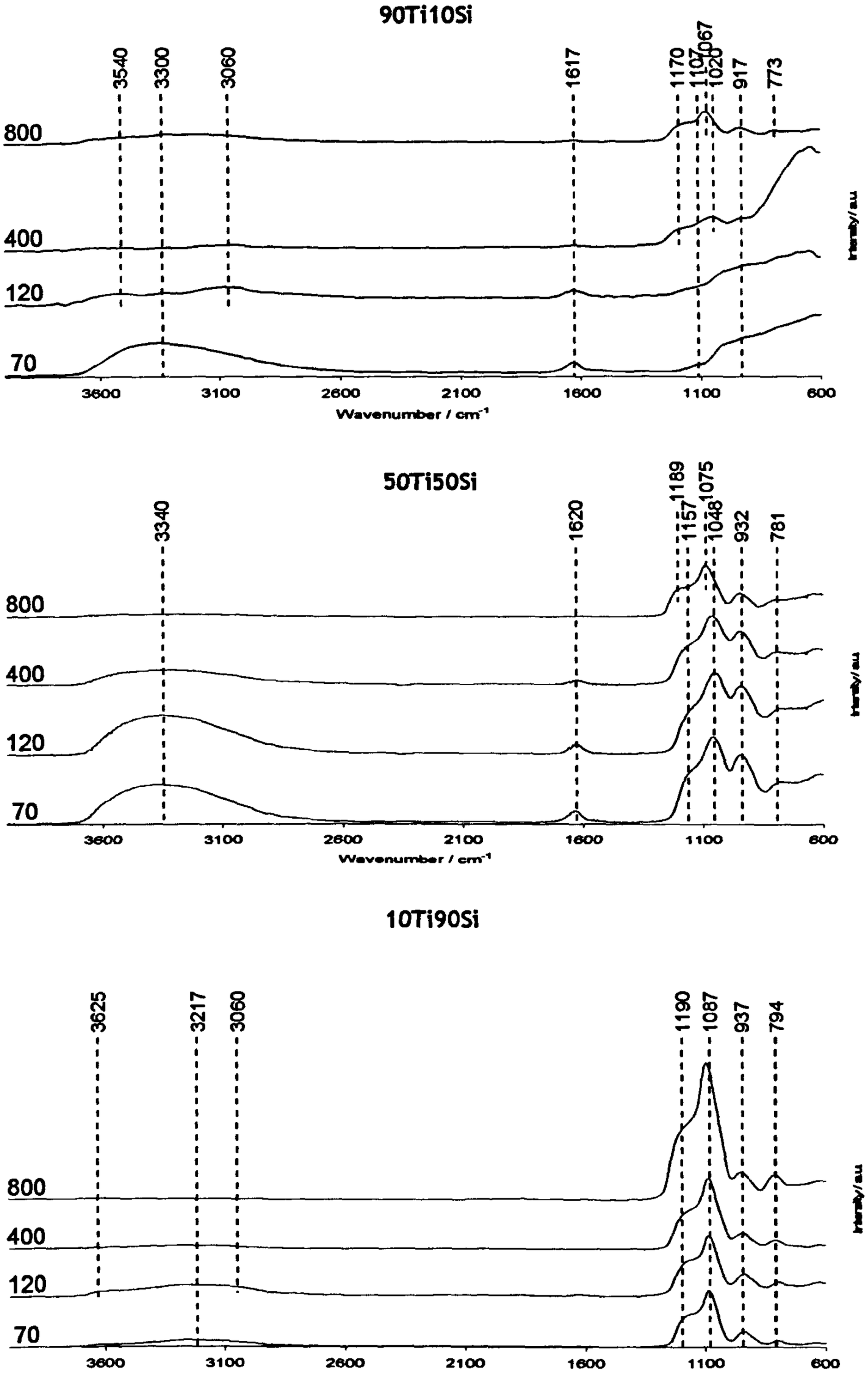

Figure 4.22: DRIFTS spectra of 90Ti10Si, 50Ti50Si, and 10Ti90Si oxides calcined at 70, 120, 400, and 800°C. Calcination temperature (in °C) given by respective plot.

4.3. Characterisation of Pd dispersed on TiO_2

4.3.1. XRD

Samples of Pd dispersed onto TiO_2,Ti - 5Pd and Ti - 1Pd, were prepared via wet impregnation of Ti70 with $Pd(NO_3)_2$ followed by heat treatments in air at 500°C and subsequently in flowing H_2 at 300°C to produce a sample of metallic Pd dispersed on TiO_2. Figure 4.23 shows the XRD patterns for the Ti - 5Pd sample after impregnation, and following the two heat treatments. In the XRD pattern for Ti - 5Pd after drying at 70°C for 24 h, no diffraction lines were observed, indicating that there were no crystalline phases present in the sample. After the 4 h calcination at 500°C, broad diffractions from brookite and anatase TiO_2 were observed. PdO was also present in the sample after this treatment, indicated by the broad hump at a 2θ value of 33.8°. The final Ti - 5Pd sample, after a 2 h heat treatment at 300°C in flowing H_2, consisted primarily of anatase TiO_2, with a small amount of brookite still present. Metallic Pd was also present in the sample, as indicated by the peaks at 40.12° and 46.66° values of 2θ. The crystallite size of the Pd, determined from the line broadening using the Scherrer equation, was *ca.* 15 nm.

The Ti - 1Pd sample exhibited the same transformations indicated by XRD after the drying, calcining and reducing treatments, however, due to the lower concentration of Pd present in the sample, peaks due to PdO were not observed in the XRD pattern after calcination. The Pd peak

at a 2θ value of 40.12° was evident in the XRD pattern of the sample after the heat treatment in flowing H_2.

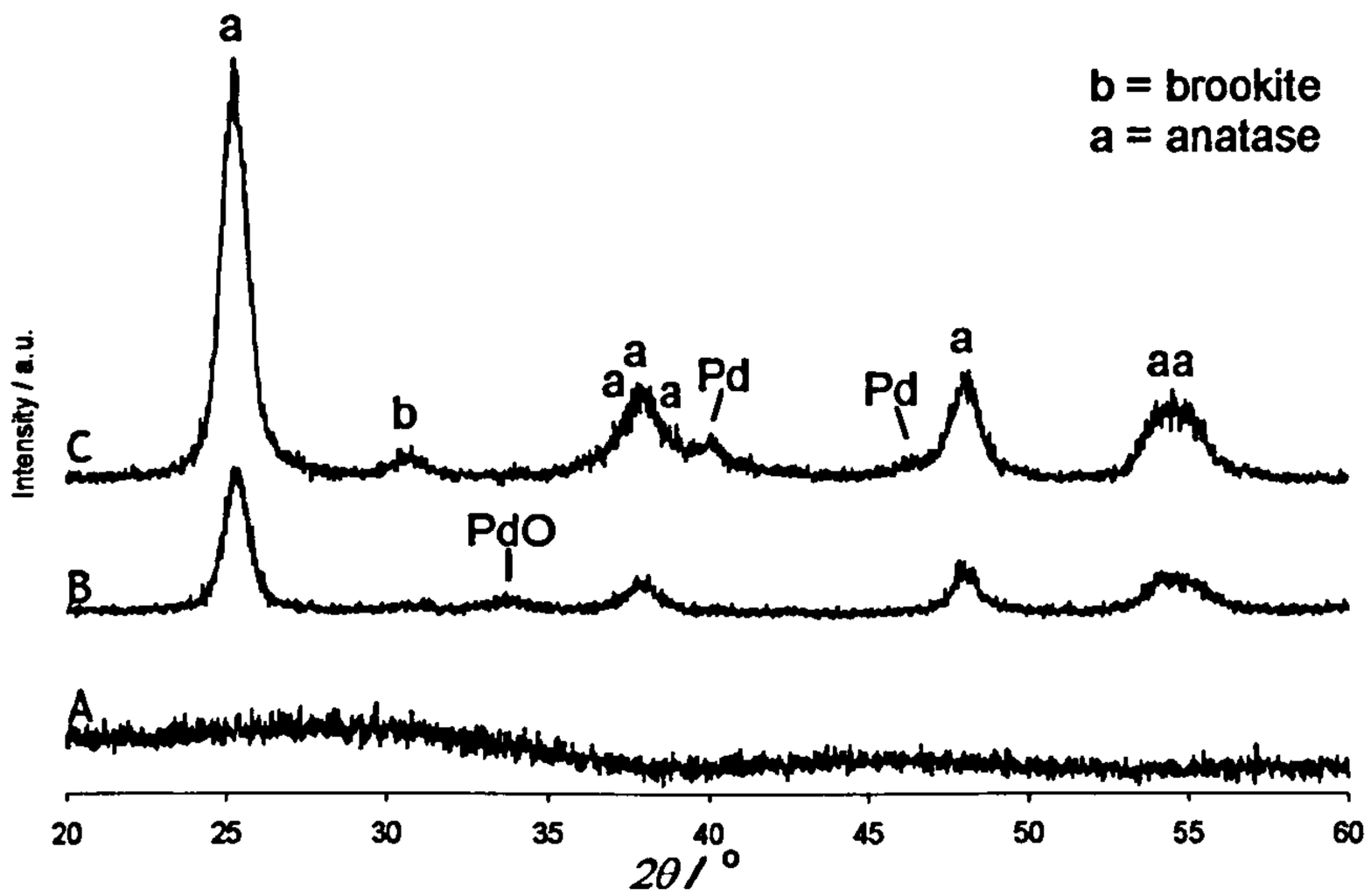

Figure 4.23: XRD patterns of 100Ti-5Pd dried at 70°C (A), 100Ti-5Pd after 4h calcined at 500°C (B), and 100Ti-5Pd after 2h in flowing H_2/Ar at 300°C (C).

4.3.2. XPS

Figure 4.24 shows the XPS wide scan data for the Ti - 5Pd sample after calcination and H_2 treatment. High resolution scans of the Ti 2p, O 1s, and Pd 3d peaks are shown in Figure 4.25. Table 4.2 is a summary of the peak positions and relative surface concentrations of Pd, Ti, and O within the sample. The asymmetry of the Pd peaks is due to shake-up singularity common to metallic samples [96], and has been fitting using asymmetric line shape fitting in CasaXPS. The peak position of the $3d_{5/2}$ peak, at 335.18 eV corresponds to the position of metallic Pd, at 335.2 eV [97].

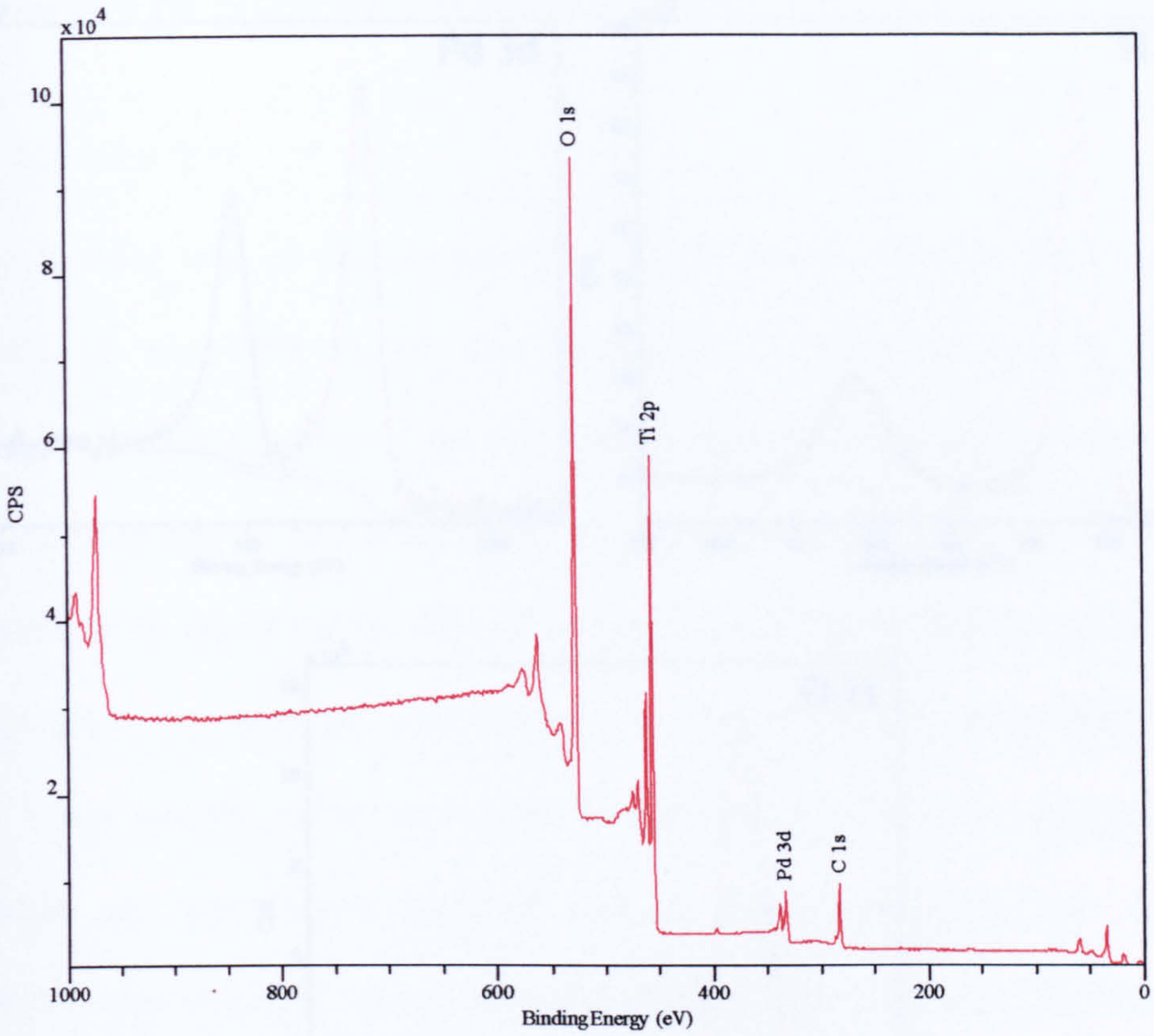

Figure 4.24: XPS wide scan of Ti - 5Pd.

Peak	Positions / eV	FWHM / eV	% Area	Relative concentration / at. %
Pd 3d	3d 5/2 = 335.2 3d 3/2 = 340.4	1.358 1.435	60 40	1.1
Ti 2p	2p 3/2 = 458.8 2p 1/2 = 464.4	1.040 2.029	66 33	29.4
O 1s	530.0	1.071	100	69.5

Table 4.2: Summary of XPS peak positions, areas, FWHM, and relative abundance, measured from high resolution scans.

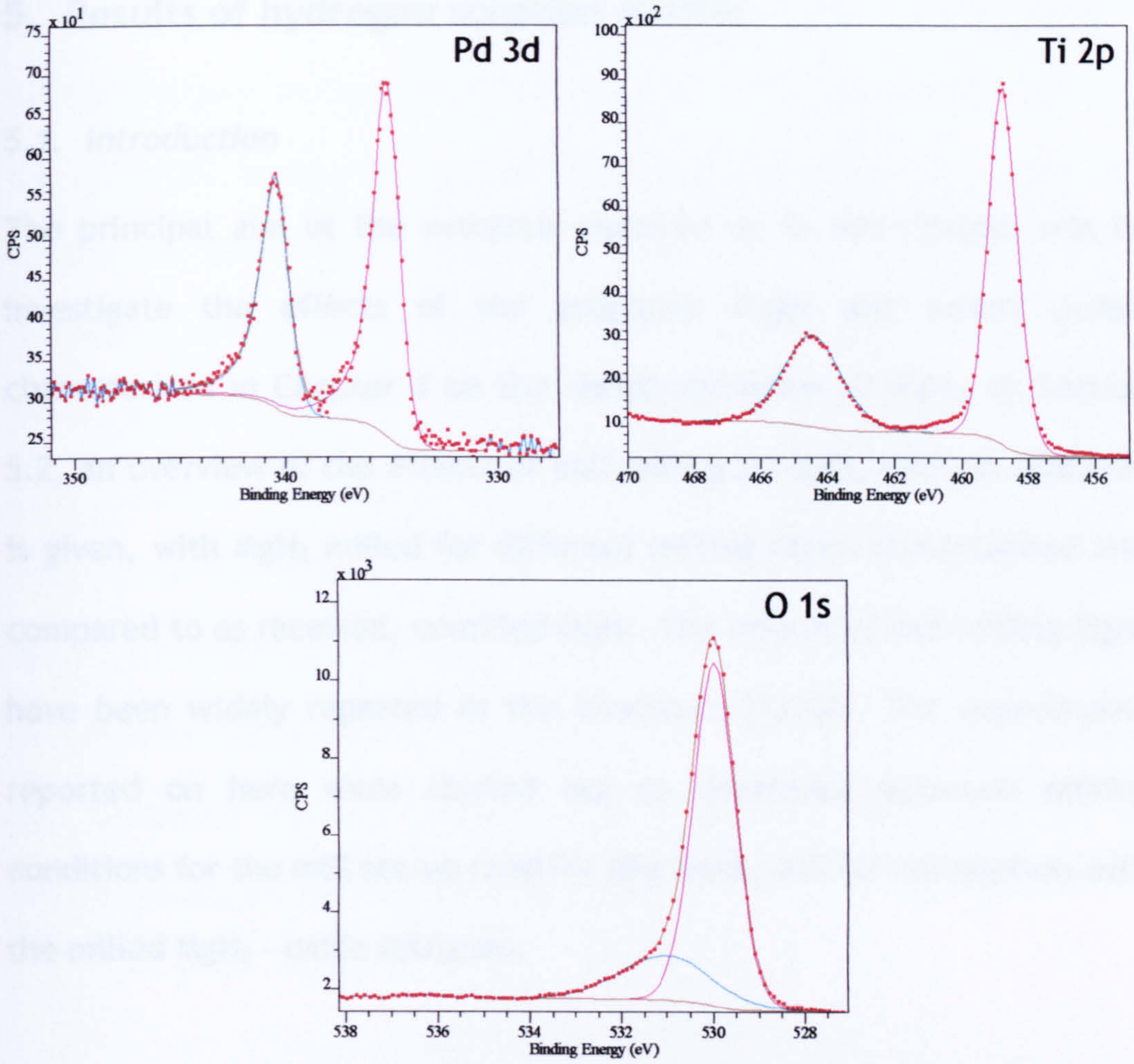

Figure 4.25: XPS spectra of Pd 3d, Ti 2p and O 1s from Ti-5Pd sample after H_2 treatment for 2 h at 300°C.

5. Results of hydrogen sorption studies

5.1. Introduction

The principal aim of the research reported on in this chapter was to investigate the effects of the prepared single and mixed oxides characterised in Chapter 4 on the dehydrogenation of MgH_2. In Section 5.2, an overview of the effects of ball milling on MgH_2 with no additives is given, with MgH_2 milled for different milling times characterised and compared to as received, unmilled MgH_2. The effects of ball milling MgH_2 have been widely reported in the literature [13,64]. The experiments reported on here were carried out to determine optimum milling conditions for the mill set-up used for this work, and for comparison with the milled MgH_2 - oxide mixtures.

Results of dehydrogenation experiments carried out using DSC-TGA-MS on the mixed MgH_2 - single oxide samples and MgH_2 - mixed oxide samples are described in Sections 5.3 and 5.4 respectively. Section 5.5 includes results of the dehydrogenation experiments on the MgH_2 - TiO_2 - Pd mixtures. In Section 5.6, characterisation of the mixtures before and after dehydrogenation using N_2 physisorption, TEM, XRD, and XPS are presented.

To further investigate the thermodynamic and kinetic properties of a number of key samples including milled MgH_2, MgH_2, MgH_2 - Ti70, and MgH_2 - Ti5Pd, experiments were carried out using TGA-MS, volumetric

and gravimetric methods. TGA-MS experiments using different heating rates were used to construct Kissinger plots and extract information on the activation energy of the dehydrogenation reactions of the samples. Results of these experiments are presented in Section 5.7. The volumetric method was used to form pressure composition isotherms for the samples at different temperatures, from which van't Hoff plots were constructed to extract thermodynamic data including enthalpy and entropy of the dehydrogenation reactions. Section 5.8 contains the results of these experiments. Finally, in Section 5.9, results of IGA experiments are presented. The gravimetric method was used to study the behaviour of the samples during cycling experiments of 10 dehydrogenation - rehydrogenation cycles.

5.2. Characterisation of milled MgH_2

5.2.1. XRD

To analyse the effects of milling on MgH_2, as received MgH_2 powder and MgH_2 milled for 5, 10, 15, and 20 h were characterised. Figure 5.1 shows the powder XRD patterns for these samples. Trace A is the diffraction pattern from as received MgH_2, prior to any milling, showing diffraction lines for β-MgH_2, with no other phases observed. An average crystallite size of 150 nm was calculated from the diffraction line broadening using the Scherrer equation. The diffraction patterns for all of the milled MgH_2 samples showed diffraction lines from β-MgH_2 as the most abundant phase. Diffraction lines representing γ-MgH_2 and a small proportion of

MgO were also observed. With increasing milling time, a broadening of the diffraction lines occurred. The decreasing average crystallite size and the strain induced by milling for the different milling times were determined from Williamson-Hall plots, and the results are summarised in Table 5.1. The average crystallite size was found to decrease from 130 Å for the MgH_2 sample milled for 5 h to 70 Å for the samples milled for 15 h and 20 h. The crystallite strain ranged from a low value of 0.15 for MgH_2 milled for 5 h up to a maximum of 0.63 for the sample milled for 15 h. A slight decrease in strain to 0.53 was observed in the sample after 20 h of milling.

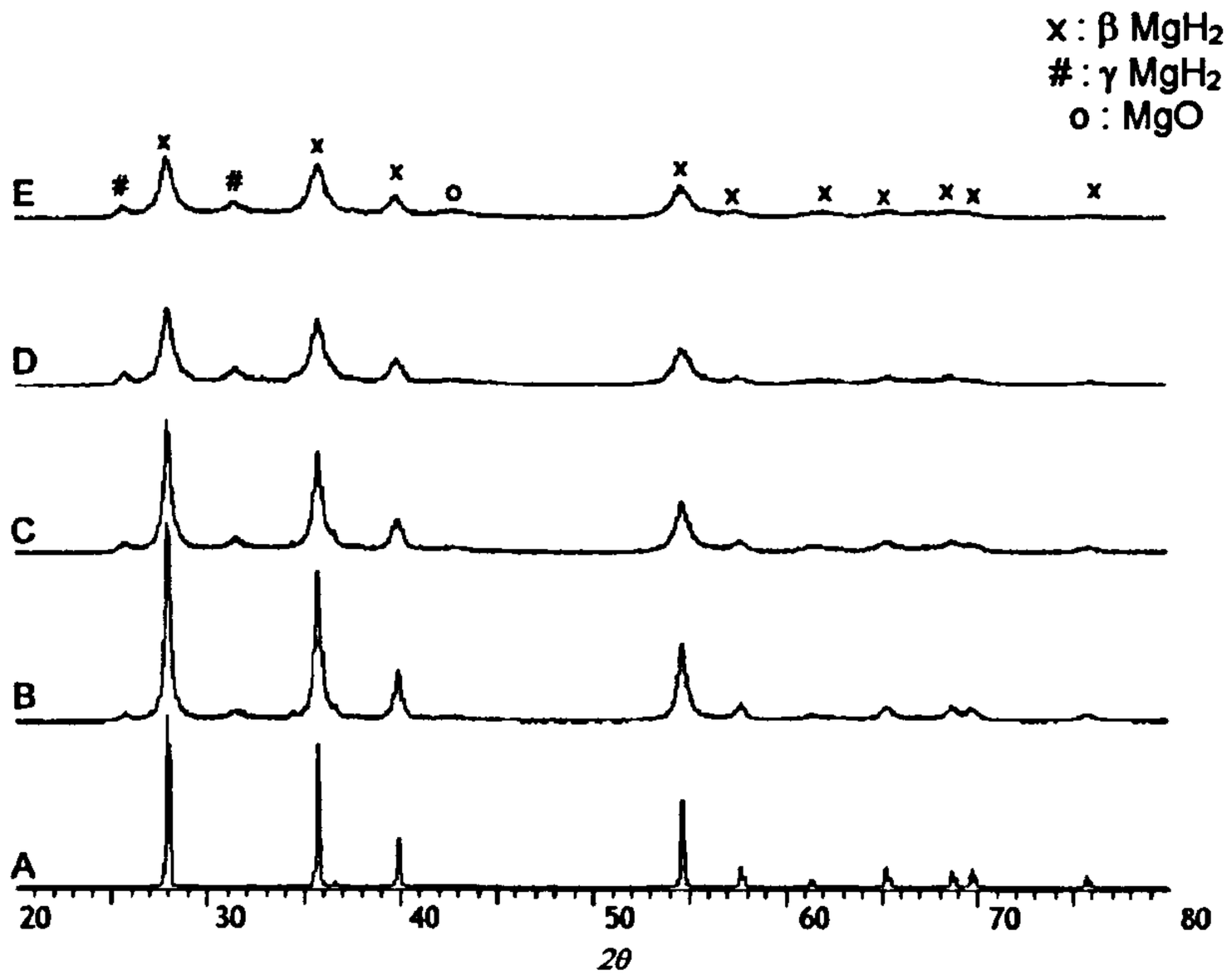

Figure 5.1: XRD patterns for as received MgH_2 (A), and MgH_2 milled for 5 h (B), 10 h (C), 15 h (D), and 20 h (E).

5.2.2. N_2 Physisorption

BET surface areas were determined for as received MgH_2, and for the MgH_2 samples after different milling times. The surface areas are

summarised in the last column of Table 5.1. The as received MgH_2 was found to have a surface area of 2 $m^2 g^{-1}$. After ball milling, the surface area increased to *ca.* 10 $m^2 g^{-1}$, with no significant variation observed with the increasing milling time.

Milling time / h	Scherrer range / Å	Williamson Hall size / Å	Williamson Hall strain / %	BET surface area / $m^2 g^{-1}$
0	1500	-	-	2
5	100 - 300	130	0.15	9
10	60-200	90	0.25	10
15	30-200	70	0.61	11
20	30-200	70	0.53	11

Table 5.1: Comparison of size, strain, and surface area of as received and milled MgH_2 samples.

5.2.3. SEM

Figure 5.2 shows SEM micrographs of as received MgH_2 and MgH_2 milled for 20 h. The as received MgH_2 was observed to be made up of flat plate-like particles with smooth surfaces appearing to range from 10 to 100 μm in size. The milled sample contained agglomerates of much finer particles, while some of the larger particles were retained. EDX analysis of the as received and milled MgH_2 samples did not detect the presence of any contaminants, such as iron from the steel milling vessels.

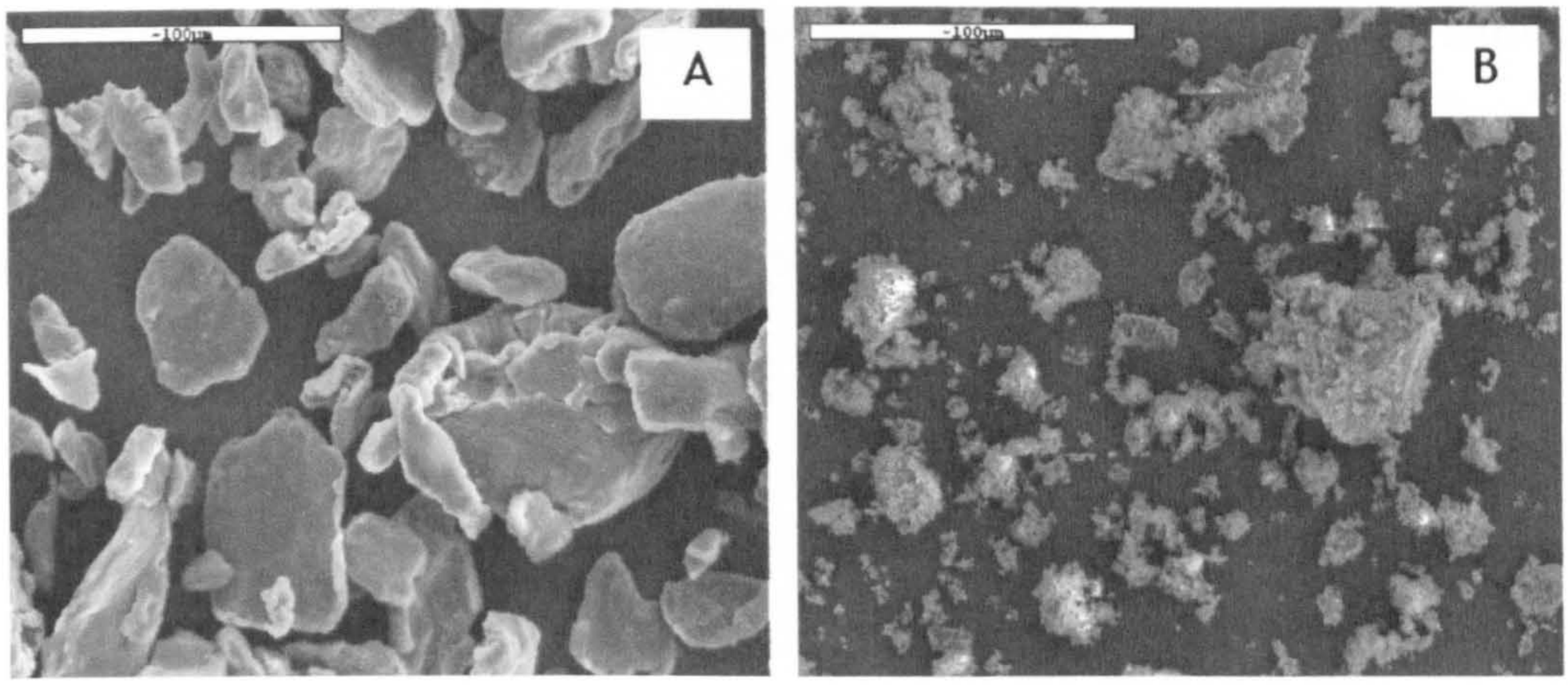

Figure 5.2: SEM micrographs of MgH_2 as received (A), and after 20 h ball milling (B).

5.2.4. DSC-TGA-MS

DSC-TGA-MS was used to determine hydrogen desorption onset temperatures for the as received and milled MgH_2 samples when heated to 500°C at a rate of 10°C min^{-1} in an atmosphere of flowing Ar. The TGA weight loss data and MS traces for hydrogen (m/z 2) are shown in Figure 5.3. As discussed in the description of the experimental method used in collecting this data in Section 3.5.7, the peaks of the MS traces appear at slightly higher temperatures than the true sample temperature due to the deviation from a non-linear heating rate that occurred during the DSC - TGA - MS experiments. Onset temperatures are taken from the weight loss traces, which correspond to the true sample temperature. This is the case for the data presented in this section and in Section 5.4.

The onset of dehydrogenation for as received MgH_2 occurred at a temperature of 391°C, and a total of 7.1 wt. % was desorbed from the sample. After ball milling, and regardless of milling time, the

dehydrogenation onset temperature was reduced to *ca.* 360°C, with a reduction in total weight loss to *ca.* 6.2 wt. %. No other desorbed species were detected by MS for any of the samples.

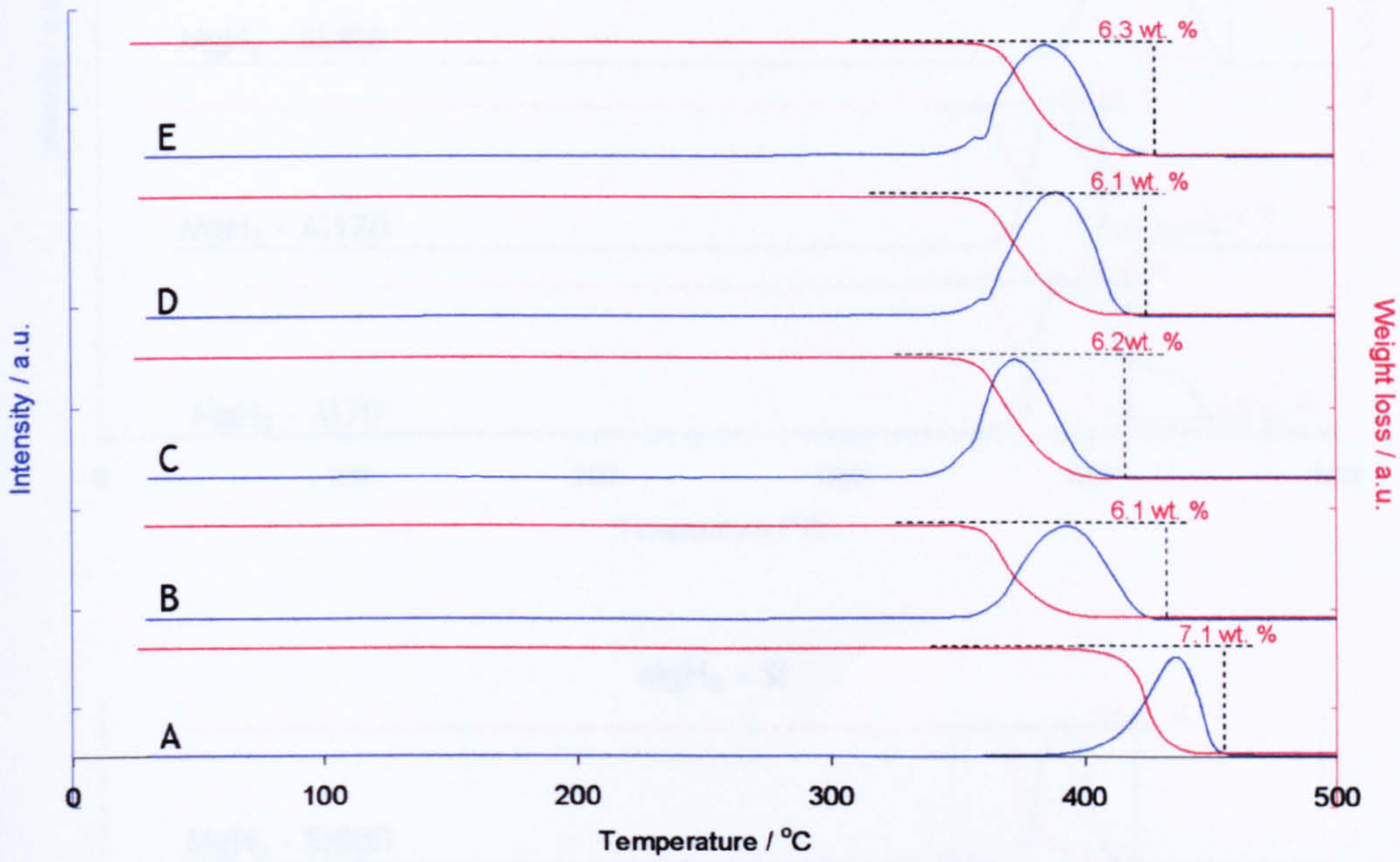

Figure 5.3: MS H_2 (m/z 2) traces for as received MgH_2 (A) and MgH_2 milled for 5 h (B), 10 h (C), 15 h (D), and 20 h (E), during heating from 30°C to 500°C at 10°C min^{-1} in Ar atmosphere.

5.3. Dehydrogenation of milled MgH_2 - single oxide mixtures

Each of the MgH_2 - single oxide samples was analysed using DSC-TGA-MS to measure the onset temperature of H_2 desorption, and to quantify the amount of hydrogen desorbed. Figures 5.4 - 5.6 show the MS H_2 and TGA weight loss traces for the MgH_2 - Al, MgH_2 - Si, MgH_2 - Ti and MgH_2 - Zr samples for the oxides calcined at temperatures of 70°C, 120°C, 400°C, and 800°C.

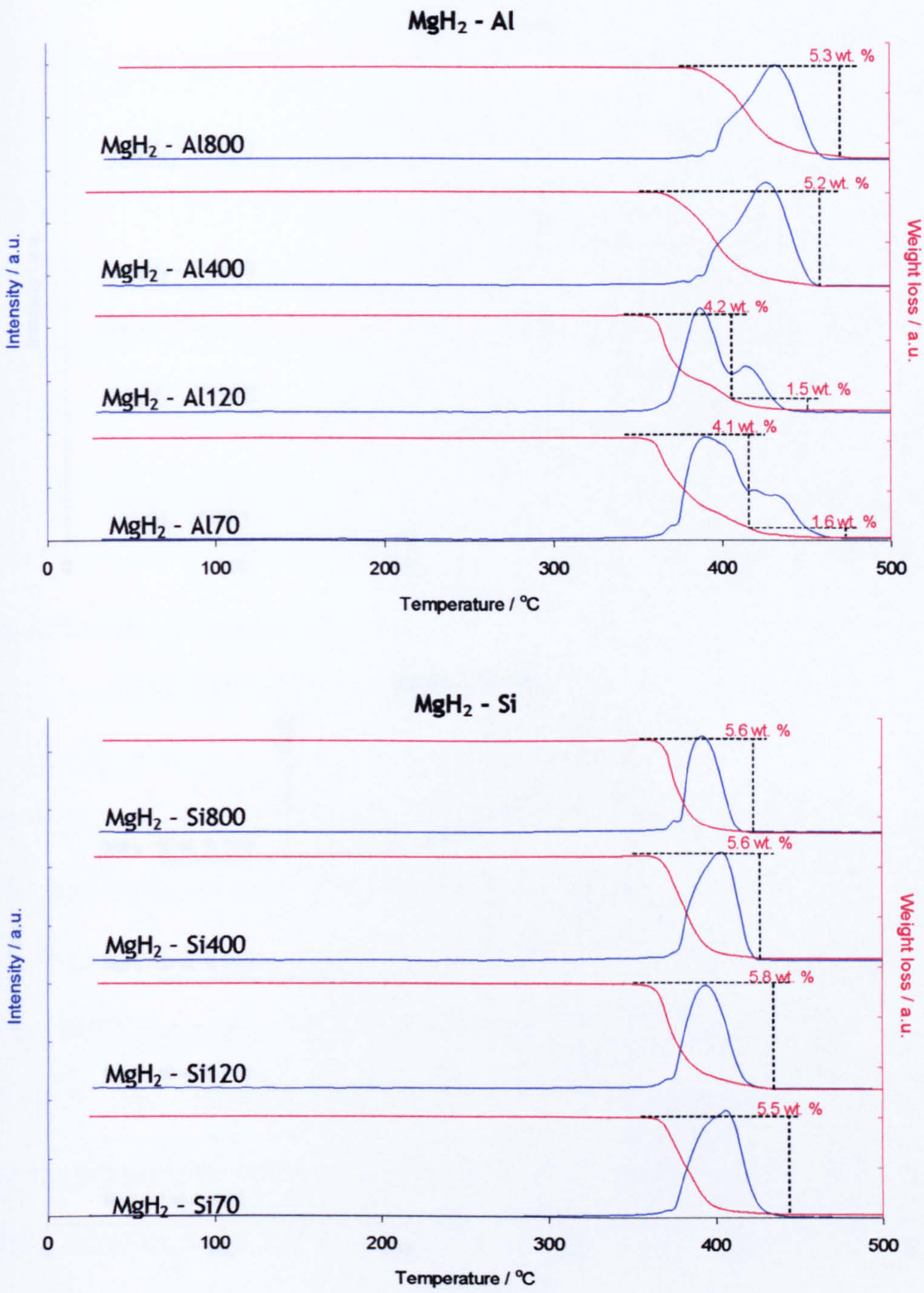

Figure 5.4: MS H_2 (m/z 2) and TGA traces for MgH_2 - Al, and MgH_2 - Si samples during heating from 30°C to 500°C at 10°C min^{-1} in Ar atmosphere.

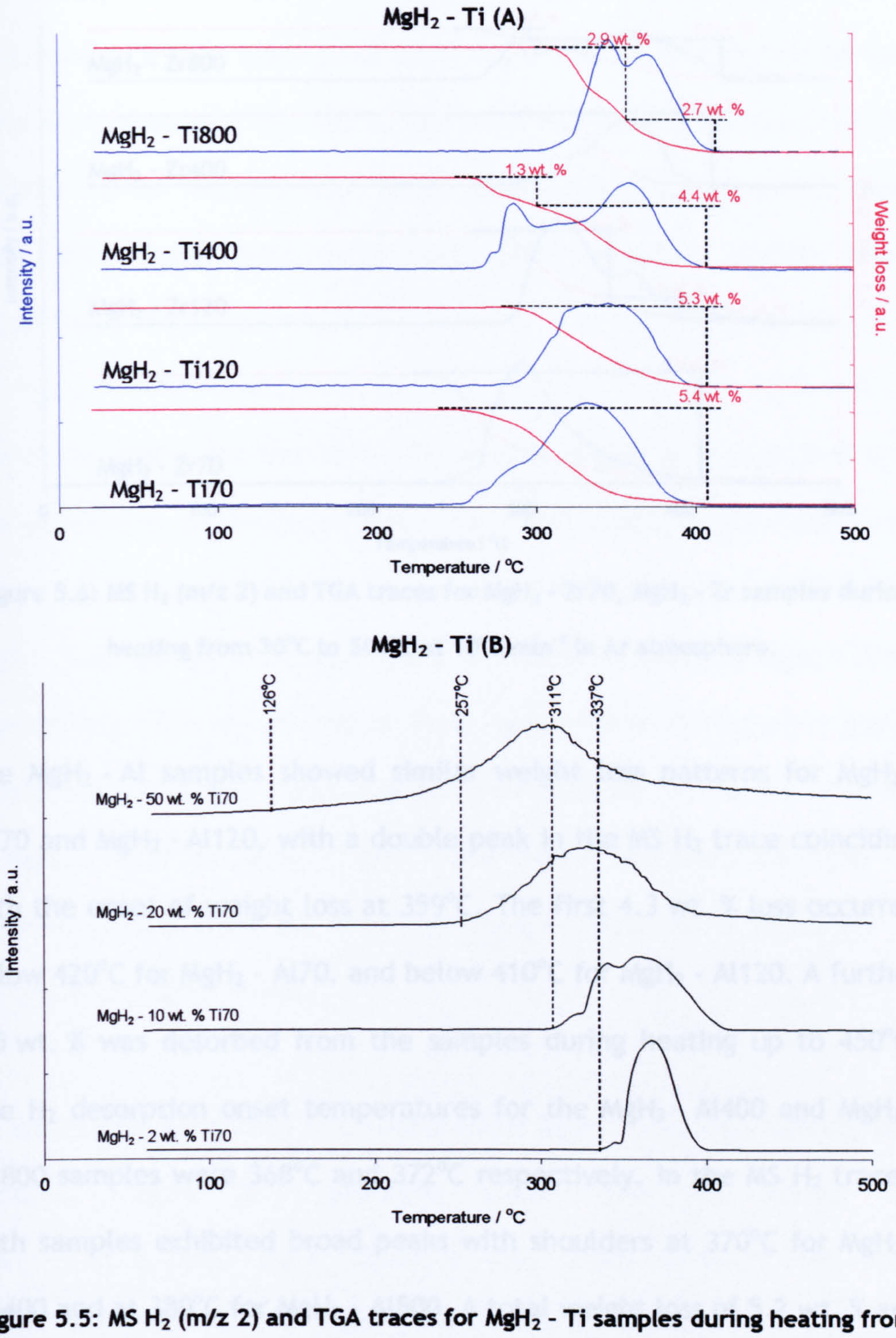

Figure 5.5: MS H_2 (m/z 2) and TGA traces for MgH_2 - Ti samples during heating from 30°C to 500°C at 10°C min^{-1} in Ar atmosphere (A). For different weight % Ti70 additions (B), MS H_2 (m/z 2) data from TPRS.

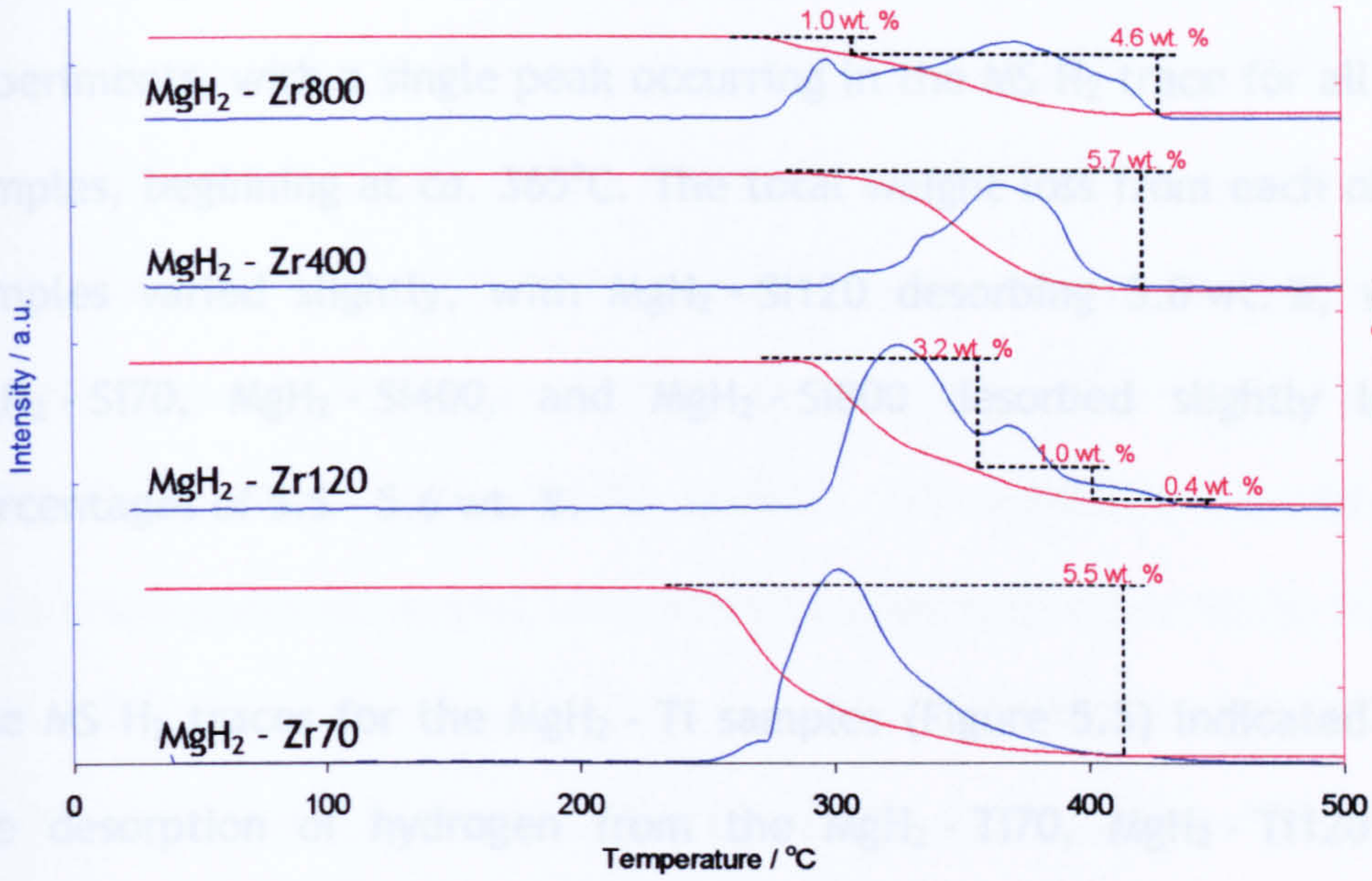

Figure 5.6: MS H_2 (m/z 2) and TGA traces for MgH_2 - Zr70, MgH_2 - Zr samples during heating from 30°C to 500°C at 10°C min^{-1} in Ar atmosphere.

The MgH_2 - Al samples showed similar weight loss patterns for MgH_2 - Al70 and MgH_2 - Al120, with a double peak in the MS H_2 trace coinciding with the onset of weight loss at 359°C. The first 4.3 wt. % loss occurred below 420°C for MgH_2 - Al70, and below 410°C for MgH_2 - Al120. A further 1.5 wt. % was desorbed from the samples during heating up to 450°C. The H_2 desorption onset temperatures for the MgH_2 - Al400 and MgH_2 - Al800 samples were 368°C and 372°C respectively. In the MS H_2 traces, both samples exhibited broad peaks with shoulders at 370°C for MgH_2 - Al400 and at 380°C for MgH_2 - Al800. A total weight loss of 5.2 wt. % and 5.3 wt. % was desorbed from the MgH_2 - Al400 and MgH_2 - Al800 samples respectively.

The four MgH_2 - Si samples all exhibited very similar behaviour in TGA-MS experiments, with a single peak occurring in the MS H_2 trace for all four samples, beginning at *ca.* 365°C. The total weight loss from each of the samples varied slightly, with MgH_2 - Si120 desorbing 5.8 wt. %, while MgH_2 - Si70, MgH_2 - Si400, and MgH_2 - Si800 desorbed slightly lower percentages of 5.5 - 5.6 wt. %.

The MS H_2 traces for the MgH_2 - Ti samples (Figure 5.5) indicated that the desorption of hydrogen from the MgH_2 - Ti70, MgH_2 - Ti120 and MgH_2 - Ti400 occurred over a broad range starting at 257°C for MgH_2 - Ti70 and at 291°C and 263°C for MgH_2 - Ti120 and MgH_2 - Ti400 respectively. The H_2 desorption from MgH_2 - Ti800 started at a higher temperature of 310°C. Double peaks were observed in the MS H_2 traces of MgH_2 - Ti400 and MgH_2 - Ti800. Total weight loss from the MgH_2 - Ti samples ranged from 5.3 wt. % for MgH_2 - Ti120 to a maximum of 5.7 wt. % for MgH_2 - Ti400.

An additional set of data was collected for MgH_2 - Ti70 with varying Ti70 content. Figure 5.5 (bottom) shows the MS traces for MgH_2 - 2 wt. % Ti70, MgH_2 - 10 wt. % Ti70, MgH_2 - 20 wt. % Ti70, and MgH_2 - 50 wt. % Ti70. The onset temperature of H_2 desorption decreased with increasing Ti70 content, from 337°C for MgH_2 - 2 wt. % Ti70 down to 126°C for MgH_2 - 50 wt. % Ti70.

The MgH_2 - Zr samples exhibited weight losses of between 4.8 wt. % and 5.7 wt. %, over the temperature range 254°C to 420°C (Figure 5.6). A broad asymmetrical peak with a maximum at 300°C was observed in the MS H_2 trace of MgH_2 - Zr70, with a smaller peak occurring at the start of H_2 desorption, between 254°C and 265°C. The MgH_2 - Zr120, MgH_2 - Zr400, and MgH_2 - Zr800 samples all exhibited multiple H_2 desorption peaks of varying intensities in their respective MS H_2 traces. MgH_2 - Zr120 desorbed most of its H_2 (3.2 wt. %) between 293°C and 355°C with two smaller distinct weight loss regions at higher temperatures, in the regions 355°C to 400°C and 400°C to 420°C. The MS H_2 trace for MgH_2 - Zr400 exhibited a broad peak with small shoulders observed at 300°C and 328°C. The MgH_2 - Zr800 sample also gave rise to a small peak corresponding to a weight loss of 1.0 wt. % with a maximum at 297°C, with the majority of H_2 lost (4.6 wt. %) indicated by a broad peak in the MS H_2 trace with a maximum at 370°C.

5.4. Dehydrogenation of milled MgH_2 - mixed oxide mixtures

The TGA-MS plots for the MgH_2 - mixed oxide mixtures are shown in Figures 5.7 to 5.12. In Figures 5.7 - 5.8, the TGA - MS traces for the MgH_2 - 90Al10Si, MgH_2 - 50Al50Si, and MgH_2 - 10Al90Si samples are presented. With the exception of the MgH_2 - 90Al10Si70 sample, the onset temperature for hydrogen desorption from all of the MgH_2 samples milled with an Al/Si mixed oxide was in the range of 360-370°C. For MgH_2 - 90Al10Si70, the dehydrogenation onset temperature was lower, at 344°C. The MgH_2 - 90Al10Si and MgH_2 - 50Al50Si samples all exhibit a

double peak shape or peak with distinct shoulder at lower temperature in the MS H_2 trace. The positions of the two maxima are at the temperatures of 385°C and 420°C respectively, with the exception of the MgH_2 - 90Al10Si70 sample, for which the peak positions are at 360°C and 385°C. With the exception of the MgH_2 - 10Al90Si70 sample, which exhibits a similar double peak in the MS H_2 trace, The MgH_2 samples milled with10Al90Si oxides all gave rise to a single maximum at *ca.* 400°C, with the MgH_2 - 10Al90Si120 and MgH_2 - 10Al90Si800 samples also displaying shoulders to lower temperature (385°C) and higher temperature (412°C). Total weight loss for the MgH_2 samples milled with Al/Si mixed oxides ranged from 5.3 wt. % for MgH_2 - 50Al50Si400 and MgH_2 - 10Al90Si 400, up to 5.9 wt. % for MgH_2 - 90Al10Si800.

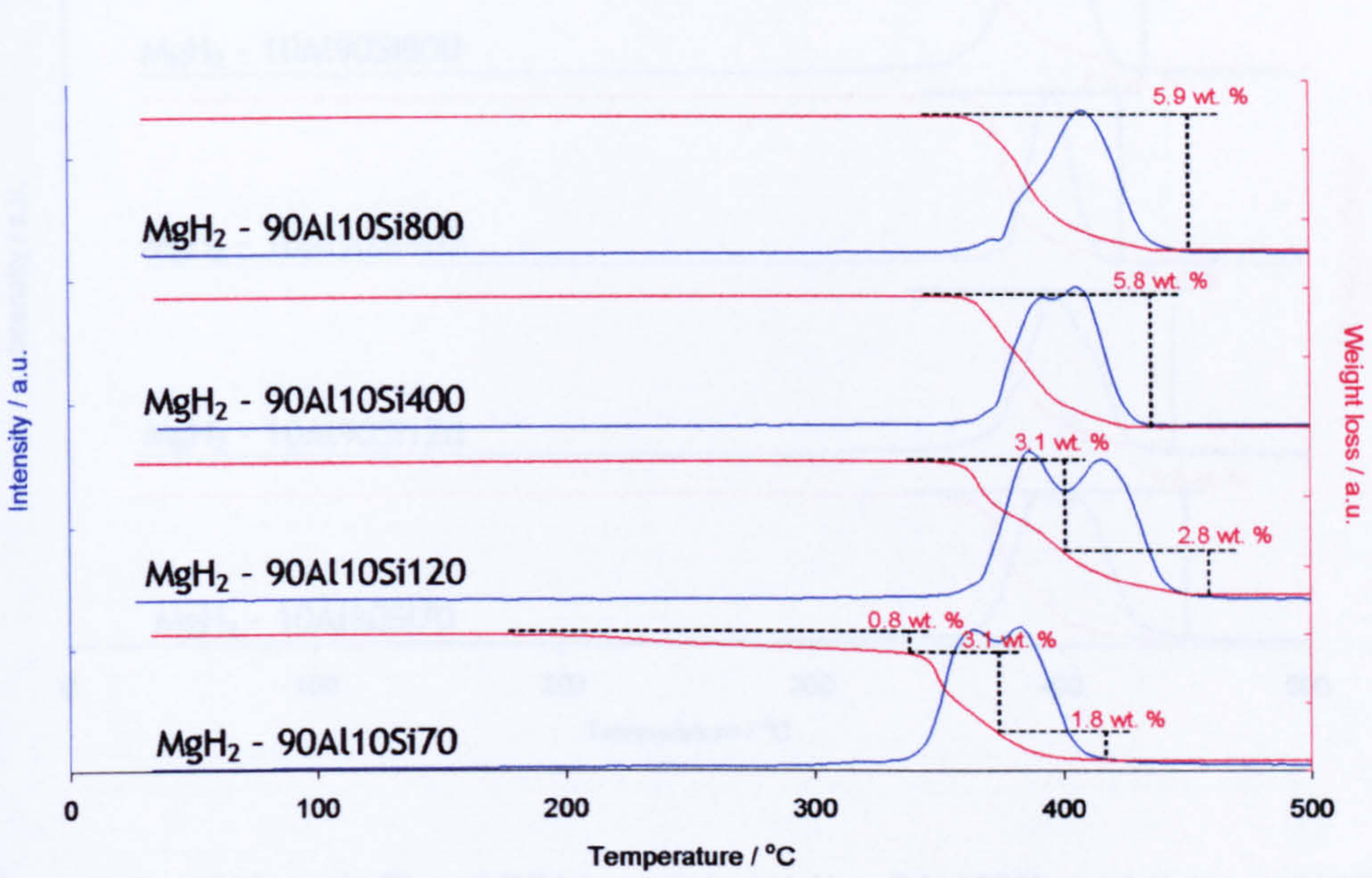

Figure 5.7: MS H_2 (m/z 2) and TGA traces for MgH_2 - 90Al10Si samples during heating from 30°C to 500°C at 10°C min^{-1} in Ar atmosphere.

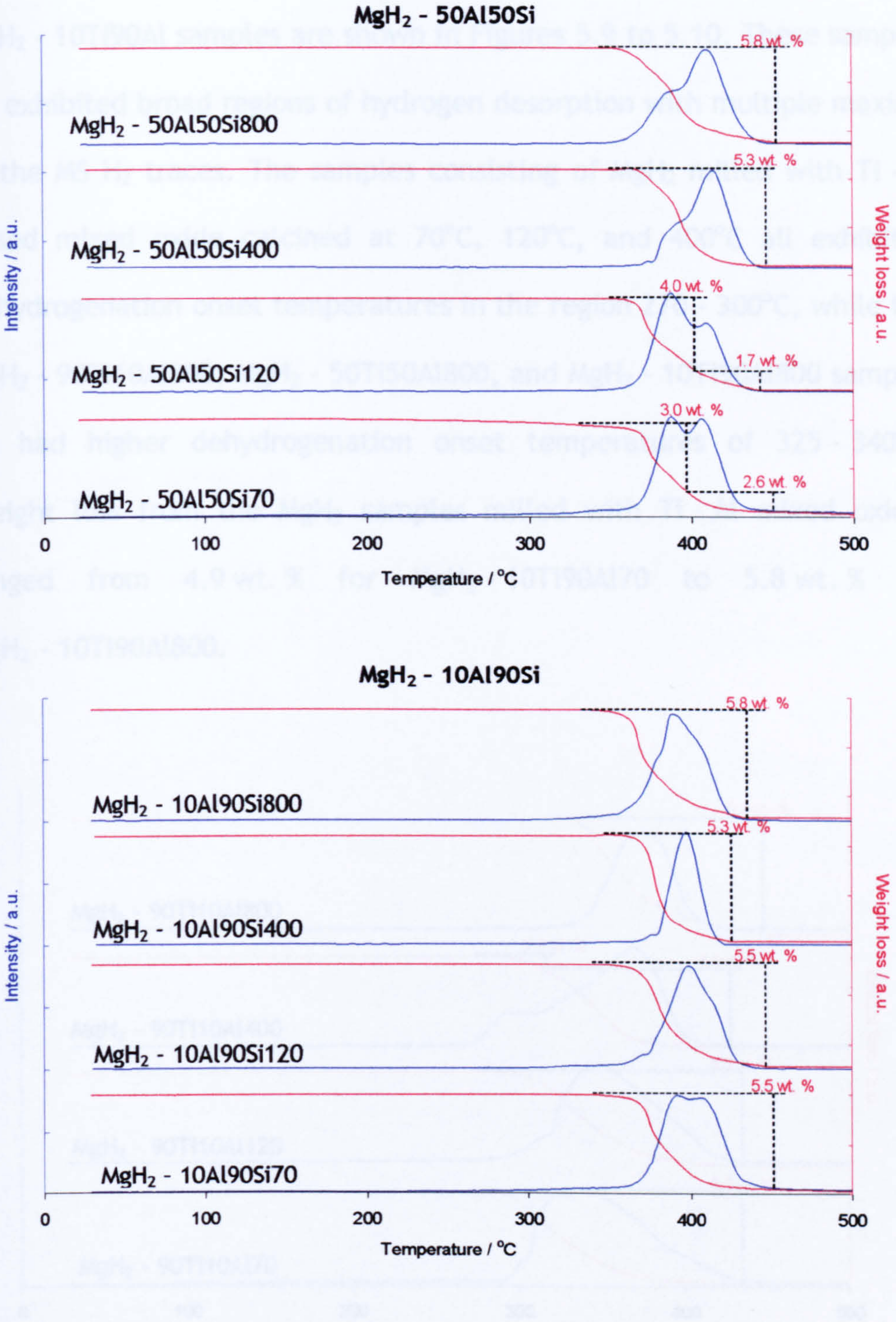

Figure 5.8: MS H_2 (m/z 2) and TGA traces for MgH_2 - 50Al50Si, and MgH_2 - 10Al90Si samples during heating from 30°C to 500°C at 10°C min^{-1} in Ar atmosphere.

TGA-MS traces for the MgH_2 - 90Ti10Al, MgH_2 - 50Ti50Al, and MgH_2 - 10Ti90Al samples are shown in Figures 5.9 to 5.10. These samples all exhibited broad regions of hydrogen desorption with multiple maxima in the MS H_2 traces. The samples consisting of MgH_2 milled with Ti - Al based mixed oxide calcined at 70°C, 120°C, and 400°C all exhibited dehydrogenation onset temperatures in the region 270 - 300°C, while the MgH_2 - 90Ti10Al800, MgH_2 - 50Ti50Al800, and MgH_2 - 10Ti90Al800 samples all had higher dehydrogenation onset temperatures of 325 - 340°C. Weight loss from the MgH_2 samples milled with Ti - Al mixed oxides ranged from 4.9 wt. % for MgH_2 - 10Ti90Al70 to 5.8 wt. % for MgH_2 - 10Ti90Al800.

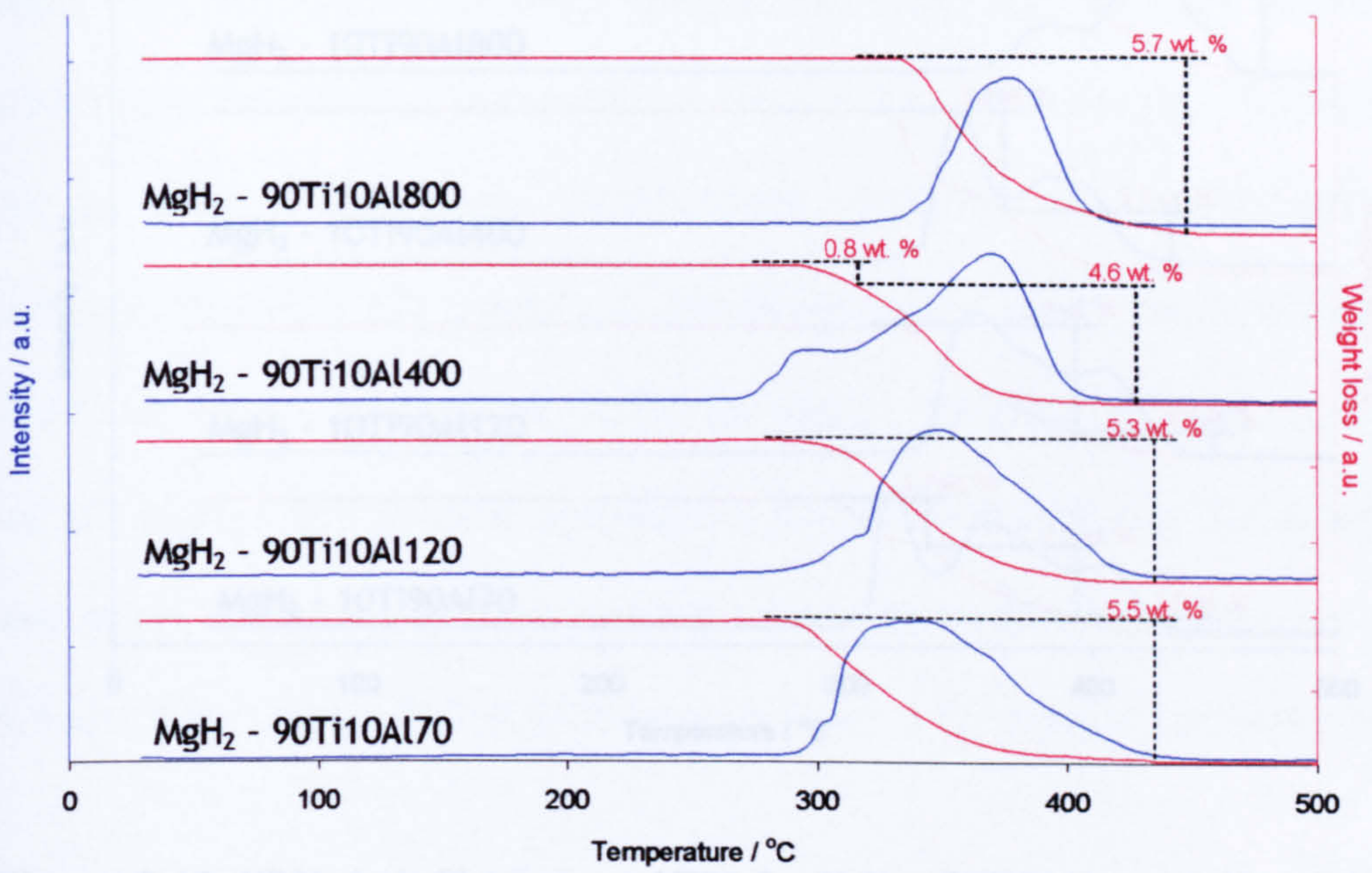

Figure 5.9: MS H_2 (m/z 2) and TGA traces for MgH_2 - 90Ti10Al samples during heating from 30°C to 500°C at 10°C min^{-1} in Ar atmosphere.

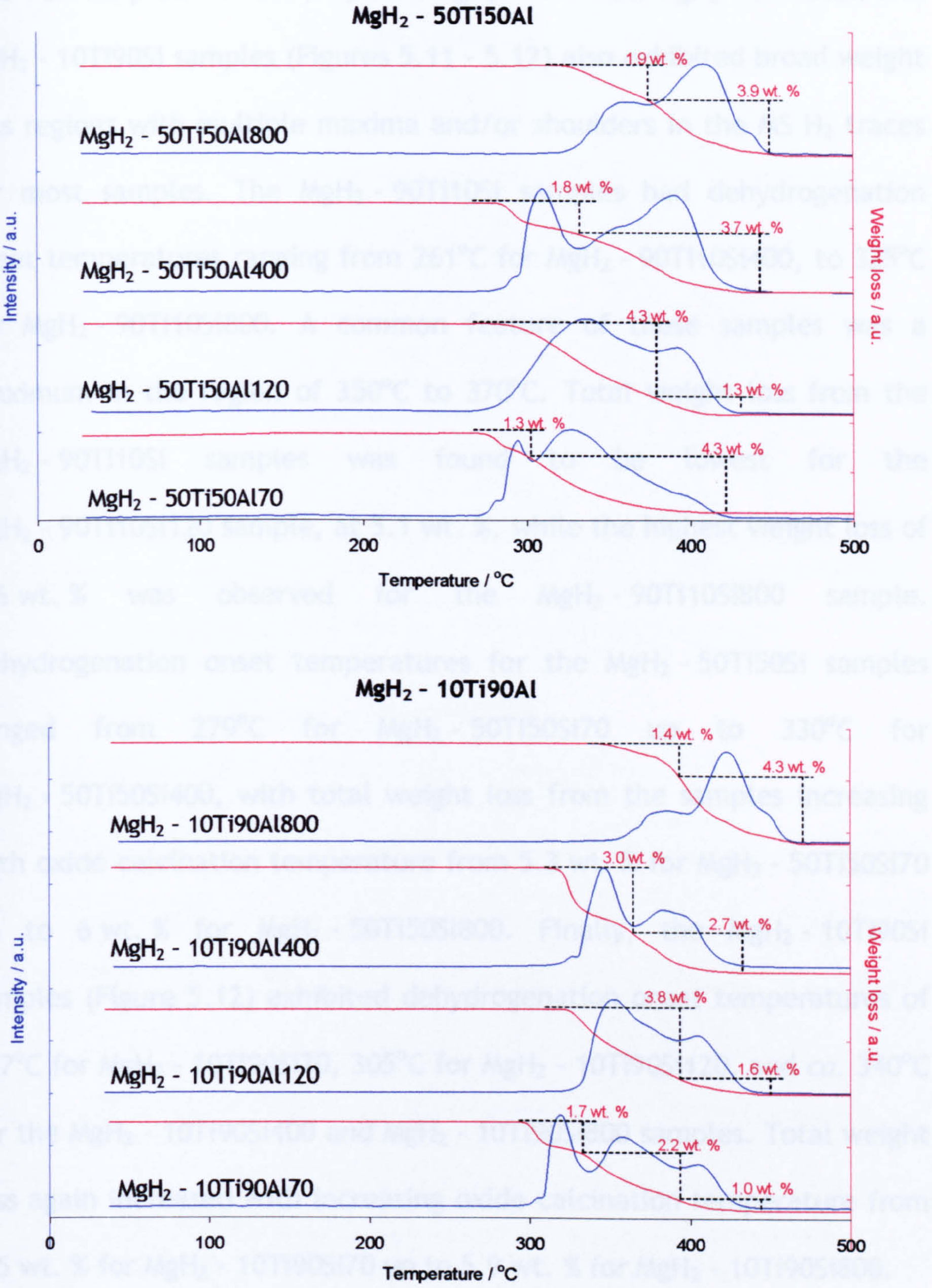

Figures 5.10: MS H_2 (m/z 2) traces and TGA for MgH_2 - 50Ti50Al and MgH_2 -10Ti90Al samples during heating from 30°C to 500°C at 10°C min^{-1} in Ar atmosphere.

The TGA-MS plots for the prepared MgH_2 - 90Ti10Si, MgH_2 - 50Ti50Si, and MgH_2 - 10Ti90Si samples (Figures 5.11 - 5.12) also exhibited broad weight loss regions with multiple maxima and/or shoulders in the MS H_2 traces for most samples. The MgH_2 - 90Ti10Si samples had dehydrogenation onset temperatures ranging from 261°C for MgH_2 - 90Ti10Si400, to 325°C for MgH_2 - 90Ti10Si800. A common feature of these samples was a maximum in the region of 350°C to 370°C. Total weight loss from the MgH_2 - 90Ti10Si samples was found to be lowest for the MgH_2 - 90Ti10Si120 sample, at 5.1 wt. %, while the highest weight loss of 5.6 wt. % was observed for the MgH_2 - 90Ti10Si800 sample. Dehydrogenation onset temperatures for the MgH_2 - 50Ti50Si samples ranged from 279°C for MgH_2 - 50Ti50Si70 up to 330°C for MgH_2 - 50Ti50Si400, with total weight loss from the samples increasing with oxide calcination temperature from 5.3 wt. % for MgH_2 - 50Ti50Si70 up to 6 wt. % for MgH_2 - 50Ti50Si800. Finally, the MgH_2 - 10Ti90Si samples (Figure 5.12) exhibited dehydrogenation onset temperatures of 297°C for MgH_2 - 10Ti90Si70, 305°C for MgH_2 - 10Ti90Si120, and *ca.* 340°C for the MgH_2 - 10Ti90Si400 and MgH_2 - 10Ti90Si800 samples. Total weight loss again increased with increasing oxide calcination temperature from 5.5 wt. % for MgH_2 - 10Ti90Si70 up to 5.9 wt. % for MgH_2 - 10Ti90Si800.

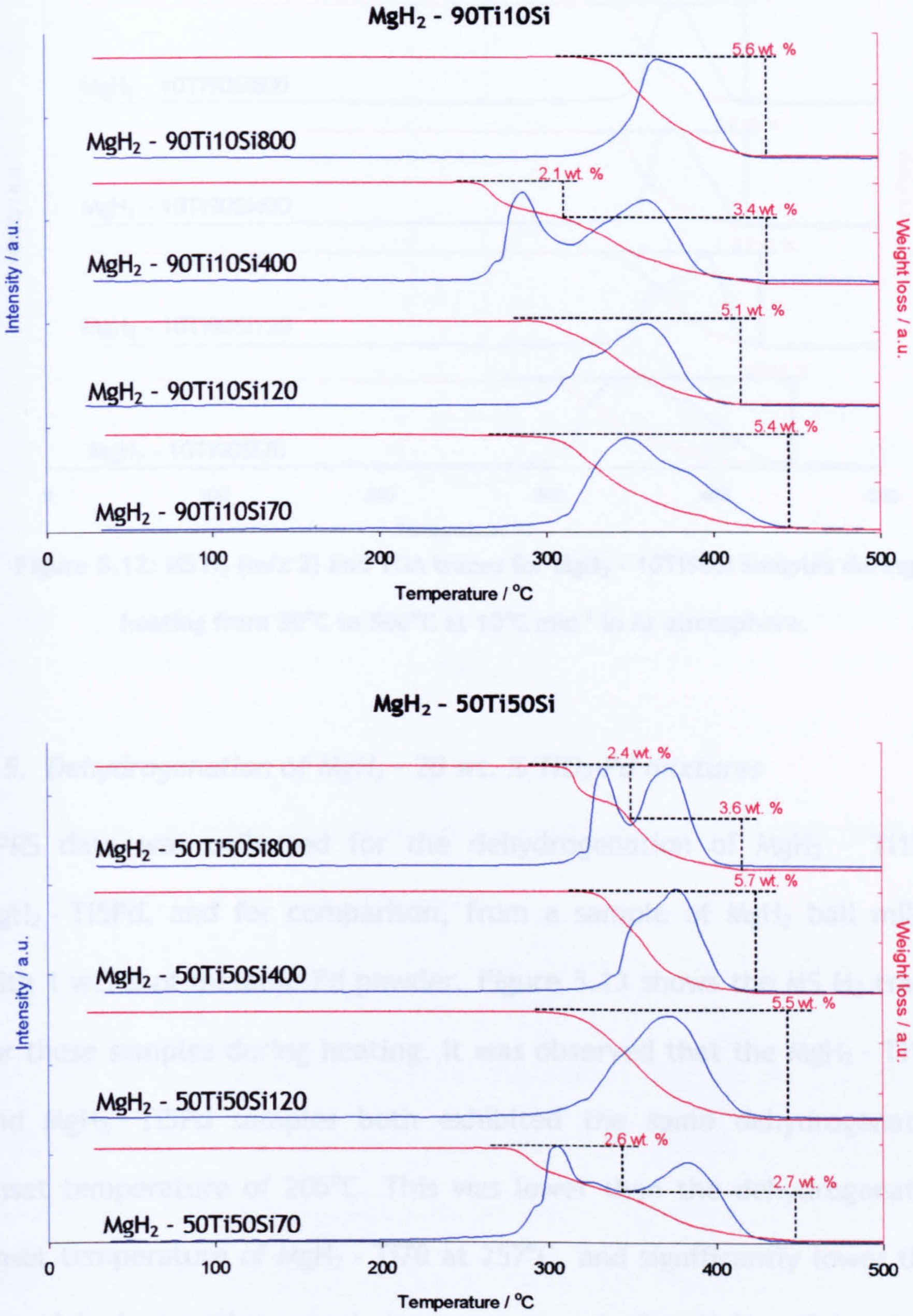

Figures 5.11: MS H_2 (m/z 2) and TGA traces for MgH_2 - 90Ti10Si (5.15) and MgH_2 - 50Ti50Si (5.16) samples during heating from 30°C to 500°C at 10°C min^{-1} in Ar atmosphere.

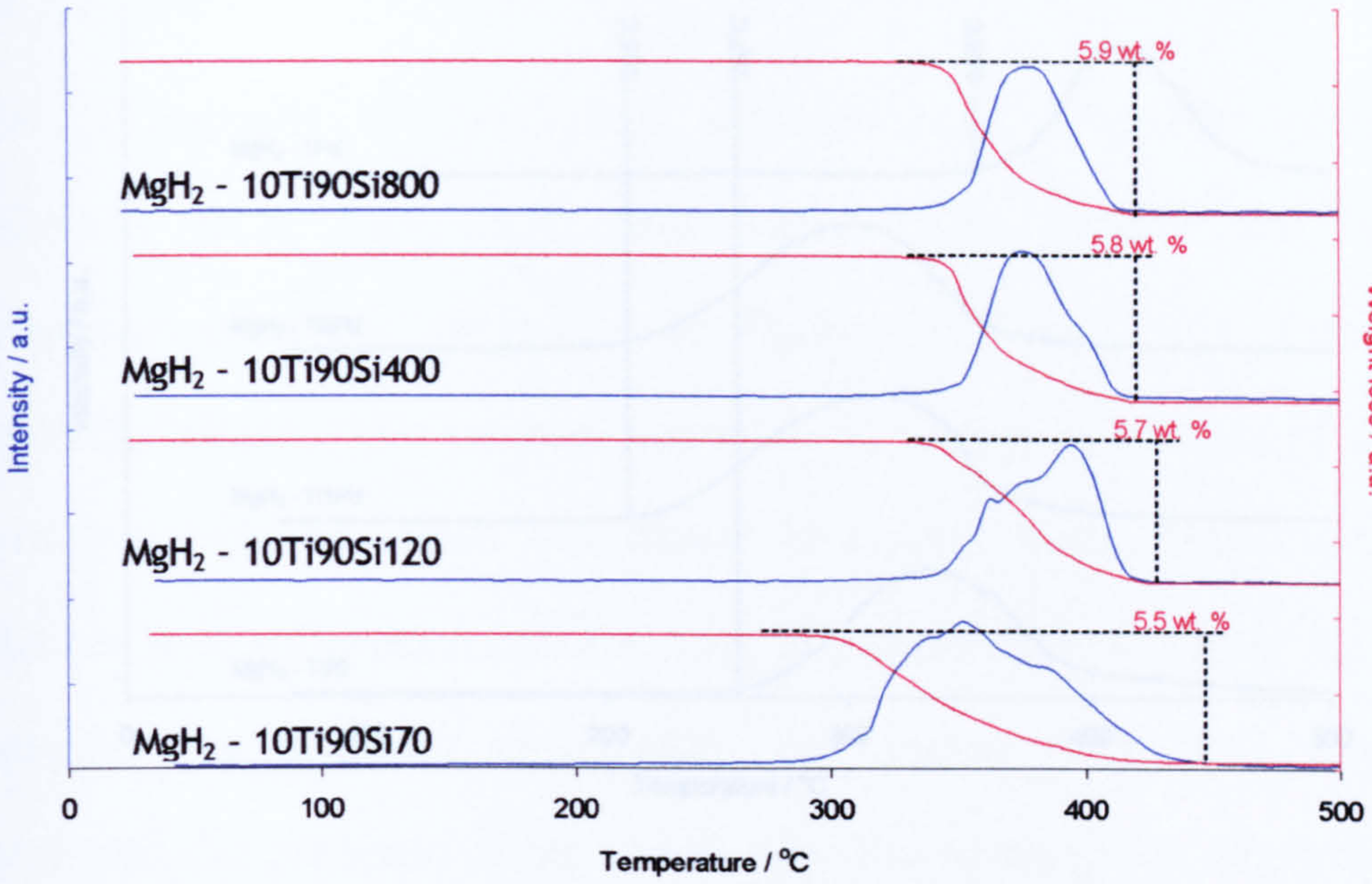

Figure 5.12: MS H_2 (m/z 2) and TGA traces for MgH_2 - 10Ti90Si samples during heating from 30°C to 500°C at 10°C min^{-1} in Ar atmosphere.

5.5. Dehydrogenation of MgH_2 - 20 wt. % TiO_2-Pd mixtures

TPRS data was collected for the dehydrogenation of MgH_2 - Ti1Pd, MgH_2 - Ti5Pd, and for comparison, from a sample of MgH_2 ball milled with 1 wt. % of metallic Pd powder. Figure 5.13 shows the MS H_2 traces for these samples during heating. It was observed that the MgH_2 - Ti1Pd and MgH_2 - Ti5Pd samples both exhibited the same dehydrogenation onset temperature of 205°C. This was lower than the dehydrogenation onset temperature of MgH_2 - Ti70 at 257°C, and significantly lower than the dehydrogenation onset temperature of the MgH_2 - 1Pd sample (358°C), which contained the same amount of Pd as MgH_2 - Ti5Pd.

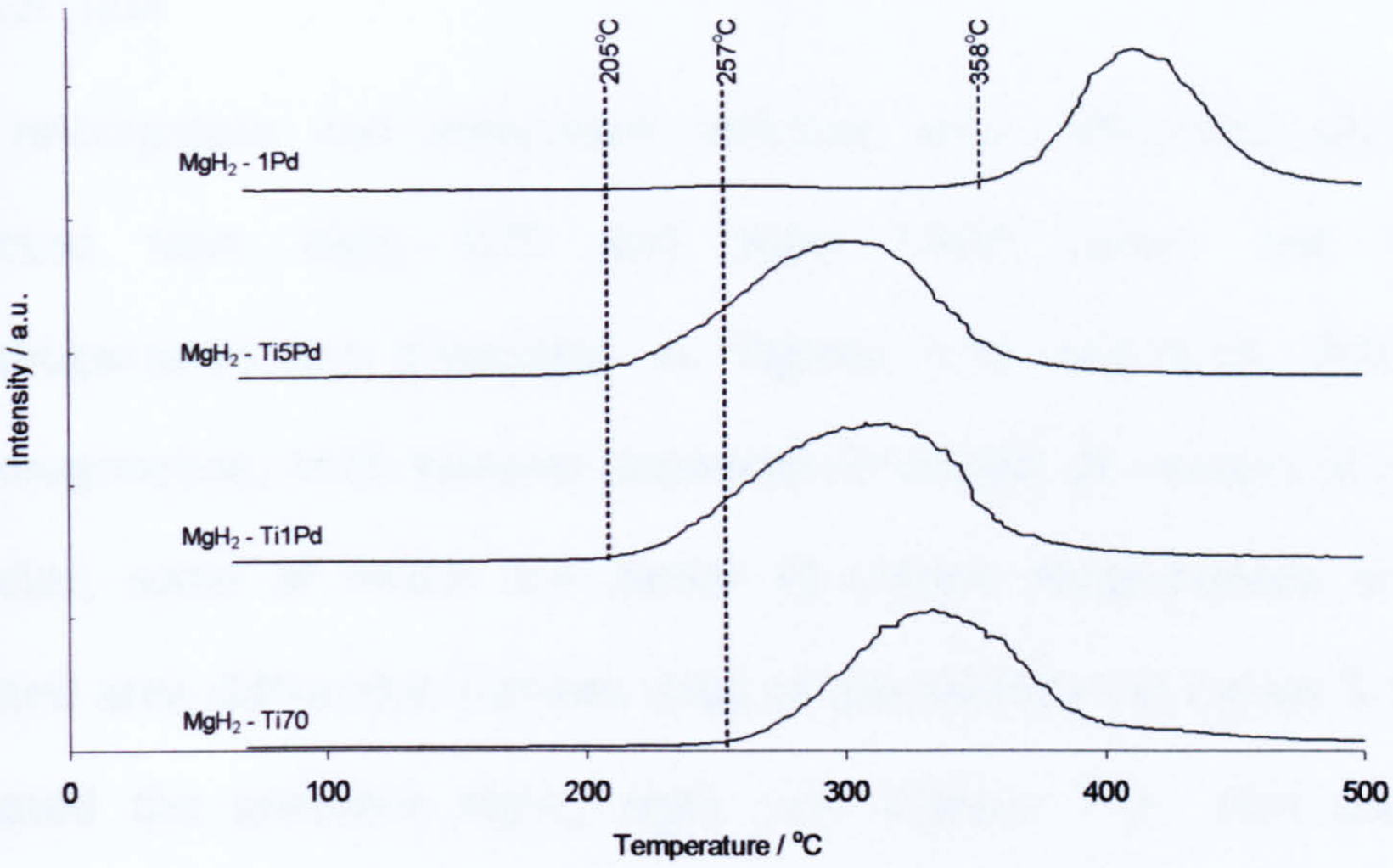

Figure 5.13: MS H_2 (m/z 2) traces for MgH_2 - Ti70, MgH_2 - Ti1Pd, MgH_2 - Ti5Pd, and MgH_2 - 1Pd during heating from 30°C to 500°C at 10°C min^{-1} in Ar atmosphere in TPRS.

5.6. Characterisation of milled MgH_2 - single and mixed oxide mixtures before and after dehydrogenation

5.6.1. N_2 Physisorption

The BET surface areas for each of the milled MgH_2-single and mixed oxide mixtures were measured using N_2 physisorption. The values of surface area were all measured to be within the error of 11 ±2 m^2 g^{-1}, which is not significantly different from the value of 10 ±2 m^2 g^{-1} determined for milled MgH_2 with no additives.

5.6.2. TEM

TEM micrographs and associated selected area diffraction patterns collected from MgH_2 - Ti70 and MgH_2 - Ti5Pd before and after dehydrogenation are presented in Figures 5.14 and 5.15. Prior to dehydrogenation, both samples appeared to consist of clusters of small particles, some of which are darker in colour. Measurement of the selected area diffraction pattern rings of the particles in Figure 5.14(A) indicated the presence MgH_2, MgO, and anatase TiO_2. EDX analysis confirmed the presence of Mg and Ti over the whole group of particles. After dehydrogenation, the darker central particle in Figure 5.14(B) appeared to be rich in Ti, with a concentration of 30 at. % from EDX quantification. The lighter bottom area was found to be 99 at. % Mg, suggesting a sintering of TiO_2 particles during dehydrogenation.

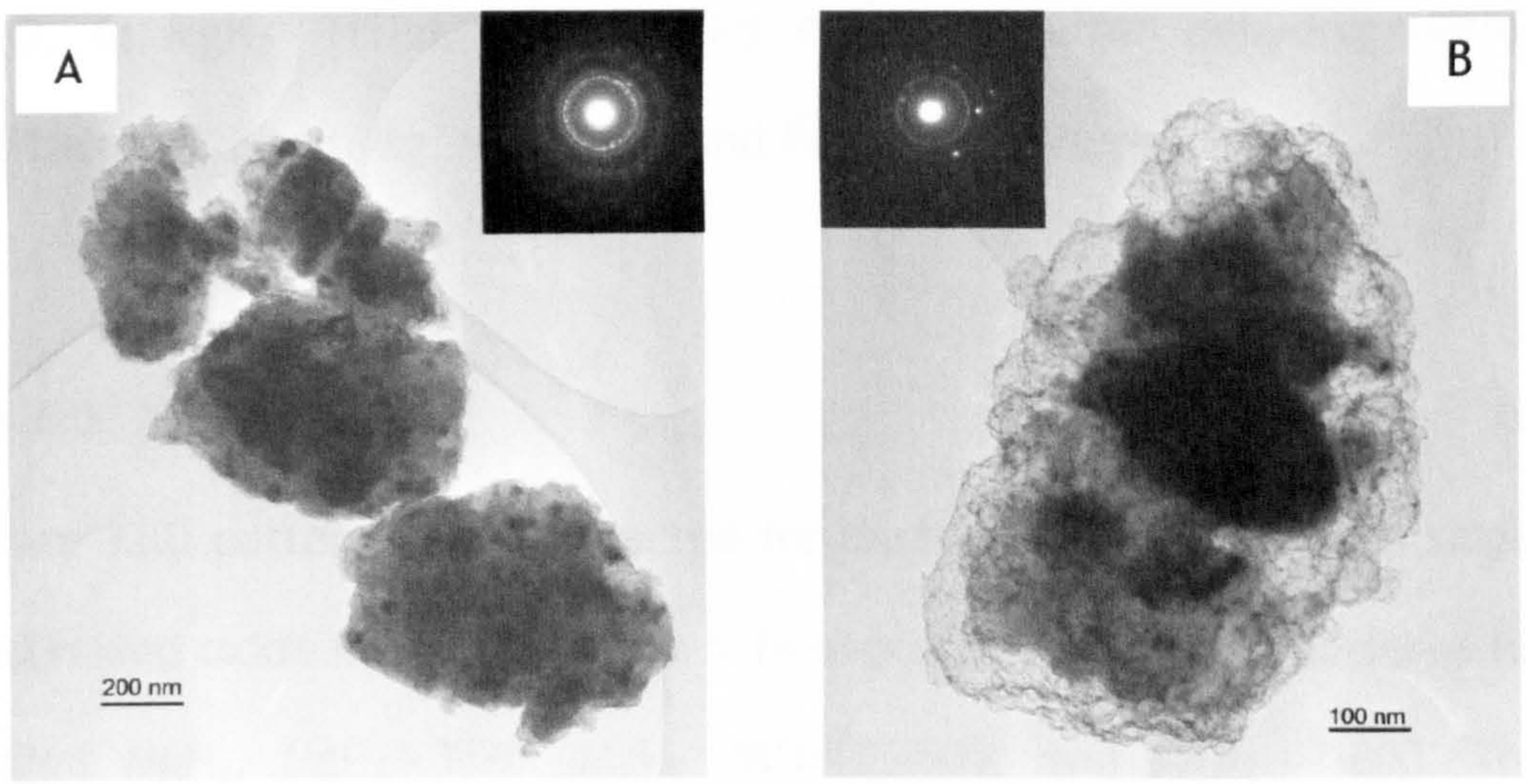

Figure 5.14: TEM micrographs and selected area diffraction patterns of MgH_2 - Ti70 (A) and MgH_2 - Ti70 after dehydrogenation (B).

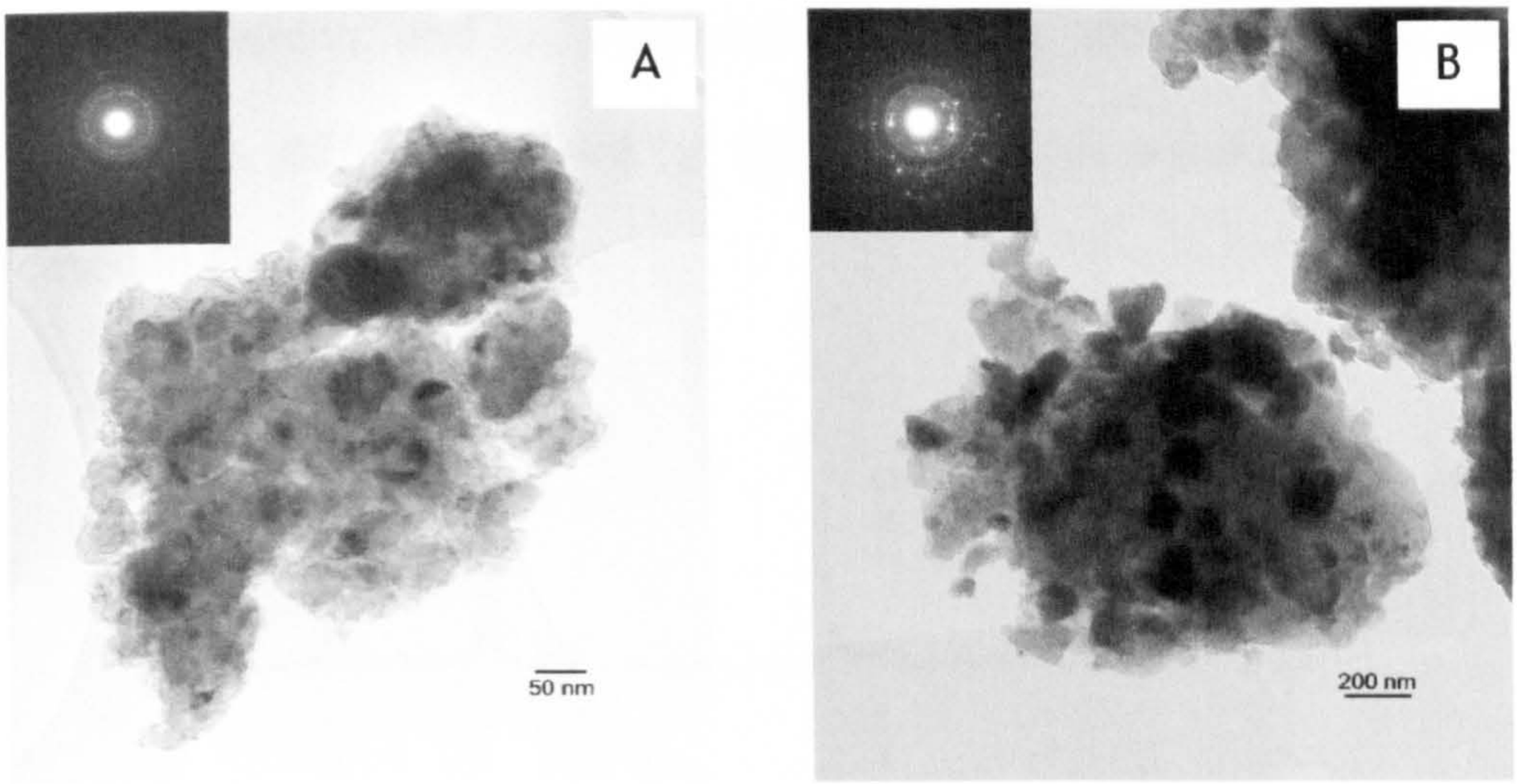

Figure 5.15: TEM micrographs and selected area diffraction patterns of MgH_2 - Ti5Pd (A) and MgH_2 - Ti5Pd after dehydrogenation (B).

For the MgH_2 - Ti5Pd samples, evidence of Pd (0.3 at. %) was found from EDX analysis of the clusters of particles both before and after dehydrogenation. Measurement of the diffraction ring spacings of the selected area diffraction patterns indicated the presence of MgH_2 and MgO, in MgH_2 - Ti5Pd, with no Pd observed. After dehydrogenation diffractions due to Mg, MgO, TiO_2 and Pd were measured.

5.6.3. XRD

Power XRD patterns were collected for each of the milled MgH_2 - single and mixed oxide mixtures. Figure 5.16 shows the diffraction patterns for milled MgH_2, MgH_2 - Ti70, MgH_2 - 90Ti10Si800, and MgH_2 - Ti800. The milled MgH_2 and MgH_2 - Ti70 samples both showed diffraction lines from the MgH_2 and MgO phases only, which is representative of the diffraction patterns for the majority of the MgH_2 - single and mixed oxide samples, with the exception of the samples containing more crystalline oxides,

the TiO_2 containing, and ZrO_2 samples calcined at 400°C and 800°C. For these samples, diffraction lines for the single oxides are also visible, as indicated in Figure 5.16.

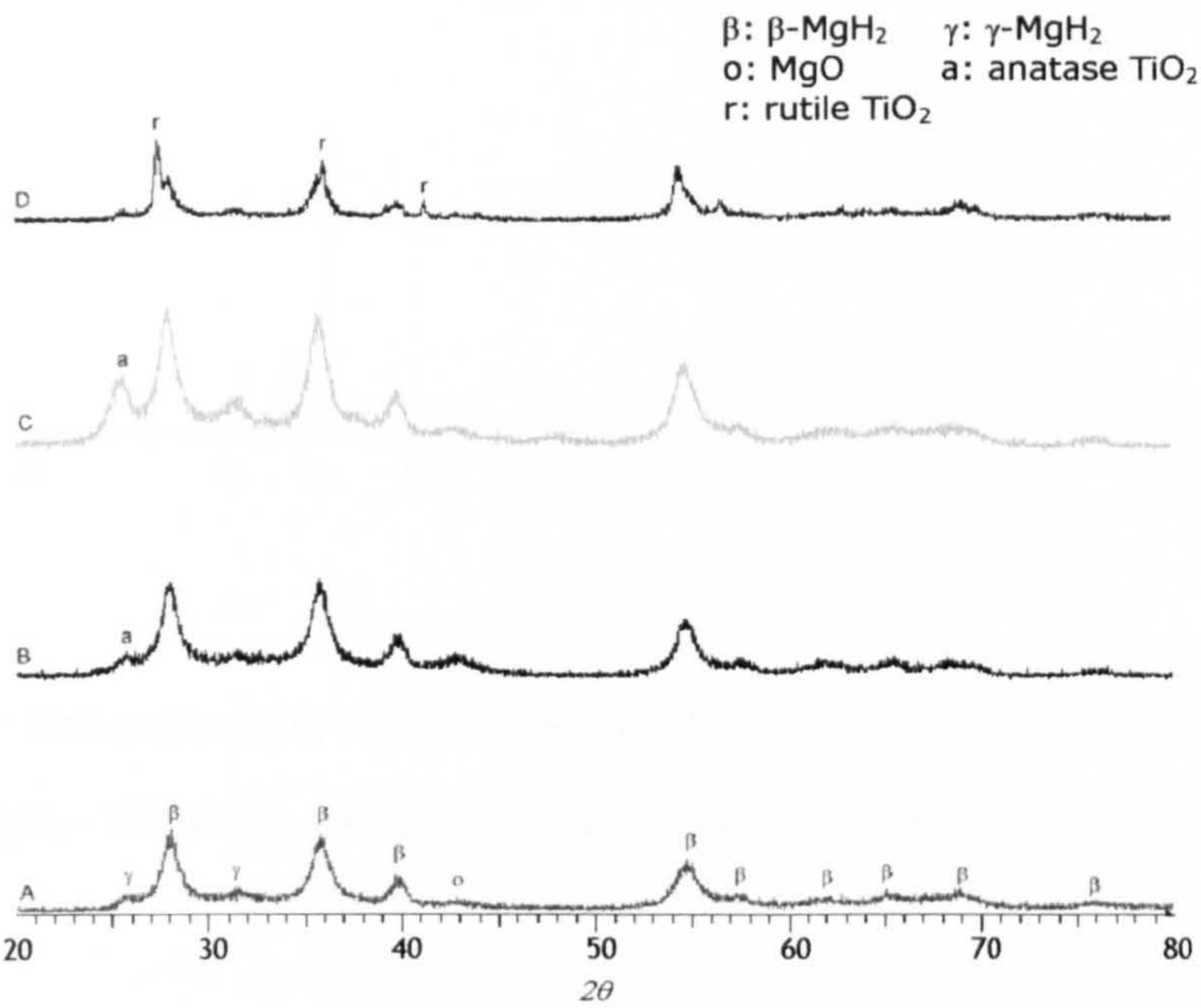

Figure 5.16: XRD patterns of milled MgH_2 (A), MgH_2 - Ti70 (B), MgH_2 - 90Ti10Si800 (C), and MgH_2 - Ti800 (D).

Powder XRD patterns were also collected for samples after dehydrogenation caused by heating to 600°C in DSC-TGA experiments. Figure 5.17 shows patterns for MgH_2, MgH_2 - Ti70, MgH_2 - 90Ti10Si800, and MgH_2 - Ti800 after dehydrogenation. Diffractions lines for metallic Mg and MgO were observed, with no other diffractions due to phases containing Ti appearing in the diffraction patterns.

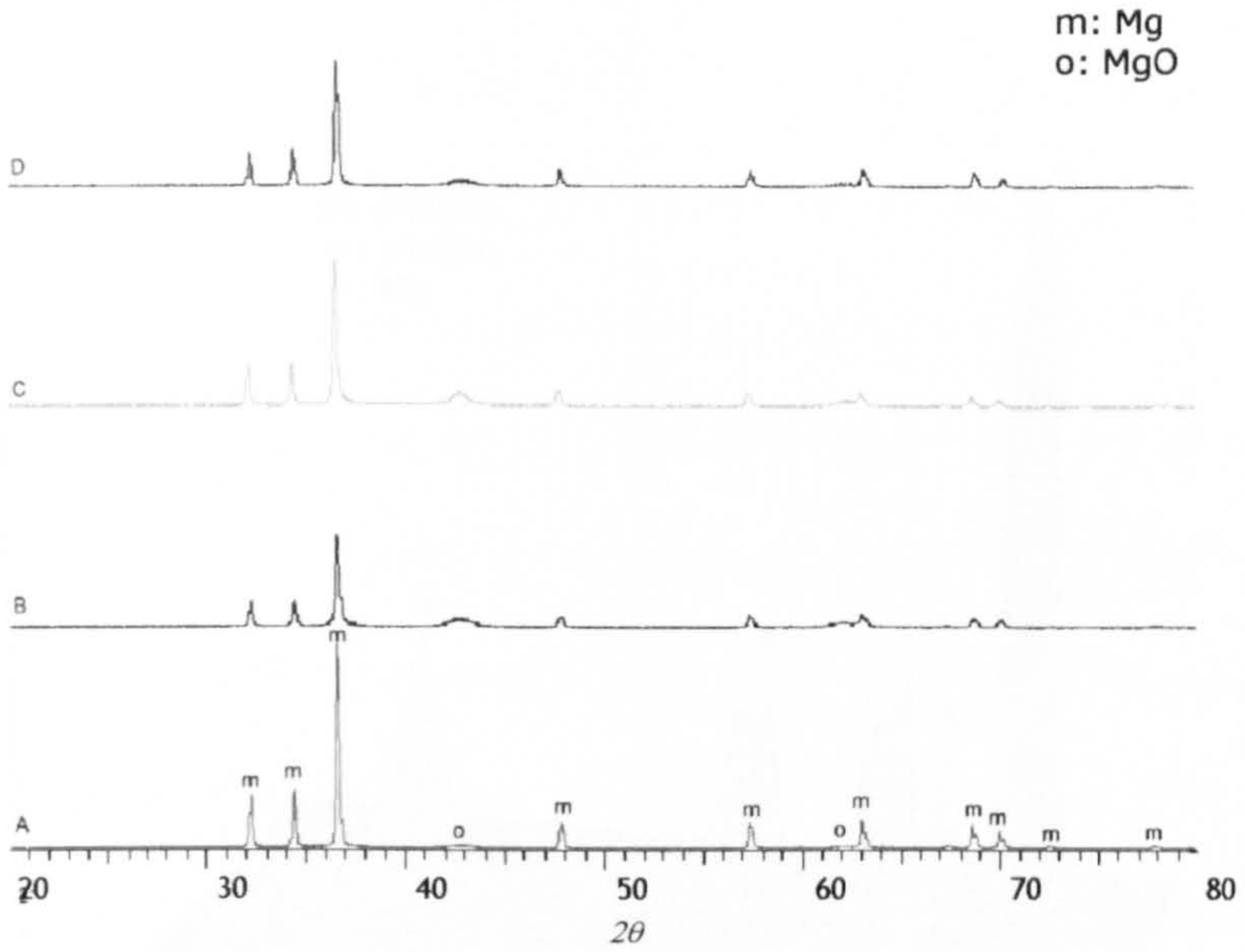

Figure 5.17: XRD patterns of MgH_2 (A), MgH_2 - Ti70 (B), MgH_2 - 90Ti10Si800 (C), and MgH_2 - Ti800 (D). All patterns measured after dehydrogenation.

5.6.4. In situ XRD

In situ XRD was used to follow the dehydrogenation of ball milled MgH_2 during heating from room temperature to 600°C at an Ar pressure of 1 bar. Figure 5.18 shows the 3D XRD pattern collected during the heating process from 150 to 600 °C. Mg starts to form at ~350°C. The metastable γ-phase is still present until the transformation from hydride to metal is complete at ~500°C. The β-MgH_2 becomes increasingly crystalline up to 450°C before transforming fully to Mg. The average crystallite size for the β-MgH_2 at each temperature is tabulated in Table 5.2.

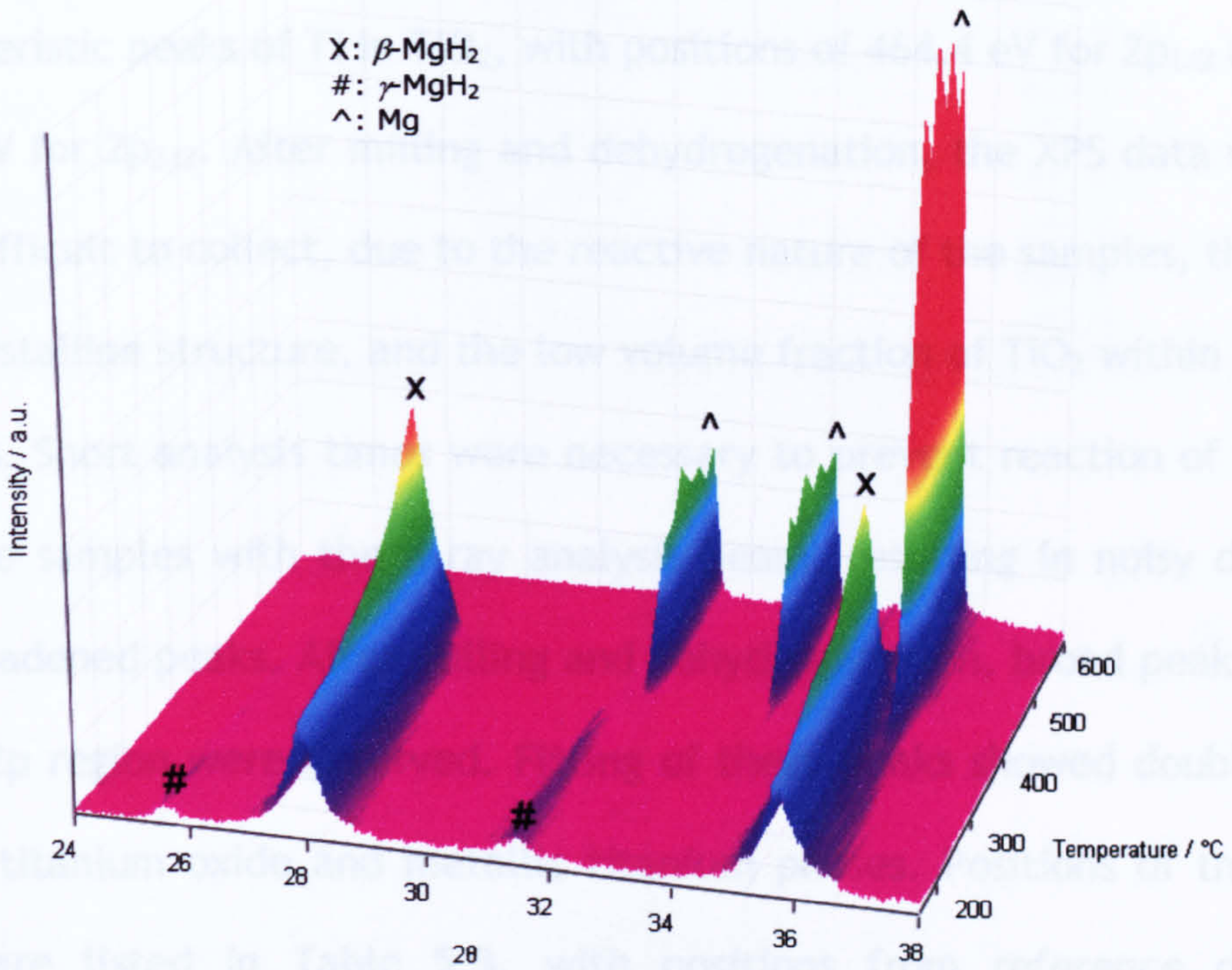

Figure 5.18: XRD data for milled MgH_2 heated from 150°C to 600°C at 10°C min^{-1} under He. An XRD scan from 24 - 38 2θ was taken every 50°C.

Temperature / °C	150	200	250	300	350	400	450
Crystallite size / nm	15	17	19	22	26	39	53

Table 5.2: Average crystallite size for β-MgH_2 phase during heating in *in situ* XRD experiment.

5.6.5. XPS

XPS of the Ti70, MgH_2 - Ti70, and MgH_2 - Ti70 after dehydrogenation was carried out to examine the nature of the Ti species before and after

milling and dehydrogenation. XPS spectra from the Ti region of these samples are shown in Figure 5.19. The Ti70 sample showed the characteristic peaks of Ti in TiO_2, with positions of 464.4 eV for $2p_{1/2}$ and 458.8 eV for $2p_{3/2}$. After milling and dehydrogenation, the XPS data was more difficult to collect, due to the reactive nature of the samples, their nanocrystalline structure, and the low volume fraction of TiO_2 within the samples. Short analysis times were necessary to prevent reaction of the sensitive samples with the X-ray analysis beam, resulting in noisy data and broadened peaks. After milling and dehydrogenation, broad peaks in the Ti 2p region were observed. Fitting of these peaks showed doublets due to titanium oxide and metallic titanium phases. Positions of these peaks are listed in Table 5.3, with positions from reference data included in Table 5.4, for comparison. The relative abundance of metallic Ti increased from approximately 30 % in the milled sample to approximately 40 % after dehydrogenation.

Sample	Peak position / eV	Assignment
Ti70 before milling	464.4	Ti^{IV} $2p_{1/2}$
	458.8	Ti^{IV} $2p_{3/2}$
MgH_2 - Ti70 after milling	464.1	Ti^{IV} $2p_{1/2}$
	458.3	Ti^{IV} $2p_{3/2}$
	459.8	Ti $2p_{1/2}$
	453.8	Ti $2p_{3/2}$
MgH_2 - Ti70 after dehydrogenation	463.8	Ti^{IV} $2p_{1/2}$
	458.0	Ti^{IV} $2p_{3/2}$
	460.6	Ti $2p_{1/2}$
	454.0	Ti $2p_{3/2}$

Table 5.3: Assignment of XPS peaks

Sample	Peak assignment	Position / eV
Ti [(a)]	Ti $2p_{1/2}$	460.0
	Ti $2p_{3/2}$	454.0
TiO [(b)]	Ti^{II} $2p_{1/2}$	460.2
	Ti^{II} $2p_{3/2}$	454.6
Ti_2O_3 [(b)]	Ti^{III} $2p_{1/2}$	462.0
	Ti^{III} $2p_{3/2}$	456.8
TiO_2 [(b)]	Ti^{IV} $2p_{1/2}$	464.6
	Ti^{IV} $2p_{3/2}$	458.9

Table 5.4: XPS Ti 2p peak positions from reference data, (a) [98] and (b) [99].

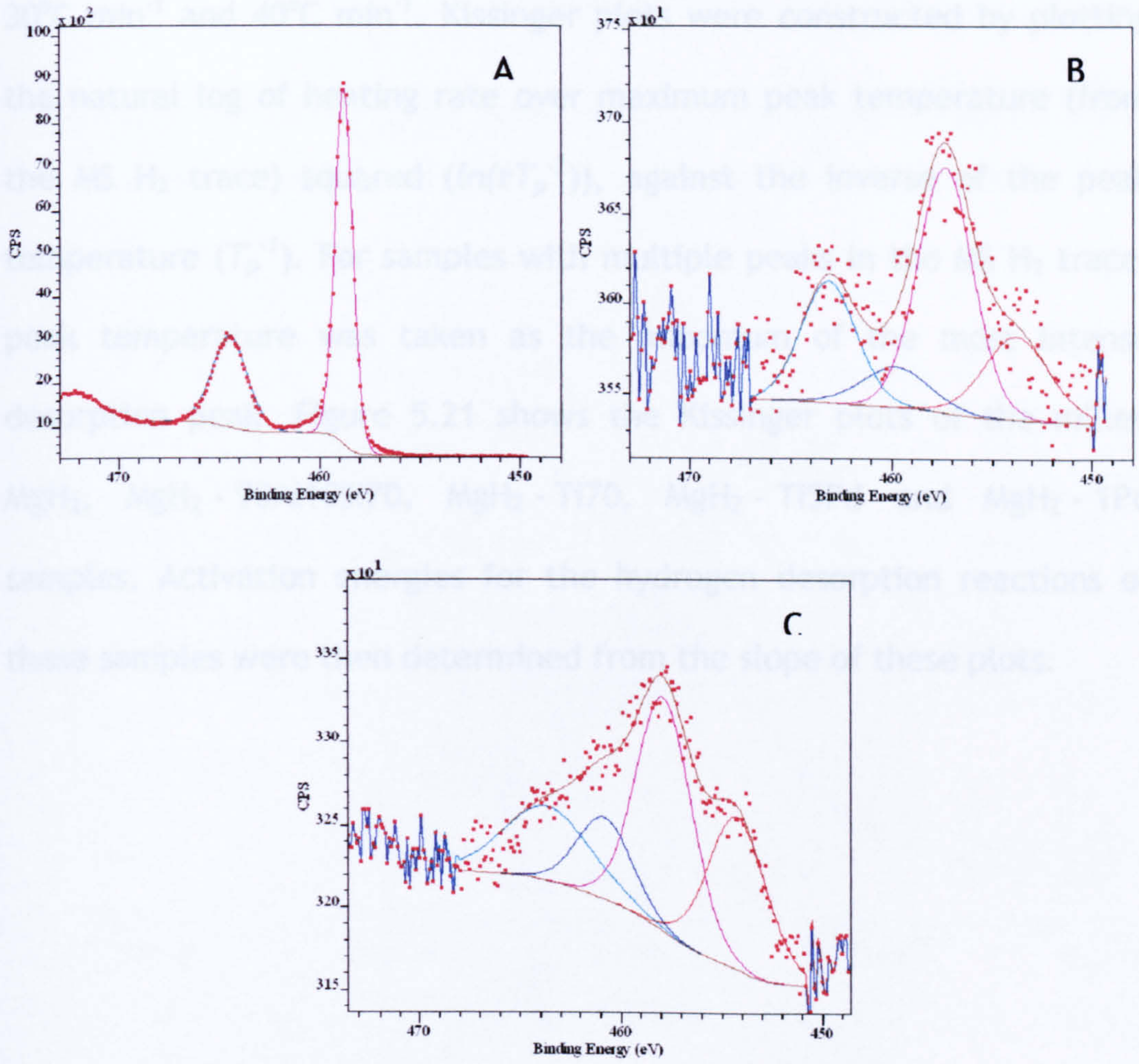

Figure 5.19: XPS Ti 2p spectra from Ti70 (A), MgH_2 - Ti70 (B), and MgH_2 - Ti70 after dehydrogenation (C).

5.7. TGA-MS study - determination of activation energy of dehydrogenation

TGA-MS was used to measure the dehydrogenation of the milled MgH_2, MgH_2 - 90Al10Si70, MgH_2 - Ti70, MgH_2 - Ti5Pd, MgH_2 - 1Pd samples using a range of heating rates. Figure 5.20 shows a sample plot of the MS H_2 traces from hydrogen desorbed from milled MgH_2 during heating from room temperature to 500°C at heating rates of 10°C min^{-1}, 20°C min^{-1}, 30°C min^{-1} and 40°C min^{-1}. Kissinger plots were constructed by plotting the natural log of heating rate over maximum peak temperature (from the MS H_2 trace) squared ($ln(rT_p^{-2})$), against the inverse of the peak temperature (T_p^{-1}). For samples with multiple peaks in the MS H_2 trace, peak temperature was taken as the maximum of the most intense desorption peak. Figure 5.21 shows the Kissinger plots of the milled MgH_2, MgH_2 - 90Al10Si70, MgH_2 - Ti70, MgH_2 - Ti5Pd and MgH_2 - 1Pd samples. Activation energies for the hydrogen desorption reactions of these samples were then determined from the slope of these plots.

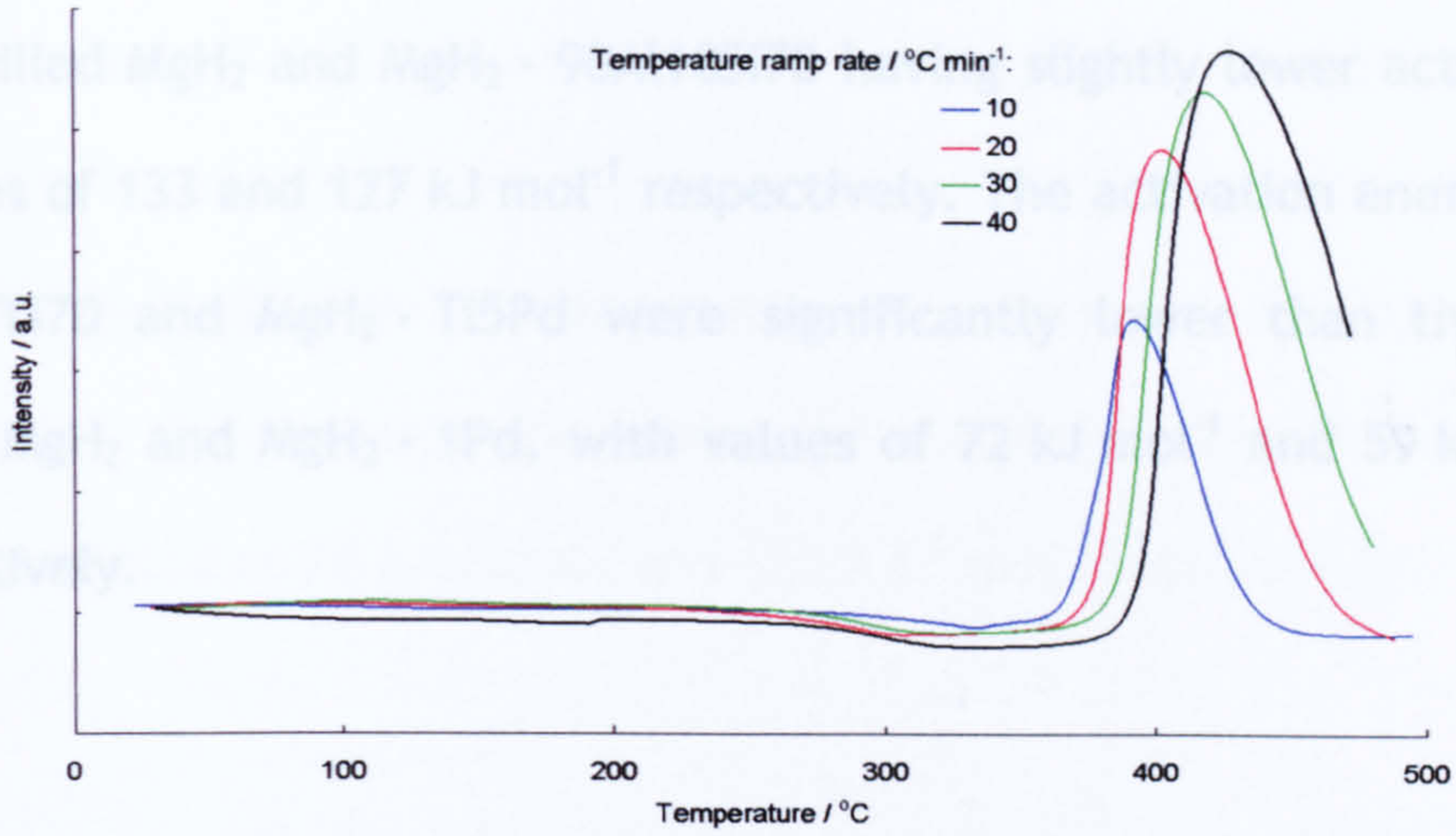

Figure 5.20: MS H_2 traces for the dehydrogenation of milled MgH_2 heated to 500°C under flowing Ar gas at heating rates of 10, 20, 30, and 40°C min^{-1}.

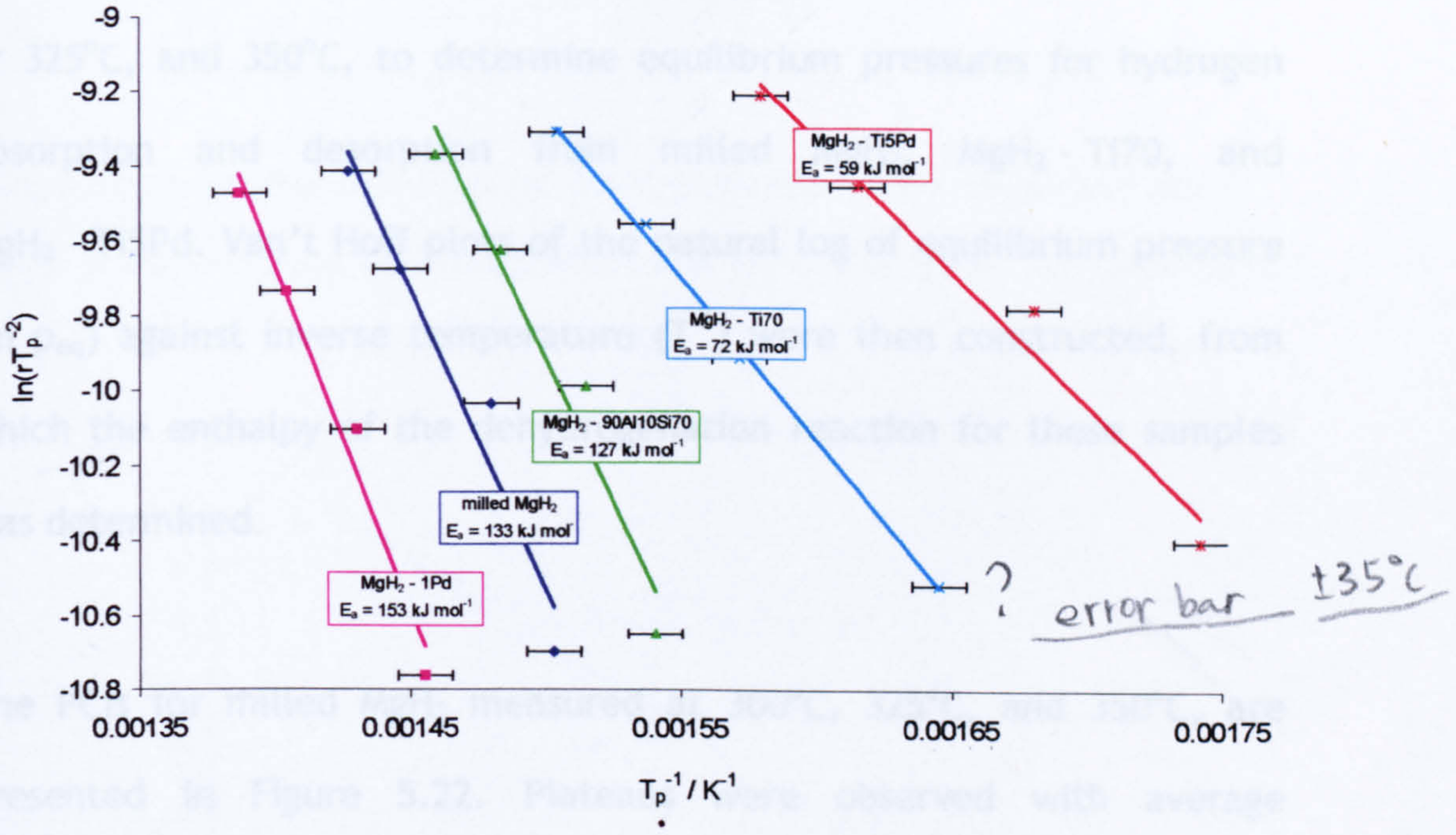

Figure 5.21: Kissinger plots showing activation energy values for the dehydrogenation of milled MgH_2, MgH_2 - 1Pd, MgH_2 - 90Al10Si70, MgH_2 - Ti70, and MgH_2 - Ti5Pd.

The highest activation energy of 153 kJ mol^{-1} was found for MgH_2 - 1Pd, with milled MgH_2 and MgH_2 - 90Al10Si70 having slightly lower activation energies of 133 and 127 kJ mol^{-1} respectively. The activation energies of MgH_2 - Ti70 and MgH_2 - Ti5Pd were significantly lower than those of milled MgH_2 and MgH_2 - 1Pd, with values of 72 kJ mol^{-1} and 59 kJ mol^{-1} respectively.

5.8. PCIs and thermodynamic data

Information on the thermodynamic stability of the prepared materials was determined from volumetric measurements carried out using a Sieverts apparatus. PCIs were constructed at temperatures of 300°C, 320 or 325°C, and 350°C, to determine equilibrium pressures for hydrogen absorption and desorption from milled MgH_2, MgH_2 - Ti70, and MgH_2 - Ti5Pd. Van't Hoff plots of the natural log of equilibrium pressure ($\ln p_{eq}$) against inverse temperature (T^{-1}) were then constructed, from which the enthalpy of the dehydrogenation reaction for these samples was determined.

The PCIs for milled MgH_2 measured at 300°C, 325°C, and 350°C, are presented in Figure 5.22. Plateaus were observed with average equilibrium pressures of 2.30 bar, 2.41 bar, and 2.83 bar, for H_2 absorption at 300°C, 325°C, and 350°C respectively, with plateau pressures of 1.29 bar, 1.84 bar, and 2.72 bar for the corresponding H_2 desorption equilibria. Total weight percent of hydrogen absorbed and

desorbed by the sample was *ca.* 6.0 wt. %, regardless of reaction temperature.

The van't Hoff plot for dehydrogenation of milled MgH_2 is presented in Figure 5.23. The enthalpy and entropy of the dehydrogenation reaction were calculated as 73.6 kJ mol^{-1} and 129 J K^{-1} mol^{-1} respectively.

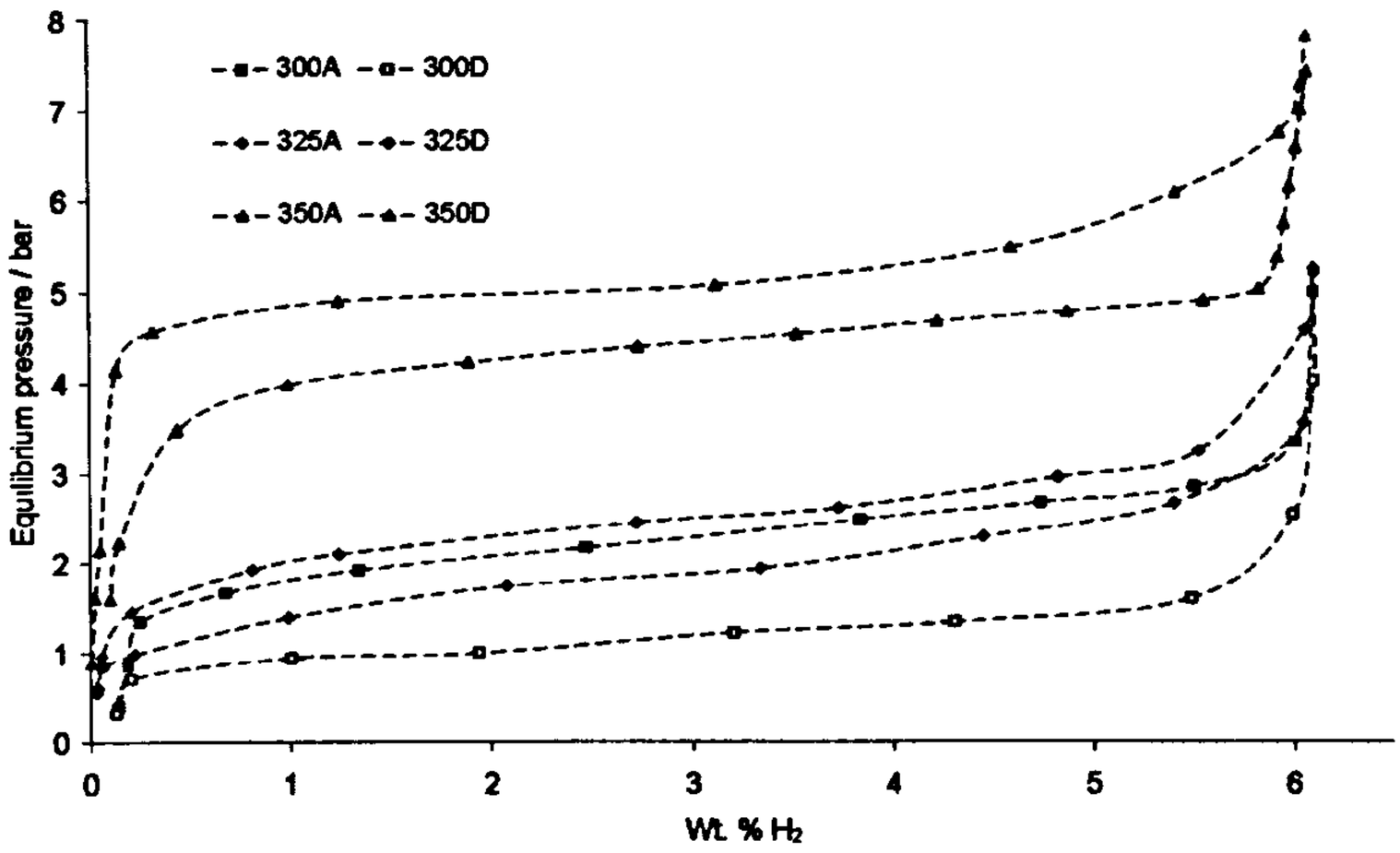

Figure 5.22: PCIs for milled MgH_2 at 300°C (absorption: 300A, desorption 300D), 325°C (absorption 320A, desorption 320D), and 350°C (absorption 350A, desorption 350D).

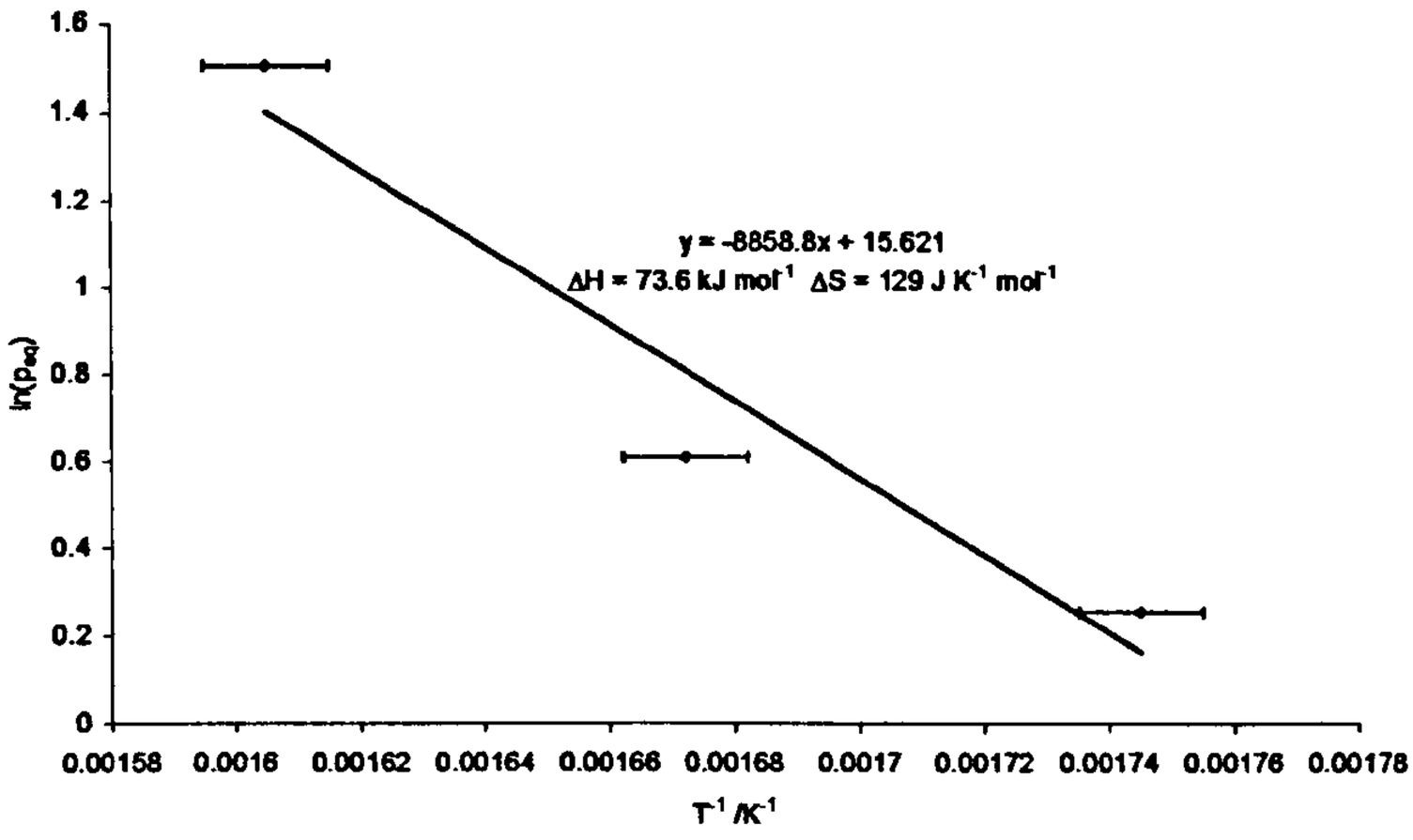

Figure 5.23: van't Hoff plots showing ΔH_r and ΔS_r for desorption of hydrogen from milled MgH_2.

In Figure 5.24, the PCIs for MgH_2 - Ti70 are shown. Equilibrium pressures of 1.52 bar, 2.66 bar, and 4.99 bar were measured for absorption at 300°C, 325°C, and 350°C. The corresponding desorption plateau pressures were found to be 1.15 bar, 2.34 bar, and 4.60 bar respectively, with total weight loss measured to be *ca.* 4.6 wt. %.

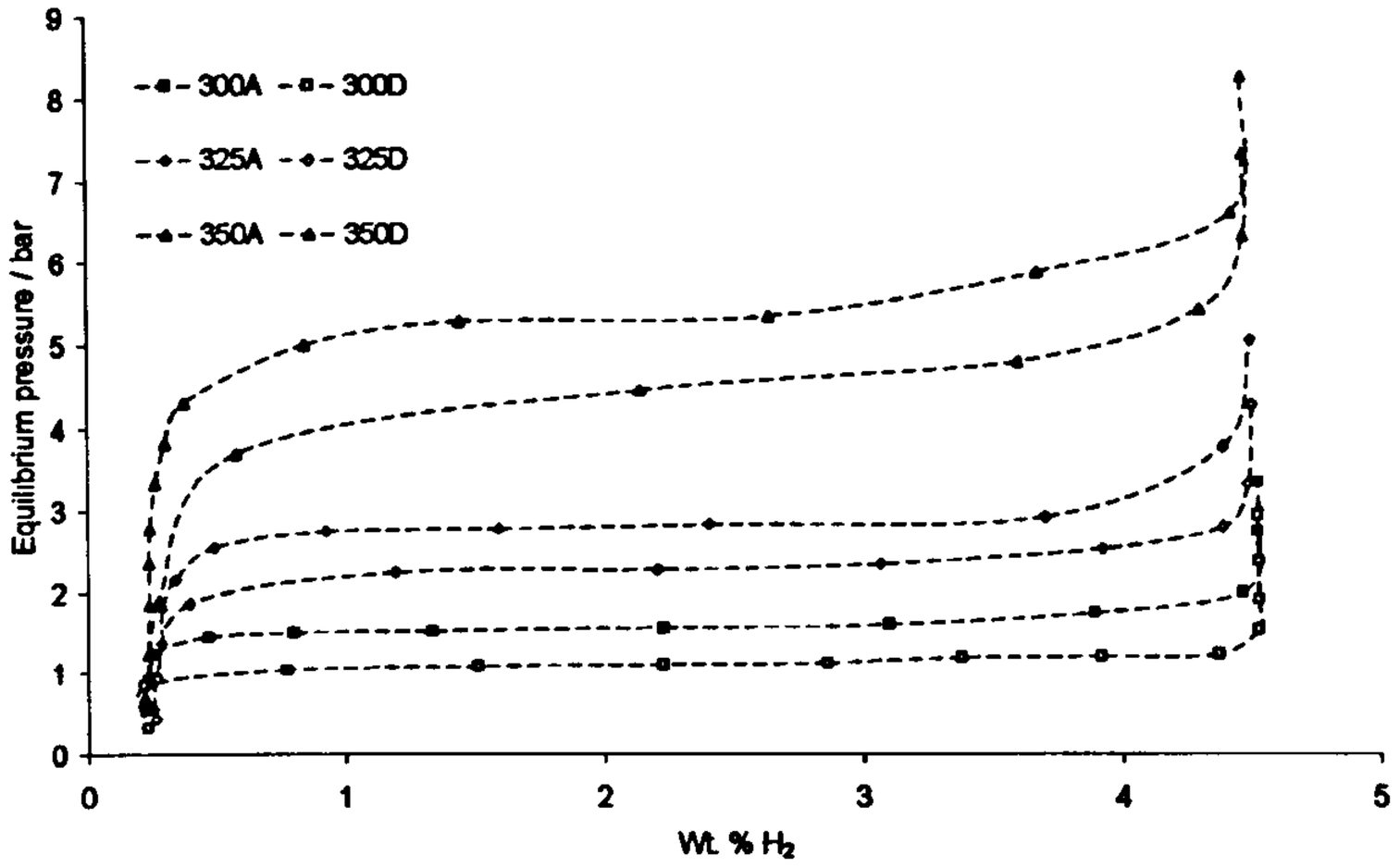

Figure 5.24: PCIs for MgH_2 - Ti70 at 300°C (absorption: 300A, desorption 300D), 325°C (absorption 325A, desorption 325D), and 350°C (absorption 350A, desorption 350D).

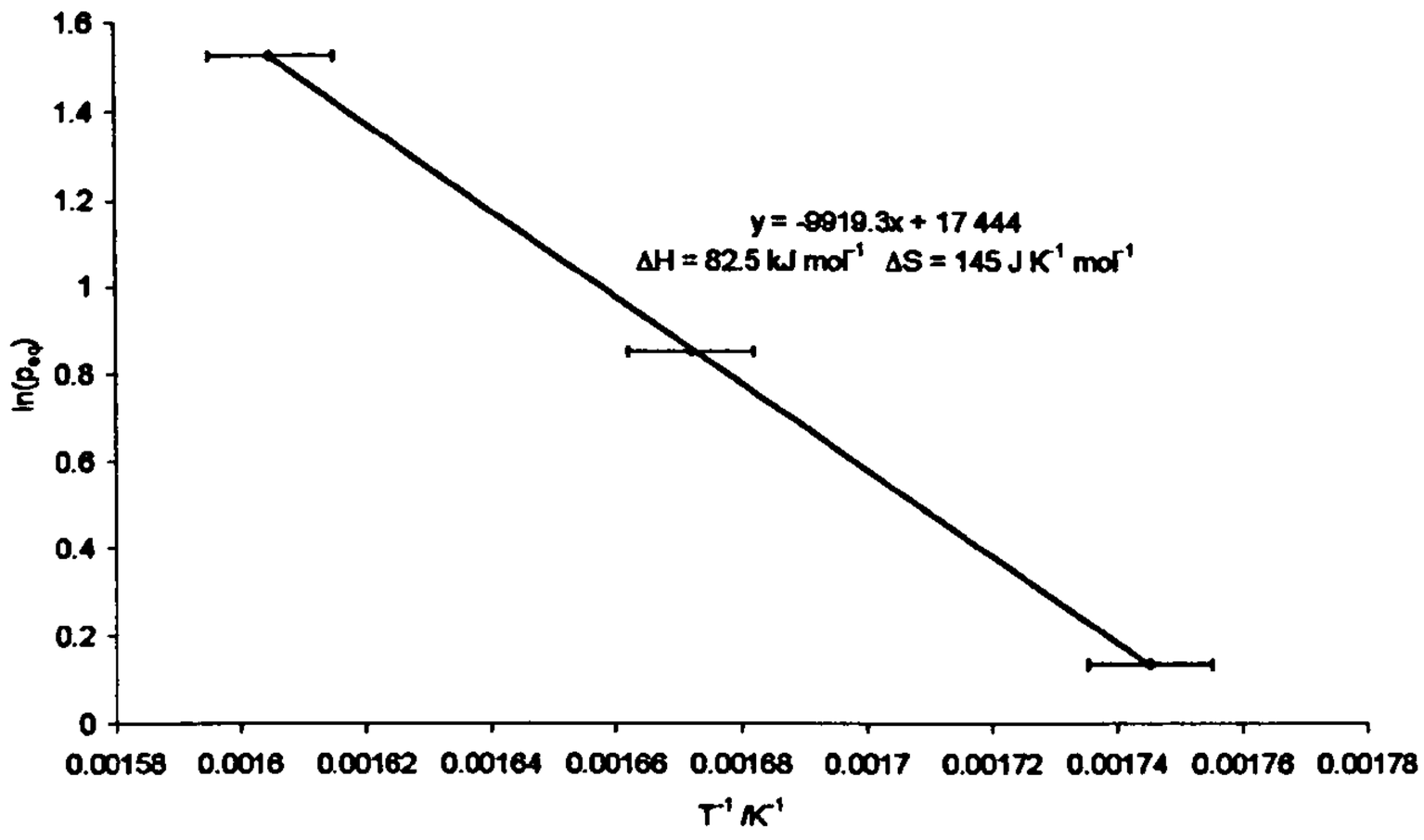

Figure 5.25: van't Hoff plot showing ΔH_r and ΔS_r for desorption of hydrogen from MgH_2 - Ti70.

Figure 5.25 shows the van't Hoff plot for the dehydrogenation of MgH_2 - Ti70. The enthalpy and entropy of dehydrogenation were calculated as 82.5 kJ mol^{-1} and 145 J K^{-1} mol^{-1}.

PCIs at 300°C, 320°C, and 350°C were also measured for the MgH_2 - Ti5Pd sample, and are shown in Figure 5.26. The plateau pressures of H_2 absorption were 1.33 bar, 2.16 bar, and 4.58 bar, at 300°C, 320°C, and 350°C respectively, with plateau pressures of 1.10 bar, 1.93 bar, and 4.28 bar for the corresponding H_2 desorption equilibria. Total weight percent of hydrogen absorbed and desorbed by the sample was *ca.* 5.0 wt. %, regardless of reaction temperature.

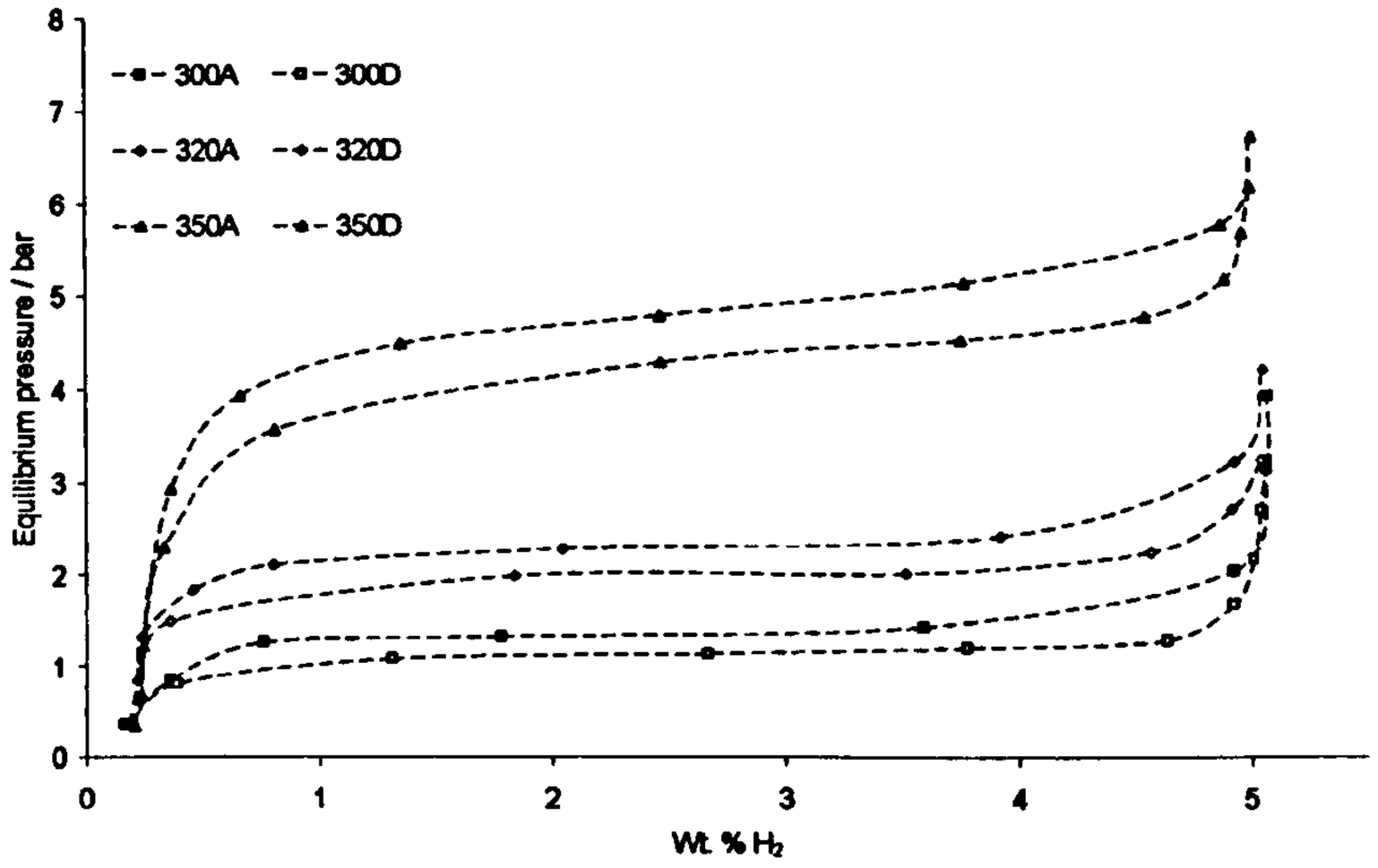

Figure 5.26: PCIs for MgH_2 - Ti5Pd at 300°C (absorption: 300A, desorption 300D), 320°C (absorption 320A, desorption 320D), and 350°C (absorption 350A, desorption 350D).

The van't Hoff plot for dehydrogenation of MgH_2 - Ti5Pd is shown in Figure 5.27. The enthalpy of the dehydrogenation reaction was calculated to be 80.7 kJ mol^{-1}, and the entropy was measured to be 142 J K^{-1} mol^{-1}.

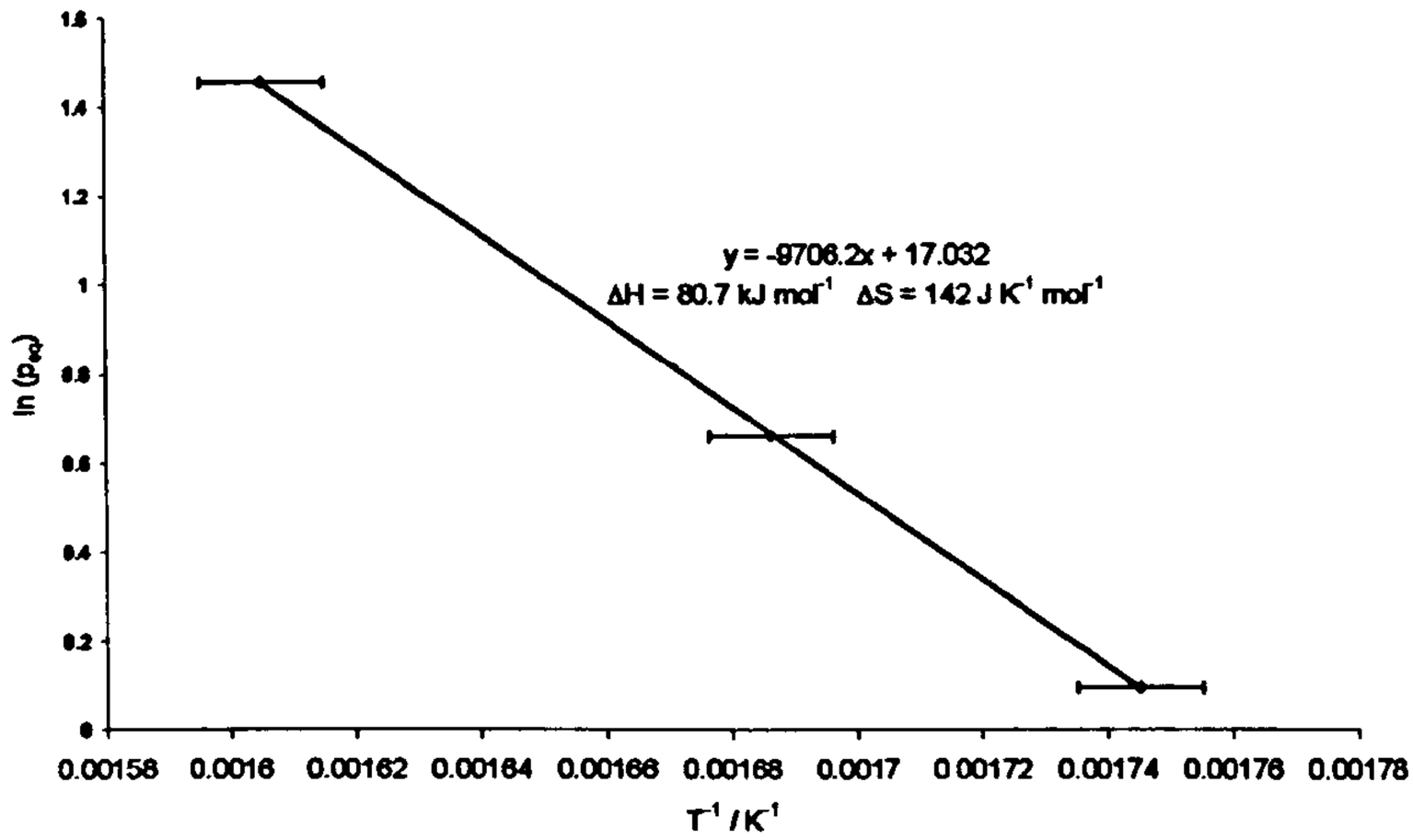

Figure 5.27: van't Hoff plot showing ΔH_r and ΔS_r for desorption of hydrogen from MgH_2 - Ti5Pd.

5.9. Hydrogen cycling experiments

The gravimetric method of measuring hydrogen absorption and desorption was used to carry out cycling experiments on a number of samples, in order to investigate the effect of repeated cycling on the kinetics of the hydrogen absorption and desorption reactions, and on the overall capacity of the samples.

Samples of Milled MgH_2, MgH_2 - Ti70, and MgH_2 - Ti5Pd, were subjected to a series of 10 cycles each, between H_2 pressures of 1×10^{-2} bar and 6 bar. The temperature was maintained at 300°C for all of the samples tested, apart from milled MgH_2. Figure 5.28 shows weight loss from

milled MgH_2 at 1 x 10^{-2} bar and 300°C. Less than 1 wt. % (< 20 % of total dehydrogenation) was lost from the sample over a period of 12 hours. Due to time constraints, and in order to speed up the kinetics of the MgH_2 desorption reaction, cycling for this sample was therefore carried out a temperature of 350°C.

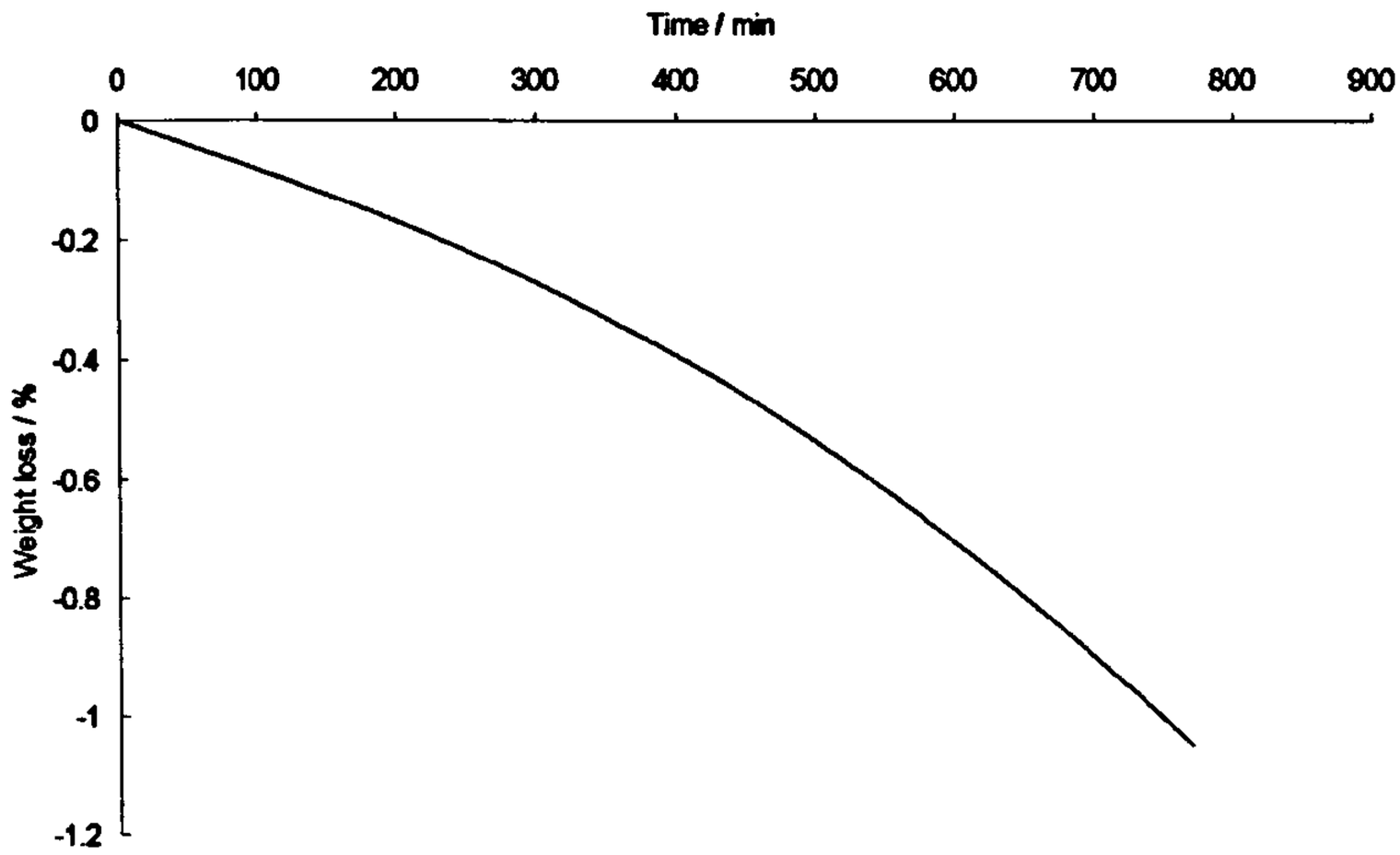

Figure 5.28: First dehydrogenation of milled MgH_2 at 300°C and 1 x 10^{-2} bar H_2.

Figures 5.29 and 5.30 show the weight percent gain and loss due to hydrogen desorption and absorption against time for milled MgH_2 at 350°C, over 10 cycles. After the third cycle, the rates of absorption and desorption had levelled off, therefore for clarity data from cycles 5 - 9 is not presented. During the first desorption cycle at 350°C and 1 x $10^{-2\ bar}$, *ca.* 80 % of the total weight loss was evolved from the sample in 12 hours. For subsequent cycles, most of the weight loss, 90 - 95 %, had occurred after 300 min (5 h). Hydrogen absorption at 350°C and 6 bar

was found to be much quicker than desorption, with the milled MgH_2 sample absorbing *ca.* 90 % of total absorption in 90 min on each cycle.

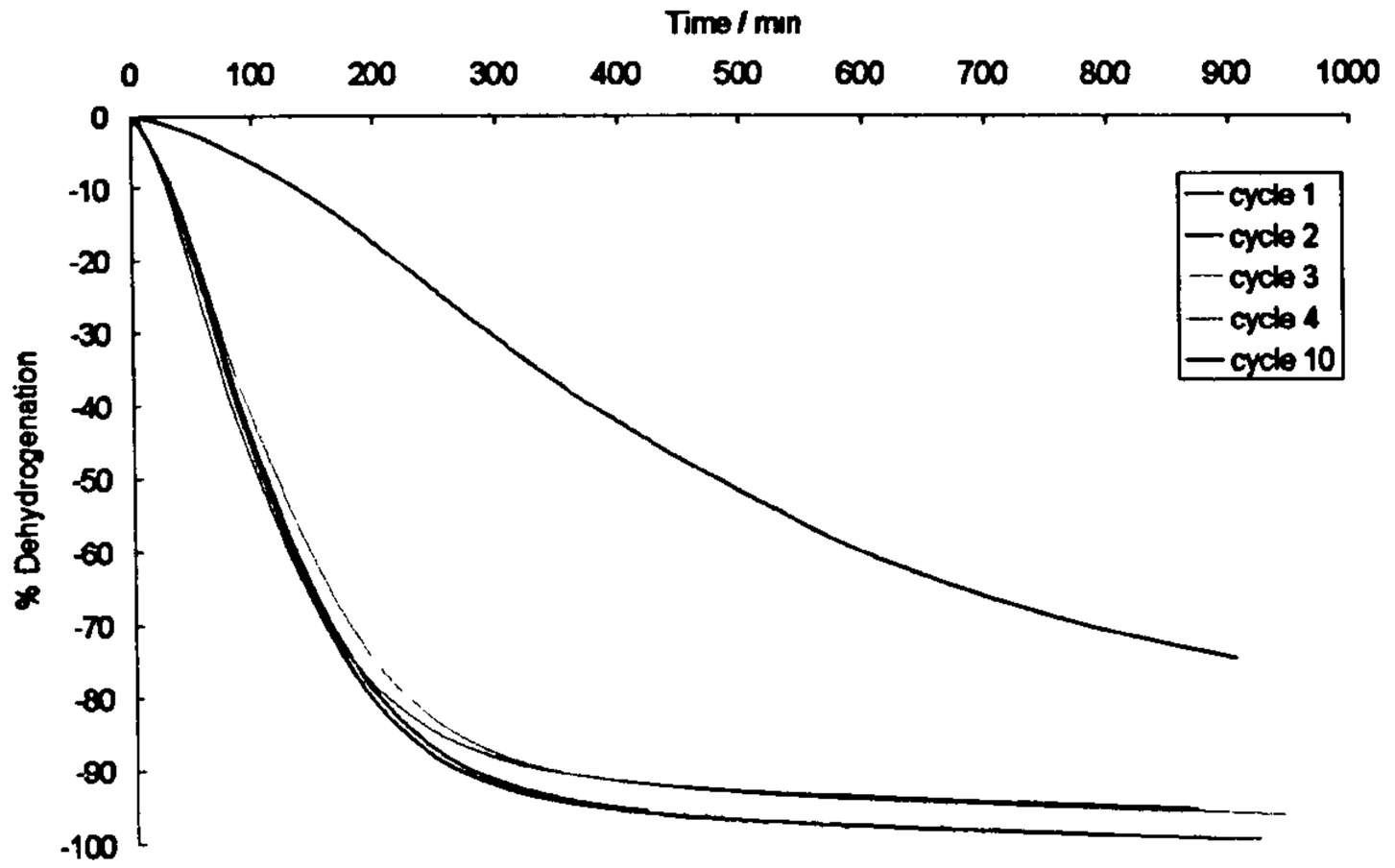

Figure 5.29: Cycling of milled MgH_2. Dehydrogenations at 350°C and 1 x 10^{-2} bar H_2.

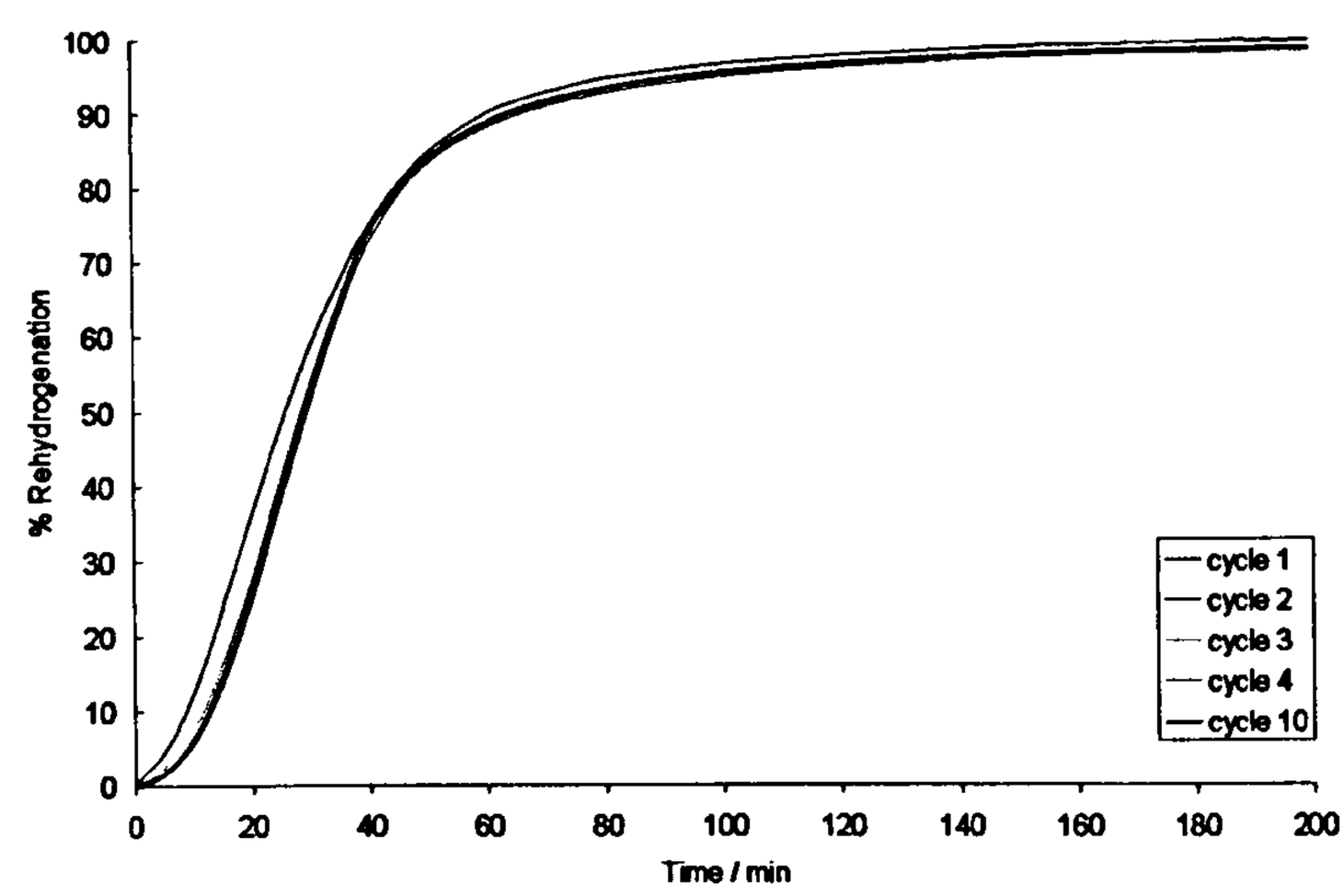

Figure 5.30: Cycling of milled MgH_2. Rehydrogenations at 350°C and 6 bar H_2.

The IGA cycling experiments carried out on the MgH_2 - Ti70 and MgH_2 - Ti5Pd samples indicated much faster kinetics for these materials. Figures 5.31 and 5.32 show the absorption and desorption cycles of MgH_2 - Ti70. For the desorption process, at 300°C and 1 x $10^{-2\ bar}$, the first desorption took 1 h for 65 % of the total H_2 to be desorbed.

Subsequent desorptions were found to be faster, with 90 - 98 % of total dehydrogenation occurring in 10 min. During the absorption cycles at 300°C and 6 bar, the rate of absorption of the first cycle was slower than for subsequent cycles, with only 50 % of the total absorbed in 20 min. On the second to fifth cycles, *ca.* 93 % of the total H_2 was absorbed by the sample in the same time period of 20 min.

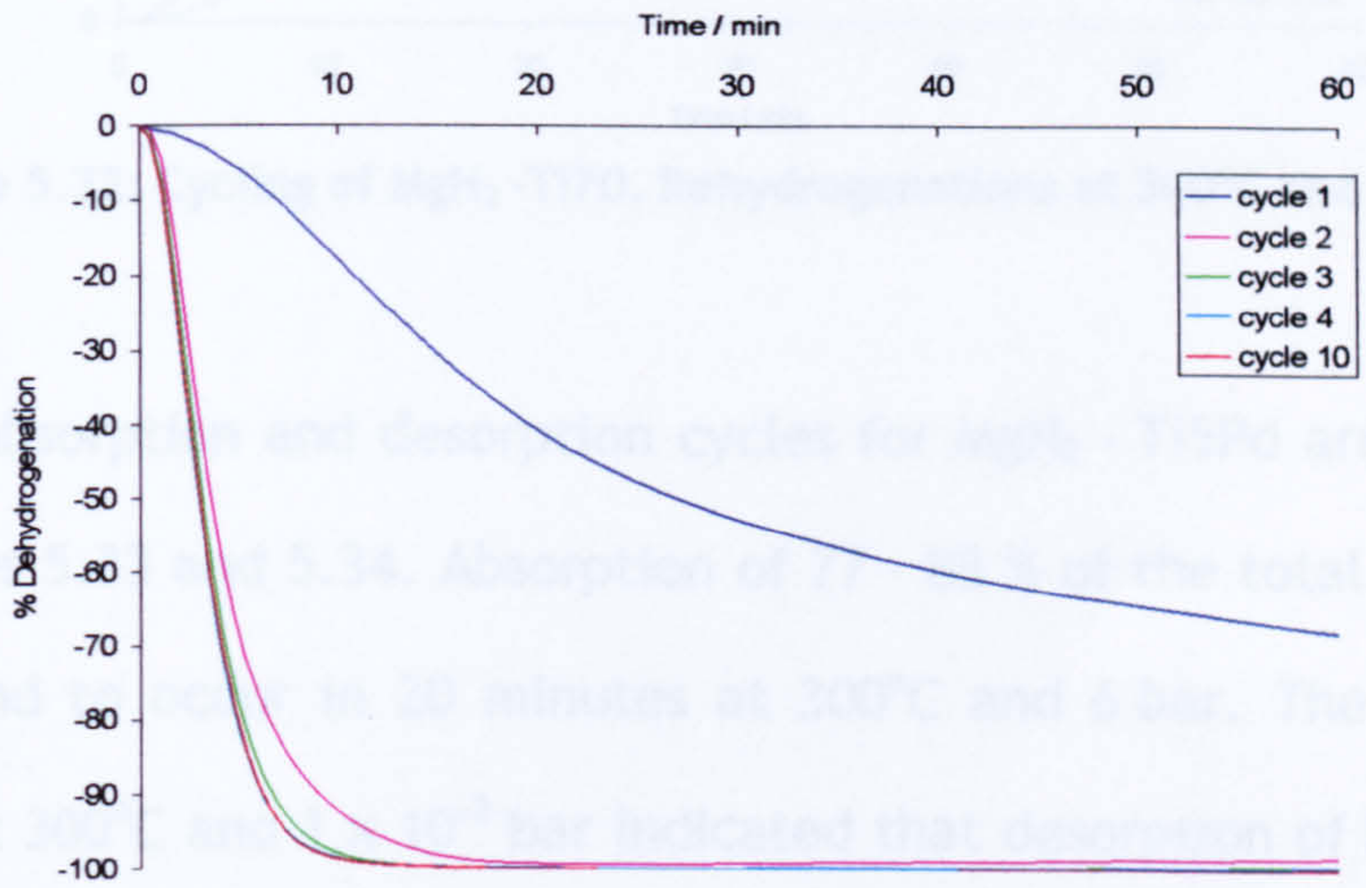

Figure 5.31: Cycling of MgH_2 - Ti70. Dehydrogenations at 300°C and 1 x 10^{-2} bar H_2.

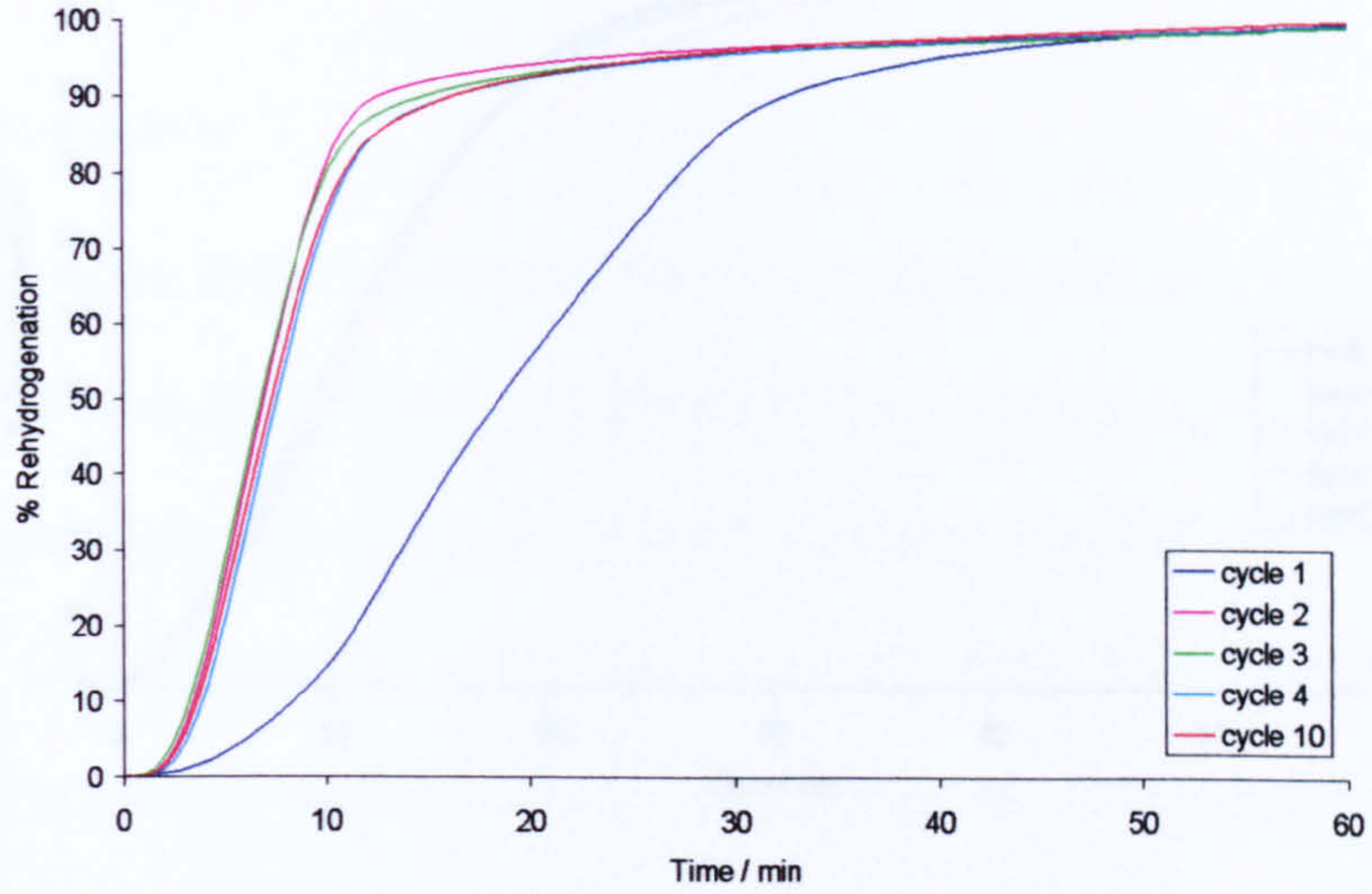

Figure 5.32: Cycling of MgH_2 -Ti70. Rehydrogenations at 300°C and 6 bar H_2.

The H_2 absorption and desorption cycles for MgH_2 - Ti5Pd are presented in Figures 5.33 and 5.34. Absorption of 77 - 83 % of the total H_2 capacity was found to occur in 20 minutes at 300°C and 6 bar. The desorption cycles at 300°C and 1 x 10^{-2} bar indicated that desorption of between 90 and 95 % of the total desorption occurred in 20 minutes.

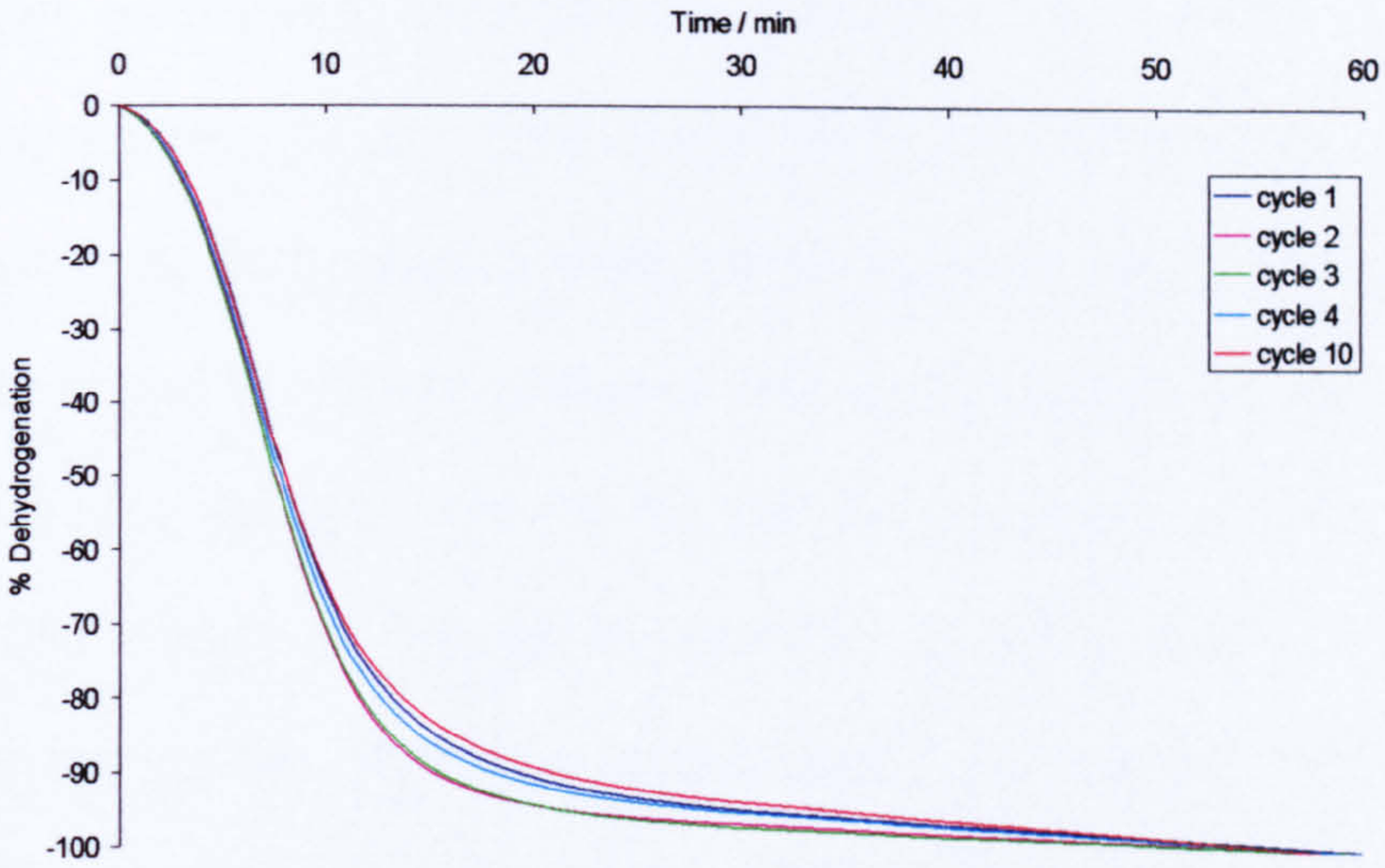

Figure 5.33: Cycling of MgH_2 - Ti5Pd. Dehydrogenations at 300°C and 1 x 10^{-2} bar H_2.

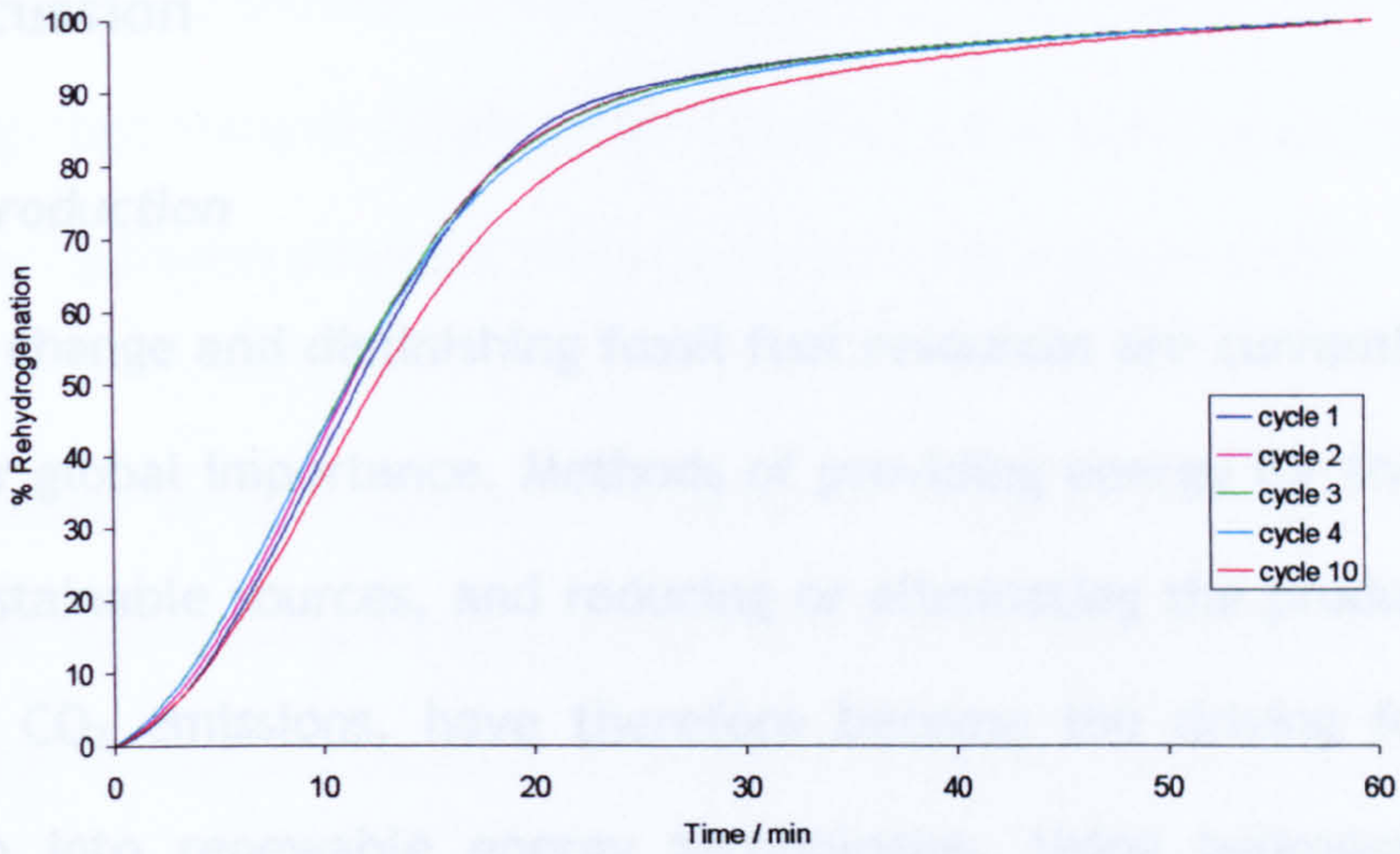

Figure 5.34: Cycling of MgH_2-Ti5Pd. Rehydrogenations at 300°C and 6 bar H_2.

6. Discussion

6.1. Introduction

Climate change and diminishing fossil fuel resources are currently issues of major global importance. Methods of providing energy for the future from sustainable sources, and reducing or eliminating the production of harmful CO_2 emissions, have therefore become the driving force for research into renewable energy technologies. Using hydrogen as an energy carrier is one method of meeting future energy demands that has resulted in widespread research into hydrogen production, hydrogen storage, and associated applications such as fuel cells.

In the field of hydrogen storage, storage in gaseous, liquid, and solid forms has been considered, with solid storage providing the highest volumetric energy density. A range of solid hydrogen storage materials have been extensively investigated, including high surface area and porous structures, binary light metal hydrides, interstitial and alloy metal hydrides, and complex light metal hydrides. As discussed in the introduction and literature review of this work, targets for the required properties of a storage material for specific applications exist, such as the US DOE target of 5-6 wt % capacity, at 100°C and 0.1 MPa, for vehicular application. Hydrogen storage materials studied to date do not meet this target, generally having lower capacities, or requiring elevated temperatures (> 300°C) to produce or release hydrogen. It should be noted that these targets are application specific, and higher

temperatures (350-1000°C) are acceptable for other applications, including stationary or large scale transport using solid oxide fuel cells (SOFC) or hydrogen powered internal combustion engines (ICE).

As discussed in the literature review in Chapter 2, MgH_2 offers a relatively high hydrogen storage capacity, but modifications are required to reduce the temperature of hydrogen desorption, and to increase the kinetics of absorption and desorption. MgH_2, with no modifications, slowly releases *ca.* 7 wt. % H_2 at T > 350°C and 1 bar H_2 pressure. Ball milling and the addition of a wide range of additives to enhance the hydrogen sorption properties of MgH_2 have been the subject of a great deal of recent research, due to the need to develop high-capacity hydrogen storage materials with fast absorption and desorption kinetics. Significant improvements in these properties have been reported, with ball milling resulting in a dehydrogenation onset temperature for MgH_2 as low as 342°C, 64°C lower than for unmilled MgH_2 [11,49]. Additives ranging from single metals [14,15], metal alloys and metal oxides [16,17], to graphite and other carbon structures [18-21] have all been mixed with MgH_2 through ball milling or reactive mechanical alloying. Nanoparticulate Ni additives have been observed to significantly reduce the dehydrogenation onset temperature of MgH_2, to ca. 150°C and the activation energy of the dehydrogenation from 323 to 94 kJ mol^{-1} [14]. Of the oxide additives studied to date, the most promising results have been reported for Nb_2O_5, which displayed desorption rates of 6 wt. % H_2

desorbed in 500 s at 250°C under vacuum conditions for a sample of MgH_2 - 0.5 mol. % Nb_2O_5 [78].

While the results reported in the literature for ball milling and additives to MgH_2 such as nanoparticulate Ni and Nb_2O_5 are promising, the resulting materials do not show the desired properties for certain hydrogen storage applications, nor are the mechanisms responsible for their behaviour fully understood. Neither mixed oxides, nor the effect of oxide preparation have previously been reported. The aims of the work carried out for this thesis were to study novel materials based on MgH_2 with additions of binary and ternary oxides that have not previously been studied, as well as to contribute further to the understanding of the mechanisms at work in the effect of these additions on the hydrogen sorption behaviour of MgH_2.

In Chapter 4, results of characterisation using techniques including XRD, DSC-TGA-MS, N_2 Physisorption, DRIFTS, SEM, and XPS provided information on the bulk and surface properties of the single, mixed and TiO_2 - Pd oxides. In this chapter, the results from Chapters 4 and 5 are examined, with the key trends in the properties of the different oxide materials and their effect on the hydrogen storage properties of MgH_2 summarised and discussed. A summary of the key trends in oxide structure and properties is given in Section 6.2, with discussion of the effects of oxide species present, heat treatment, and Pd additions, on the structure and properties of the different oxides. Section 6.3 contains

a discussion of the effect of ball milling and oxide additions on the particle size, structure, and hydrogen sorption behaviour of MgH_2, summarising and discussing the results of Chapter 5, with focus on the most effective additives and the mechanisms involved in their behaviour.

6.2. Properties of single, mixed and Pd-modified metal oxides

6.2.1. Effect of heat treatment temperature on single Al, Si, Ti and Zr metal oxides

The different heat treatments at temperatures of 70°C, 120°C, 400°C, and 800°C used in preparing the single oxide samples resulted in a range of materials with varying bulk structure, particle size and surface area. Calcining the oxides induced bulk structure transformations in the Al, Ti, and Zr oxide samples, as observed in the XRD patterns for these oxides (Figures 4.1 - 4.4). The Al70 sample, as dried at 70°C, had a boehmite structure, which transformed to a γ-alumina structure during heat treatment to 800°C. The transformations at these temperatures were expected, in agreement with previous studies of the behaviour of sol-gel alumina [100]. Both the TiO_2 and ZrO_2 samples were amorphous after heating at 70°C and 120°C. Heating to 400°C and 800°C resulted in transformation to crystalline phases, anatase and rutile TiO_2, and monoclinic and tetragonal ZrO_2. As expected, the SiO_2 samples did not show any evidence of crystalline phases present in the XRD patterns, regardless of calcination temperature. Amorphous SiO_2 is known not to crystallise until >2000°C [101].

From the TGA-MS and DRIFTS data presented in Sections 4.2.3 and 4.2.4, it was observed that the changes in bulk crystal structure for the Al, Ti and Zr oxide samples were accompanied by loss of water from the samples. For the alumina samples, a loss of 5 wt. % water below 120°C was attributed to physisorbed water on the sample surface, as the boehmite structure persisted in the Al70 and Al120 samples. The water loss of 18 wt. % between 120 and 500°C can be associated with the loss of water due to the transformation from boehmite (AlOOH) to γ-alumina (Al_2O_3) which was observed to be present from the XRD patterns of Al400 and Al800. These water losses coincided with the reduction in intensity of the OH groups observed in the DRIFTS traces of the alumina samples as calcination temperature was increased.

Water loss from the Ti70 and Zr70 samples during heating was found to be very similar, with a total weight loss of 23 wt. % and 18 wt. %, respectively. This weight loss was associated with H_2O desorbing from the surface of the oxides at temperatures below 350°C, coinciding with the transformation from amorphous to crystalline structure. From the DRIFTS traces, no IR absorbance in the OH regions were detected for the Ti800 or Zr800 samples, confirming that water and OH groups were removed from these samples, however, low intensity peaks at 3355 cm^{-1} in the trace for Ti400 and at 3357 cm^{-1} for Zr400 suggest that some OH groups were still present in these samples.

The SiO_2 samples remained amorphous regardless of heat treatment temperature, however, water loss corresponding to a weight loss of 11 wt. % was observed in the TGA-MS trace during heating of Si70, which was not associated with any bulk crystal structure transformations. The DRIFTS patterns for the SiO_2 samples (Figure 4.18) also indicated the presence of water and OH groups in all samples, with diminishing intensity as calcination temperature was increased.

The N_2 physisorption measurements of surface area for the single oxides presented in Table 4.1 suggested a relationship between surface area and the calcination temperature of the sample, which corresponded to the changes in crystal structure observed in XRD. The surface area changes with calcination temperature for the alumina and silica samples were quite small for calcination temperatures up to 400°C, with more significant decreases in surface area observed after the 800°C calcinations. These results are in agreement with studies of Nguefack *et al.*, who reported constant surface area of 300 $m^2 g^{-1}$ despite loss of water for alumina treated to 400°C, followed by a linear decrease in surface area for higher temperature heat treatments, following the transformation to transitional aluminas, to 45 $m^2 g^{-1}$ after heating to 1100°C [102]. From the XRD patterns of these samples (Figure 4.1), it was observed that the alumina samples remained nano-crystalline with broad diffraction peaks at all calcination temperatures indicating the presence of very small crystallites, while the SiO_2 samples (Figure 4.2) remained amorphous at all calcination temperatures. Some anomalous

behaviour of increasing surface area with increasing calcination temperature was observed, particularly with the Si70, Si120, and Si400 samples. Such behaviour has previously been attributed to the effect of porosity and pore-fluid surface tension [103]. In this case, water is likely to remain present in pores after low temperature heat treatment, causing a lower surface area which increases after water has been removed from pores after higher temperature heat treatments.

The surface areas of the TiO_2 and ZrO_2 samples both decreased with increasing calcination temperature, with large decreases in surface area coinciding with the transition from amorphous to crystalline structure between 120°C and 400°C. For TiO_2, the surface area decreased from 390 $m^2 g^{-1}$ for Ti120 to 135 $m^2 g^{-1}$ for Ti400, while the decrease in surface area for Zr120 to Zr400 was from 165 $m^2 g^{-1}$ to 40 $m^2 g^{-1}$. Further decreases in surface area of the TiO_2 and ZrO_2 samples are associated with the transformations in crystal structure and sintering that occurred during calcination at 800°C.

6.2.2. Effect of heat treatment temperature on mixed Al-Si, Ti-Al, and Ti-Si oxides

The changes in crystal structure induced by heat treatment of the mixed oxide samples were similar to those for the single oxides discussed in Section 6.2.1, with the XRD patterns showing diffractions due to the individual oxide phases present in the samples.

For samples with an Al component, the transformation from boehmite to γ-alumina occurred between 120°C and 400°C, as in the case of the single oxide samples. However, for the samples containing TiO_2, the temperature at which the crystal structure transformation of the TiO_2 phase occurred was affected by the ratio and species of oxide present in the samples. The presence of a second oxide species, either alumina or silica, appeared to suppress the transformation from anatase to rutile TiO_2. The principal diffraction lines present in the XRD pattern of the Ti800 sample were from the rutile phase of TiO_2, while for the mixed oxides 50Ti50Al800, 10Ti90Al800, 90Ti10Si800, 50Ti50Si800 and 10Ti90Si800, anatase was found to be the more abundant phase. The effect of additives on the anatase-rutile phase transformation has been previously documented [104-108], with both alumina and silica reported to act as strong structural promoters for anatase. The transformation from anatase to rutile is generally thought to occur via two Ti-O bonds breaking in the anatase structure, rearranging the Ti-O octahedra from the corner-sharing anatase structure to edge-sharing rutile. The effect of dopants or impurities on the transformation is not fully understood, but dopants are thought to affect the presence of Ti interstitials and oxygen vacancies within the lattice [109,110].

The TGA-MS water loss data from the mixed oxides generally showed a combination of water loss peaks corresponding to water evolved from the different oxide species present. For example, the 90Al10Si70 sample showed four peaks in the MS H_2O trace, corresponding to the similar

water loss peaks found for the Al70 sample, with an extra peak at 230°C, in the same temperature region as observed for the Si70 sample. The DRIFTS patterns for the mixed oxide samples all showed a corresponding decrease in the intensity of the peaks due to OH species as calcination temperature of the samples was increased.

In the Al/Si - O fingerprint region of the DRIFTS traces for the Al - Si mixed oxides (<1200 cm^{-1}), the band for Si-O-Si bonding found at ~1092 cm^{-1} is observed to shift to lower wavenumber with increasing Al content, indicating substitution of Si with Al, and the presence of bonding between Si-O-Al species in the mixed oxides [94]. This substitution results in a charge imbalance and the introduction of site defects. The extra negative charge introduced by trivalent aluminium is compensated by a proton, resulting in a Brønsted acid site. Lewis acid, or electron deficient, sites arise where trigonally coordinated Al and Si sites are formed by removing hydroxyl groups during heating.

The N_2 physisorption surface area measurements of the Al-Si mixed oxides presented in Table 4.1 indicated very little difference in surface area of the 90Al10Si and 50Al50Si samples with increasing calcination temperature, while the 10Al90Si samples showed a distinct decrease in surface area as calcination temperature increased from 270 $m^2 g^{-1}$ for 10Al90Si70 to 60 $m^2 g^{-1}$ for 10Al90Si800. The Ti - Al and Ti - Si samples all showed a decrease in surface area with increasing calcination temperature coinciding with increasing crystallinity of the samples

indicated by the XRD patterns. These trends in surface area were very similar to those observed for the single metal oxides described earlier, and can be attributed to similar effects of loss of water from the samples, crystal structure transformations, and sintering. The surface areas of the alumina and silica rich mixtures with TiO_2 after heat treatment at 800°C were generally found to be higher than that for the single metal oxide TiO_2, providing further evidence for the Al_2O_3 and SiO_2 present in the samples acting to promote the anatase TiO_2 structure and suppress sintering and the transformation to rutile.

6.2.3. Structure of TiO_2 - Pd samples

From the XRD and XPS results (Sections 4.3.1 and 4.3.2), it was observed that the TiO_2 - 1Pd and TiO_2 - 5Pd samples both showed a similar evolution in structure during the preparation and heat treatment processes, resulting in samples of small particles (10 - 15 nm) of metallic Pd on a primarily anatase TiO_2 phase. Although the Pd particles were not definitely resolved in TEM images, their presence was confirmed by EDX analysis.

6.3. Effect of ball milling and oxide additives on hydrogen sorption behaviour of MgH_2

6.3.1. Background

In discussing the hydrogen sorption properties of MgH_2, a distinction must be made between the thermodynamic and kinetic behaviour. MgH_2 is

relatively thermodynamically stable and the equilibrium absorption and desorption of hydrogen at 1 bar H_2 will only occur spontaneously at temperatures above 279°C. Addition of certain metals can affect the thermodynamic stability of MgH_2, through direct alloying resulting in the formation of a less stable alloy hydride, such as Mg_2NiH_4, which will have a lower equilibrium desorption temperature (50 - 60°C lower than MgH_2), but also a significantly lower hydrogen capacity (3.16 wt. %) [111]. Rather than destabilising the hydride, the majority of metal oxide and other additives to MgH_2 have been found to enhance the kinetics of the absorption and desorption of hydrogen, through altering the mechanisms of hydrogen absorption and desorption, and therefore lowering the associated activation energies. This results in faster rates of hydrogen absorption and desorption.

Hydrogen desorption is generally measured by one of two methods. The first is thermal desorption, covering methods in which a sample is heated at a specified temperature ramp rate in an atmosphere of flowing inert gas (He or Ar). The DSC-TGA-MS studies carried out for this thesis employ a thermal desorption method. From this method, a hydrogen desorption onset temperature is generally reported. This is not a thermodynamic equilibrium desorption temperature, as the hydrogen evolved from the sample is immediately removed by the flowing inert gas, driving hydrogen from the sample at lower than the equilibrium temperature for 1 bar H_2 pressure. Some of the lowest hydrogen desorption onset temperatures reported to date were in the region of 150 - 200°C for

MgH_2 ball milled with nanoparticulate Ni [14]. The Ni is proposed to act as a catalyst, decreasing the activation energy for hydrogen desorption, and thereby improving the kinetics of hydrogen desorption from the MgH_2. Ni is also known to form an alloy with Mg, resulting in Mg_2NiH_4, a less thermodynamically stable hydride that decomposes at a lower temperature of 255°C and has a capacity of 3.16 wt. %. Instead of a catalytic effect, some alloy formation may be responsible for the faster hydrogen desorption from MgH_2 ball milled with nanoparticulate Ni.

The second method of measuring hydrogen sorption behaviour of metal hydrides is the use of gravimetric or volumetric systems. The IGA and Sieverts experiments carried out for this work are examples of gravimetric and volumetric systems, respectively. These are generally operated under static rather than flowing gas conditions, in which the hydrogen is absorbed or desorbed under equilibrium conditions at a set temperature and pressure. Results obtained from gravimetric or volumetric methods generally include rates of absorption and desorption of hydrogen. Thermodynamic data including enthalpies and entropies of reaction can also be calculated using these methods. Un-modified MgH_2 requires extended periods of time to desorb hydrogen (>15 h at 350°C and 1 bar H_2 for *ca.* 4 wt. % desorption). To date, reports in the literature on ball milling and additives have shown that 6 wt. % H_2 can be desorbed in as little as 500 s at 250°C under vacuum conditions for a sample of MgH_2 - 0.5 mol. % Nb_2O_5 [78].

6.3.2. Ball milling of MgH_2

Ball milling as a method of reducing particle size, introducing defects, and forming a metastable phase of MgH_2 has been widely reported as an effective way of lowering the dehydrogenation onset temperature and enhancing the kinetics of absorption and desorption of hydrogen from MgH_2 [11,13,49,51,64,80,112,113]. The results presented in Section 5.2 indicated that ball milling for 20 h reduced the average crystallite size of MgH_2 from 1500 Å to 70 Å, corresponding with an increase in BET surface area from 2 to 11 $m^2 g^{-1}$. SEM images of the MgH_2 powder after ball milling (fig 5.2) indicated that these small crystallites formed clusters of *ca.* 5 - 50 μm in diameter. XRD provided evidence of the formation of a small proportion of the metastable γ-MgH_2 phase with an abundance of *ca.* 11 vol. %. The dehydrogenation onset temperature of the milled MgH_2 sample determined from TGA-MS experiments was 360°C, which was 30°C lower than for the as received MgH_2.

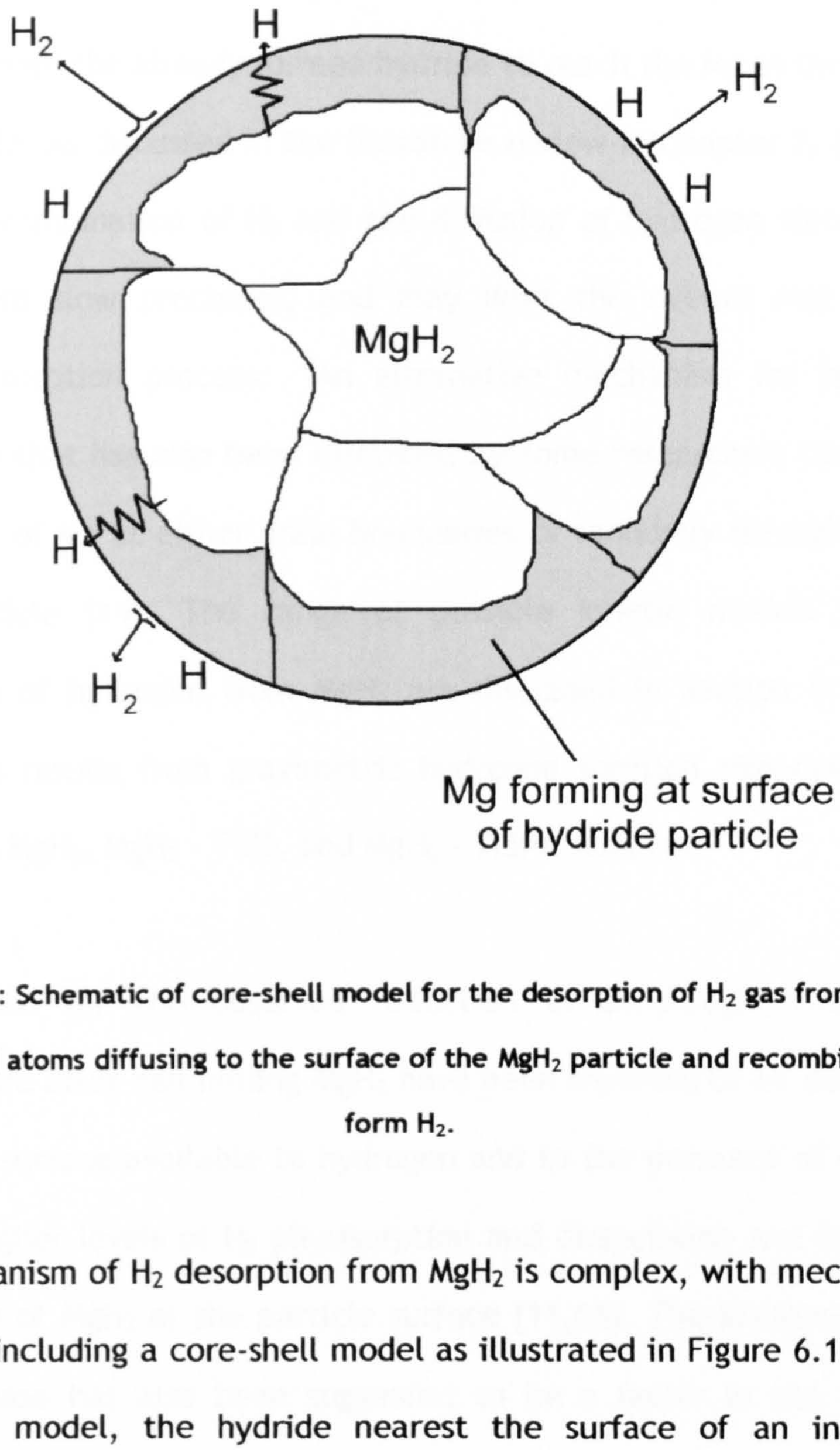

Figure 6.1: Schematic of core-shell model for the desorption of H_2 gas from MgH_2, showing H atoms diffusing to the surface of the MgH_2 particle and recombining to form H_2.

The mechanism of H_2 desorption from MgH_2 is complex, with mechanisms proposed including a core-shell model as illustrated in Figure 6.1. In this core-shell model, the hydride nearest the surface of an individual hydride particle is converted first, as hydrogen atoms diffuse to the surface and recombines to form H_2. The hydrogen diffusion pathway increases in length as further hydrogen from closer to the core is lost, resulting in an increase in the thickness of the Mg layer at the surface of the particle [64,114]. For absorption of H_2, the reverse process occurs, whereby the H-H bond is broken at the surface of the Mg. MgH_2 then

forms at the surface of the particle first, followed by diffusion of H atoms through the already formed hydride to reach the Mg at the core of the particle. As discussed in the literature review in Chapter 2, both the surface recombination of H_2 and the diffusion of hydrogen through the particle are slow processes, and may limit the overall rate of the hydrogen sorption process. An alternative mechanism for hydrogen desorption that has also been discussed by some researchers consists of nucleation of Mg at either grain boundaries or randomly throughout the MgH_2 particle [14]. The range of possible kinetic models for the desorption of hydrogen from MgH_2 are discussed in Section 6.3.4 and applied to results from gravimetric hydrogen sorption experiments on the milled MgH_2, MgH_2 - Ti70, and MgH_2 - Ti5Pd samples.

The reasons for the observed reduction in dehydrogenation onset temperature after ball milling MgH_2 have been reported to be due to the increased surface available to hydrogen and to the presence of defects, causing higher levels of H_2 physisorption and dissociation and enhanced nucleation of MgH_2 at the particle surface [11,64]. The presence of the γ-MgH_2 phase has also been suggested to be a factor in the reduced dehydrogenation onset temperature [49,51].

To investigate the latter, *in situ* XRD (Section 5.6.4) was used in this investigation to study the dehydrogenation of MgH_2 during heating. It was observed that the metastable γ-phase of MgH_2 did not decompose at a lower temperature than the β-MgH_2, as has been previously suggested

[49,51]. Both phases remained present during heating up to 400°C, at which point the MgH_2 was fully converted to Mg. The peaks from γ-MgH_2 only diminished in intensity at the same temperature as the β-MgH_2. In addition, the γ-phase was no longer observed to be present after subsequent cycling of the material, although the dehydrogenation onset temperature remained 30°C lower than for unmilled MgH_2. These results indicate that the γ-MgH_2 does not play a significant role in the reduced desorption onset temperature of ball milled MgH_2.

From the increased surface area values, SEM showing reduced particle size, and XRD showing broad lines indicative of reduced crystallinity and smaller crystallite size, it was concluded that the increased surface area and defects and vacancies caused by ball milling, and not the presence of γ-MgH_2, were the most significant factors in causing the reduced dehydrogenation onset temperature of the MgH_2.

From the DSC - TGA - MS experiments presented in Section 5.2.4, the H_2 capacities obtained after ball milling were observed to be 0.8 - 1 wt. % lower than for the unmilled MgH_2, dropping from 7.1 wt. % before ball milling to *ca.* 6.2 wt. % after milling. This reduced capacity is in part due to oxidation of the MgH_2 occurring during ball milling, as shown by the presence of very weak MgO peaks in the XRD of ball milled samples. Friedrichs *et al.* have previously reported a passivating MgO layer found on ball milled Mg and MgH_2 even after handling in an inert atmosphere [115]. Ball temperatures of over 200°C have been reported to arise in

planetary style ball mills such as the Fritsch P5 used in this study, with local temperatures possibly reaching >600°C [48]. These temperatures are significantly higher than the temperature required for dehydrogenation, and could also result in some loss of hydrogen from the sample, lowering the measured dehydrogenation. The presence of MgO observed in the XRD patterns, along with results from the cycling experiments presented in Section 5.9, provide support for the formation of MgO causing the reduction in H_2 capacity of the sample, rather than dehydrogenation during milling. If H_2 had been lost during milling, the full capacity would return upon subsequent rehydrogenation cycles. This was not observed to be the case, with H_2 capacity remaining the same upon cycling.

6.3.3. Effect of oxide additives on dehydrogenation of MgH_2

Oxide additions to MgH_2 have previously been reported to reduce the dehydrogenation temperature and increase the kinetics of hydrogen desorption and absorption [16,17,77,79]. As discussed in detail in the literature review in Chapter 2, this enhancement in hydrogen absorption and desorption properties has been attributed to a number of factors, including the variable oxidation state of the oxide additive, and the "pathway effect" of the oxide providing a route for hydrogen diffusion [79], but the mechanisms by which different oxide additives act is not yet fully understood.

The results of the TGA-MS studies on the dehydrogenation of the milled MgH_2 - oxide mixtures presented in Sections 5.3 - 5.5 suggested a number of trends in the behaviour of the different samples. To summarise the effects of the different oxide species on hydrogen desorption from the samples, the chart in Figure 6.2 indicates the dehydrogenation onset temperature and the oxide surface area (prior to ball milling) for each sample.

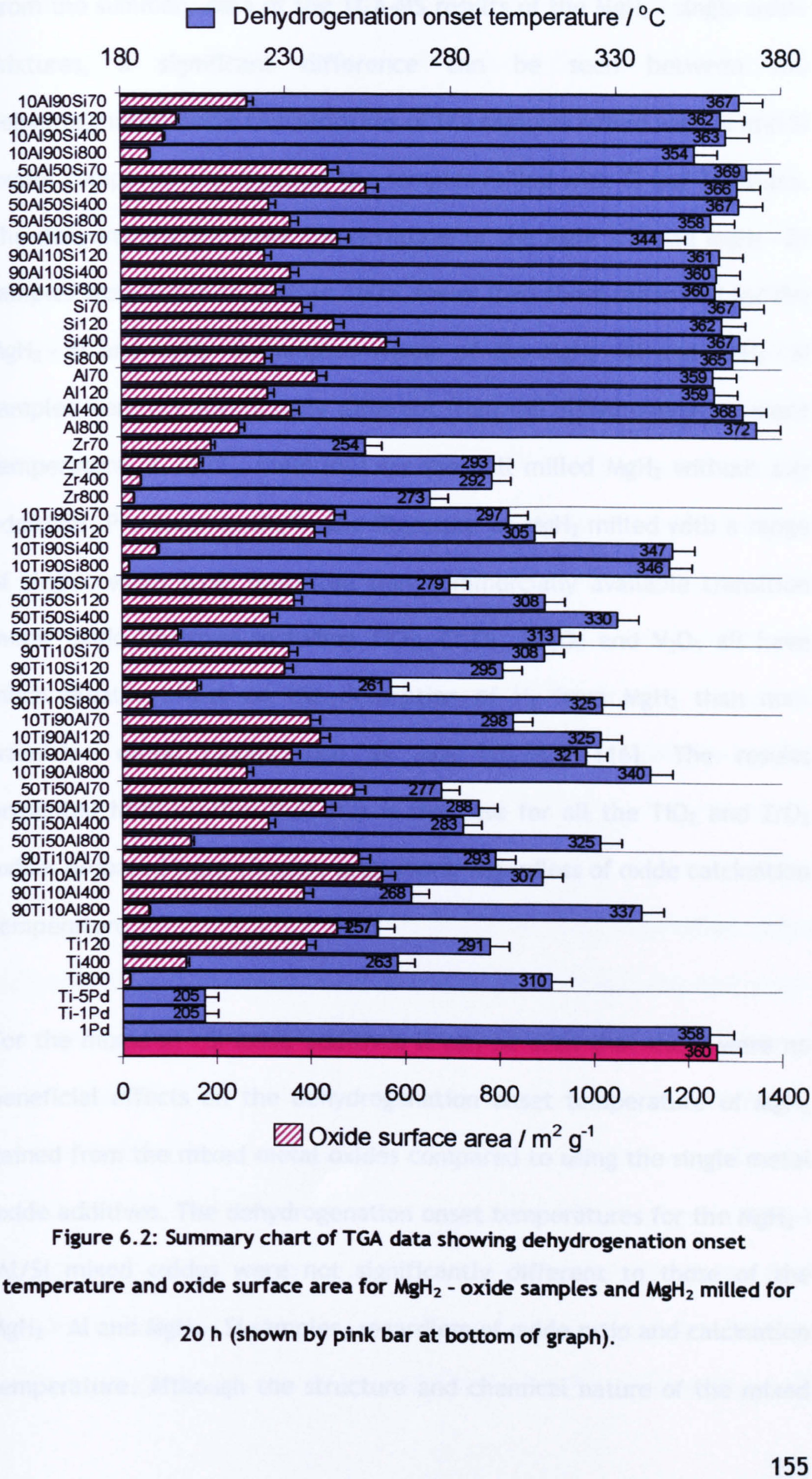

Figure 6.2: Summary chart of TGA data showing dehydrogenation onset temperature and oxide surface area for MgH_2 - oxide samples and MgH_2 milled for 20 h (shown by pink bar at bottom of graph).

From the summary data of the TGA-MS results of the MgH_2 - single oxide mixtures, a significant difference can be seen between the dehydrogenation onset temperatures of the samples milled with Al and Si oxides compared with those of the samples milled with Ti and Zr oxides. The dehydrogenation onset temperatures of the MgH_2 - Ti and MgH_2 - Zr samples were between 50°C to 100°C lower than those measured for the MgH_2 - Al and MgH_2 - Si samples. Those of the MgH_2 - Al and MgH_2 - Si samples were not significantly different from the dehydrogenation onset temperature of 360°C, measured for the ball milled MgH_2 without any additives. Previous reports in the literature on MgH_2 milled with a range of single oxides have suggested that commercially available transition metal oxide additives including TiO_2, Cr_2O_3, Nb_2O_5 and V_2O_5 all have much greater effect on the desorption of H_2 from MgH_2 than non-transition metal oxides such as SiO_2 [16,78,81,116]. The results presented here confirm that this is the case for all the TiO_2 and ZrO_2 oxides prepared from alkoxide precursors, regardless of oxide calcination temperature.

For the mixed Al - Si oxide additives it can be seen that there were no beneficial effects on the dehydrogenation onset temperature of MgH_2 gained from the mixed metal oxides compared to using the single metal oxide additives. The dehydrogenation onset temperatures for the MgH_2 - Al/Si mixed oxides were not significantly different to those of the MgH_2 - Al and MgH_2 - Si samples, regardless of oxide ratio and calcination temperature. Although the structure and chemical nature of the mixed

Al - Si oxides was different to that of the component binary oxides, with the formation of Al-O-Si bonding as discussed in Section 6.2.2, this did not have any beneficial effect on the dehydrogenation of MgH_2.

The TGA-MS results of dehydrogenation of the MgH_2 - Ti/Al and MgH_2 - Ti/Si mixed oxides indicate that the mixed oxides do not provide a synergistic effect on the dehydrogenation behaviour of MgH_2 when compared with the results of dehydrogenation of the MgH_2 - Ti single oxide samples. The dehydrogenation onset temperatures of the MgH_2 - Ti/Al and MgH_2 - Ti/Si samples were generally found to be higher than those of the MgH_2 - Ti samples and in general increased with decreasing Ti/Al and Ti/Si oxide ratio. These results indicate a dilution of the effect of the active species, directly related to the amount of TiO_2 present, with no synergistic effect from the addition of a second oxide component.

For a given system where a positive effect on dehydrogenation onset temperature was apparent, such as the MgH_2 - Ti mixtures, the oxide calcination temperature did have an effect on the onset temperature of dehydrogenation. The trend was not a simple linear relationship between oxide calcination temperature and T_{onset}. These effects have not been previously reported in prior literature. The lowest dehydrogenation onset temperature in this system was 257°C, observed for the MgH_2 - Ti70 sample. An increase in T_{onset} to 291°C was then observed for the TiO_2 calcined at 120°C. For the oxide calcined at 400°C, a lower T_{onset} of

263°C was observed. TiO_2 calcined at 800°C resulted in a higher dehydrogenation onset temperature of 310°C. A similar trend is apparent for the majority of the mixed oxide samples containing a TiO_2 component. A few exceptions exist, particularly in the TiO_2 - SiO_2 systems, where the samples containing mixed oxides richer in SiO_2 (50Ti50Si and 10Ti90Si), tend to display an increase in T_{onset} up to the 400°C oxide calcination, followed by a levelling off or small decrease for the oxides calcined at 800°C.

At 70°C and 120°C, the XRD of the TiO_2 samples indicated an amorphous structure, while crystalline anatase and rutile were the abundant phases for the TiO_2 calcined at 400°C and 800°C, respectively. While all of the different TiO_2 structures have a positive effect on reducing T_{onset} of the MgH_2, the amorphous structure of the oxide dried at 70°C generally appears to have the greatest effect. This can be attributed to the higher surface area and surface water generally present on the lower temperature oxides, discussed below. There is also a clear trend suggesting that for the crystalline samples, the anatase crystal structure is most effective at lowering T_{onset}. For 100Ti, 90Ti10Al, 50Ti50Al, and 10Ti90Al, the oxides calcined at 400°C all predominantly have an anatase crystal structure, and in all cases exhibit the lowest T_{onset} excluding the oxides dried at 70°C. In the case of the Ti - Si oxides, the SiO_2 was observed to be more effective than the Al_2O_3 at suppressing the structural transformation of the TiO_2. This results in anatase not being formed until calcination at 800°C. It would appear that it is the anatase

TiO_2 present in MgH_2 - 50Ti50Si800 and MgH_2 - 10Ti90Si800 which causes these two samples to have lower T_{onset} than MgH_2 - 50Ti50Si400 and MgH_2 - 10Ti90Si400, which did not appear to contain anatase TiO_2.

Another significant difference between the oxides calcined at different temperatures is in their surface areas, as indicated in the summary chart in Figure 6.2. Oxides with lower surface area and thus larger particle size will inherently be less well dispersed within the MgH_2 - oxide mixture, and therefore provide fewer active sites for enhancing hydrogen desorption. With the exception of a few samples, namely MgH_2 - Ti400 and MgH_2 - 90Ti10Si400, there is a general trend of increasing dehydrogenation onset temperature with decreasing oxide surface area, confirming that a higher surface area and smaller particle size is desirable for an active added species, to be most effective in lowering the dehydrogenation onset temperature of MgH_2. The exceptions mentioned indicate samples where the presence of the more active anatase component outweighs the effect of the lower surface area.

The presence of physisorbed water and OH groups on the surface of the oxides may be another factor affecting dehydrogenation from MgH_2 - oxide mixtures. From the TGA-MS studies of the oxides dried at 70°C (Section 4.2.3) loss of water from the samples was observed as temperature increased. The DRIFTS studies of the oxides (Section 4.2.4) also showed the reduction in surface OH groups as calcination

temperature of the oxides was increased, with the majority of oxides showing no peaks from water or OH groups after calcination at 400°C and 800°C. Water reacts readily with MgH_2 via the spontaneous reaction:

$$MgH_{2(s)} + 2H_2O_{(l)} \rightarrow Mg(OH)_{2(s)} + 2H_{2(g)} \qquad \Delta H = -277 \text{ kJ mol}^{-1} \quad [117]$$

This reaction, occurring during the ball milling process, would result in a loss of hydrogen from the original MgH_2 starting material, and therefore a reduced H_2 capacity. For MgH_2 - Ti70, the oxide on its own was found to lose *ca.* 22 wt. % of water during heating to 500°C. Assuming the reaction followed that shown above, the reaction of this evolved water with the MgH_2 would result in a decrease in expected H_2 capacity by *ca.* 0.2 wt. %. Total weight loss would be expected to be higher from samples milled with oxides calcined at higher temperatures, due to the removal of water from the surface of the oxide during calcination. This was generally found to be the case, with MgH_2 - Ti400 and MgH_2 - Ti800 exhibiting H_2 weight losses of 5.6 and 5.7 wt. %, while MgH_2 - Ti70 and MgH_2 - Ti120 had lower capacities of 5.4 and 5.3 wt. % respectively. This is very close to the predicted reduction in capacity due to reaction with water from the oxides. XRD of the oxides did not show the presence of $Mg(OH)_2$, however, if a thin surface layer had formed on the surface of MgH_2 particles, it would have insignificant volume fraction to result in detectable diffraction lines.

Therefore, there are three main factors contributing to the effect that the different oxide calcination temperatures have on the dehydrogenation onset temperature of the milled samples. The first is bulk oxide crystal structure, the second is oxide surface area, and the third is the presence of surface water and OH groups. It appears to be a combination of these factors which results in the trend in dehydrogenation onset temperatures for samples containing a TiO_2 component.

The surface area and dispersion of the transition metal oxide species, such as Cr_2O_3, have been shown to have a considerable effect on its ability to enhance the dehydrogenation of MgH_2 [81]. For low oxide concentrations (0.4 - 17 wt. %) of Nb_2O_5, increasing oxide concentration has been found to enhance hydrogen desorption rates from MgH_2, however, the effect of adding concentrations > 20 wt. % has not been previously reported for any oxide. The effect of TiO_2 concentration on the dehydrogenation onset temperature of MgH_2 is shown in Figure 6.3. As TiO_2 concentration was increased, the dehydrogenation onset temperature initially decreased up to 20 wt. % Ti70 addition, and appeared to level off with the further increase in TiO_2 concentration to 50 wt. % Ti70, which was accompanied by a broadening of the desorption peak. An oxide concentration between 20 and 50 wt. % resulted in a maximum effect on the dehydrogenation onset temperature of MgH_2. Further oxide addition is likely to have resulted in agglomeration of the

TiO_2 during ball milling, reducing the overall number of available active species and hindering any further beneficial effect of the oxide.

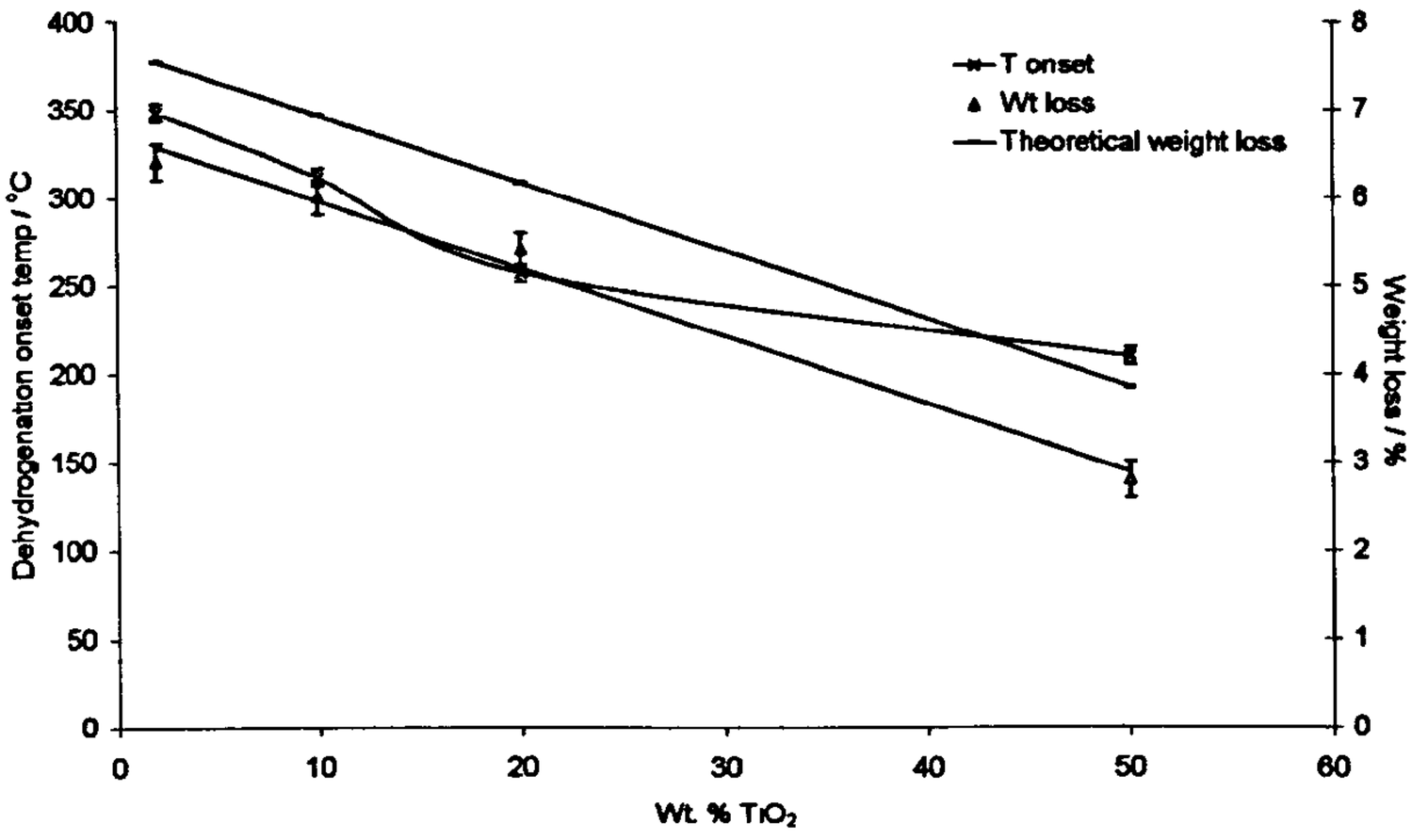

Figure 6.3: Dehydrogenation onset temperature and weight loss against amount of TiO_2 added to MgH_2. Theoretical weight loss based on MgH_2 capacity of 7.6 wt. %.

The TGA-MS results of the dehydrogenation of MgH_2 - Ti1Pd and MgH_2 - Ti5Pd show the positive effects of dispersing Pd onto TiO_2 prior to milling with MgH_2. Dehydrogenation onset temperatures of 205°C, 50-100°C lower than for the MgH_2 - Ti samples, were observed, regardless of Pd loading. The dehydrogenation onset temperature of MgH_2 - Ti5Pd was *ca.* 150°C lower than for a sample of MgH_2 milled with the same weight % of metallic Pd. Pd is known to act as a catalyst for the dissociation and surface recombination of H_2, as reported by Zaluska *et al.*[63,64]. The dispersion of Pd onto the surface of TiO_2 prior to ball milling with MgH_2 studied in this work appeared to enhance the effect of the Pd. The reason for this improved behaviour is due to the smaller particle size of

the Pd achieved by the wet impregnation method, when compared with milling with metallic Pd of a larger particle size (<40 μm). From XRD, the crystallite size of the Pd on TiO_2 was measured to be 15 nm. By using the preparation method to achieve highly dispersed nanoparticulate Pd, a greater number of active sites for H_2 recombination were present in the sample, greatly enhancing the dehydrogenation onset temperature of MgH_2, and reducing the amount of costly Pd required.

6.3.4. Investigation of the thermodynamics and kinetics of hydrogen sorption from MgH_2 with oxide additives

To further investigate the active species and mechanisms of H_2 desorption and absorption by MgH_2 with oxide additives, specifically TiO_2 and TiO_2-Pd, TGA-MS, Sieverts, and IGA experiments were carried out to calculate thermodynamic and kinetic information for these reactions. Due to the length and nature of these experiments, a selection of the samples that showed the best dehydrogenation characteristics was made, with milled MgH_2 also studied for comparison purposes. Characterisation of samples before and after dehydrogenation was carried out with XRD and XPS.

The information obtained from the TGA-MS, Sieverts, and IGA experiments carried out on samples including milled MgH_2, MgH_2 - Ti70, and MgH_2 - Ti5Pd included values of activation energy, plateau pressures, enthalpy and entropy of dehydrogenation reactions, and rates of dehydrogenation and rehydrogenation over a number of cycles. The

equilibrium temperature (T_{eq}) for spontaneous desorption of hydrogen was calculated from the experimental enthalpy and entropy data. A summary of these values for the different samples is given in Table 6.1.

Sample		Milled MgH_2	MgH_2 - Ti70	MgH_2 - Ti5Pd
$E_a \pm 2$ / kJ mol^{-1} (D)		133	72	59
$\Delta H \pm 1$ / kJ mol^{-1} (D)		74	83	81
$\Delta S \pm 2$ / J K^{-1} mol^{-1} (D)		129	145	141
T_{eq} / °C		294	295	296
Equilibrium pressure / bar (300°C)	*(A)*	1.29	1.15	1.10
	(D)	2.30	1.52	1.33
Time for 90 % of total⁺ absorption/desorption after 5 cycles * / min	*(A)*	192	24	25
	(D)	233	6	15

Table 6.1: Summary of dehydrogenation and rehydrogenation behaviour of selected samples. (A) = absorption, (D) = desorption.

⁺Total absorption/desorption refers to rate of absorption/desorption being less than 3×10^{-3} wt. % per minute.

***Temperature of cycling was 350°C for milled MgH_2 and 300°C for all other samples.**

The values of enthalpy and entropy determined from van't Hoff plots for the milled MgH_2, MgH_2 - Ti70, and MgH_2 - Ti5Pd samples indicate similar thermodynamics for all three samples. The enthalpy value of 74 kJ mol^{-1} for milled MgH_2 is matches the reported value of 74 kJ mol^{-1} for MgH_2 [10]. The enthalpy values for the MgH_2 - Ti70 and MgH_2 - Ti5Pd samples are higher than for milled MgH_2, however, an associated increase in entropy of the system was also observed, resulting in very similar overall thermodynamic behaviour, with a temperature in the region of 294-

296°C required for spontaneous dehydrogenation of all three samples at 1 bar H_2 pressure. The effect of the additives was therefore in enhancing the kinetics of hydrogen sorption, as indicated by the activation energy values and the IGA cycling data.

The activation energy values in Table 6.1, determined from TGA-MS experiments using a range of heating rates, indicated that the MgH_2 - Ti70 and MgH_2 - Ti5Pd samples had significantly lower activation energy values than the milled MgH_2 and MgH_2 - 1Pd samples, indicating that the presence of the additives Ti70 and Ti5Pd lowered the activation energy barrier for the dehydrogenation of the samples. The activation energy of 133 kJ mol^{-1} for milled MgH_2 is consistent with reported values of 120 - 142 kJ mol^{-1} [11,118-120]. An activation energy of 153 kJ mol^{-1} for MgH_2 - 1Pd indicates that the Pd added as metallic Pd during ball milling was not effective in reducing the activation energy of MgH_2 dehydrogenation. There are no previously reported values of activation energies for the dehydrogenation of MgH_2 with TiO_2 or TiO_2 - Pd additives, however, values in the region of 63 - 83 kJ mol^{-1} have been reported for additions of Nb_2O_5 [70,78,80]. For metallic additions, an activation energy of 94 kJ mol^{-1} for MgH_2 milled with Ni [14]. These lower activation energies are related to the mechanisms of hydrogen desorption from the different samples, to be discussed in Section 6.3.6.

As shown in Table 6.1, cycling of the samples in the IGA showed much faster kinetics for both desorption and absorption of hydrogen from

MgH_2 - Ti70 and MgH_2 - Ti5Pd, compared with milled MgH_2. In the case of milled MgH_2 and MgH_2 - Ti70, the rates of hydrogen desorption and absorption improved during the first 3 - 4 cycles, before reaching stable rates of absorption and desorption as listed in Table 6.1. The rates of hydrogen desorption and absorption from MgH_2 - Ti5Pd were stable from the first cycle, as shown in Figures 5.33 and 5.34.

6.3.5. Active species in the dehydrogenation of MgH_2 - TiO_2

For the most effective additives, those milled with a TiO_2 component, further characterisation was carried out with the aim of understanding the active species responsible for enhancing the dehydrogenation of MgH_2. For MgH_2 - Ti70, a reduction of the TiO_2 was observed to occur during the first dehydrogenation of the sample. The presence of increased amounts of MgO observed in XRD of MgH_2 - TiO_2 samples after milling and dehydrogenation compared with MgH_2 milled with no additives, as shown in Figures 5.16 - 5.17, provides evidence for the loss of oxygen from the TiO_2 as it was reduced. XRD of MgH_2 - TiO_2 samples after dehydrogenation also shows no diffraction lines from TiO_2, suggesting that the oxide is no longer present in the sample, or has become nanocrystalline or amorphous and is therefore no longer detectable by XRD. No lines due to metallic Ti were observed in the XRD patterns after dehydrogenation, indicating that the reduced form of Ti may be amorphous or nanocrystalline.

XPS was used to attempt to further understand the nature of the Ti species present in the samples before and after milling and dehydrogenation. The Ti70 sample showed the characteristic peaks of Ti in TiO_2, with positions of 464.4 kV for $2p_{1/2}$ and 458.8 kV for $2p_{3/2}$. These matched well with values reported in the literature [99]. After milling and dehydrogenation, broadened peaks in the Ti 2p region were observed. Milling is a very destructive high energy process resulting in the introduction of defects in the crystal structures of the materials. This leads to less structured bonding at the surface of the samples, resulting in a range of X-ray photoelectron emission energies, hence broader peaks were observed.

Fitting of the XPS data of the samples before and after dehydrogenation, presented in Section 5.6.5, showed that there were two doublets corresponding to two distinct types of Ti species present in these samples. The position of the $2p_{3/2}$ peak of the most abundant component was 458.3 eV for the milled sample and 458.0 eV after dehydrogenation. Given the broadening of the peaks it is likely that these are still due to TiO_2 as they match more closely to the literature value for TiO_2 than for Ti_2O_3, as shown in Table 5.4.

The position of the $2p_{3/2}$ peak of the second doublet was 453.8 eV after milling, and 454.0 eV after dehydrogenation, indicating a Ti species of lower oxidation state. These values are very close to those reported in the literature for metallic Ti [98], suggesting that complete reduction of

some of the TiO_2 has occurred. The relative abundance of metallic Ti increased from approximately 30 % in the milled sample to approximately 40 % after dehydrogenation, indicating that more TiO_2 is reduced during dehydrogenation.

Peshev *et al.* suggested that Ti of a lower oxidation state than +4 can be caused by the high local temperatures arising during milling [121]. The Gibb's free energies of oxidation of Ti and Mg at 300K are given below, showing that Ti will readily reduce at the expense of oxidation of Mg.

$$2Mg + O_2 \rightarrow 2MgO \qquad \Delta G\ (300K) = -1141\ kJ\ mol^{-1}$$

$$Ti + O_2 \rightarrow TiO_2 \qquad \Delta G\ (300K) = -810\ kJ\ mol^{-1}$$

It is logical that the same reactions will occur during dehydrogenation at elevated temperature, and are the cause of the further reduction observed in the XPS data after dehydrogenation.

As the hydrogen absorption and desorption rates improve over the first few cycles, it is likely that further reduction of the TiO_2 occurred during this period resulting in more active metal Ti species being formed. In previous reports on the behaviour of Nb_2O_5 milled with MgH_2, a similar reduction of the niobium oxide has been reported, although it was still proposed that it was a sub-oxide of the form $Nb_2O_{3.67}$, and not a metallic Nb species, that was active in promoting the dehydrogenation of MgH_2 [79].

In order to further confirm metallic Ti species as the active component in the hydrogen desorption and absorption reactions of MgH_2, a sample of MgH_2 ball milled with titanium metal rather than titanium oxide, was prepared and characterised. Metallic Ti has previously been reported as an effective catalyst for the sorption of hydrogen in MgH_2 with fast kinetics of 5 min for complete hydrogen desorption at 300°C, although details of the Ti particle size and dispersion were not included [59]. In the present work, a 10 wt. % addition of Ti metal (particle size < 44 μm), was used, to give approximately the same wt. % of Ti as in a 20 wt. % TiO_2 addition. The dehydrogenation onset temperature of the MgH_2 - Ti(m) sample was found to be 250°C. This is slightly lower in temperature than for any of the MgH_2 - TiO_2 samples studied, and suggests that metallic Ti is slightly more effective than TiO_2 at lowering the activation energy barrier for dehydrogenation of MgH_2. The rate of hydrogen absorption and desorption from the MgH_2-Ti(m) sample did not improve upon cycling, and remained fairly slow, requiring >200 min to reach 90 % of full desorption, even after 10 cycles, compared to 6 minutes for MgH_2 - Ti70. The principle reason for the slow kinetics with the addition of metallic Ti are most likely to be due to the initial large particle size of the additive resulting in poor dispersion throughout the MgH_2. The small size and dispersion of the metallic Ti introduced through milling with sol-gel TiO_2, and its subsequent reduction, was therefore far more effective at providing a high dispersion of active species than ball milling with crystalline titanium powder. The cycling experiments showed that adding the active Ti species as a component of TiO_2, which

is then reduced upon ball milling and during initial cycles between 6 bar and $1x10^{-3}$ bar H_2 at 300°C, was a more effective way of introducing Ti to the system. As the particle size for Ti metal used in the previously reported literature was not reported [59], it cannot be determined whether a difference in Ti particle size was responsible for the faster kinetics observed. The results reported in this thesis would suggest that particle size is certainly likely to be a major contributing factor, although differences in sample preparation and analysis methods may also contribute to the different results observed.

The explanation for the effectiveness of the anatase crystal structure of TiO_2 compared to the rutile form in aiding the dehydrogenation of MgH_2, as discussed in Section 6.3.3, can be explained in relation to the reduction of the TiO_2 forming the active species. The reason for anatase TiO_2 appearing to be more effective is likely to relate to the ease of its reduction resulting in the formation of the metallic Ti species. Reports in the literature suggest that the mechanisms and rates of the reduction of rutile and anatase TiO_2 are very similar [122]. This would suggest that the rutile TiO_2 should in fact be more effective than the anatase in enhancing the dehydrogenation of MgH_2. The reason this is not the case is due to the surface area of oxides. Rutile TiO_2 may reduce more readily than anatase when measured per surface area, but the much lower surface area of the rutile samples means that on a mass basis, the anatase, having more exposed surface per unit mass, loses more oxygen and is thus more effective.

6.3.6. Kinetics and mechanisms of hydrogen desorption from MgH_2

A number of kinetic models are available to attempt to explain the complex mechanisms of hydrogen desorption from MgH_2 and MgH_2 with oxide additions. Barkhordarian *et al.* described a range of possible models, which they applied to absorption and desorption data from samples of MgH_2 - Nb_2O_5 [56]. These models have been applied to the desorption data collected from the gravimetric analysis of the milled MgH_2, MgH_2 - Ti70, and MgH_2 - Ti5Pd samples in this study. The equations for the models are given in equations 6.1 - 6.5.

SC1 $$\alpha = kt$$ equation 6.1

JMA3 $$[-\ln(1-\alpha)]^{\frac{1}{3}} = kt$$ equation 6.2

JMA2 $$[-\ln(1-\alpha)]^{\frac{1}{2}} = kt$$ equation 6.3

CV3 $$1-[1-\alpha]^{\frac{1}{3}} = kt$$ equation 6.4

CV2 $$1-[1-\alpha]^{\frac{1}{2}} = kt$$ equation 6.5

In all of the above equations, α represents the transformed fraction, k is the reaction constant, and t is the time. Equation 6.1 represents a surface controlled reaction (SC1) where chemisorption of hydrogen is the

rate-limiting step. Equations 6.2 and 6.3 are Johnson-Mehl-Avrami models (JMA3 and JMA2), which represent models of nucleation and growth at random points in the bulk and surface of the material, illustrated by the schematic in Figure 6.4.

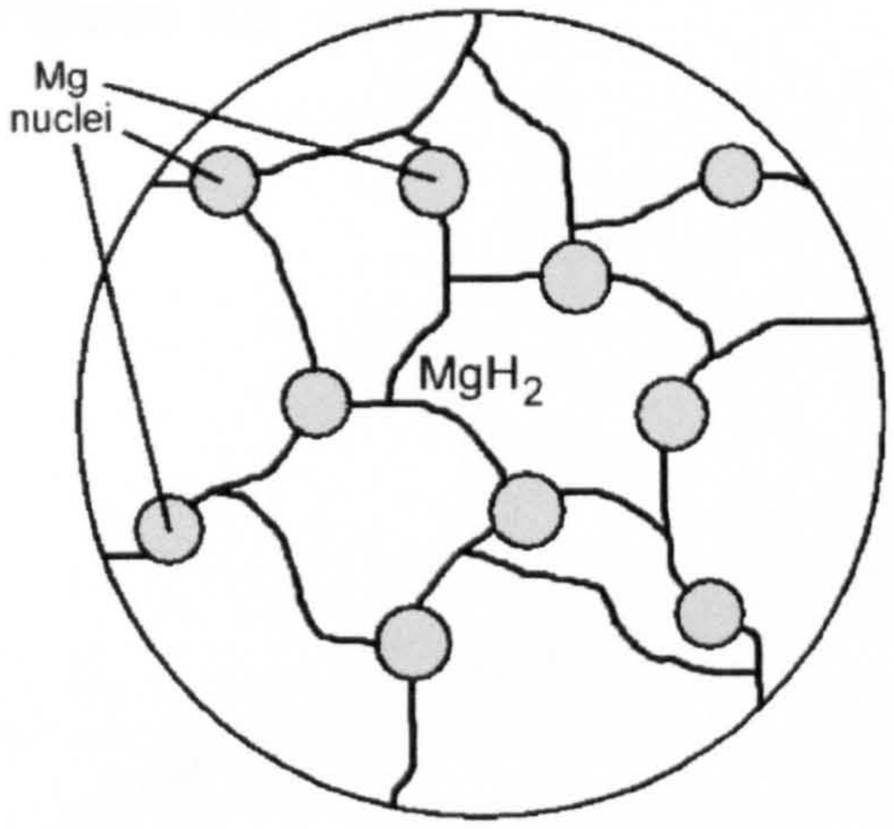

Figure 6.4: Schematic of JMA model of nucleation and growth.

The two different equations represent two-dimensional (equation 6.3, JMA2), and three-dimensional (equation 6.2, JMA3) growth of nuclei. In the JMA models, the rate-limiting step is the velocity of the moving interface between the metal and the hydride.

Equations 6.4 and 6.5 are equations for contracting volume models in which nucleation starts at the surface of the sample and then moves into the bulk, towards the core of the particle. The contracting volume model was represented by the core-shell schematic in Figure 6.1. Equations 6.4 and 6.5 are for three-dimensional (equation 6.4, CV3) or two-dimensional (equation 6.5, CV2) growth.

For the desorption data (on the 5th cycle) of milled MgH_2, MgH_2 - Ti70, and MgH_2 - Ti5Pd, the experimental data of converted fraction, α, was inserted into the left hand side of each of the kinetic equations 6.1 - 6.5 and plotted against time, with the linear trend lines also plotted, showing which equation was the best fit to the experimental data. These plots are given in Figures 6.5 - 6.8.

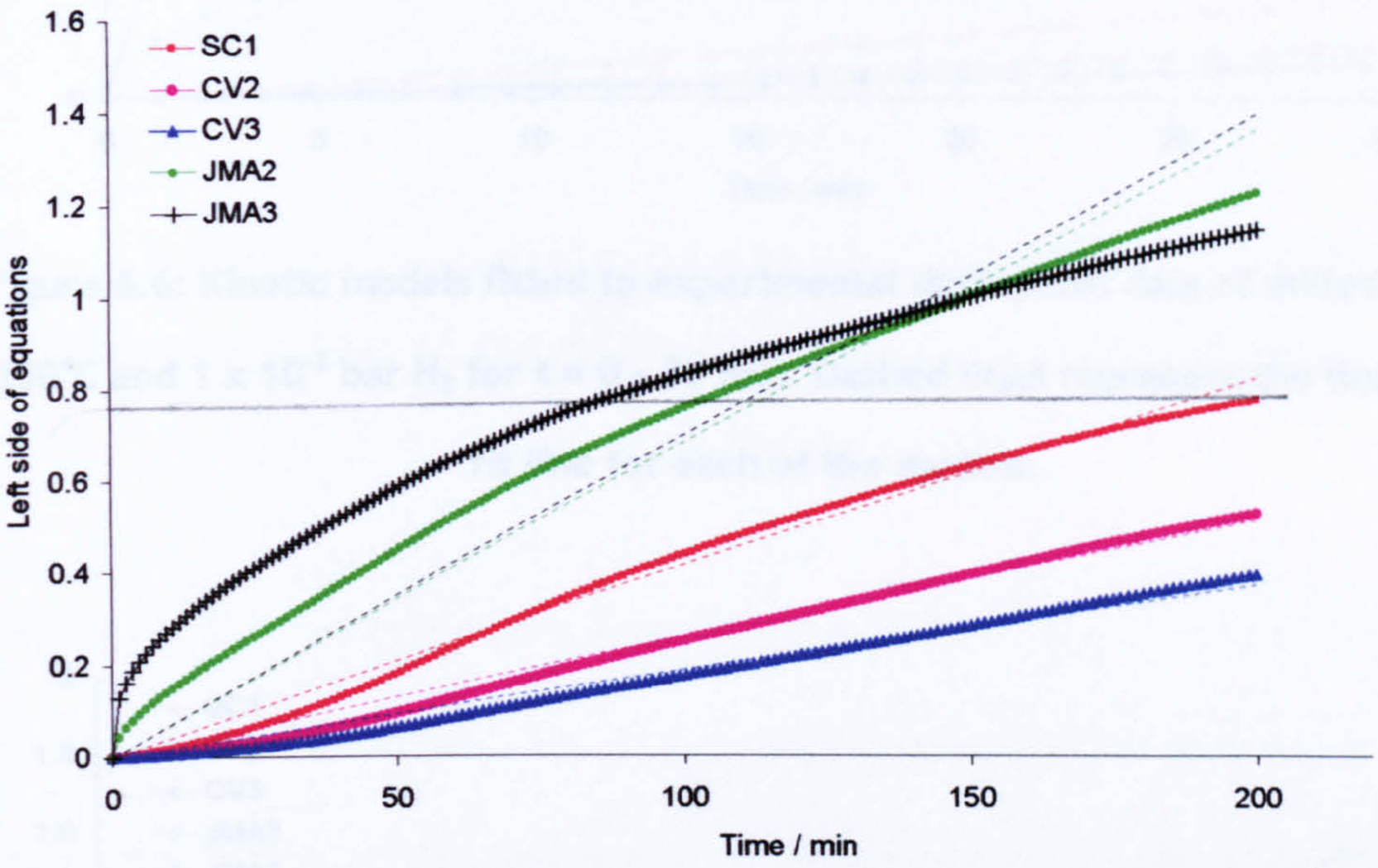

Figure 6.5: Kinetic equations fitted to experimental desorption data of milled MgH_2 at 350°C and 1 x 10^{-2} bar H_2. Dashed lines represent the linear best fit line for each of the models.

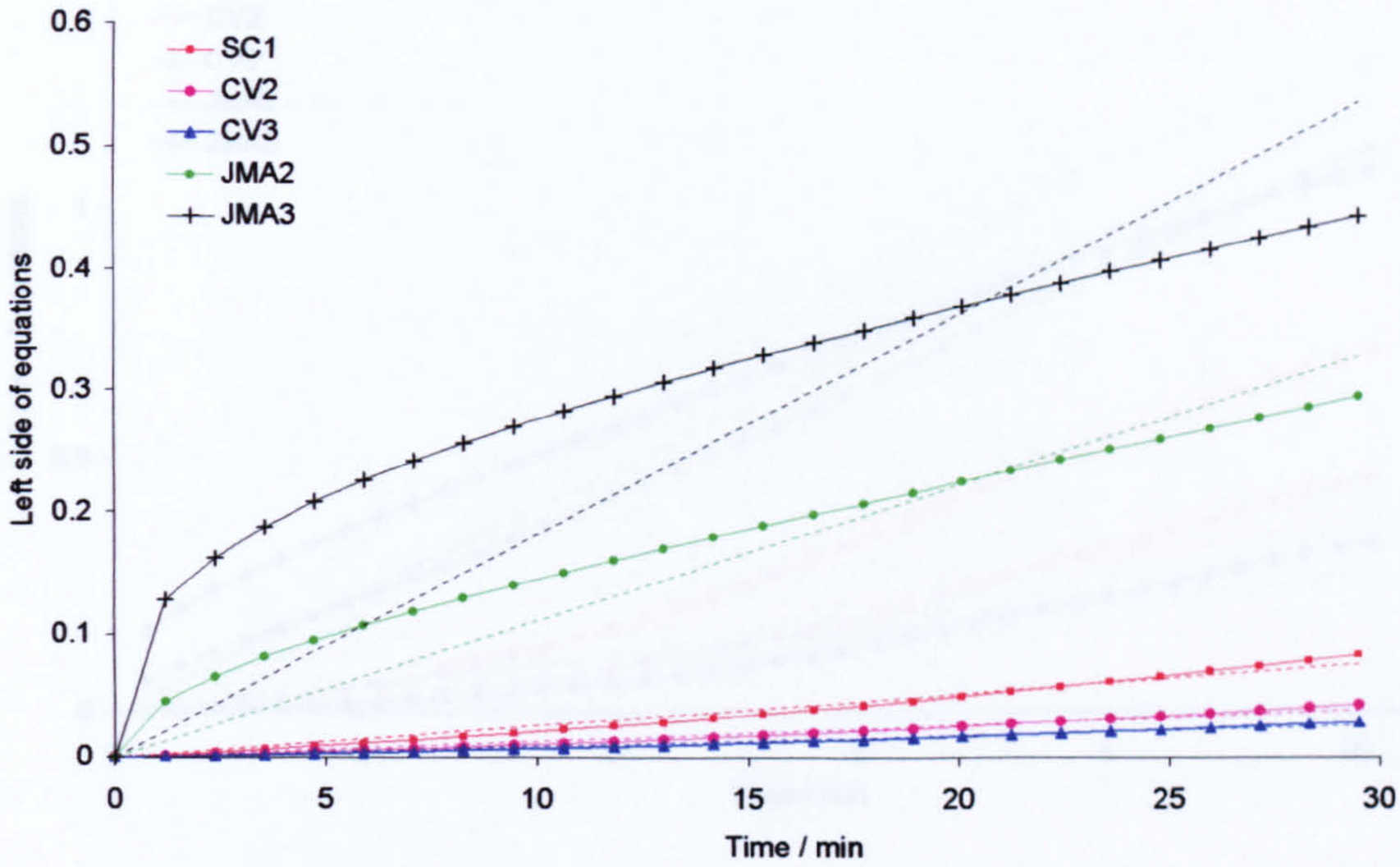

Figure 6.6: Kinetic models fitted to experimental desorption data of milled MgH_2 at 350°C and 1 x 10^{-2} bar H_2 for t = 0 - 30 min. Dashed lines represent the linear best fit line for each of the models.

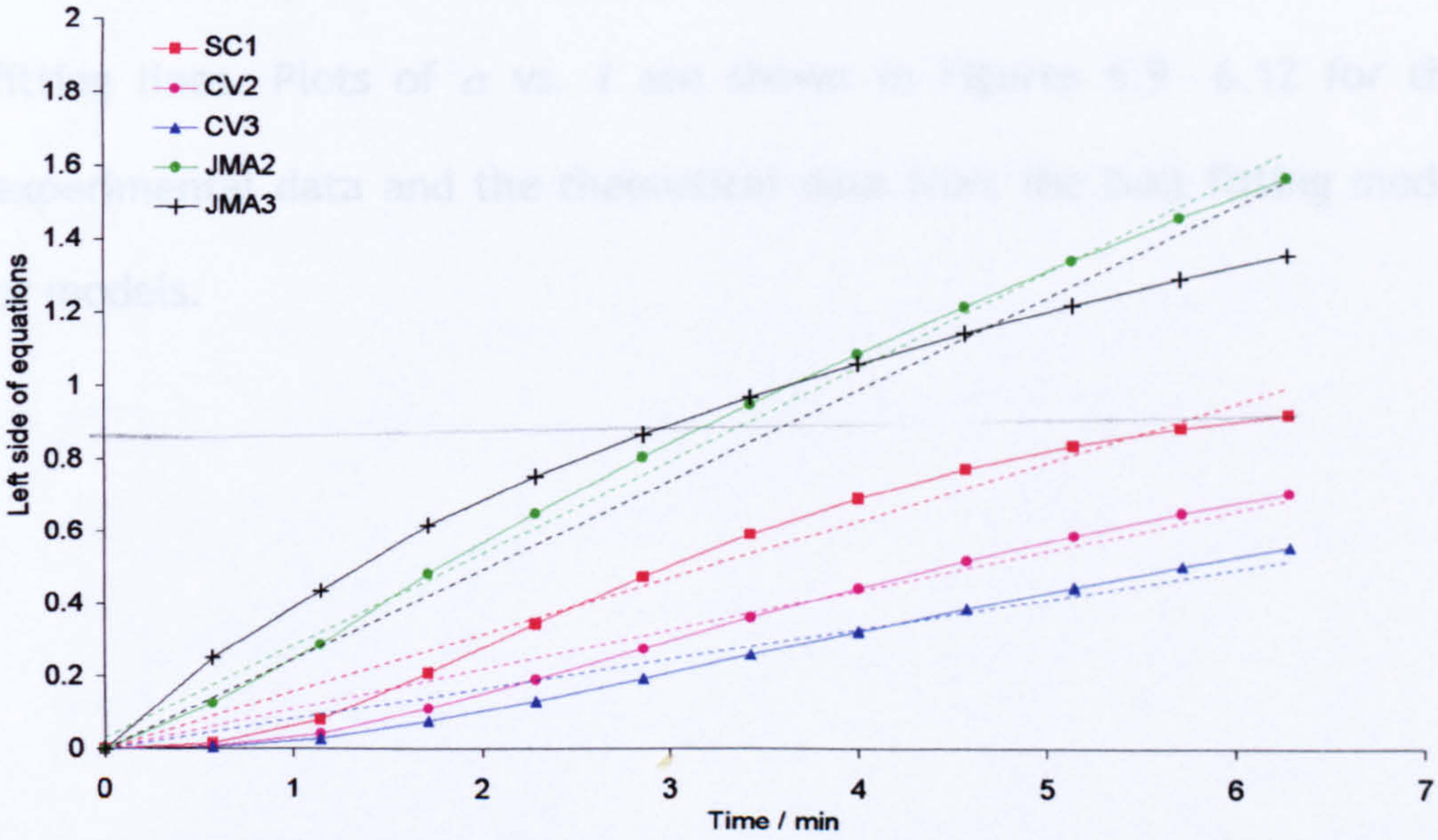

Figure 6.7: Kinetic models fitted to experimental desorption data of MgH_2 - TI70 at 300°C and 1 x 10^{-2} bar H_2. Dashed lines represent the linear best fit line for each of the models.

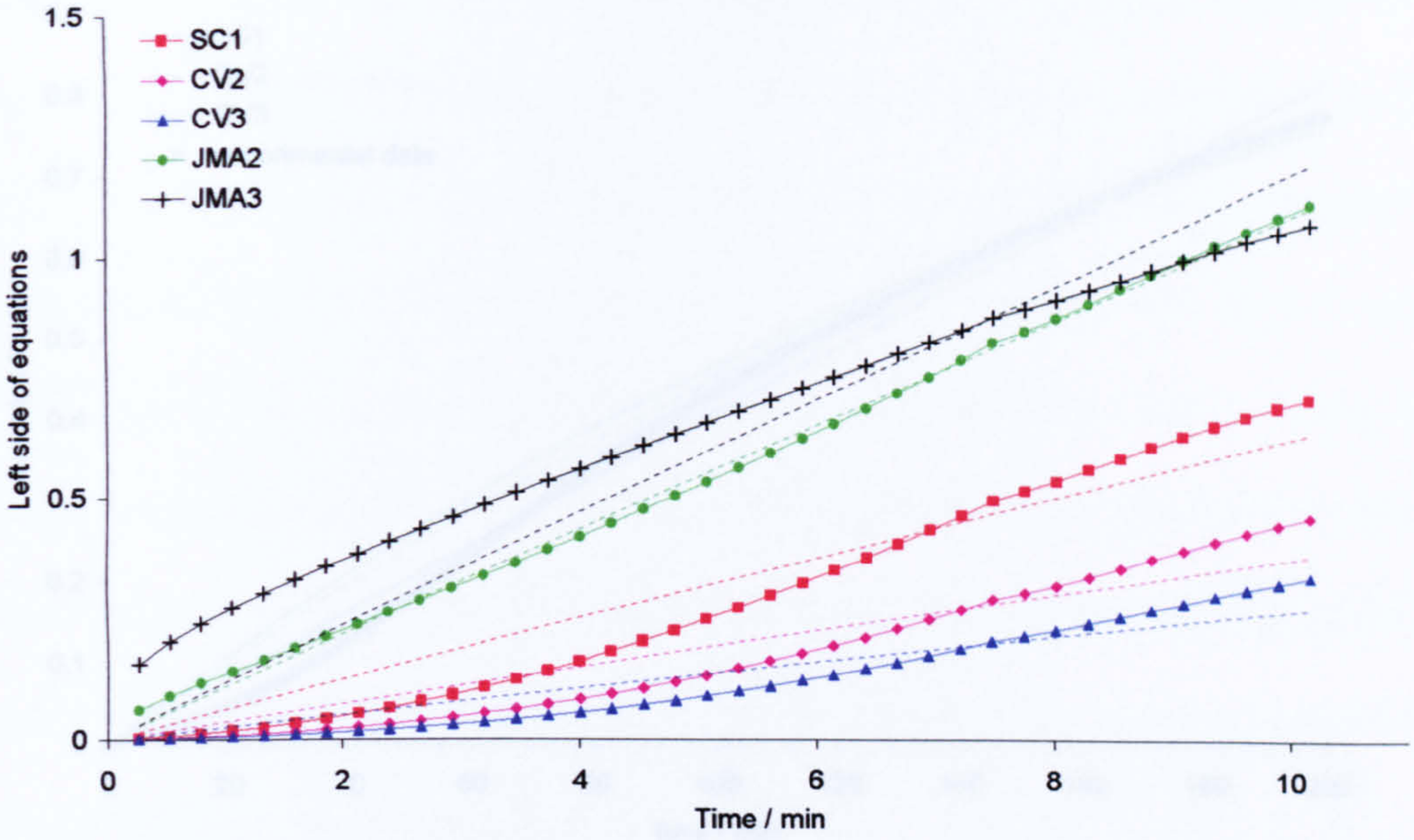

Figure 6.8: Kinetic models fitted to experimental desorption data of MgH_2 - Ti5Pd at 300°C and 1 x 10^{-2} bar H_2. Dashed lines represent the linear best fit line for each of the models.

Values for the rate constant *k* were calculated from the slope of the best fitting lines. Plots of α vs. *t* are shown in Figures 6.9 - 6.12 for the experimental data and the theoretical data from the best fitting model or models.

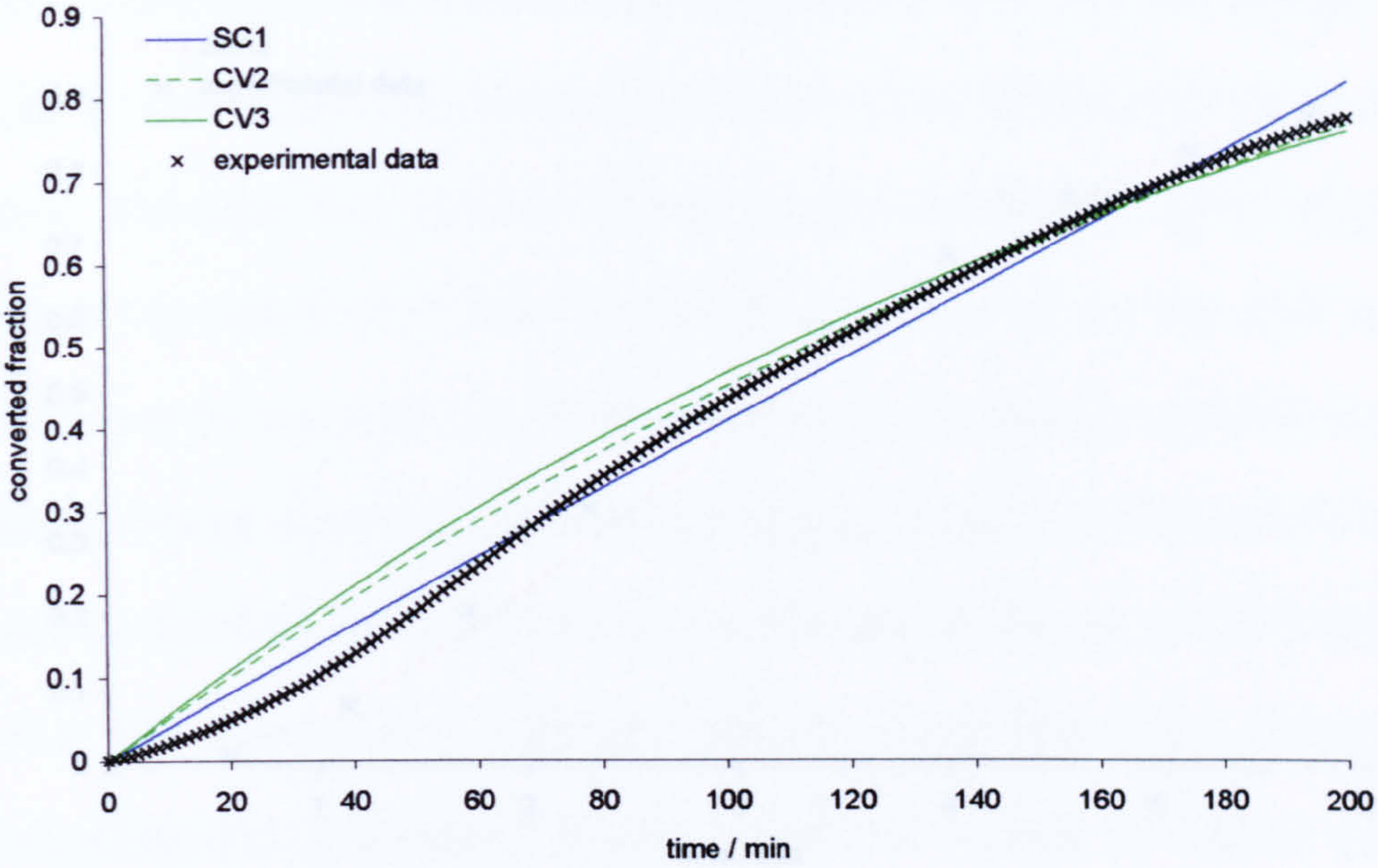

Figure 6.9: Converted fraction vs. time for milled MgH_2 experimental data and closest fitting models for t < 200 min.

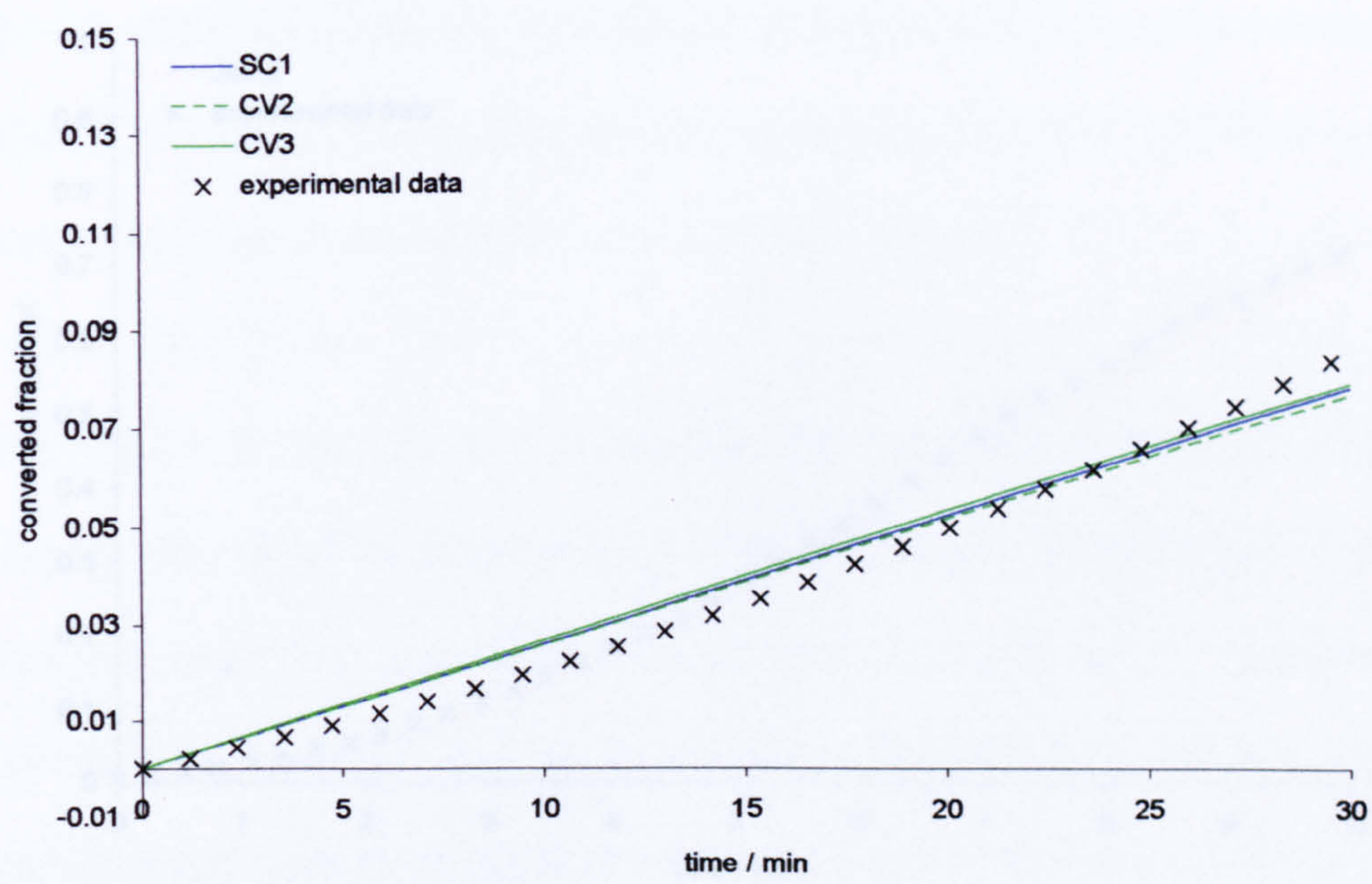

Figure 6.10: Converted fraction vs. time for milled MgH_2 experimental data and closest fitting models for t < 30 min.

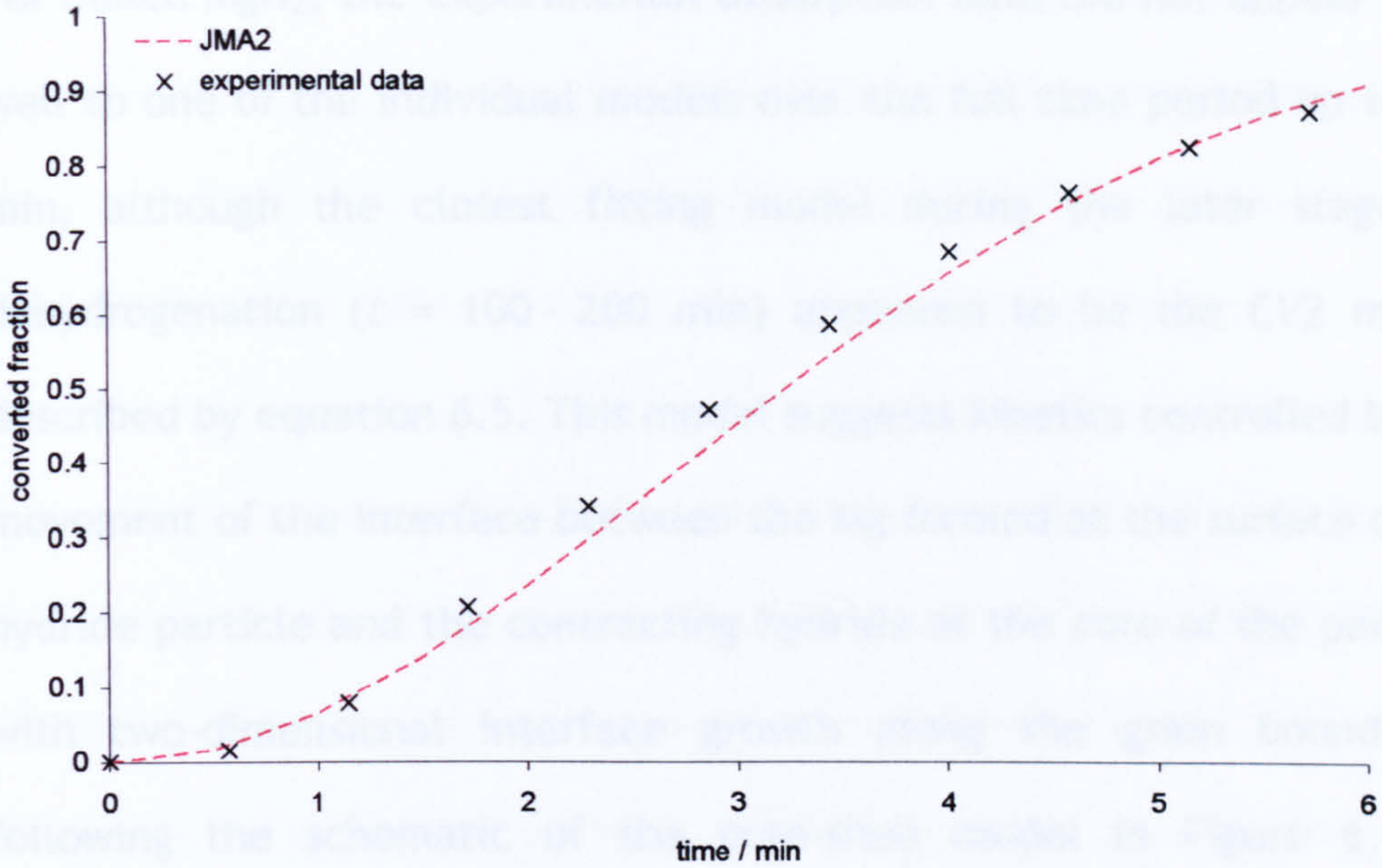

Figure 6.11: Converted fraction vs. time for MgH_2 - Ti70 experimental data and closest fitting model.

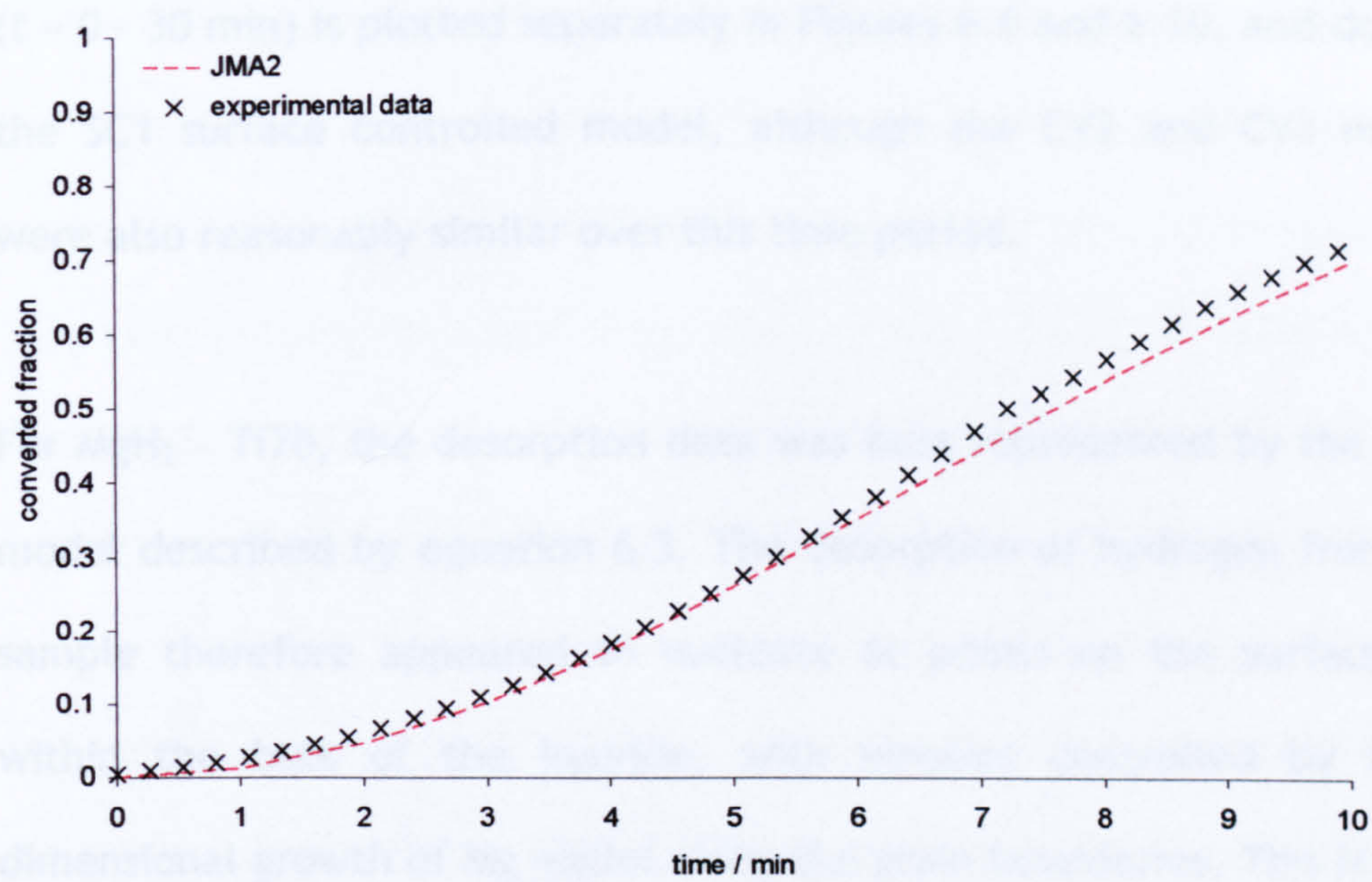

Figure 6.12: Converted fraction vs. time for MgH_2 - Ti70 experimental data and closest fitting model.

For milled MgH_2, the experimental desorption data did not appear to fit well to one of the individual models over the full time period up to 200 min, although the closest fitting model during the later stages of dehydrogenation (t = 100 - 200 min) appeared to be the CV2 model, described by equation 6.5. This model suggests kinetics controlled by the movement of the interface between the Mg formed at the surface of the hydride particle and the contracting hydride at the core of the particle, with two-dimensional interface growth along the grain boundaries, following the schematic of the core-shell model in Figure 6.1, as proposed by Zaluska *et al.*[64]. A number of groups have suggested an initial surface controlled reaction for dehydrogenation of milled MgH_2 [14,44]. The data from the early stage dehydrogenation process (t = 0 - 30 min) is plotted separately in Figures 6.6 and 6.10, and does fit the SC1 surface controlled model, although the CV2 and CV3 models were also reasonably similar over this time period.

For MgH_2 - Ti70, the desorption data was best represented by the JMA2 model described by equation 6.3. The desorption of hydrogen from this sample therefore appeared to nucleate at points on the surface and within the bulk of the hydride, with kinetics controlled by the 2 dimensional growth of Mg nuclei along the grain boundaries. This is to be expected, as grain boundaries provide a lower energy route for diffusion. These results suggest that the presence of the active Ti species provided active sites within the grain boundaries for the nucleation of Mg.

The desorption data from the MgH_2 - Ti5Pd sample was also best represented by the JMA2 model, indicating a similar mechanism to that shown by MgH_2 - Ti70, of nucleation and growth of Mg along the grain boundaries of the MgH_2.

From the hydrogen cycling behaviour of the samples shown in Section 5.9, it was observed that both the milled MgH_2 and MgH_2 – Ti70 samples displayed slower hydrogen desorption kinetics on the first cycle, suggesting an activation process was necessary to achieve the faster kinetics observed in subsequent cycles. In contrast, MgH_2 - Ti5Pd did not show a slow first desorption. This suggests that the presence of the Pd served to activate the desorption process from the first cycle. Zaluska *et al.* have reported the strong effect of Pd on the dissociation of H_2 at the Mg surface overcoming the detrimental effect of surface oxidation [64]. It appears that the Pd added here, through the milling of MgH_2 with TiO_2 - Pd, behaved in a similar manner, to enhance the recombination of H atoms to form H_2 at the surface of the MgH_2 and eliminate the need for activation of the sample during an initial cycle.

Although this first desorption was significantly faster than the first desorption from MgH_2 - Ti70, on subsequent cycles the hydrogen desorption from MgH_2 - Ti70 was actually faster than the rate observed for MgH_2 - Ti5Pd. The presence of the Pd therefore appeared to act primarily to activate the initial hydrogen desorption, and did not have any further beneficial effect. It is therefore likely that the active Ti

species located within the grain boundaries of the MgH_2 were responsible for the sustained fast desorption kinetics, following the JMA2 model of nucleation and growth. The reason for hydrogen desorption rate from the MgH_2 - Ti5Pd sample being slower than that for MgH_2 -Ti70 after the first cycle is likely to be caused by the difference in the structure and surface area of the TiO_2 that was added in each case. The Ti5Pd had been subjected to a heat treatment at 500°C, resulting in a more crystalline sample with larger crystallite size and a lower surface area. This Ti5Pd was therefore likely to be less well dispersed within the MgH_2 upon ball milling, resulting in a less effective additive.

Barkhordarian *et al.* found that the kinetics of dehydrogenation from their MgH_2 - Nb_2O_5 samples generally followed a contracting volume model of 2 - dimensional interface growth [56], unlike the data presented here for TiO_2 and TiO_2 - Pd additives, which was best modelled by the JMA model of 2-dimensional growth of nuclei. This suggests that different mechanisms are responsible for the behaviour of these different additives. Unlike the TiO_2 additives studied here, Nb_2O_5 is generally not observed to reduce during ball milling and cycling to the same extent as TiO_2, with no evidence of any structural transformation of the Nb_2O_5 phase in some studies where Nb_2O_5 is proposed to act as the catalyst for H_2 desorption [78,80]. A degree of reduction was suggested by Friedrichs *et al.*, who used XPS analysis and showed a reduction in the Nb species present after cycling, and evidence of a $MgNb_2O_{3.67}$ phase in XRD taken after cycling of ball milled MgH_2 - Nb_2O_5 [79]. In contrast, for

other nanoparticulate metal additives, such as Ni, the JMA model has been shown to be a good representation of the dehydrogenation kinetics [14]. These results may explain the different mechanisms at work for Nb_2O_5 and TiO_2, where there is strong evidence pointing towards metallic Ti as the active species in increasing the rate of MgH_2 dehydrogenation. The active Ti species appear to be located within the grain boundaries of the MgH_2, providing nucleation sites for Mg. In contrast, for Nb_2O_5, the oxide phase is thought to be located at the surface of the MgH_2, acting as a catalyst for chemisorption [56].

6.4. Overview

A number of significant outcomes have resulted from this investigation of oxide additives to MgH_2, including the development of novel additives and an understanding of the mechanisms by which the studied oxide additives influence the hydrogen sorption properties of MgH_2. TiO_2 and TiO_2 - Pd were found to be highly beneficial in reducing dehydrogenation onset temperatures and increasing rates of hydrogen absorption and desorption in MgH_2. In Table 6.3, the key results of this work are presented, along with data from the literature showing previously reported results for other oxide and metal additives to MgH_2.

Additive	Form of additive	Amount added / wt. %	Milling conditions	Average MgH_2 grain size after milling	Effect of additive on H_2 Desorption		Reference
					Thermodynamics	Kinetics	
TiO_2	Sol-gel dried at 70°C	20	Balled milled under Ar for 20 h.	10 nm	T_{onset} = 257°C. ΔH_{des} = 82.5 kJ mol^{-1} ΔS_{des} = 145 J mol^{-1} K^{-1}	90 % complete in 6 min at 300°C in 0.01 MPa H_2. E_a = 72 kJ mol^{-1}.	Reported in this thesis
TiO_2 - 5Pd	Sol-gel dried at 70°C.	20	Balled milled under Ar for 20 h.	10 nm	T_{onset} = 205°C. ΔH_{des} = 80.7 kJ mol^{-1} ΔS_{des} = 141 J mol^{-1} K^{-1}	90 % complete in 15 min at 300°C in 0.01 MPa H_2. E_a = 59 kJ mol^{-1}.	Reported in this thesis
Ti	Commercial, crystalline.	10	Balled milled under Ar for 20 h.	10 nm	T_{onset} = 250°C. ΔH_{des} and ΔS_{des} not reported.	90 % complete in > 200 min at 300°C in 0.01 MPa H_2.	Reported in this thesis
Cr_2O_3	Commercial, crystalline.	1.2	Ball milled under Ar for 20 h + 100 h.	21 nm	Not reported.	Complete in 15 min at 300°C in vacuum. (Deteriorates on cycling).	[82]
Nb_2O_5	Commercial, crystalline.	5	Ball milled under Ar for 20 h + 100 h.	Not reported.	Not reported.	Complete in 8.5 min at 250°C in vacuum. E_a = 62 kJ mol^{-1}.	[78]
TiO_2	Commercial, Rutile.	20	RMA of Mg under H_2 for up to 6 h.	20 nm	Not reported.	Complete in 9 min at 350°C in 0.1 MPa H_2.	[76]
TiO_2	No details given.	3	Ball milled under Ar for 20 h + 100 h.	20 nm	Not reported.	Complete in 8 min at 300°C in vacuum.	[16]

Table 6.3: Comparison of results to literature values for additives to MgH_2.

Additive	Form of additive	Amount added / wt. %	Milling conditions	Average MgH_2 grain size after milling	Effect of additive on H_2 Desorption		Reference
					Thermodynamics	Kinetics	
Pd	Commercial, nanocrystalline.	1	Ball milled under Ar for up to 20 h.	20-30 nm	Not reported.	Complete in 40 min at 330°C (pressure not reported)	[64]
Ni	Commercial, nanocrystalline.	4.5	Ball milled under H_2 for up to 2 h.	Not reported	T_{onset} = 150°C ΔH_{des} and ΔS_{des} not reported.	90 % complete in 100 min at 163°C under flowing He. E_a = 94 kJ mol^{-1}.	[14]
Ti	Commercial, crystalline	9	Ball milled under Ar for up to 20 h.	Not reported	T_{onset} not reported ΔH_{des} = 77 kJ mol^{-1}* ΔS_{des} = 136 J mol^{-1} K^{-1}*	Complete in 5 min at 300°C in 0.015 MPa H_2. E_a = 71.1 kJ mol^{-1}.	[59]

Table 6.3 (continued): Comparison of results to literature values for additives to MgH_2.

*** Calculated from Van't Hoff plot presented in the reference paper.**

Direct comparison of these results can be difficult, due to the wide range of oxide concentrations, milling processes, and experimental methods used in analysis of the samples, however, it can be seen that the hydrogen sorption behaviour of MgH_2 ball milled with the Ti70 and Ti5Pd additives reported in this thesis resulted in materials with similar hydrogen sorption properties to the best results previously reported in the literature for all other additives.

The hydrogen sorption properties of the materials developed in this work are comparable to those of other additives reported in the literature, and they do offer a number of advantages. For practical application, the ability of a hydrogen storage material to maintain fast hydrogen sorption kinetics upon repeated cycling is of great importance. MgH_2 with additions of Cr_2O_3 and nanoparticulate Ni have both been shown to deteriorate on cycling [14,82], which was not the case with the Ti70 oxide, which reached stable hydrogen absorption and desorption rates after the first cycle.

The relative abundance and cost of a hydrogen storage material is also of importance for the widespread application of these materials. Ti is both readily available and relatively inexpensive. While Nb_2O_5 has been shown to have slightly faster hydrogen sorption kinetics than the Ti70 additive [78], Ti is 300 times more abundant that Nb, making its availability less of a concern were it to be included in a hydrogen storage material for widespread use.

The other TiO_2 additives previously reported in the literature were commercially produced oxides. In the study by Wang *et al.*, the oxide was of the rutile form, and even at a temperature of 350°C, complete desorption of H_2 took 9 min. Although the oxide particle size was not reported, a commercial rutile TiO_2 is likely to have a much higher particle size than the sol-gel prepared Ti70 oxide sample reported in this work, and this is the likely cause of the slower desorption kinetics, compared to 6 min at 300°C reported here for MgH_2 - Ti70. Neither the oxide structure nor particle size are reported for the TiO_2 used by Oelerich *et al.*[16]. Although similar hydrogen desorption kinetics were reported to those found for MgH_2 - Ti70, the samples were ball milled for 120 h, 6 times longer than for MgH_2 - Ti70. It is likely that this length of ball milling was required to reduce the particle size and increase the dispersion of the TiO_2, however, this length of time, amounting to 5 days, is extremely energy demanding and costly.

The MgH_2 - Ti metal system reported by Liang *et al.* showed very promising hydrogen sorption kinetics. However, the amount of Ti present in their system (9 wt. %) was significantly higher than the abundance of Ti metal present in the MgH_2 - Ti70 sample (4 wt. %), determined from XPS analysis, while the desorption kinetics of the two systems were very similar. This suggests that the mechanism of delivering the active Ti metal species through milling with sol-gel TiO_2, and its subsequent reduction, therefore provided a higher number and dispersion of active sites. Clearly, further work is required to fully investigate this method in

comparison to ball milling directly with metallic Ti, in terms of cost implications, as well as the effect on hydrogen capacity and sorption kinetics.

The addition of Pd as a component of the Ti5Pd additive is a significant breakthrough in terms of providing a highly effective delivery mechanism for Pd, a well-known H_2 dissociation catalyst, to the surface of MgH_2. Very low concentrations of Pd (0.2 - 1 wt. %) were introduced by this method, and were shown to have a highly beneficial effect in activating the first desorption and absorption cycles of MgH_2.

In addition to the novel materials that have been thoroughly characterised in this work, results relating to the effect of the different crystal structures of TiO_2 were reported, and the reduction of TiO_2 to more active metallic Ti was discussed. A significant contribution to the understanding of the mechanisms of hydrogen sorption in these materials has also been made. Mixed metal oxides based on Al and Si oxides were also investigated. As the mechanisms of catalysis involved in the desorption of hydrogen from MgH_2 are not yet fully understood, and acids are known to catalyse the decomposition of MgH_2 via hydrolysis, it was initially thought that solid acid catalysts of this type may have had a beneficial effect. Although it was shown that these materials did not affect the hydrogen sorption behaviour of MgH_2, this is still a significant result as these materials have not previously been studied for this application.

In the following chapter, conclusions of the work carried out for this thesis are presented. Future work arising as a result of this investigation are summarised in Chapter 8.

7. Conclusions

The work carried out for this thesis included the preparation and characterisation of a range of single and mixed oxide materials, as well as palladium - modified oxides. These oxides were based on Al_2O_3, SiO_2, TiO_2 and ZrO_2. The characterisation of the oxides by a range of techniques resulted in an understanding of their surface and bulk properties, including structure, surface area, and surface species. Structures ranging from amorphous to highly crystalline were produced, with crystal structures dependent on calcination temperature and oxide components. Surface areas of the oxides covered a broad range, between 15 and 550 $m^2 g^{-1}$.

The prepared oxides, the majority of which have not previously been studied for their effect on hydrogen sorption of MgH_2, were ball milled with MgH_2 powder, and the mixtures were characterised with a number of techniques to gain insight into their structure and properties. The principal aim of the work was to investigate the influence of the different oxides on the desorption and absorption of hydrogen in MgH_2. From this work, a number of conclusions can be drawn, which contribute to the overall understanding of the effect of ball milling and oxide additives on the thermodynamics and kinetics of hydrogen sorption in MgH_2.

The positive effect of ball milling on the temperature and kinetics of hydrogen sorption in MgH_2 has been widely studied, and the ball milling

studies carried out in this work found similar results to those previously reported. Characterisation carried out using *in situ* XRD resulted in the conclusion that the transformation of the β-MgH_2 to the metastable γ-phase during ball milling was not significant in influencing the dehydrogenation of ball milled MgH_2.

The oxides containing a TiO_2 component were found to be most effective in lowering the dehydrogenation onset temperature of MgH_2, with the single oxide TiO_2 dried at 70°C having the greatest effect, lowering the dehydrogenation onset temperature to 257°C. The other transition metal oxide studied, ZrO_2, was found to have a similar positive effect, while the Al_2O_3 and SiO_2 oxides did not exhibit the same influence on the dehydrogenation onset temperature of MgH_2.

Of the mixed oxides prepared from TiO_2, Al_2O_3, and SiO_2, only those containing a TiO_2 component showed a beneficial effect on the onset temperature of dehydrogenation of MgH_2, directly related to the amount of TiO_2 present. The Al_2O_3 or SiO_2 only diluted the effect of the active species, with no synergistic effect from the addition of a second oxide component.

A key result arising from this work is the previously unreported influence of the oxide calcination temperature in changing the effect of the TiO_2 on the dehydrogenation of MgH_2. The results suggest that the anatase form of TiO_2 is more effective at lowering the dehydrogenation onset

temperature of MgH_2 than the rutile TiO_2 formed after calcination at 800°C.

A reduction of the Ti (4+) in TiO_2 to metallic Ti appears to result in the formation of the active species responsible for catalysing the MgH_2 dehydrogenation reaction. Although both anatase and rutile TIO_2 reduce at similar rates, the surface area of the oxide also plays a critical role in its effect. The higher surface area of the anatase TiO_2 in MgH_2 - Ti400 resulted in a high dispersion of active sites throughout the MgH_2, compared to the lower surface area rutile TiO_2 in MgH_2 - Ti800.

Results of studies of Pd metal dispersed onto the surface of TiO_2 showed this to be an effective method of introducing active Pd metal into the MgH_2, resulting in a dehydrogenation onset temperature of 205°C for a 0.2 wt. % addition of Pd.

By fitting isothermal desorption data with a range of kinetic models, it was found that hydrogen desorption from ball milled MgH_2 occurred via a combination of surface controlled and contracting volume models, with the rate controlled by the movement of the interface between the forming Mg and the MgH_2 at the core of a particle. Upon addition of the TiO_2 or Pd-TiO_2 species, the mechanism was found to change, with the data fitting a Johnson-Mehl-Avrami model of Mg nucleation and growth throughout the bulk and at the surface of the MgH_2 particle.

The prepared materials, particularly MgH_2 ball milled with high surface area TiO_2 and Pd-TiO_2, displayed excellent hydrogen sorption properties, with dehydrogenation onset temperatures comparable to those previously reported for transition metal oxide and metal additives. The dehydrogenation onset temperature of 205°C for MgH_2 - Ti1Pd and MgH_2 - Ti5Pd is very promising, at nearly 200°C lower than that for unmilled MgH_2. Rates of hydrogen absorption and desorption were also dramatically improved by the addition of TiO_2 and Pd-TiO_2.

The search for a hydrogen storage material that could be integrated with a fuel cell for vehicular application is ongoing, and the materials studied here still do not meet the necessary targets of capacity and operating temperature, however, the detailed study carried out contributes further to the understanding of these materials and their behaviour, as well as providing scope for future work in the area, as discussed in the following chapter.

8. Future Work

The research undertaken for this thesis was the first study of metal hydrides for hydrogen storage conducted at the University of Nottingham. The results contribute to the overall understanding of MgH_2 and the effect of oxide additives, particularly TiO_2, on hydrogen sorption behaviour, and also provide a basis for future work in this area.

TiO_2 and Pd-TiO_2 materials showed promising effects on the hydrogen sorption of MgH_2, and the characterisation of the mixtures before and after dehydrogenation suggest that it is the reduction of the TiO_2 to metallic Ti that is responsible for enhancing the desorption kinetics. Although addition of the oxide results in a reduction in the overall H_2 capacity of the material, the oxide has been shown to act as a highly effective method of achieving a high dispersion of active Ti due to its small particle size. Based on the results presented in this work, it would be expected that further reducing the particle size of both the magnesium hydride and the additive would result in faster hydrogen sorption kinetics at lower temperature. Ball milling could be optimised to achieve further reduction in particle size, however, ball milling is a very energy intensive process and it is very difficult to achieve a narrow particle size distribution.

An alternative method for producing nm scale particles or smaller with a narrow particle size distribution is through supercritical fluid processes. Research into developing a supercritical fluid method for production of

Mg, TiO_2 and/or Ti particles could prove to be a very effective way of further building on the research presented in this thesis. It has been shown that it is possible to produce a wide variety of nm scale particles using supercritical fluids. It should also be possible to precipitate other metal or oxide species onto Mg in situ, forming intimately mixed nm-sized hydrogen storage materials.

To further understand the nature and role of the active species in the MgH_2 - TiO_2 systems, further characterisation of the materials would be of benefit. To further understand the nature of the active species with the sample before and after dehydrogenation, an additional technique such as EXAFS (extended X-ray absorption fine edge structure), could be used to probe the local bonding of the individual elements.

Neutron diffraction is a powerful technique often used in studies of hydrogen storage materials, to understand the interaction of the hydrogen with the other species in the sample. A powder neutron diffraction study on these materials could provide valuable information on their structure before, during, and after hydrogen desorption and absorption.

The Pd - modified TiO_2 samples provided a very effective means of introducing small quantities of well dispersed active metal species into the MgH_2. Metal-modified transition metal oxides have not previously been studied as additives for MgH_2, and it would be logical to pursue

these materials further in future investigations. Reducing the concentration of Pd on the TiO_2 from 5 wt. % to 1 wt. % did not result in an increase in the dehydrogenation onset temperature of MgH_2, and it would therefore be of value to determine the minimum quantity of costly Pd required to maintain the beneficial effect. Other active metals and transition metal oxide supports could also be investigated to determine whether more effective combinations exist, resulting in even faster sorption kinetics at lower temperatures.

For application as hydrogen storage materials linked to fuel cells or ICEs, a number of practical considerations must be taken into account. For example, investigation of the response of the materials to longer term cycling (>100 cycles), and studies of the effect of impurities in hydrogen gas on the behaviour of the samples in the short and long - term would be of value. Issues such as heat transfer and safe handling of the materials would also need to be considered in achieving a real hydrogen storage system for practical application.

9. References

[1] J. T. Houghton, Y. Ding, D. J. Griggs, M. Noguer, P. J. van der Linden, and D. Xiaosu, in *IPCC Third Assessment Report: Climate Change 2001* (Cambridge University Press, Cambridge, 2001), p. 944.

[2] DTI, *Our energy future - creating a low carbon economy*. (2003).

[3] P. P. Edwards, V. L. Kusnetsov, W. I. F. David, and N. Brandon, *Foresight article - Hydrogen and fuel cells: towards a sustainable energy future*. (Office of Science and Innovation, 2006).

[4] J. J. Reilly and G. D. Sandrock, Sci.Am. **242** (2), 118 (1980).

[5] D. L. Stojic, M. P. Marceta, S. P. Sovilj, and S. S. Miljanic, J. Power Sources **118** (1-2), 315 (2003).

[6] Z. W. Liu, K. W. Jun, H. S. Roh, and S. E. Park, J. Power Sources **111** (2), 283 (2002).

[7] S. U. M. Khan, M. Al-Shahry, and W. B. Ingler, Science **297** (5590), 2243 (2002).

[8] A. Zuttel, Mater. Today **6** (9), 24 (2003).

[9] T. Riis and G. Sandrock, *Hydrogen Production and Storage - R&D Priorities and Gaps*. (IEA Publications, Paris, 2006).

[10] B. Vigeholm, J. Kjoller, B. Larsen, and A. S. Pedersen, J. Less-Common Met. **89** (1), 135 (1983).

[11] J. Huot, G. Liang, S. Boily, A. Van Neste, and R. Schulz, J. Alloy. Compd. **295**, 495 (1999).

[12] J. L. Bobet, B. Chevalier, M. Y. Song, and B. Darriet, J. Alloy. Compd. **356**, 570 (2003).

[13] N. Hanada, T. Ichikawa, S. I. Orimo, and H. Fujii, J. Alloy. Compd. **366** (1-2), 269 (2004).

[14] N. Hanada, T. Ichikawa, and H. Fujii, J. Phys. Chem. B **109** (15), 7188 (2005).

[15] F. C. Gennari, F. J. Castro, G. Urretavizcaya, and G. Meyer, J. Alloy. Compd. **334**, 277 (2002).

[16] W. Oelerich, T. Klassen, and R. Bormann, J. Alloy. Compd. **315** (1-2), 237 (2001).

[17] M. Terzieva, M. Khrussanova, and P. Peshev, Int. J. Hydrog. Energy **16** (4), 265 (1991).

[18] C. X. Shang and Z. X. Guo, J. Power Sources **129** (1), 73 (2004).

[19] D. Chen, L. Chen, S. Liu, C. X. Ma, D. M. Chen, and L. B. Wang, J. Alloy. Compd. **372** (1-2), 231 (2004).

[20] H. Imamura, M. Kusuhara, S. Minami, M. Matsumoto, K. Masanari, Y. Sakata, K. Itoh, and T. Fukunaga, Acta Mater. **51** (20), 6407 (2003).

[21] J. Huot, M. L. Tremblay, and R. Schulz, J. Alloy. Compd. **356**, 603 (2003).

[22] P. W. Atkins, *Physical Chemistry*, 6 ed. (Oxford University Press, Oxford, 1998).

[23] G. Sandrock, J. Alloy. Compd. **295**, 877 (1999).

[24] W. Grochala and P. P. Edwards, Chem. Rev. **104** (3), 1283 (2004).

[25] D. G. Ivey and D. O. Northwood, J. Mater. Sci. **18** (2), 321 (1983).
[26] A. J. Maeland, Int. J. Hydrog. Energy **28** (8), 821 (2003).
[27] B. Bogdanovic, R. A. Brand, A. Marjanovic, M. Schwickardi, and J. Tolle, J. Alloy. Compd. **302** (1-2), 36 (2000).
[28] B. Bogdanovic and G. Sandrock, MRS Bull. **27** (9), 712 (2002).
[29] K. J. Gross, G. J. Thomas, and C. M. Jensen, J. Alloy. Compd. **330**, 683 (2002).
[30] G. Sandrock, K. Gross, and G. Thomas, J. Alloy. Compd. **339** (1-2), 299 (2002).
[31] D. L. Sun, T. Kiyobayashi, H. T. Takeshita, N. Kuriyama, and C. M. Jensen, J. Alloy. Compd. **337**, L8 (2002).
[32] B. Bogdanovic and M. Schwickardi, J. Alloy. Compd. **253**, 1 (1997).
[33] B. Bogdanovic, M. Felderhoff, S. Kaskel, A. Pommerin, K. Schlichte, and F. Schuth, Adv. Mater. **15** (12), 1012 (2003).
[34] K. J. Gross, G. Sandrock, and G. J. Thomas, J. Alloy. Compd. **330**, 691 (2002).
[35] G. Sandrock and R. C. Bowman, J. Alloy. Compd. **356**, 794 (2003).
[36] P. Jolibois, Compt. Rend. Acad. Sci. Paris **155**, 353 (1912).
[37] F. H. Ellinger, C. E. Holley, B. B. McInteer, D. Pavone, R. M. Potter, E. Staritzky, and W. H. Zachariasen, J. Am. Chem. Soc. **77** (9), 2647 (1955).
[38] J. F. Stampfer, C. E. Holley, and J. F. Suttle, J. Am. Chem. Soc. **82** (14), 3504 (1960).
[39] T. N. Dymova, Z. K. Sterlyadkina, and V. G. Safronov, Russ. J. Inorg. Chem. **6**, 389 (1961).
[40] A. San-Martin and F. D. Manchester, Bull. Alloy Phase Diagrams **8** (5), 431 (1987).
[41] T. Noritake, M. Aoki, S. Towata, Y. Seno, Y. Hirose, E. Nishibori, M. Takata, and M. Sakata, Appl. Phys. Lett. **81** (11), 2008 (2002).
[42] K. N. Semenenko, V. N. Verbestkii, Y. A. Kalashnikov, N. V. Temofeeva, and M. I. Ioffe, Vest. Mosk. Univ. Ser. 2 , Khim. **19**, 718 (1978).
[43] J. P. Bastide, B. Bonnetot, J. M. Letoffe, and P. Claudy, Mat. Res. Bull. **15**, 1215 (1980).
[44] K. Bohmhammel, B. Christ, and G. Wolf, Thermochim. Acta **310** (1-2), 167 (1998).
[45] B. Bogdanovic, K. Bohmhammel, B. Christ, A. Reiser, K. Schlichte, R. Vehlen, and U. Wolf, J. Alloy. Compd. **282** (1-2), 84 (1999).
[46] L. Belkbir, E. Joly, and N. Gerard, Int. J. Hydrog. Energy **6** (3), 285 (1981).
[47] R. K. Rajamani, P. Songfack, and B. K. Mishra, Powder Technol. **108** (2-3), 116 (2000).
[48] L. Takacs and J. S. McHenry, J. Mater. Sci. **41** (16), 5246 (2006).
[49] R. A. Varin, T. Czujko, and Z. Wronski, Nanotechnology **17** (15), 3856 (2006).
[50] R. A. Varin, S. Li, and A. Calka, J. Alloy. Compd. **376** (1-2), 222 (2004).
[51] F. C. Gennari, F. J. Castro, and G. Urretavizcaya, J. Alloy. Compd. **321** (1), 46 (2001).

[52] M. Song, D. Lee, and I. Kwon, Met. Mater. Int. **10** (1), 69 (2004).
[53] M. Terzieva, M. Khrussanova, P. Peshev, and D. Radev, Int. J. Hydrog. Energy **20** (1), 53 (1995).
[54] P. Tessier and E. Akiba, J. Alloy. Compd. **295**, 400 (1999).
[55] P. Selvam, B. Viswanathan, C. S. Swamy, and V. Srinivasan, Int. J. Hydrog. Energy **11** (3), 169 (1986).
[56] G. Barkhordarian, T. Klassen, and R. Bormann, J. Alloy. Compd. **407** (1-2), 249 (2006).
[57] R. W. P. Wagemans, J. H. van Lenthe, P. E. de Jongh, A. J. van Dillen, and K. P. de Jong, J. Am. Chem. Soc. **127** (47), 16675 (2005).
[58] J. Charbonnier, P. de Rango, D. Fruchart, S. Miraglia, L. Pontonnier, S. Rivoirard, N. Skryabina, and P. Vulliet, J. Alloy. Compd. **383** (1-2), 205 (2004).
[59] G. Liang, J. Huot, S. Boily, A. Van Neste, and R. Schulz, J. Alloy. Compd. **292** (1-2), 247 (1999).
[60] G. Liang, J. Huot, S. Boily, A. Van Neste, and R. Schulz, J. Alloy. Compd. **291** (1-2), 295 (1999).
[61] Z. Dehouche, R. Djaozandry, J. Huot, S. Boily, J. Goyette, T. K. Bose, and R. Schulz, J. Alloy. Compd. **305** (1-2), 264 (2000).
[62] L. Zaluski, A. Zaluska, and J. O. StromOlsen, J. Alloy. Compd. **253**, 70 (1997).
[63] L. Zaluski, A. Zaluska, P. Tessier, J. O. Strom-Olsen, and R. Schulz, J. Alloy. Compd. **217** (2), 295 (1995).
[64] A. Zaluska, L. Zaluski, and J. O. Strom-Olsen, J. Alloy. Compd. **288** (1-2), 217 (1999).
[65] F. von Zeppelin, H. Reule, and M. Hirscher, J. Alloy. Compd. **330**, 723 (2002).
[66] K. Yoshimura, Y. Yamada, and M. Okada, Surf. Sci. **566**, 751 (2004).
[67] P. Hjort, A. Krozer, and B. Kasemo, J. Alloy. Compd. **237** (1-2), 74 (1996).
[68] J. F. Pelletier, J. Huot, M. Sutton, R. Schulz, A. R. Sandy, L. B. Lurio, and S. G. J. Mochrie, Phys. Rev. B **63** (5), art. no. 052103 (2001).
[69] J. Huot, J. F. Pelletier, G. Liang, M. Sutton, and R. Schulz, J. Alloy. Compd. **330**, 727 (2002).
[70] J. Huot, J. F. Pelletier, L. B. Lurio, M. Sutton, and R. Schulz, J. Alloy. Compd. **348** (1-2), 319 (2003).
[71] G. Liang, S. Boily, J. Huot, A. Van Neste, and R. Schulz, J. Alloy. Compd. **268** (1-2), 302 (1998).
[72] M. Zhu, Y. Gao, X. Z. Che, Y. Q. Yang, and C. Chung, J. Alloy. Compd. **330**, 708 (2002).
[73] J. L. Bobet, E. Akiba, and B. Darriet, Int. J. Hydrog. Energy **26** (5), 493 (2001).
[74] P. Tessier and E. Akiba, J. Alloy. Compd. **302** (1-2), 215 (2000).
[75] J. F. R. de Castro, S. F. Santos, A. L. M. Costa, A. R. Yavari, W. J. Botta F., and T. T. Ishikawa, J. Alloy. Compd. **376**, 251 (2004).
[76] P. Wang, A. M. Wang, H. F. Zhang, B. Z. Ding, and Z. Q. Hu, J. Alloy. Compd. **313**, 218 (2000).

[77] G. Barkhordarian, T. Klassen, and R. Bormann, Scr. Mater. **49** (3), 213 (2003).
[78] G. Barkhordarian, T. Klassen, and R. Bormann, J. Alloy. Compd. **364** (1-2), 242 (2004).
[79] O. Friedrichs, J. C. Sanchez-Lopez, C. Lopez-Cartes, T. Klassen, R. Bormann, and A. Fernandez, J. Phys. Chem. B **110**, 7845 (2006).
[80] D. Fatay, A. Revesz, and T. Spassov, J. Alloy. Compd. **399** (1-2), 237 (2005).
[81] J. L. Bobet, S. Desmoulins-Krawiec, E. Grigorova, F. Cansell, and B. Chevalier, J. Alloy. Compd. **351** (1-2), 217 (2003).
[82] Z. Dehouche, T. Klassen, W. Oelerich, J. Goyette, T. K. Bose, and R. Schulz, J. Alloy. Compd. **347** (1-2), 319 (2002).
[83] M. Song, I. Kwon, S. Kwon, C. Park, H. Park, and J. S. Bae, Int. J. Hydrog. Energy **31** (1), 43 (2006).
[84] M. Guvendiren, E. Bayboru, and T. Ozturk, Int. J. Hydrog. Energy **29** (5), 491 (2004).
[85] A. S. Pedersen, J. Kjoller, B. Larsen, B. Vigeholm, and J. A. Jensen, Int. J. Hydrog. Energy **9** (9), 799 (1984).
[86] B. Bogdanovic and B. Spliethoff, Int. J. Hydrog. Energy **12** (12), 863 (1987).
[87] G. Friedlmeier, A. Manthey, M. Wanner, and M. Groll, J. Alloy. Compd. **231** (1-2), 880 (1995).
[88] B. D. Cullity and S. R. Stock, *Elements of X-ray Diffraction*, 3rd ed. (Prentice Hall, 2001).
[89] D. Briggs and M. P. Seah, *Practical Surface Analysis: Auger and X-ray Photoelectron Spectroscopy*, 2nd ed. (John Wiley and Sons Ltd., 1992).
[90] Sivasanker, in *Catalysis Principles and Applications*, edited by B. Viswanathan, S. Sivasanker, and A.V. Ramaswamy (Narosa Publishing, New Delhi, 2002), pp. 362.
[91] S. D. Jackson, D. Lennon, and J. M. McNamara, in *Catalysis in Application*, edited by S.D. Jackson, J.S.J. Hargreaves, and D. Lennon (The Royal Society of Chemistry, Cambridge, 2003), pp. 39.
[92] A. K. Aboul-Gheit, S. M. Abdel-Hamid, and A. E. Awadallah, in *Catalysis in Application*, edited by S.D. Jackson, J.S.J. Hargreaves, and D. Lennon (The Royal Society of Chemistry, Cambridge, 2003), pp. 186.
[93] E. Finocchio, G. Busca, S. Rossini, U. Cornaro, V. Piccoli, and R. Miglio, Catal. Today **33** (1-3), 335 (1997).
[94] C. Hernandez and A. C. Pierre, J. Sol-Gel Sci. Technol. **20** (3), 227 (2001).
[95] H. R. Sahu and G. R. Rao, Bull. Mater. Sci. **23** (5), 349 (2000).
[96] S. Doniach and M. Sunjic, J. Phys. C Solid State Phys. **3** (2), 285 (1970).
[97] F. X. Zhang, J. X. Chen, X. Zhang, W. L. Gao, R. C. Jin, and N. J. Guan, Catal. Today **93-95**, 645 (2004).
[98] A. Ermolieff, P. Bernard, S. Marthon, and P. Wittmer, Surf. Interface Anal. **11** (11), 563 (1988).

[99] D. Gonbeau, C. Guimon, G. Pfisterguillouzo, A. Levasseur, G. Meunier, and R. Dormoy, Surf. Sci. **254** (1-3), 81 (1991).
[100] D. L. Trimm and A. Stanislaus, Appl. Catal. **21** (2), 215 (1986).
[101] J. E. Shelby, *Introduction to glass science and technology*, 2nd ed. (The Royal Society of Chemistry, Cambridge, 2005).
[102] M. Nguefack, A. F. Popa, S. Rossignol, and C. Kappenstein, Phys. Chem. Chem. Phys. **5** (19), 4279 (2003).
[103] S. L. Hietala, D. M. Smith, C. J. Brinker, A. J. Hurd, A. H. Carim, and N. Dando, J. Am. Ceram. Soc. **73** (10), 2815 (1990).
[104] A. Gutierrez-Alejandre, M. Trombetta, G. Busca, and J. Ramirez, Microporous Mater. **12**, 79 (1997).
[105] S. Sivakumar, C. P. Sibu, P. Mukundan, P. K. Pillai, and K. G. K. Warrier, Mater. Lett. **58** (21), 2664 (2004).
[106] P. Cheng, M. P. Zheng, Q. Huang, Y. P. Jin, and M. Y. Gu, J. Mater. Sci. Lett. **22** (16), 1165 (2003).
[107] J. M. G. Amores, V. S. Escribano, and G. Busca, J. Mater. Chem. **5** (8), 1245 (1995).
[108] L. Yi, G. Ramis, G. Busca, and V. Lorezelli, J. Mater. Chem. **4** (11), 1755 (1994).
[109] R. D. Shannon and J. A. Pask, J. Am. Ceram. Soc. **48** (8), 391 (1965).
[110] C. N. R. Rao, A. Turner, and J. M. Honig, J. Phys. Chem. Solids **11** (1-2), 173 (1959).
[111] E. David, J. Mater. Process. Technol. **162**, 169 (2005).
[112] J. Huot, I. Swainson, and R. Schulz, Ann. Chim. Sci. Mat. **31** (1), 135 (2006).
[113] J. F. Fernandez and C. R. Sanchez, J. Alloy. Compd. **340** (1-2), 189 (2002).
[114] B. Vigeholm, K. Jensen, B. Larsen, and A. S. Pedersen, J. Less-Common Met. **131**, 133 (1987).
[115] O. Friedrichs, J. C. Sanchez-Lopez, C. Lopez-Cartes, M. Dornheim, T. Klassen, R. Bormann, and A. Fernandez, Appl. Surf. Sci. **252** (6), 2334 (2006).
[116] T. Klassen, W. Oelerich, and R. Bormann, in *Metastable, Mechanically Alloyed and Nanocrystalline Materials, Ismanam-2000* (2001), Vol. 360-3, pp. 603.
[117] M. H. Grosjean, M. Zidoune, L. Roue, and J. Y. Huot, Int. J. Hydrog. Energy **31** (1), 109 (2006).
[118] A. Karty, J. Grunzweiggenossar, and P. S. Rudman, J. Appl. Phys. **50** (11), 7200 (1979).
[119] J. S. Han, M. Pezat, and J. Y. Lee, J. Less-Common Met. **130**, 395 (1987).
[120] C. M. Stander, J. Inorg. Nucl. Chem. **39** (2), 221 (1977).
[121] P. Peshev, M. Khrussanova, D. Chakarov, M. Terzieva, and T. Marinova, Mat. Res. Bull. **24** (2), 207 (1989).
[122] J. E. Rekoske and M. A. Barteau, J. Phys. Chem. B **101** (7), 1113 (1997).